

Jane J. Meiforth

**New Zealand kauri trees – Identification and canopy stress analysis with optical
remote sensing and LiDAR data**

A thesis submitted in fulfilment of a joint PhD agreement for the degrees:

Doctor of Philosophy (Dr Phil.)

at the University of Canterbury, New Zealand

School of Forestry

Main supervisor: Professor Dr David Norton

Examiner / Berichterstatter: Dr Bradley Case

and

Doctor rerum naturalium (Dr rer. nat.)

at Trier University, Germany

Faculty VI, Environmental Remote Sensing and Geoinformatics

Main supervisor: Professor Dr Joachim Hill

Examiner / Berichterstatter:

Dr Martin Schlerf

8. October 2020

Acknowledgments

My sincere thanks go to all people and institutions who supported this project! It would not have been possible without you!

First of all, I like to thank my main supervisors, Univ.-Prof. Joachim Hill and Univ.-Prof. David Norton at the Universities of Trier and Canterbury for their ongoing support and advice. Joachim, you taught me not only science background but also showed me the art of storytelling in science, which made your presentations and the discussions with you always both entertaining and instructive. David, you were my anchor to the Canterbury University, and I would not have made it without your experienced guidance and support – many thanks! I am grateful to my co-supervisors Dr Henning Buddenbaum (University of Trier) and Dr James Shepherd (Manaaki Whenua Landcare Research) for believing in me, your prompt responses and your valuable help. Dr Justin Morgenroth (University of Trier) and Dr Michael Watt (Scion) were involved in the first part of the project. I enjoyed our discussions and hope that we can cooperate in the future.

Both the setup at two Universities, the extensive data collection and technical delays etc. posed challenges to the administration. My special thanks go to Univ.-Prof. Bruce Manley, Jeanette Allen, Vicki Wilton and Michelle van Rheede at the University of Canterbury, as well as Nichole Gellner, Dr Achim Röder and Dr Johannes Stoffels at the University of Trier for your patience and professional support to master the administrative procedures and requirements.

This project would not have been possible without the assistance on the ground for the work and data collection in the Waitakere Ranges. I am grateful to Yue Chin Chew, Dr Nick Waipara and Lee Hill from Auckland Council, who helped to establish the project and provided data and support for the fieldwork. I would also like to thank the staff of the Arataki visitor centre, Fredrik Hjelm from Biosense / The Living Tree Company and Dr Joanne Peace for their excellent help and guidance during the fieldwork. And I like to thank the Kauri Dieback Programme (Planning and Intelligence Team) for constructive feedback and support during this research.

I very much enjoyed the time with my colleagues at the University of Trier. Thank you for your warm welcome, the inspiring discussions and our pleasant trips to the beautiful surroundings of Trier!

Last but most important, a sincere thanks to my family and friends for all your support, understanding, patience, encouragement and for just being there for me!

Funding

The Kauri Dieback Programme (NZ) funded most of the remote sensing data (Ministry for Primary Industries agreement no 17766). The University of Canterbury, the University of Trier and FrontierSI (former CRCSI) Australia and Landcare Research provided scholarships for living costs, fieldwork, equipment and additional LiDAR data. Digital Globe and Blackbridge provided grants for satellite data. Auckland Council supported the fieldwork and supplied LiDAR data and aerial images. Rapidlasso and Harris Geospatial helped with grants for software licenses. Landcare Research provided field equipment and salary for living costs. The first publication was funded by the Open Access Fund of the University of Trier and the German Research Foundation (DFG) within the Open Access Publishing funding programme. Landcare Research financed the publication costs of the 2nd and 3rd paper. Dr Henning Buddenbaum was supported within the framework of the EnMAP project (FKZ 50 EE 1530) by the German Aerospace Center (DLR) and the Federal Ministry of Economic Affairs and Energy.

Published material

The material covered in the Chapters II and III has previously been published in:

Meiforth, J.J.; Buddenbaum, H.; Hill, J.; Shepherd, J.; Norton, D.A. Detection of New Zealand Kauri Trees with AISA Aerial Hyperspectral Data for Use in Multispectral Monitoring. *Remote Sensing*. 2019, 11, 2865.

Meiforth, J.J.; Buddenbaum, H.; Hill, J.; Shepherd, J. Monitoring of Canopy Stress Symptoms in New Zealand Kauri Trees Analysed with AISA Hyperspectral Data. *Remote Sensing*. 2020, 12, 926.

Changes to the published version are marked with footnotes (pages 34, 50, 81).

The following publication in Chapter IV was submitted to the journal “Remote Sensing” and was still under review at the time of the submission of this thesis:

Meiforth, J.J.; Buddenbaum, H.; Hill, J.; Shepherd, J.; Dymond J. 2020: Stress Detection in New Zealand Kauri Canopies with WorldView-2 Satellite and LiDAR Data. *Remote Sensing*. 2020

Abstract (English)

The endemic New Zealand kauri trees (*Agathis australis* (D.Don) Lindl.) are a key species in New Zealand's northern indigenous forests. As one of the largest and longest-lived trees in the world, mature kauri are a tourist attraction and have high cultural significance for local Māori. However, the trees are threatened by the deadly kauri dieback disease (*Phytophthora agathidicida* (PA)). Over the last decade, PA has been detected throughout most of the kauri distribution area. PA is a soil-borne pathogen that enters the trees via the root system and causes collar rot, thereby blocking the transport of water and nutrients to the canopy, eventually killing the tree.

This thesis aims to develop methods based on remote sensing to automatically identify kauri trees and detect stress symptoms in their canopy. It is important to note that canopy stress symptoms are not proof of an infection. The reference data used here include 3165 precisely located crowns from three study sites in the Waitakere Ranges west of Auckland. They cover a representative range of both kauri and associated tree species in different forest ecotypes and stand situations. The selection of kauri crowns includes a range of phenological varieties, such as colour variants, growth stages and stress symptom levels.

The structure of this thesis follows three research questions, which form the basis of three scientific papers. The first paper aims to identify kauri trees with optical remote sensing. A distinct spectral pattern of kauri crowns could be discovered with the use of an airborne AISA Fenix hyperspectral image in the far near-infrared part of the spectrum. The paper presents a method to distinguish kauri with no to medium symptoms from dead and dying tree crowns and other canopy species with no to medium symptoms. High user's and producer's accuracies of 94.6% and 94.8% for the class "kauri" were achieved in a Random Forest classification using five spectral indices on five wavelengths (670–1209 nm). The kauri spectra showed a high separability to the spectra of 21 other canopy species and vegetation. However, the distinction between dead and dying trees and other tree species turned out to be more difficult. A minimum crown diameter of 3 m was defined for the 1 m pixel resolution to minimize the effect of mixed pixels. The overall accuracy (OA) for the three target classes could be improved from 91.7% to 93.8% by combining "kauri" and "dead/dying" trees into one class, separately classifying low and high forest stands and a binning to 10 nm bandwidths.

The second paper focuses on an analysis of reflectance patterns for different stress levels and growth stages in kauri crowns. The analysis was again based on hyperspectral images and 1258 manually edited reference crowns of "kauri" and "dead/dying" trees. The field assessment for stress symptoms was complemented with an evaluation of visible canopy symptoms in Red-Green-Blue (RGB) aerial images. An image guideline for stress assessment based on aerial images was developed. A Normalised Difference Vegetation Index (NDVI) in the near-infrared/red spectral range and indices with bands in the near-infrared

and red-edge were identified as the most important band combinations to describe the full range of stress responses. However, pigment-sensitive indices with bands in the green and red spectral ranges are more important for describing first stress symptoms and stress responses in smaller trees with denser foliage. Five indices on six bands in the visible to near-infrared region (450–970 nm) achieved a correlation of 0.93 with a Random Forest regression for the description of five stress symptom levels from non-symptomatic to dead. A stratified approach with individual models for pre-segmented low and high forest stands improved the overall performance. Additional bands in the far near-infrared region improved the root mean square error (RMSE) slightly from 0.43 to 0.42 but not the correlation.

In the third paper, the use of WorldView-2 satellite data (8 multispectral bands, 1.8 m pixel resolution pan-sharpened to 0.45 m) in combination with LiDAR data was tested for the stress detection with 1089 manually edited reference crowns of kauri and dead and dying trees. Five basic levels of canopy stress symptoms, from non-symptomatic to dead, were further refined for the first symptom stages based on field observations and aerial images. The minimum crown diameter for the use of WorldView-2 attributes for stress detection was defined as 4 m to avoid mixed pixels and to detect dying top branches in smaller crowns. Attributes from only the WorldView-2 image resulted in a correlation of 0.89 (RMSE 0.48, mean absolute error (MAE) 0.34) in a Random Forest regression for crowns larger than 4 m in diameter. This result can be improved to a correlation of 0.92 (RMSE 0.43, MAE 0.31) with additional LIDAR attributes, including intensity values. The selection of attributes confirms the findings from the second study, with an NDVI on near-infrared and red bands as the most important spectral index for the full range of stress symptoms. It also confirms the higher importance of pigment-sensitive indices with green, red and red-edge bands for the detection of first stress symptoms. These initial symptoms are more related to changes in the foliage than the crown architecture.

The results of this thesis present a methodical basis for kauri identification and stress detection using remote sensing data. The methods presented here require further testing and refinement with reference data in other forest areas and should be applied in the full processing chain with automatic crown-segmentation. However, when this has been done, remote sensing methods have considerable potential for automated monitoring of canopy stress symptoms in kauri trees.

Zusammenfassung (German)

Die endemischen Kauri Bäume Neuseelands (*Agathis australis* (D.Don) Lindl.) sind ein wichtiger Bestandteil der wenigen verbliebenen einheimischen Waldbestände im Norden des Landes. Als eine der größten Baumarten in Neuseeland sind sie eine Attraktion für Touristen und haben eine wichtige kulturelle und spirituelle Bedeutung für die indigene Bevölkerungsgruppe der Māori. Die aggressive und tödliche Baumkrankheit „*Phytophthora agathidicida*“ (PA) wurde innerhalb des letzten Jahrzehnts über weite Teile des Verbreitungsgebietes der Kauri Bäume nachgewiesen. Der Organismus lebt im Boden, er infiziert die Kauri Bäume über das Wurzelsystem und blockiert den Transport von Wasser und Nährstoffen in die Kronen. Ein Nachweis des Erregers ist bislang nur im Labor anhand von Bodenproben möglich. Das bisherige Monitoring stützt sich überwiegend auf Feldarbeit und der manuellen Auswertung von Luftbildern aus Flugzeugen und Helikoptern.

Diese Arbeit hat zum Ziel, anhand von Fernerkundungsdaten Methoden zu entwickeln, die sowohl die automatische Identifizierung der Kauri Bäume ermöglichen als auch eine Beschreibung von Stress-Symptomen im Kronenbereich der Bäume. Die Waitakere Ranges wurden als Studiengebiet ausgewählt, da sie Kauri Bestände in einer repräsentativen Verteilung bezüglich der Waldtypen, Bestandes Situation, Altersstufen und Symptomklassen beinhalten. Die Referenzdaten umfassen 3165 präzise lokalisierten Baumkronen in einer repräsentative Auswahl von Kauri und assoziierten Baumarten. Die Arbeit gliedert sich in drei Abschnitte: Der Identifizierung von Kauri Bäumen, der Analyse und Beschreibung von Stress-Symptomen in Kauri Kronen und der Anwendung von WorldView-2 Satellitendaten in Kombination mit LiDAR Daten zur Stressanalyse.

Im ersten Abschnitt geht es um die Identifizierung von Kauri Bäumen mittels optischer Fernerkundung. Anhand eines Hyperspektralbildes mit einem AISA Fenix Sensor konnte für die Kauri Kronen ein charakteristisches spektrales Muster im Nahen Infrarot Bereich nachgewiesen werden. Kauri Spektren zeigen eine hohe Differenzierbarkeit von 21 benachbarten Baumarten. Kauri Kronen bei denen die Kronenarchitektur noch intakt ist lassen sich in einer Random Forest Klassifizierung mit hoher Genauigkeit von über 94% (Nutzer- und Produzenten-Genauigkeit von 94.6% und 94.8%) von anderen Baumarten und Bäumen mit schweren Kronenschäden bzw. Totbäumen unterscheiden. Dieses Ergebnis beruht auf einer Auswahl von fünf Indizes auf fünf Wellenlängen im Sichtbaren bis Nahen Infrarot Bereich (670 - 1209 nm). Die Unterscheidung der stark geschädigten Kronen von anderen Baumarten ist hingegen nicht so eindeutig. Die Gesamtgenauigkeit für Kronen mit einem Mindestdurchmesser von 3 m konnte von 91.7% auf 93.8% gesteigert werden, indem die Kauri Bäume mit den stark geschädigten Bäumen zu einer Klasse zusammengefasst wurden, niedrige und hohe Waldbestände anhand separater Modelle analysiert wurden und die Wellenlängen der ausgewählten Indizes auf 10 nm Bandbreite gemittelt wurden.

Im Fokus des zweiten Manuskripts steht die Analyse und Beschreibung von Stress-Symptomen in Kronenspektren für unterschiedliche Größenklassen. Die Studie basiert auf dem Hyperspektralbild und 1258 manuell editierten Kronen von Kauri Bäumen und stark geschädigten Kronen bzw. Totbäumen. Die Beschreibung und Einschätzung von fünf Symptomstufen aus der Feldarbeit wurde anhand einer Luftbildauswertung ergänzt. Zu den wichtigsten Erkenntnissen der Studie gehört, dass Vegetationsindizes auf Wellenlängen im roten und nahen Infrarotbereich mit Band-Kombinationen im Nahen Infrarot und „Red-Edge“ die gesamte Bandbreite der Stress-Symptome am besten beschreiben. Hingegen sind pigment-sensitive Indizes mit Wellenlängen im grünen und roten Spektralbereich wichtig für die Beschreibung von kleinen Kronen mit dichtem Blattwerk. Fünf Indizes im Sichtbaren bis Nahen Infrarotbereich (450 – 970 nm) erreichten eine Korrelation von 0.93 in einer Random Forest Regression für fünf Symptomstufen. Dieses Ergebnis konnte in einem stratifizierten Ansatz für niedrige und hohe Waldbestände verbessert werden, während mit zusätzlichen Indizes im nahen Infrarot lediglich der RMSE leicht verbessert wurde von 0.43 auf 0.42, die Korrelation allerdings unverändert blieb.

Im dritten Manuskript wird die Eignung eines WorldView-2 (WV2) Satellitenbildes (8 Multispektralbänder, 1.8 m Auflösung, „pan-sharpened“ auf 0.45 m) in Kombination mit LiDAR Daten zur Beschreibung von Stress-Symptomen getestet. Die Referenzdaten umfassen eine Einstufung von 1089 Kronen in fünf Symptomstufen, mit einer feineren Unterteilung der ersten beiden Symptomstufen. Ein Minimum-Kronendurchmesser von 4 m wurde ermittelt für die Anwendung der WV2 Satellitendaten, zur Vermeidung von „mixed pixels“ und zur Erkennung von abgestorbenen Kronenspitzen in kleinen Baumkronen. Anhand von WV2 Attributen konnte eine Korrelation von 0.89 (RMSE 0.48, MAE 0.34) in einer kronenbasierten Random Forest Regression erzielt werden, während zusätzliche LiDAR Attribute zur Stressanalyse die Korrelation auf 0.92 steigerten (RMSE 0.43, MAE 0.31). Die ausgewählten Attribute bestätigen die Ergebnisse aus der Hyperspektralanalyse. Ein Vegetationsindex auf Bändern im roten und nahen Infrarot Bereich konnte als wichtigster Index zur Beschreibung der gesamten Bandbreite von Stress-Symptomen im Kronenbereich bestätigt werden, während pigment-sensitive Indizes mit Bändern im grünen, roten und „red-edge“ Spektrum, eine wichtige Bedeutung für die Beschreibung der ersten Stress-Symptome haben.

Die Ergebnisse dieser Studie beschreiben eine methodische Basis für die Identifizierung von Kauri Bäumen und die Beschreibung von Stress-Symptomen im Kronenbereich. Die präsentierten Methoden sollten in anderen Waldregionen und in einer vollständigen Prozessierung mit automatischer Kronensegmentierung getestet werden.

Co-Authorship declaration



Deputy Vice-Chancellor's Office
Postgraduate Research Office

Co-Authorship Form

This form is to accompany the submission of any thesis that contains research reported in co-authored work that has been published, accepted for publication, or submitted for publication. A copy of this form should be included for each co-authored work that is included in the thesis. Completed forms should be included at the front (after the thesis abstract) of each copy of the thesis submitted for examination and library deposit.

Please indicate the chapter/section/pages of this thesis that are extracted from co-authored work and provide details of the publication or submission from the extract comes:

The three papers were conducted as publications in co-authorship with members of Trier and Canterbury University and Manaaki Whenua Landcare research. See attached overview for details about the authors.

Please detail the nature and extent (%) of contribution by the candidate:

Jane Meiforth was the lead author for the conceptualization, methodology, data acquisition, analysis, writing and visualisation of the three papers. Her contribution was at least 90% of the total work. Please see overview in the attachment for detailed tasks performed by the authors.

Certification by Co-authors:

If there is more than one co-author then a single co-author can sign on behalf of all

The undersigned certifies that:

- The above statement correctly reflects the nature and extent of the Doctoral candidate's contribution to this co-authored work
- In cases where the candidate was the lead author of the co-authored work he or she wrote the text

Name: *Dr. Henning Buddenbaum* Trier, Germany Date: *11 May 2020*

Signature:

A handwritten signature in blue ink that reads 'Henning Buddenbaum'. The signature is written in a cursive style with a long, sweeping underline.

Attachment – overview over Author contributions

Paper 1 “Detection of New Zealand Kauri Trees with AISA Aerial Hyperspectral Data for Use in Multispectral Monitoring”

Authors: Jane J. Meiforth (J.M.), Henning Buddenbaum (H.B.), Joachim Hill (J.H.), James Shepherd (J.S.) and David A. Norton (D.N.)

Author Contributions: Conceptualisation, J.M.; methodology, J.M.; software, J.M.; validation, J.M.; formal analysis, J.M.; investigation, J.M.; resources, J.M. and J.S.; data curation, J.M.; writing—original draft preparation, J.M.; writing—review and editing, J.M., H.B., J.H., J.S. and D.N.; visualisation, J.M.; supervision, H.B., J.H., J.S. and D.N.; project administration, J.M. and D.N.; and funding acquisition, J.M., D.N. and J.H.

Paper 2 “Monitoring of canopy stress symptoms in New Zealand kauri trees - analysed with AISA hyperspectral data”

Authors: Jane J. Meiforth (J.M.), Henning Buddenbaum (H.B.), Joachim Hill (J.H.) and James Shepherd (J.S.)

Paper 2 Author Contributions: Conceptualization, J.M.; methodology, J.M.; software, J.M.; validation, J.M.; formal analysis, J.M.; investigation, J.M.; resources, J.M., J.S.; data curation, J.M.; writing—original draft preparation, J.M.; writing—review and editing, J.M., H.B., J.H., J.S.; visualisation, J.M.; supervision, H.B., J.H., J.S.; project administration, J.M., J.H.; funding acquisition, J.M., J.H., J.S.

Paper 3 “Stress Detection in New Zealand Kauri Canopies with WorldView-2 Satellite and LiDAR Data”

Authors: Jane J. Meiforth (J.M.), Henning Buddenbaum (H.B.), Joachim Hill (J.H.), James Shepherd (J.S.) and John Dymond (J.D.)

Paper 3 Author Contributions: Conceptualization, J.M., J.H., J.S., and J.D.; methodology, J.M., J.H., H.B.; software, J.M.; validation, J.M.; formal analysis, J.M.; investigation, J.M.; resources, J.M. and J.S.; data curation, J.M.; writing—original draft preparation, J.M.; writing—review and editing, J.M., H.B., J.H., J.S., and J.D.; visualization, J.M.; supervision, H.B., J.H., and J.S.; project administration, J.M. and J.H.; funding acquisition, J.M., J.H., J.S., and J.D.

Content

Acknowledgments.....	i
Funding.....	ii
Published material.....	ii
Abstract (English).....	iii
Zusammenfassung (German).....	v
Co-Authorship declaration.....	vii
Content.....	ix
List of Figures.....	x
List of Tables.....	xii
List of Abbreviations.....	xiii
Glossary.....	xiii
Chapter I.....	1
Introduction	
1 Kauri and kauri dieback in New Zealand.....	2
2 Kauri dieback monitoring.....	4
3 Remote sensing systems for forest species identification and stress analysis.....	4
4 Forest remote sensing in New Zealand.....	9
5 Objectives.....	10
6 Methodical approach.....	11
7 References.....	14
Chapter II.....	22
Detection of New Zealand Kauri Trees with AISA Aerial Hyperspectral Data for Use in Multispectral Monitoring	
Chapter III.....	55
Monitoring of Canopy Stress Symptoms in New Zealand Kauri Trees - analysed with AISA Hyperspectral Data	
Chapter IV.....	99
Stress Detection in New Zealand Kauri Canopies with WorldView-2 Satellite and LiDAR Data	
Chapter V.....	134
Synthesis	
1 Main findings.....	135
2 Conclusions and outlook.....	138
3 References.....	141
Appendix - Curriculum Vitae.....	142

List of Figures

Figure II-1 Kauri growth classes used in this study, depending on the mean crown diameter (cdm).....	26
Figure II-2 Location of the Waitakere Ranges on the North Island of New Zealand west of Auckland City.....	27
Figure II-3 Reference crowns (total 3165), used in the analysis, per class and diameter.....	30
Figure II-4 Mean spectra of the target classes “kauri”, “dead/dying” and “other” with standard deviations.....	32
Figure II-5 Jeffries–Matusita separability [61] of the three target classes for different spectral ranges.	33
Figure II-6 Mean spectra of kauri (thick black line) and six selected other canopy species (grey) that got most easily confused with kauri.	34
Figure II-7 Mean spectra of kauri and five other canopy species that have the highest separabilities from the kauri spectrum in this study.....	34
Figure II-8 Mean spectra of the target classes “kauri”, “dead/dying” and “other” with standard deviations.....	36
Figure II-9 Performance of selected indices and index combinations to identify the class “dead/dying” and to distinguish between “kauri” and “other vegetation” with an RF classification.....	38
Figure II-10 Performance of the final 4–8-band index combinations to distinguish the three target classes “kauri”, “dead/dying” and “other” canopy vegetation.	38
Figure II-11 RGB images of the three first bands of MNF transformations from (a) the VIS to NIR1 spectral range; (b) VIS to NIR2; and (c) the full spectral range from VIS to SWIR.	39
Figure II-12 Histograms for selected indices on sunlit pixels for all crown diameters, with the class “kauri” marked in light blue, the class “dead/dying” in red and the class “other” in dark blue.	39
Figure II-13 Overall accuracies for two selected sets of six and eight bands in the visible to NIR1 range.	40
Figure II-14 Combined results of 10 RF classifications with a 5-fold stratified random split with different seed values.....	42
Figure III-1 Kauri growth classes used in this study, according to the mean crown diameter.....	58
Figure III-2 Mature kauri stand in different foliage colour variations in the Waitakere Ranges shown in (a) oblique view and (b) nadir view.....	58
Figure III-3 Study sites in the Waitakere Ranges with reference crowns marked in orange.....	63
Figure III-4 Workflow for the preparation of crown-based attributes that were used in the analysis.	64
Figure III-5 Crown size classes of the reference crowns (total 1258), used in the analysis per low and high forest stand situation.....	67
Figure III-6 Inter-crown (a, b) and within-crown (c, d) spectral variability for the sunlit part of 189 non-symptomatic small kauri crowns (a, c) and 337 large kauri crowns with no visible stress symptoms (b, d).	70
Figure III-7 Mean spectra and standard deviation of kauri in three symptom classes: Non-symptomatic, medium symptoms and dead trees.....	71
Figure III-8 Spectra of kauri in three different size classes according to their mean crown diameter (cdm) sorted according to three symptom levels.	72

Figure III-9 Boxplot diagrams of the predicted values versus the actual reference crown values for crowns in all sizes classes.....	74
Figure III-10 Resulting maps (a, c, e) and corresponding RGB aerial images (b, d, f) (2016) of a pixel-based application of the baseline index combination for two forest stands with marked reference crowns and their reference symptom class values..	80
Figure IV-1 Kauri crown size classes: Small, medium, and large, as a profile on a Light Detection and Ranging (LiDAR) point cloud (a, b, c) and on 7.5 cm RGB aerial images below (d, e, f).	102
Figure IV-2 (a) Location of the Waitakere Ranges on the North Island of New Zealand west of Auckland City, with the natural range of kauri distribution and PA-positive samples. (b) Study sites and extent of the remote sensing datasets in the Waitakere Ranges, with reference crowns marked in orange.	103
Figure IV-3 Position of WV2 bands and kauri spectra for non-symptomatic, medium and dead crowns based on (a) the AISA hyperspectral image and (b) the pan-sharpened WV2 multispectral bands.....	108
Figure IV-4 Aerial images from (a) non-symptomatic, several states of decline (b-f), to (g) dead kauri in a medium-size (mean diameter 4 to 12.2 m).	110
Figure IV-5 Reference crowns in a high kauri stand (a) and a low stand (b), with symptom values from 1 = non-symptomatic to 5 = dead, on a NIR1-Green-Blue composite of the WorldView-2 (WV2) image.....	111
Figure IV-6 Workflow diagram for the attribute calculation.	112
Figure IV-7 Raster datasets of selected attributes with reference crowns marked as red polygons with labelled stress values.....	114
Figure IV-8 Bar chart showing the absolute numbers of outliers (error > 1) in four crown diameter classes and five aggregated stress levels for a RF regression with nine attributes in a 10-fold cross validation.....	116
Figure IV-9. A combination of jitter- and boxplot diagrams for an RF regression on WV2 attributes for the seven stress levels, based on (a) crowns with a diameter larger than 3 m and (b) crowns with a diameter larger than 4 m.....	116
Figure IV-10 Boxplot for the predicted and actual values from an RF regression on the seven-level reference scheme for crowns with a diameter larger than 4 m (total 895).	117
Figure IV-11 Correlations (a) and RMSE (b) of WV2 and LiDAR attributes for an RF regression on seven stress symptom levels.....	119

List of Tables

Table II-1. Spectral ranges with wavelengths used in this study.....	25
Table II-2 Confusion matrix and user’s and producer’s accuracies for a RF classification of kauri and ten neighbouring tree species on the full hyperspectral range of the AISA image (first 25 bands of a 35 band MNF transformation) evaluated with a 10-fold cross-validation for the seed value 1.	35
Table II-3 Overview of selected indices for the identification of the three target classes in the visible to NIR1 spectral range (448–970 nm).	40
Table II-4 Overall accuracies with standard deviations of the default, test and final setups.....	43
Table III-1 Spectral ranges with wavelengths used in this study.	59
Table III-2 Overview of stress symptom classes in the reference crowns per size class according to the mean diameter.....	66
Table III-3 Indices and regression results for the full spectral range (VIS to SWIR2).	76
Table III-4 Indices and regression results for the VIS-NIR1 spectral range.	78
Table III-5 Index selection for the identification of kauri.....	79
Table III-6 Resulting correlations, mean absolute errors (MAE) and root mean squared errors (RMSE) for a Random Forest (RF), M5P and Linear Regression (LR) on a 5-band index combination in the VIS-NIR2 range, that was selected for the identification of kauri.....	79
Table IV-1 WorldView-2 image: Wavelengths, bandwidths, and spatial resolution	107
Table IV-2 Distribution of crown size classes according to their mean diameter per stress symptom level for the refined 7 step reference system with symptom levels from 1 = non-symptomatic to 5 = dead.....	110
Table IV-3. Test of different minimum crown diameters for WV2 attributes for all crowns for seven stress levels. 116	
Table IV-4. Selection of WV2 attributes and their importance for a description of the seven-level reference scheme for canopy stress symptoms.	117
Table IV-5 Performance of an RF regression for the basic five-level reference scheme and the refined reference scheme with seven stress levels based on WV2 attributes for crowns with a diameter larger than 4 m. 117	
Table IV-6 Confusion matrix for an RF classification to identify dead and dying trees (level 4 and 5) with WV2 and LiDAR attributes for crowns with a diameter larger than 4 m (895 total).....	118
Table IV-7 Performance of an RF regression for the first stress symptoms and seven stress levels with and without LiDAR attributes.....	119
Table IV-8 Selected attributes for a stress analysis with WV2 and LiDAR attributes for seven stress levels and the first symptoms of stress (level 1 to 3) for crowns with a diameter larger than 4 m.....	119
Table IV-9 Accuracies for an RF classification to identify dead and dying trees (level 4 and 5) with WV2 and LiDAR attributes for crowns with a diameter larger than 3 m and larger than 4 m.	120

List of Abbreviations

CHM	Crown Height Model	RE	RapidEye satellite
CV	Curriculum Vitae	RF	Random Forest
DBH	Stem Diameter at Breast Height	RMSE	Root Mean Squared Error
DSM	Digital Surface Model	SVM	Support Vector Machine
DTM	Digital Terrain Model	SWIR	Short-wave Infrared (1467 – 2337 nm*)
FWHM	Full width at half maximum	UAcc	User’s accuracy
GCP	Ground Control Point	VI	Vegetation Index
GNSS	Global Navigation Satellite System	VIS	Visible (437 – 700 nm)
GPS	Global Positioning System	WV2	WorldView-2 satellite
LiDAR	Light Detection and Ranging	WV3	WorldView-3 satellite
MAE	Mean Absolute Error		
MNF	Minimum Noise Fraction Transformation		
MPI	Ministry for Primary Industries		
NIR	Near-Infrared (700 – 1327 nm*)		
NIR1	First Near-Infrared (700 – 970 nm*)		
NIR2	Far Near-Infrared (970 – 1327 nm*)		
OA	Overall accuracy		
PAN	Panchromatic band		
PC	Principal component		
PA	Phytophthora agathidicida		
PAcc	Producer’s accuracy		
RGB	Red-Green-Blue		
RCP	Receive Channel Processing Function		

* wavelengths used in this study according to the bands in the AISA Fenix image

Glossary

10-fold cross-validation – A technique to evaluate predictive models by randomly partitioning the original sample into a 9 training subsamples to train the model, and one test set to evaluate it. The process is repeated 10 times, so that each of the 10 subsamples is used once as the validation data.

airborne imagery - Imagery taken from an aircraft or other flying object.

chlorophyll - A green photosynthetic pigment found in plants, algae, and cyanobacteria.

confusion matrix – A table layout that allows visualization of the performance of an algorithm. Each row of the matrix represents the instances in a predicted class while each column represents the instances in an actual class.

co-occurrence matrix - A matrix that is defined over an image to be the distribution of pixel values at a given offset as a texture measure.

correlation – statistical relationship between two variables.

crown-height model – ground normalized raster height model in a forest area, so that each raster cell represents the actual canopy height over the ground height.

deciduous tree – A tree that will lose its foliage for part of the year—typically during the fall season.

image destriping - Process of removing artificial stripes or streaks from images, caused e.g. by sensor anomalies.

endemic tree – A native tree restricted to a certain area.

epiphytes – Plants growing on another plant or object but are not parasitic as they derive their moisture and nutrients from their surrounding environment.

fluorescence - Emission of light by a substance that has absorbed light or other electromagnetic radiation.

Global Navigation Satellite System - A constellation of satellites providing signals from space that transmit positioning navigation and timing data to receivers.

ground control points - Points on the ground with known coordinates.

hyperplane - In geometry, a hyperplane is a subspace whose dimension is one less than that of its ambient space.

hyperspectral imaging - Collection and processing information from across the electromagnetic spectrum at a very large number of wavelengths.

leaf area index - The one-sided green leaf area per unit ground surface area in broadleaf canopies.

light detection and ranging - A remote sensing method that uses light in the form of a pulsed laser to measure distances to the earth.

linear regression - A linear approach to modelling the relationship between a dependent variable and one or more explanatory (independent) variables.

M5P regression – a combination of a conventional decision tree with linear regression functions at the nodes.

minimum noise transformation - a linear transformation of two separate principal components analysis rotations with the aim to reduce the dimensionality of a (hyperspectral) dataset and remove noise.

multispectral sensor – A sensor that measures reflected energy within usually 3 to 10 different specific bands of the electromagnetic spectrum.

Munsell Hue-, Saturation-, and Value-Transformation – A transformation of an image with red, green, and blue reflectance values to values of Hue, Saturation, and Value.

non-parametric classifiers – Classifiers that do not make distributional assumptions on the data.

object-based image analysis - Geospatial image analysis based on based on information from a set of similar pixels called objects or image objects.

ortho imagery - A uniform-scale image where corrections have been made for feature displacement such as building tilt and for scale variations caused by terrain relief, sensor geometry, and camera tilt.

orthorectification - Process of removing the effects of image perspective (tilt) and relief (terrain) effects for the purpose of creating a planimetrically correct image. The resultant orthorectified image has a constant scale wherein features are represented in their 'true' positions.

panchromatic image - Greyscale image based on a wide range of wavelengths of light, typically spanning a large part of the visible part of the spectrum.

terrain model - A mathematical representation (model) of the ground surface, in which a unique elevation value is assigned to each pixel.

pixel-based image analysis – Image analysis based on the spectral information in each pixel.

producer's accuracy - Map accuracy from the point of view of the map maker (the producer). It indicates how often real features on the ground are correctly shown on the classified map.

user's accuracy - Accuracy from the point of view of a map user. It indicates how often the class on the map will actually be present on the ground.

random forest - An ensemble learning method that constructs a multitude of decision trees and outputs the class that is the mode of the classes (classification) or mean prediction (regression) of the individual trees.

remote sensing - Process of detecting and monitoring the physical characteristics of an area by measuring its reflected and emitted radiation at a distance typically from satellite or aircraft.

spaceborne imagery – Imagery taken by a spacecraft like a satellite.

standard deviation - In statistics, the standard deviation is a measure of the amount of variation or dispersion of a set of values.

support vector machine – A non-parametric supervised learning model with representations of the examples as points in space. These are mapped so that the examples of the separate categories are divided by a gap that is as wide as possible. New examples are then mapped into that same space and predicted to belong to a category based on the side of the gap on which they fall.

digital surface model – A geospatial model that represents the earth's surface with absolute height values and includes all objects on it.

wrapper evaluation method – A feature selection method for attribute combinations with a specified machine learning algorithm based on a defined evaluation criterion. They use a search algorithm to search through the space of possible features and evaluate each subset by running a model on the subset. They can be computationally expensive and have a risk of over fitting to the model.

zonal statistic - Statistics on values of a raster within the zones of another dataset

Chapter I

Introduction

This chapter provides background information on the subject of kauri trees and kauri dieback disease (section 1) and current monitoring methods as well as user requirements for the monitoring (section 2). It also gives an overview of the use of different remote sensing systems for species identification and stress analysis, both internationally and in New Zealand, which informed the decisions for the sensors used in this study (sections 3 and 4). Based on this broader research context, the objectives and the structure of this study are derived in section 5. General methodical decisions regarding the study area, the analysis approach and field data are explained in section 6, as well as main challenges.

The following chapters (II-IV) present the three papers that describe the analyses undertaken for kauri identification and stress detection. The final Chapter (V) includes a synthesis, with a summary of the main findings and conclusions and an outlook for further research. References are listed at the end of each Chapter. A short Curriculum Vitae (CV) is provided in the appendix.

1 Kauri and kauri dieback in New Zealand

As an isolated southern archipelago, New Zealand has developed a unique native flora, and approximately 80% of the species are endemic [1,2]. Before the arrival of people in New Zealand, ca. 800 years ago, 80% of the land was covered in dense forest [3,4]. Historical fires, land clearing and logging [3] reduced the area of indigenous forests cover to approximately 23.9% of New Zealand's land surface area or just about 6.3 million hectares [5]. According to Steward 2010 [6], only about 7500 ha of primary forests remain, while the rest of the area is secondary forests.

The endemic New Zealand kauri trees (*Agathis australis* (D. Don) Lindl.) are an essential element of the evergreen indigenous forests of the northern North Island [2,7-10]. Kauri are New Zealand's only representative of the *Araucariaceae* family [8], with other members mainly found in the tropics and subtropics across the South Pacific and South-East Asia [6]. The natural distribution of kauri extends throughout the warm temperate to sub-humid climatic zones north of 38°07'S [8], from sea level up to approximately 360 m elevation [7]. Kauri were extensively logged from the 17th to the early 20th century by European settlers since they provide excellent timber. The logging left only scattered mature stands in areas with difficult access, such as ridges, steep slopes and remote valleys [6]. The actual distribution of kauri, therefore, is more an expression of logging and preservation activities than of ecological preferences [6].

Kauri trees grow both in mixed species-rich forests with podocarp and broadleaved species as well as in homogenous kauri dominated stands [11]. Young kauri often develop under cover of so-called nursery plants, such as kānuka (*Kunzea ericoides*). Forests with kauri are often structurally complex, with remains of primary stands and single mature trees combined with second-growth forests in different stages of

development [6,12].

The acidic, tannin-rich leaf litter of kauri influences the biochemical composition of the soil [13,14]. Kauri are a key species for these forest ecosystems and impact the species composition and nutrient cycle [10]. With a massive stem and heights between 30 and 50 m [6], occasionally reaching 60 m [1], mature kauri trees are among the largest tree species in New Zealand forests. The impressive appearance of mature kauri stands makes them a major tourist attraction. Also, the existing kauri stands are of high cultural and spiritual significance for the local Māori and are closely linked to their genesis beliefs [15].

Kauri dieback disease (*Phytophthora agathidicida* (PA)) is a soil-borne pathogen that was first confirmed by Beever et al. [16], published in 2009, as a new pathogen for New Zealand and was taxonomically described by Weir in 2015 [17]. There is evidence that the pathogen has affected kauri in New Zealand for several decades, but it was not detected earlier since it was first misidentified [18,19]. Its origin is still unknown. One theory is an import through plants and soil material from the Central and South Pacific Ocean region [20].

The disease is highly infectious for kauri trees of all ages and size classes [21,22]. It enters the tree through the roots and causes collar rot, which blocks the transport of water and nutrients to the canopy, leading to defoliation and ultimately killing the trees [23]. The first visible symptoms start in the top of the canopy as yellowing and leaf loss. They are difficult to assess from the ground, especially in high stands and with dense undergrowth. The occurrence of symptoms is often heterogenic within a kauri stand. In larger crowns, different parts of the canopy can show symptoms with varying levels of severity depending on the extent of the damage in the root and stem system. Other causes of stress (e.g. drought [24] and other diseases [22]) can both intensify the progress of PA and also cause similar symptoms in the canopy. Lausch et al. [25] discuss that ecosystems usually face the combined effects of multiple stress factors, with an increasing influence of climate change.

PA has spread throughout the kauri distribution area and threatens the New Zealand kauri species and associated forest ecosystems [16]. There are indications that the pathogen uses other tree species as hosts and can partly also affect these species [16,26]. PA was declared an unwanted organism in 2008 under New Zealand's Biosecurity Act (1993), and its management is a strategic priority of the New Zealand Conservation and Biosecurity Authorities [27].

2 Kauri dieback monitoring

Proof of the presence of the PA pathogen requires, for the time being, laboratory analysis of soil samples. The monitoring of the disease includes the location of kauri stands, an assessment of stress symptoms, evaluation of changes from the previous seasons, targeted soil sampling and laboratory analysis for proof of an infection [28-30].

Overview mapping to determine the location of kauri and evaluate canopy stress symptoms is currently based on a manual interpretation of orthophotos, photos taken from a helicopter and oblique aerial images [28,31]. These methods allow a flexible assessment, independent of cloud cover (e.g. with overview flights in spring to plan the fieldwork for the coming summer season). However, the current methods are elaborate and time-consuming, especially for large areas. Furthermore, several studies have confirmed that manual interpretation of stress symptoms is biased by the subjective judgement of the interpreter [32,33].

From a user perspective, stress assessment should ideally be objective, repeatable, cost-efficient across all scales and able to detect the full range of symptom stages from non-symptomatic to dead. The description of the first signs of stress in kauri canopies is especially important to inform the implementation of early measures to prevent further spread. With regard to an often heterogenic manifestation of stress symptoms in kauri stands, the analysis should, if possible, allow for the assessment of single trees. The results should be spatially aligned with existing Light Detection and Ranging (LiDAR) data so that individual trees can be identified in the field (e.g. for targeted soil sampling).

3 Remote sensing systems for forest species identification and stress analysis

Remote sensing (RS) systems have been successfully used in numerous studies to identify forest species [34-36] and to describe canopy conditions [35,37-42]. Lausch et al. [25] provide a comprehensive overview of the characteristics of forest plants, populations and communities that can be described by space-borne remote sensing (“spectral traits”) and their variations (“spectral trait variations”). The identification of species and stress symptoms by RS is further elaborated in the introductory paragraphs of Chapters II and III. The following sections provide a general overview of space- and airborne RS systems suitable for monitoring kauri trees. Conclusions regarding the choice of sensors in this study are explained at the end of the paragraphs.

The selection of an appropriate set of remote sensing systems for kauri remote sensing should take into account their availability and spectral and spatial resolution according to the required object size and level of detail, available resources, the planned extent of the acquisition and terrain situations.

Unmanned aerial vehicles (UAV) systems are not included in this overview, since the limited coverage of UAV excludes their use in the scope of this study for large scale monitoring in often inaccessible terrain [43]. However, larger battery capacities and regulations for flights beyond the line of sight are under development and will increase the operational range of UAV systems [44].

3.1 Use of spaceborne optical sensors for tree species and stress detection

Spaceborne optical sensors are the most cost-efficient option to cover large areas. The standardised sensor models and a high percentage of nadir coverage ease the data processing [45], while fixed overflight times and reduced spectral and spatial resolutions present limitations [46]. Since the first missions in the early 1970s, the Landsat 1-5 TM and 7ETM+ sensors and from the late 1990s the Spot 4 and 5 sensors, are among the most widely used satellite systems to assess the health and composition of forest stands [40,45]. They cover basic red-green-blue (RGB) and near-infrared (NIR) wavelengths and have a spatial resolution between 10 and 30 m in the multispectral bands. Examples of the use of Landsat-derived indices are the assessment of foliar moisture levels in conifer forests [47] and the mapping of forest composition and structure in coastal Oregon, USA [48]. The spatiotemporal dynamics observed in time series of Landsat and Spot data proved to be useful for mapping forest stand compositions [49-51].

The launch of sensors with higher spatial resolution in the multispectral and panchromatic bands, such as Quickbird-2 in 1999 (0.6 to 2.8 m²) and IKONOS-2 in 2001 (1-4 m²), allowed for the inclusion of textural attributes and crown-level analysis. Spectral and spatial attributes of IKONOS imagery were used to investigate inventory data for homogenous forest stands, including species composition, crown closure and age [52,53]. Textural attributes derived from the IKONOS panchromatic channel improved the discrimination of three health levels in *Robinia* trees from 79.5% to 96.9% overall accuracy (OA) compared to only spectral attributes. The high spatial resolution of Quickbird-2 data also enabled object-based approaches for tree species identification [54], and to identify canopy symptoms of a fungal infection in *Pinus radiata* plantations [55].

Recent developments have increased the spectral resolution of commercially available spaceborne images. The launch of the 5-band RapidEye (RE) mission in 2009 and the 8-band WorldView-2 and -3 (WV2, WV3) missions in 2010 and 2014 introduced additional multispectral bands in the visible (VIS) to NIR range (RE 440–850nm, WV2 427–1040nm). In particular, an additional band in the red-edge region helps to detect a decline in photosynthetic activity [56-58]. The high spatial resolution in the panchromatic channels (RE 2.5 m and WV2 0.45 m) improved the description of structural forest attributes [59,60]. Immitzer et al. [61] used WV2 data to classify ten tree species with an OA of 82% in a temperate forest in Austria. Waser et al. [58] achieved an OA of 83% in classifying seven tree species in a mixed forest in

Germany, and Peerbhay et al. [62] distinguished six commercial forest species with an OA of 85.42%. This new generation of satellites also features higher temporal resolution with revisit times of one day for RE satellites and a combination of WV2 and WorldView-3 data. This increases the chance to acquire cloud-free images in a time series to capture, for example, seasonal changes for species identification [63,64] and to monitor temporal variations in stress responses [35,39,42,65,66].

A new generation of small satellites [67], such as the SkySat and PlanetScope constellations from the US-based company Planet [68], offer high spatial resolution images (1 to 3.7 m ground resolution) with high revisit times for comparably low costs. However, the lightweight CubeSat technology [69] reduces the spectral resolution, with only four bands (RGB and NIR) available for the standard imagery of the SkySat and PlanetScope constellations. The newly launched PlanetScope satellites also have a red-edge band [68].

Freely available, non-commercial satellites feature high spectral resolutions in the visible to short-wave infrared spectral regions. The Landsat-8 OLI sensor [70] has ten multispectral bands (433–1250 nm), and the Sentinel-2A sensor [71] has thirteen (443–2202 nm). However, the spatial resolutions (10 to 60 m for Sentinel-2A and 15 to 100 m for Landsat-8) are not suitable for single crown analysis and restrict the use of these sensors to stand-based analysis [72]. The use of Sentinel-2 to detect drought stress in deciduous forest communities in Germany was demonstrated by Dotzler et al. [73].

Several spaceborne hyperspectral missions are currently planned [74,75], such as ENMAP [76] and PRISMA [77]. However, the spatial resolution of 30 m is still too coarse for an assessment of the scattered distribution of kauri stands.

We decided to acquire a WV2 satellite image to test the suitability of spaceborne imagery for stress detection because of its high spatial and spectral resolution. The 1.8 m resolution of the multispectral bands and the 0.45 m resolution of the panchromatic band allowed a crown-based analysis with a pan-sharpened image. The high spectral resolution with, among others, a red-edge and two near-infrared bands in addition to standard bands are suitable for canopy stress detection. The high temporal frequency of one day for the combined WV2 and WV3 missions and the possibility to pre-order an image for a defined area made it possible to secure cloud-free images in the humid climate of the Waitakere Ranges. The WV2 image was acquired at the same as the hyperspectral image.

3.2 Use of airborne sensors for tree species- and stress detection

In contrast to spaceborne missions with fixed overflight times, airborne sensors operated from crewed aircraft allow higher spatial resolutions and offer more flexibility to acquire images on cloud-free days during time windows with high sun elevation. However, they are more expensive and elaborate to process.

Airborne hyperspectral sensors, such as the HySpex, HyMAP and AISA sensors, feature narrow bandwidths and cover wavelength intervals from the visible to short-wave infrared in a continuous spectral response. Hyperspectral airborne sensors have proven to be superior to the use of spaceborne multispectral sensors for forest tree species identification [34,78-83]. They also allow a detailed analysis of biochemical and biophysical canopy characteristics [36,84-88]. However, due to their high acquisition costs, complex system maintenance and elaborate image correction and processing requirements, they are used currently for detailed research studies rather than for repeated monitoring of large areas. In the context of forest species identification and stress monitoring, a value of airborne hyperspectral sensors lies in their use to detect characteristic spectral features and to identify the best bands and indices that describe these features. These selected bands can then be implemented for large-area coverage with multispectral airborne and spaceborne sensors. Several studies also used airborne hyperspectral data to simulate the performance of satellite data [73,89].

Airborne multispectral sensors have a limited number of bands; however, they are better suited for large-area monitoring than airborne hyperspectral sensors. They feature a wide field of view, large signal-to-noise ratio and lower costs for image acquisition and maintenance [25,34].

Airborne LiDAR technology provides accurate three-dimensional height point clouds from canopy to ground level [90-92]. As active sensor systems, LiDAR sensors are less dependent on weather conditions than optical sensors, and they operate under cloud cover. Airborne LiDAR data form the basis for the segmentation of homogenous forest stands [93,94] and individual tree crowns [95-100] as a pre-requisite for object-based canopy analysis [34,58,61,101]. LiDAR data has been used successfully to assess stress-induced structural changes in tree canopies caused by defoliation [99,102] and has proven to be especially useful for detecting deteriorated crowns of dying and dead trees [103-105]. However, in dense vegetation, only a few LiDAR signals reach the ground, which impairs the accuracy of the LiDAR height measures.

High accuracies up to 97% can be achieved with LiDAR data to distinguish between deciduous and coniferous trees [106] and to classify forest stands according to their structure [93,99]. Some studies successfully utilised LiDAR data for tree species identification [98,107-109]. However, the more common use for species identification is to add LiDAR attributes as additional spatial attributes to the spectral information of optical sensors [34,110-119]. The combination of LiDAR attributes and multi- and hyperspectral data also improved the assessment of forest health indicators [36,40]. The intensity information of LiDAR returns provides spectral information in the near-infrared, with the potential to improve the mapping of canopy compositions [107,120,121]. However, LiDAR surveys are expensive and thus not frequently available for regular monitoring.

For this study, we decided to acquire airborne hyperspectral imagery with an AISA Fenix sensor and airborne LiDAR data in combination with an aerial image.

Images from AISA hyperspectral sensors were successfully used in other studies for tree species identification and canopy stress detection (see Chapter IV-1.3). The full spectral range, from the visible to short-wave infrared (378–2495 nm) allows the analysis of the spectral response of kauri canopies in different growth and stress conditions as well as other canopy species. Spectral signatures for different tree species and crown conditions can be derived, which can be used for a spectral unmixing of imagery with larger pixel sizes like, e.g. Sentinel-2A. The 1 m pixel resolution of the AISA image is suitable for an object-based analysis on crown level. It also offers the possibility for resampling to simulate imagery with a coarser pixel resolution. Another purpose for the decision of this sensor was to test its useability in forest environments. The sensor was recently acquired by Massey University and is the first hyperspectral sensor operated from crewed aircraft by a New Zealand research institution.

The airborne LiDAR dataset provides height information which is uncorrelated to the optical data and allows to derive spatial attributes and perform a crown segmentation for an object-based approach. With a Laser Pulse Repetition Rate up to 800kHz, the RIEGL LMS-Q1560 LiDAR sensor used in this study delivers a high penetration rate in the dense forest vegetation, which resulted in sufficient ground returns (0.5 ground returns/m²) to generate a 1 m terrain model. An average of 35 returns/m² allows a detailed description of spatial crown attributes. The simultaneous acquisition of a 15 cm RGB aerial image secured a spatial match with the LiDAR data so that it could be used as a reference for the manual assessment of canopy stress symptoms and helped with the crown segmentation. Special care was given to an accurate, sub-pixel spatial alignment of the hyperspectral dataset with the LiDAR data by orthorectification with ground control points.

3.3 Analysis approaches with regards to scale

The decision for an object-based or pixel-based analysis is closely linked to the available spatial resolution of the remote sensing data and the size and spectral variance of the target objects.

An object-based approach allows the integration of contextual information like object statistics, textures, and neighbour relationships. It also makes it easier to combine different data sources, since they only must match on object scale, not pixel scale. The object-based statistics are well-suited to handling a high variance in target objects and are superior to pixel-based methods for single tree crown analysis (see Chapter IV-1.3). Prior object segmentation is elaborate and introduces mistakes of over- and under-segmentation. The analysis results in only one accumulated value per object. A change detection or any future comparison is bound to the use of the same object units. This approach requires a pixel size that is significantly smaller than the average size of the objects of interest, which excludes the currently freely available satellites for analysis on tree crown level. However, the fusion of multispectral bands with a

higher-resolution panchromatic channel, so-called PAN sharpening, allows the creation of a higher-spatial-resolution multispectral image.

A pixel-based approach, on the other hand, is easier to calculate since it does not require a prior object segmentation. The resulting map gives wall-to-wall information about the whole area. However, the integration of spatial information is more difficult, and it does not allow to use contextual information and object statistics. The pixel size should ideally match the spatial resolution of the target objects [66]. A higher spatial resolution increases the variability between neighbouring pixels and can cause a problematic “salt and pepper” effect [66]. Images with larger pixel sizes, in contrast, are more prone to classification errors caused by mixed reflectance values with the influence of shadows, understory vegetation and soil.

An intermediate approach is an object-based aggregation of a pixel-based analysis. Since the analysis is pixel-based, the size of the objects is more flexible and can also be changed for different reporting purposes. It delivers wall-to-wall information for the whole area, which gives a more comprehensive picture for a stress symptom analysis. And it allows the use of homogenous stand units, which are a lot easier to define from LiDAR data than a crown segmentation.

4 Forest remote sensing in New Zealand

Indigenous forests cover nearly 24% of New Zealand’s land surface area [122]. However, RS applications and research in New Zealand forest areas mainly provide information on introduced commercial forestry species (e.g. pine trees), with a predominant focus on LiDAR metrics from local acquisitions [123-127].

Native forest ecosystems have been analysed with spaceborne optical sensors in the scope of a nationwide land cover classification [122,128]. Other RS studies in New Zealand indigenous forests looked at mapping forest canopy conditions [129], mangrove types [130] and the segmentation of woody patches [131]. A few studies have been conducted to analyse the spectral responses of native shrubs and trees in New Zealand, including gorse [132] and oak trees [133]. Knowledge on optical properties of conifer versus broadleaf species are mainly based on studies in temperate forests in the Northern hemisphere (see Chapter III-1.2 for more details and literature). At the beginning of this study, no information on spectral properties of kauri crowns and neighbouring species was available in the literature, that could be used in the context of air- or spaceborne remote sensing.

A recent study focused on the identification of two native forest species showed promising results in a New Zealand primary forest with very high resolution (3 cm) RGB orthoimagery based on UAV acquisition [136]. UAV multispectral images also improved satellite-based stress detection in plantation trees [137,138]

and the detection of invasive conifers species [139]. Zhang [140] achieved an accuracy of approximately 80% in an object-based classification of regenerating bushland with a UAV-based true colour mosaic. Moreover, tower-based hyperspectral data helped to analyse herbicide damage in pine trees [141].

Airborne LiDAR data are becoming more available in New Zealand and offer the possibility for individual tree crown-segmentation in native forest ecosystems, as analysed by Zörner et al. [134]. LiDAR data was also used to analyse carbon stock in native New Zealand forest stands [135]. So far, no study has been published with an accurate automatic crown segmentation in native New Zealand kauri forests or a description of spatial attributes of kauri crowns, that could help with kauri identification based on remote sensing data.

Researchers in New Zealand only recently gained access to an airborne AISA hyperspectral sensor, which was mainly applied for precision agriculture in pasture lands [142,143] and land use classification [144]. So far, no studies have been published on the use of airborne hyperspectral data in native forest ecosystems in New Zealand.

5 Objectives

A holistic approach to forest health monitoring would ideally assess all main canopy species in a forest ecosystem [25,145]. However, this requires a more thorough investigation of the reflectance properties of New Zealand's indigenous tree species. Particularly since different species in other ecosystems have shown individual stress responses [146-148]. With regard to the fast progress and severity of kauri dieback disease, the limited framework of this PhD study focuses on kauri trees. The main objective is to develop methods based on RS to identify kauri crowns and to assess symptoms of stress in the upper canopy of kauri trees. The study was designed to result in recommendations to support cost-efficient monitoring that can be applied to larger areas. It is structured in three papers.

The first two papers address the lack of knowledge on spectral crown properties in kauri and associated tree species. They focus on a detailed spectral analysis of over 20 canopy species with an emphasis of kauri crowns in different growth stages and health classes, based on the hyperspectral image. The need of the management for large-scale implementation is addressed in these papers by defining methods for the kauri identification and stress detection on selected bands and index combinations, that are suitable for the use on airborne multispectral sensors. As a more cost-efficient solution, the third paper explores the use of a WV02 satellite image in combination with LiDAR data for object-based stress detection. According to the requirements from the management, the method emphasises the detection of first stress symptoms. The following objectives were defined:

Paper 1. “Detection of New Zealand Kauri Trees with AISA Aerial Hyperspectral Data for Use in Multispectral Monitoring”

- Objective 1: Identify and compare the spectra of kauri and associated canopy tree species with no to medium stress symptoms and analyse their spectral characteristics and separability.
- Objective 2: Identify and describe the best spectral indices for the separation of the three target classes “kauri”, “dead/dying trees” and “other” canopy vegetation.
- Objective 3: Define an efficient classification method to differentiate the three target classes that is applicable for large-area monitoring with multispectral sensors.

Paper 2. “Monitoring of Canopy Stress Symptoms in New Zealand Kauri Trees Analysed with AISA Hyperspectral Data”

- Objective 1: Identify the best band and index combinations to detect stress symptoms in kauri crowns for both the full spectral range (visible to short-wave infrared) and the visible to first NIR spectral range. The selected band combinations should not exceed six wavelengths to be suitable for a multispectral platform.
- Objective 2: Test the performance of a pre-defined band combination for stress detection, which was defined in Meiforth et al. [11], to locate kauri trees.
- Objective 3: Test the performance of the indices selections that was developed on mean crown values with a pixel-based approach.

Paper 3: “Stress Detection in New Zealand Kauri Canopies with WorldView-2 Satellite and LiDAR Data”

- Objective 1: Test the performance of WV2 attributes for crown-based stress detection in kauri trees and define the recommended minimum crown size.
- Objective 2: Test a two-step method on WV2 attributes by first identifying dead and dying trees in a classification and then applying a regression for the remaining stress symptom levels.
- Objective 3: Test the performance of LiDAR attributes in combination with WV2 data for canopy stress detection.

6 Methodical approach and challenges

While the choice of sensors was already discussed in section I-3, this Chapter highlights basic methodical decisions and challenges with regards to the study area and the fieldwork. Further details on the methods and analytical techniques are provided in the Chapters II-IV.

6.1 Choice of the study area

Three study sites in the Waitakere Ranges Heritage Area, northwest of central Auckland, were chosen for the data acquisition in cooperation with the Auckland Council kauri dieback surveillance team. The sites cover a range of kauri trees in different growth and health classes in a representative selection of forest stand situations and ecotypes [149]. A wide network of walking tracks allowed easy access to the investigated forest stands. Existing aerial images and LiDAR data and the results of ongoing fieldwork by Auckland Council staff provided a good foundation for preparing the study [28,31]. However, the influence of humid winds from the adjacent sea impeded the acquisition of cloud-free images. Further, the varied terrain, with steep slopes and elevations up to 336 m, posed challenges to the fieldwork and the accurate positioning of the reference crowns on the RS data.

6.2 Fieldwork and reference data

The high number of canopy species in kauri forests and the wide range of growth classes, stress symptoms, forest types and stand situations required a large number of reference crowns to capture these variations in a representative selection as well as statistically valid numbers. Extensive fieldwork over two seasons allowed the use of 3165 reference crowns for the analysis of species and stress levels as well as for detailed analysis of certain aspects of interest (e.g. early stress symptoms and species with a similar shape or foliage characteristics to kauri). However, the removal of crowns in shadow areas led to a different number of reference crowns in the hyperspectral and WorldView-2 datasets.

Special attention was given to accurate positioning of the reference crowns. A circular plot method with a mapping grade Global Navigation Satellite System (GNSS) was chosen to locate reference crowns during the first field season in dense forest stands with poor reception. A high resolution 15 cm RGB aerial image became available after the first field season. In combination with the LiDAR height models, this allowed for the direct identification of crowns in open stands during the second field season with a field tablet.

The large number of reference crowns in remote areas, and limited field capacity did not allow for quantitative measurements of canopy parameters, such as chlorophyll content or leaf area index. To minimise the subjective error related to manual assessment of canopy characteristics with different observers [33], standardised procedures and guidelines were followed, such as percentage ranges of crown coverage and dead branches by the Department of Conservation [152].

The high-resolution aerial images (15 cm and 7.5 cm), which eventually became available for both seasons, allowed the assessment of canopy stress symptoms, in accordance with other studies [153,154]. An

image guideline for the assessment of canopy stress symptoms in kauri trees based on aerial images was compiled for five stress levels in three growth classes. The 50 cm resolution of older digital RGB aerial images was found to be insufficient for locating small crowns and assessing the canopy condition.

6.3 Analysis approach

The intention of this study was to use a pixel-based approach where possible to avoid the dependency on an elaborate and error-prone automatic crown segmentation. For the kauri identification (Chapter II) a high spectral separability of kauri crowns to other canopy species allowed a pixel-based analysis. However, if the characteristic bands for the kauri identification are not available, a combination with LiDAR data in an object-based approach is necessary to obtain accuracies over 90%. A correspondent crown-based analysis for kauri identification with WV2 and LiDAR data was already conducted but could not be included in this thesis because of time restrictions for the submission.

For stress detection (Chapters III and IV), the analysis had to be crown-based to match the crown-based reference data. However, a first test of a pixel-based application of the model showed promising results. This option should be further explored to enable an easy to apply, wall-to-wall analysis of canopy stress symptoms, independent of a prior crown segmentation.

6.4 Main technical and organisational challenges

A main organisational challenge was a delay in the acquisition of the hyperspectral image with short notice for over a year from 2016 to 2017. Consequently, it does not match the LiDAR and aerial acquisitions from 2016. This delay required two field seasons with a repeated assessment of stress symptoms for all recorded kauri crowns. The data acquisition had been initially scheduled for the beginning of the summer season in late December to January to capture the phenologically more stable summer aspect of kauri forests and to avoid the influence of a possible drought. However, because of organisational, technical and weather constraints, the acquisitions in both seasons were delayed until March. Luckily, both summers were relatively moist, so no drought effects had affected the canopy conditions. From a technical perspective, the atmospheric correction and orthorectification of the hyperspectral image were a lot more elaborate and time-consuming than expected and lead to further delays in the time plan. Political differences between the stakeholders of the kauri dieback program during the time of this PhD posed additional challenges.

7 References

1. Allan, H.H.; Moore, L.B.; Edgar, E. *Flora of New Zealand*; RE Owen Wellington: 1961; Vol. 1.
2. McGlone, P.; Richardson, S.J.; Jordan, G.J. Comparative biogeography of New Zealand trees: species richness, height, leaf traits and range sizes. *N. Z. J. Ecol.* **2010**, *34*, 137–151.
3. Newsome, P. *The vegetative cover of New Zealand. Water & Soil Miscellaneous Publication 112*; Water and Soil Directorate, Ministry of Works and Development: Wellington, NZ, 1987.
4. Wardle, P. *Vegetation of New Zealand*; Cambridge University Press: Cambridge, UK, 1991.
5. Dymond, J.R.; Shepherd, J.D.; Newsome, P.F.; Belliss, S. Estimating change in areas of indigenous vegetation cover in New Zealand from the New Zealand Land Cover Database (LCDB). *N. Z. J. Ecol.* **2017**, *41*, 56–64.
6. Steward, G.A.; Beveridge, A.E. A review of New Zealand kauri (*Agathis australis* (D. Don) Lindl.): its ecology, history, growth and potential for management for timber. *New Zealand Journal of Forestry Science* **2010**, *40*, 33–59.
7. Cockayne, L. *The Vegetation of New Zealand*, 2nd ed.; Wilhelm Engelmann Verlag: Leipzig, Germany, 1928.
8. Ecroyd, C. Biological flora of New Zealand 8. *Agathis australis* (D. Don) Lindl. (Araucariaceae) Kauri. *N. Z. J. Bot.* **1982**, *20*, 17–36.
9. Wisser, S.K.; Hurst, J.M.; Wright, E.F.; Allen, R.B. New Zealand's forest and shrubland communities: a quantitative classification based on a nationally representative plot network. *Applied Vegetation Science* **2011**, *14*, 506–523.
10. Wyse, S.V.; Burns, B.R.; Wright, S.D. Distinctive vegetation communities are associated with the long-lived conifer *Agathis australis* (New Zealand kauri, Araucariaceae) in New Zealand rainforests. *Austral Ecol.* **2014**, *39*, 388–400.
11. Singers, N.J.; Rogers, G.M. A classification of New Zealand's terrestrial ecosystems. *Sci. Conserv.* **2014**, 325.
12. Burns, B.; Leathwick, J. Vegetation-environment relationships at Waipoua Forest, Northland, New Zealand. *N. Z. J. Bot.* **1996**, *34*, 79–92.
13. Silvester, W.; Orchard, T. The biology of kauri (*Agathis australis*) in New Zealand. Production, biomass, carbon storage, and litter fall in four forest remnants. *N. Z. J. Bot.* **1999**, *37*, 553–571.
14. Silvester, W.B. The biology of kauri (*Agathis australis*) in New Zealand 11. Nitrogen cycling in four kauri forest remnants. *N. Z. J. Bot.* **2000**, *38*, 205–220.
15. Nuttall, P.; Ngakuru, W.; Marsden, M. Te Roroa effects assessment for Kauri Dieback disease—(Phytophthora taxon *Agathis*—PTA). Report prepared for Te Roroa and the Kauri Dieback Joint Agency Response by Wakawhenua, 2010.
16. Beaver, R.E.; Waipara, N.W.; Ramsfield, T.D.; Dick, M.A.; Horner, I.J. Kauri (*Agathis australis*) under threat from *Phytophthora*. *Phytophthoras in Forests and Natural Ecosystems* **2009**, 74.
17. Weir, B.S.; Paderes, E.P.; Anand, N.; Uchida, J.Y.; Pennycook, S.R.; Bellgard, S.E.; Beaver, R.E. A taxonomic revision of *Phytophthora* Clade 5 including two new species, *Phytophthora agathidicida* and *P. coccois*. *Phytotaxa* **2015**, *205*, 21–38.
18. Gadgil, P.D. *Phytophthora heveae*, a pathogen of Kauri. *New Zealand Journal of Forestry Science* **1974**, *4*, 59–63.
19. Bellgard, S.; Weir, B.; Pennycook, S.R.; Paderes, E.P.; Winks, C.; Beaver, R.E.; Williams, S. Specialist phytophthora research: biology, pathology, ecology and detection of PTA. Final report for the New Zealand Ministry for Primary Industries, 2013.
20. Beauchamp, T.; Waipara, N. Surveillance and management of kauri dieback in New Zealand. In Proceedings of the 7th Meeting of the International Union of Forest Research Organizations (IUFRO), Working Party S07-02; p. 142.
21. Horner IJ, H.E. Pathogenicity of four *Phytophthora* species on kauri: in vitro and glasshouse trials. *New Zealand Plant Protection*, **2014**, *67*, 54–59.
22. Scott, P.; Williams, N. *Phytophthora* diseases in New Zealand forests. *NZ Journal of Forestry* **2014**, *59*, 14–21.
23. Bellgard, S.; Pennycook, S.; Weir, B.; Ho, W.; Waipara, N. *Phytophthora agathidicida*. *Forest Phytophthoras* **2016**, *6* (1) 8p. <http://dx.doi.org/10.5399/osu/fp.5.1.3748>
24. Macinnis-Ng, C.; Wyse, S.; Veale, A.; Schwendenmann, L.; Clearwater, M.J.T. Sap flow of the southern conifer, *Agathis australis* during wet and dry summer. *Trees* **2016**, *30*, 19–33. <https://doi.org/10.1007/s00468-015-1164-9>

25. Lausch, A.; Erasmi, S.; King, D.; Magdon, P.; Heurich, M. Understanding forest health with remote sensing-part I—a review of spectral traits, processes and remote-sensing characteristics. *Remote Sensing* **2016**, *8*, 1029.
26. Ryder, J.; Burns, B. What is the host range of *Phytophthora agathidicida* in New Zealand. In Proceedings of Plant Protection Society Conference 2016.
27. MPI. Kia toitu he kauri – keep kauri standing. New Zealand's strategy for managing kauri dieback disease. Report. 2014, 24. <https://www.kauridieback.co.nz/media/1393/kauri-diebackstrategy-2014-final-web.pdf>, accessed 01. May 2018
28. Waipara, N.; Hill, S.; Hill, L.; Hough, E.; Horner, I. Surveillance methods to determine tree health, distribution of kauri dieback disease and associated pathogens. *New Zealand Plant Protection* **2013**, *66*, 235–241.
29. McDougal, R.; Bellgard, S.; Scott, P.; Ganley, B. Comparison of a real-time PCR assay and soil bioassay technique for detection of *Phytophthora* taxon “*Agathis*” from soil. *Kauri Dieback Response, MPI Contract Report* **2014**, 53789.
30. Singh, J.; Curran-Cournane, F.; Waipara, N.; Schwendenmann, L.; Lear, G. *Comparison of methods used to detect the organism responsible for kauri dieback, Phytophthora agathidicida, from soil samples*; Technical Report, Auckland Council, 2017.
31. Jamieson, A.; Bassett, I.; Hill, L.; Hill, S.; Davis, A.; Waipara, N.; Hough, E.; Horner, I. Aerial surveillance to detect kauri dieback in New Zealand. *New Zealand Plant Protection* **2014**, *67*, 60–65.
32. Ghosh, S.; Innes, J.L.; Hoffmann, C. Observer variation as a source of error in assessments of crown condition through time. *For. Sci.* **1995**, *41*, 235–254.
33. Bock, C.; Poole, G.; Parker, P.; Gottwald, T. Plant disease severity estimated visually, by digital photography and image analysis, and by hyperspectral imaging. *Crit. Rev. Plant Sci.* **2010**, *29*, 59–107.
34. Fassnacht, F.E.; Latifi, H.; Stereńczak, K.; Modzelewska, A.; Lefsky, M.; Waser, L.T.; Straub, C.; Ghosh, A. Review of studies on tree species classification from remotely sensed data. *Remote Sensing of Environment* **2016**, *186*, 64–87.
35. Lausch, A.; Erasmi, S.; King, D.; Magdon, P.; Heurich, M. Understanding forest health with remote sensing-part II—a review of approaches and data models. *Remote Sensing* **2017**, *9*, 129.
36. Thenkabail, P.S.; Lyon, J.G.; Huete, A. *Fundamentals, Sensor Systems, Spectral Libraries, and Data Mining for Vegetation*; CRC Press, 2018.
37. Silva, C.R.; Olthoff, A.; de la Mata, J.A.D.; Alonso, A.P. Remote monitoring of forest insect defoliation. A review. *Forest Systems* **2013**, *22*, 377–391.
38. Smith, A.M.S.; Falkowski, M.J.; Greenberg, J.A.; Tinkham, W.T. Remote sensing of vegetation structure, function, and condition: special issue. *Remote Sensing of Environment* **2014**, *154*, 319–321, doi:10.1016/j.rse.2014.05.002.
39. Hall, R.; Castilla, G.; White, J.; Cooke, B.; Skakun, R.J. Remote sensing of forest pest damage: a review and lessons learned from a Canadian perspective. *The Canadian Entomologist* **2016**, *148*, S296–S356.
40. Pause, M.; Schweitzer, C.; Rosenthal, M.; Keuck, V.; Bumberger, J.; Dietrich, P.; Heurich, M.; Jung, A.; Lausch, A.J.R.S. In situ/remote sensing integration to assess forest health—a review. **2016**, *8*, 471.
41. Senf, C.; Seidl, R.; Hostert, P. Remote sensing of forest insect disturbances: current state and future directions. *International journal of applied earth observation and geoinformation* **2017**, *60*, 49–60.
42. Stone, C.; Mohammed, C. Application of remote sensing technologies for assessing planted forests damaged by insect pests and fungal pathogens: a review. *Current Forestry Reports* **2017**, *3*, 75–92.
43. Whitehead, K.; Hugenholtz, C.H.; Myshak, S.; Brown, O.; LeClair, A.; Tamminga, A.; Barchyn, T.E.; Moorman, B.; Eaton, B. Remote sensing of the environment with small unmanned aircraft systems (UASs), part 2: scientific and commercial applications. *Journal of Unmanned Vehicle Systems* **2014**, *2*, 86–102.
44. CAA. Drones - Webpage of the Civil Aviation Authority in New Zealand. Available online: <https://www.aviation.govt.nz/drones/> (accessed on 15 March 2020).
45. Wang, J.; Sammis, T.W.; Gutschick, V.P.; Gebremichael, M.; Dennis, S.O.; Harrison, R.E. Review of satellite remote sensing use in forest health studies. *The Open Geography Journal* **2010**, *3*, 28–42.
46. Kuenzer, C.; Ottinger, M.; Wegmann, M.; Guo, H.; Wang, C.; Zhang, J.; Dech, S.; Wikelski, M. Earth observation satellite sensors for biodiversity monitoring: potentials and bottlenecks. *International Journal of Remote Sensing* **2014**, *35*, 6599–6647.

47. Toomey, M.; Vierling, L.A. Multispectral remote sensing of landscape level foliar moisture: techniques and applications for forest ecosystem monitoring. *Canadian Journal of Forest Research* **2005**, *35*, 1087–1097.
48. Ohmann, J.L.; Gregory, M.J. Predictive mapping of forest composition and structure with direct gradient analysis and nearest-neighbor imputation in coastal Oregon, USA. *Canadian Journal of Forest Research* **2002**, *32*, 725–741.
49. Beck, R.N.; Gessler, P.E. Development of a Landsat time series for application in forest status assessment in the Inland Northwest United States. *Western Journal of Applied Forestry* **2008**, *23*, 53–62.
50. Puzzolo, V.; De Natale, F.; Giannetti, F. Forest species discrimination in an alpine mountain area using a fuzzy classification of multi-temporal SPOT (HRV) data. In Proceedings of IGARSS 2003, 2003 IEEE International Geoscience and Remote Sensing Symposium. IEEE Cat. No. 03CH37477; pp. 2538–2540.
51. Zhu, X.; Liu, D. Accurate mapping of forest types using dense seasonal Landsat time-series. *ISPRS Journal of Photogrammetry and Remote Sensing* **2014**, *96*, 1–11.
52. Chubey, M.S.; Franklin, S.E.; Wulder, M.A. Object-based analysis of Ikonos-2 imagery for extraction of forest inventory parameters. *Photogrammetric Engineering & Remote Sensing* **2006**, *72*, 383–394.
53. Kayitakire, F.; Hamel, C.; Defourny, P. Retrieving forest structure variables based on image texture analysis and IKONOS-2 imagery. *Remote Sensing of Environment* **2006**, *102*, 390–401.
54. Ke, Y.; Quackenbush, L.J.; Im, J. Synergistic use of QuickBird multispectral imagery and LIDAR data for object-based forest species classification. *Remote Sensing of Environment* **2010**, *114*, 1141–1154.
55. Poona, N.K.; Ismail, R. Discriminating the occurrence of pitch canker fungus in *Pinus radiata* trees using QuickBird imagery and artificial neural networks. *Southern Forests: A Journal of Forest Science* **2013**, *75*, 29–40.
56. Eitel, J.U.; Vierling, L.A.; Litvak, M.E.; Long, D.S.; Schulthess, U.; Ager, A.A.; Krofcheck, D.J.; Stoscheck, L. Broadband, red-edge information from satellites improves early stress detection in a New Mexico conifer woodland. *Remote Sensing of Environment* **2011**, *115*, 3640–3646.
57. Ortiz, S.; Breidenbach, J.; Kändler, G.J.R.S. Early detection of bark beetle green attack using TerraSAR-X and RapidEye data. **2013**, *5*, 1912–1931.
58. Waser, L.T.; Küchler, M.; Jütte, K.; Stampfer, T. Evaluating the potential of WorldView-2 data to classify tree species and different levels of ash mortality. *Remote Sensing* **2014**, *6*, 4515–4545.
59. Wallner, A.; Elatawneh, A.; Schneider, T.; Knoke, T. Estimation of forest structural information using RapidEye satellite data. *Forestry: An International Journal of Forest Research* **2015**, *88*, 96–107.
60. Pu, R.; Cheng, J. Mapping forest leaf area index using reflectance and textural information derived from WorldView-2 imagery in a mixed natural forest area in Florida, US. *International Journal of Applied Earth Observation and Geoinformation* **2015**, *42*, 11–23.
61. Immitzer, M.; Atzberger, C.; Koukal, T. Tree species classification with random forest using very high spatial resolution 8-band WorldView-2 satellite data. *Remote Sensing* **2012**, *4*, 2661–2693.
62. Peerbhay, K.Y.; Mutanga, O.; Ismail, R. Investigating the capability of few strategically placed Worldview-2 multispectral bands to discriminate forest species in KwaZulu-Natal, South Africa. *IEEE Journal of Selected Topics in Applied Earth Observations and Remote Sensing* **2013**, *7*, 307–316.
63. Hill, R.; Wilson, A.; George, M.; Hinsley, S. Mapping tree species in temperate deciduous woodland using time-series multi-spectral data. *Applied Vegetation Science* **2010**, *13*, 86–99.
64. Elatawneh, A.; Rappl, A.; Rehush, N.; Schneider, T.; Knoke, T. Forest tree species communities identification using multi phenological stages RapidEye data: case study in the forest of Freising. *From the basics to the service* **2013**, 21–38.
65. Verbesselt, J.; Robinson, A.; Stone, C.; Culvenor, D. Forecasting tree mortality using change metrics derived from MODIS satellite data. *For. Ecol. Manage.* **2009**, *258*, 1166–1173.
66. Meddens, A.J.; Hicke, J.A.; Vierling, L.A.J.R.S.o.E. Evaluating the potential of multispectral imagery to map multiple stages of tree mortality. **2011**, *115*, 1632–1642.
67. Chen, X.; Zhao, Y.; Zhu, X.; Bai, Y.; Zhang, Y. Micro/Nano-Satellites: opportunities and challenges. *Aerospace China* **2016**, *6*.

68. Planet-Labs-Inc. Planet imagery product specifications. Available online: https://assets.planet.com/docs/Planet_Combined_Imagery_Product_Specs_letter_screen.pdf (accessed on 4 October 2020).
69. Woellert, K.; Ehrenfreund, P.; Ricco, A.J.; Hertzfeld, H. Cubesats: Cost-effective science and technology platforms for emerging and developing nations. *Adv. Space Res.* **2011**, *47*, 663–684.
70. Markham, B.; Storey, J.; Morfitt, R. *Landsat-8 Sensor Characterization and Calibration*. Multidisciplinary Digital Publishing Institute, 2015.
71. Drusch, M.; Del Bello, U.; Carlier, S.; Colin, O.; Fernandez, V.; Gascon, F.; Hoersch, B.; Isola, C.; Laberinti, P.; Martimort, P. Sentinel-2: ESA's optical high-resolution mission for GMES operational services. *Remote Sensing of Environment* **2012**, *120*, 25–36.
72. Wang, H.; Pu, R.; Zhu, Q.; Ren, L.; Zhang, Z. Mapping health levels of Robinia pseudoacacia forests in the Yellow River delta, China, using IKONOS and Landsat 8 OLI imagery. *International Journal of Remote Sensing* **2015**, *36*, 1114–1135.
73. Dotzler, S.; Hill, J.; Buddenbaum, H.; Stoffels, J. The potential of EnMAP and Sentinel-2 data for detecting drought stress phenomena in deciduous forest communities. *Remote Sensing* **2015**, *7*, 14227–14258.
74. Transon, J.; d'Andrimont, R.; Maignard, A.; Defourny, P. Survey of hyperspectral earth observation applications from space in the sentinel-2 context. *Remote Sensing* **2018**, *10*, 157.
75. Hill, J.; Buddenbaum, H.; Townsend, P.A. Imaging spectroscopy of forest ecosystems: perspectives for the use of space-borne hyperspectral earth observation systems. *Surveys in Geophysics* **2019**, *40*, 553–588.
76. Guanter, L.; Kaufmann, H.; Segl, K.; Foerster, S.; Rogass, C.; Chabrillat, S.; Kuester, T.; Hollstein, A.; Rossner, G.; Chlebek, C. The EnMAP spaceborne imaging spectroscopy mission for earth observation. *Remote Sensing* **2015**, *7*, 8830–8857.
77. Loizzo, R.; Guarini, R.; Longo, F.; Scopa, T.; Formaro, R.; Facchinetti, C.; Varacalli, G. PRISMA: the Italian hyperspectral mission. In Proceedings of IGARSS 2018-2018 IEEE International Geoscience and Remote Sensing Symposium; pp. 175–178.
78. Carlson, K.M.; Asner, G.P.; Hughes, R.F.; Ostertag, R.; Martin, R.E. Hyperspectral remote sensing of canopy biodiversity in Hawaiian lowland rainforests. *Ecosystems* **2007**, *10*, 536–549.
79. Féret, J.-B.; Asner, G.P. Tree species discrimination in tropical forests using airborne imaging spectroscopy. *IEEE Transactions on Geoscience and Remote Sensing* **2013**, *51*, 73–84.
80. Baldeck, C.A.; Asner, G.P.; Martin, R.E.; Anderson, C.B.; Knapp, D.E.; Kellner, J.R.; Wright, S.J. Operational tree species mapping in a diverse tropical forest with airborne imaging spectroscopy. *PloS one* **2015**, *10*, e0118403.
81. Ferreira, M.P.; Zortea, M.; Zanotta, D.C.; Shimabukuro, Y.E.; de Souza Filho, C.R. Mapping tree species in tropical seasonal semi-deciduous forests with hyperspectral and multispectral data. *Remote Sensing of Environment* **2016**, *179*, 66–78.
82. Laurin, G.V.; Puletti, N.; Hawthorne, W.; Liesenberg, V.; Corona, P.; Papale, D.; Chen, Q.; Valentini, R. Discrimination of tropical forest types, dominant species, and mapping of functional guilds by hyperspectral and simulated multispectral Sentinel-2 data. *Remote Sensing of Environment* **2016**, *176*, 163–176.
83. Richter, R.; Reu, B.; Wirth, C.; Doktor, D.; Vohland, M. The use of airborne hyperspectral data for tree species classification in a species-rich Central European forest area. *International Journal of Applied Earth Observation and Geoinformation* **2016**, *52*, 464–474.
84. Asner, G.P. *Hyperspectral remote sensing of canopy chemistry, physiology, and biodiversity in tropical rainforests. Hyperspectral remote sensing of tropical and sub-tropical forests*; CRC Press: Boca Raton, FL, USA, 2008; pp. 261–296.
85. Ghiyam, A.; Shafri, H.Z. A review on hyperspectral remote sensing for homogeneous and heterogeneous forest biodiversity assessment. *International Journal of Remote Sensing* **2010**, *31*, 1837–1856.
86. Kaufmann, H.E.A. *Hyperspectral Algorithms: Report in the Frame of EnMAP Preparation Activities*; Deutsches GeoForschungsZentrum GFZ: Potsdam, 2010, Volume 10/08.
87. Jensen, J.R. *Introductory digital image processing : A remote sensing perspective*, 4th edition ed.; Glenview, IL Pearson Education, Inc: 2016.

88. Chavana-Bryant, C.; Malhi, Y.; Wu, J.; Asner, G.P.; Anastasiou, A.; Enquist, B.J.; Caravasi, E.G.C.; Doughty, C.E.; Saleska, S.R.; Martin, R.E. Leaf aging of Amazonian canopy trees as revealed by spectral and physiochemical measurements. *New Phytol.* **2017**, *214*, 1049–1063.
89. Clasen, A.; Somers, B.; Pipkins, K.; Tits, L.; Segl, K.; Brell, M.; Kleinschmit, B.; Spengler, D.; Lausch, A.; Förster, M. Spectral unmixing of forest crown components at close range, airborne and simulated Sentinel-2 and EnMAP spectral imaging scale. *Remote Sensing* **2015**, *7*, 15361–15387.
90. Wehr, A.; Lohr, U. Airborne laser scanning—an introduction and overview. *ISPRS Journal of Photogrammetry and Remote Sensing* **1999**, *54*, 68–82.
91. Popescu, S.C. Lidar remote sensing. *Advances in environmental remote sensing: Sensors, Algorithms, and Applications* **2011**, 57–84.
92. Sabatini, R.; Richardson, M.A.; Gardi, A.; Ramasamy, S. Airborne laser sensors and integrated systems. *Progress in Aerospace Sciences* **2015**, doi:10.1016/j.paerosci.2015.07.002.
93. Zimble, D.A.; Evans, D.L.; Carlson, G.C.; Parker, R.C.; Grado, S.C.; Gerard, P.D. Characterizing vertical forest structure using small-footprint airborne LiDAR. *Remote Sensing of Environment* **2003**, *87*, 171–182.
94. Koch, B.; Straub, C.; Dees, M.; Wang, Y.; Weinacker, H. Airborne laser data for stand delineation and information extraction. *International Journal of Remote Sensing* **2009**, *30*, 935–963, doi:10.1080/01431160802395284.
95. Vauhkonen, J.; Ene, L.; Gupta, S.; Heinzl, J.; Holmgren, J.; Pitkänen, J.; Solberg, S.; Wang, Y.; Weinacker, H.; Hauglin, K.M. Comparative testing of single-tree detection algorithms. *Proceedings of SilviLaser* **2010**, *14*, 17.
96. Kaartinen, H.; Hyypä, J.; Yu, X.; Vastaranta, M.; Hyypä, H.; Kukko, A.; Holopainen, M.; Heipke, C.; Hirschmugl, M.; Morsdorf, F. An international comparison of individual tree detection and extraction using airborne laser scanning. *Remote Sensing* **2012**, *4*, 950–974.
97. Jakubowski, M.; Li, W.; Guo, Q.; Kelly, M. Delineating individual trees from lidar data: a comparison of vector- and raster-based segmentation approaches. *Remote Sensing* **2013**, *5*, 4163–4186, doi:10.3390/rs5094163.
98. Cao, L.; Coops, N.C.; Innes, J.L.; Dai, J.; Ruan, H.; She, G. Tree species classification in subtropical forests using small-footprint full-waveform LiDAR data. *International Journal of Applied Earth Observation and Geoinformation* **2016**, *49*, 39–51.
99. Latifi, H.; Fassnacht, F.E.; Müller, J.; Tharani, A.; Dech, S.; Heurich, M. Forest inventories by LiDAR data: a comparison of single tree segmentation and metric-based methods for inventories of a heterogeneous temperate forest. *International Journal of Applied Earth Observation and Geoinformation* **2015**, *42*, 162–174, doi:10.1016/j.jag.2015.06.008.
100. Zhen, Z.; Quackenbush, L.J.; Zhang, L. Trends in automatic individual tree crown detection and delineation—evolution of LiDAR data. *Remote Sensing* **2016**, *8*, 333.
101. Weih, R.C.; Riggan, N.D. Object-based classification vs. pixel-based classification: Comparative importance of multi-resolution imagery. *The International Archives of the Photogrammetry, Remote Sensing and Spatial Information Sciences* **2010**, *38*, C7.
102. Solberg, S.; Næsset, E.; Hanssen, K.H.; Christiansen, E. Mapping defoliation during a severe insect attack on Scots pine using airborne laser scanning. *Remote Sensing of Environment* **2006**, *102*, 364–376.
103. Kim, Y.; Yang, Z.; Cohen, W.B.; Pflugmacher, D.; Lauver, C.L.; Vankat, J.L. Distinguishing between live and dead standing tree biomass on the North Rim of Grand Canyon National Park, USA using small-footprint lidar data. *Remote Sensing of Environment* **2009**, *113*, 2499–2510.
104. Kantola, T.; Vastaranta, M.; Yu, X.; Lyytikäinen-Saarenmaa, P.; Holopainen, M.; Talvitie, M.; Kaasalainen, S.; Solberg, S.; Hyypä, J. Classification of defoliated trees using tree-level airborne laser scanning data combined with aerial images. *Remote Sensing* **2010**, *2*, 2665–2679.
105. Vastaranta, M.; Kantola, T.; Lyytikäinen-Saarenmaa, P.; Holopainen, M.; Kankare, V.; Wulder, M.; Hyypä, J.; Hyypä, H. Area-based mapping of defoliation of Scots pine stands using airborne scanning LiDAR. *Remote Sensing* **2013**, *5*, 1220–1234.
106. Koenig, K.; Höfle, B. Full-Waveform airborne laser scanning in vegetation studies—a review of point cloud and waveform features for tree species classification. *Forests* **2016**, *7*, 198.

107. Korpela, I.; Ørka, H.O.; Maltamo, M.; Tokola, T.; Hyyppä, J. Tree species classification using airborne LiDAR—effects of stand and tree parameters, downsizing of training set, intensity normalization, and sensor type. *Silva Fenn.* **2010**, *44*, 319–339.
108. Li, J.; Hu, B.; Noland, T.L. Classification of tree species based on structural features derived from high density LiDAR data. *Agricultural and Forest Meteorology* **2013**, 171–172, 104–114, doi:10.1016/j.agrformet.2012.11.012.
109. Cao, L.; Coops, N.C.; Innes, J.L.; Dai, J.; Ruan, H.; She, G. Tree species classification in subtropical forests using small-footprint full-waveform LiDAR data. *International Journal of Applied Earth Observation and Geoinformation* **2016**, *49*, 39–51.
110. Leckie, D.; Gougeon, F.; Hill, D.; Quinn, R.; Armstrong, L.; Shreenan, R. Combined high-density lidar and multispectral imagery for individual tree crown analysis. *Canadian Journal of Remote Sensing* **2003**, *29*, 633–649.
111. Holmgren, J.; Persson, Å.; Söderman, U. Species identification of individual trees by combining high resolution LiDAR data with multi-spectral images. *International Journal of Remote Sensing* **2008**, *29*, 1537–1552.
112. Dinuls, R.; Erins, G.; Lorencs, A.; Mednieks, I.; Sinica-Sinavskis, J. Tree species identification in mixed Baltic forest using LiDAR and multispectral data. *IEEE Journal of Selected Topics in Applied Earth Observations and Remote Sensing* **2012**, *5*, 594–603.
113. Dalponte, M.; Bruzzone, L.; Gianelle, D. Tree species classification in the Southern Alps based on the fusion of very high geometrical resolution multispectral/hyperspectral images and LiDAR data. *Remote Sensing of Environment* **2012**, *123*, 258–270, doi:10.1016/j.rse.2012.03.013.
114. Ghosh, A.; Fassnacht, F.E.; Joshi, P.K.; Koch, B. A framework for mapping tree species combining hyperspectral and LiDAR data: role of selected classifiers and sensor across three spatial scales. *International Journal of Applied Earth Observation and Geoinformation* **2014**, *26*, 49–63.
115. Heinzel, J.; Koch, B. Investigating multiple data sources for tree species classification in temperate forest and use for single tree delineation. *International Journal of Applied Earth Observation and Geoinformation* **2012**, *18*, 101–110.
116. Latifi, H. *Characterizing Forest Structure by Means of Remote Sensing: A Review*; INTECH Open Access Publisher, 2012.
117. Ørka, H.O.; Gobakken, T.; Næsset, E.; Ene, L.; Lien, V. Simultaneously acquired airborne laser scanning and multispectral imagery for individual tree species identification. *Canadian Journal of Remote Sensing* **2012**, *38*, 125–138.
118. Sasaki, T.; Imanishi, J.; Ioki, K.; Morimoto, Y.; Kitada, K. Object-based classification of land cover and tree species by integrating airborne LiDAR and high spatial resolution imagery data. *Landsc. Ecol. Eng.* **2012**, *8*, 157–171.
119. Machala, M.; Zejdová, L. Forest mapping through object-based image analysis of multispectral and LiDAR aerial data. *European Journal of Remote Sensing* **2014**, *47*, 117–131.
120. Kim, S.; McGaughey, R.J.; Andersen, H.-E.; Schreuder, G. Tree species differentiation using intensity data derived from leaf-on and leaf-off airborne laser scanner data. *Remote Sensing of Environment* **2009**, *113*, 1575–1586.
121. Ørka, H.O.; Næsset, E.; Bollandsås, O.M. Classifying species of individual trees by intensity and structure features derived from airborne laser scanner data. *Remote Sensing of Environment* **2009**, *113*, 1163–1174.
122. Dymond, J.R.; Shepherd, J.D.; Newsome, P.F.; Gapare, N.; Burgess, D.W.; Watt, P. Remote sensing of land-use change for Kyoto Protocol reporting: the New Zealand case. *Environmental Science & Policy* **2012**, *16*, 1–8.
123. Tomppo, E.; Goulding, C.; Katila, M. Adapting Finnish multi-source forest inventory techniques to the New Zealand preharvest inventory. *Scand. J. For. Res.* **1999**, *14*, 182–192.
124. Stephens, P.R.; Kimberley, M.O.; Beets, P.N.; Paul, T.S.; Searles, N.; Bell, A.; Brack, C.; Broadley, J. Airborne scanning LiDAR in a double sampling forest carbon inventory. *Remote Sensing of Environment* **2012**, *117*, 348–357.
125. Watt, P.J.; Watt, M.S. Development of a national model of tree volume from LiDAR metrics for New Zealand. *Remote Sensing of Environment* **2013**, *34*, doi:10.1080/01431161.2013.798053.
126. Dash, J.P.; Marshall, H.M.; Rawley, B. Methods for estimating multivariate stand yields and errors using k-NN and aerial laser scanning. *Forestry* **2015**, *88*, doi:10.1093/forestry/cpu054.
127. Puliti, S.; Dash, J.P.; Watt, M.S.; Breidenbach, J.; Pearse, G.D. A comparison of UAV laser scanning, photogrammetry and airborne laser scanning for precision inventory of small-forest properties. *Forestry: An International Journal of Forest Research* **2020**, *93*, 150–162.

128. Dymond, J.R.; Shepherd, J.D. The spatial distribution of indigenous forest and its composition in the Wellington region, New Zealand, from ETM+ satellite imagery. *Remote sensing of Environment* **2004**, *90*, 116–125.
129. Trotter, C.M.; Brown, L.J. Monitoring forest canopy condition by remote sensing; Department of Conservation: 1999; Vol. 14.
130. Gao, J. A hybrid method toward accurate mapping of mangroves in a marginal habitat from SPOT multispectral data. *International Journal of Remote Sensing* **1998**, *19*, 1887–1899.
131. Müller, M.U.; Shepherd, J.D.; Dymond, J.R. Support vector machine classification of woody patches in New Zealand from synthetic aperture radar and optical data, with LiDAR training. *Journal of Applied Remote Sensing* **2015**, *9*, 095984.
132. Shepherd, J.; Lee, W. Satellite mapping of gorse at regional scales. *New Zealand plant protection* **2002**, 95–98.
133. Pairman, D. *Hyperspectral Trial for Oak Species Detection*. Landcare Research NZ, 2004; p. 36.
134. Zörner, J.; Dymond, J.R.; Shepherd, J.D.; Wisser, S.K.; Jolly, B. LiDAR-based regional inventory of tall trees—Wellington, New Zealand. *Forests* **2018**, *9*, 702.
135. Coomes, D.A.; Šafka, D.; Shepherd, J.; Dalponte, M.; Holdaway, R. Airborne laser scanning of natural forests in New Zealand reveals the influences of wind on forest carbon. *Forest Ecosystems* **2018**, *5*, 10.
136. Kattenborn, T.; Eichel, J.; Wisser, S.; Burrows, L.; Fassnacht, F.E.; Schmittlein, S. Convolutional Neural Networks accurately predict cover fractions of plant species and communities in Unmanned Aerial Vehicle imagery. *Remote Sensing in Ecology and Conservation* **2020**. doi: 10.1002/rse2.146
137. Dash, J.P.; Watt, M.S.; Pearse, G.D.; Heaphy, M.; Dungey, H.S. Assessing very high resolution UAV imagery for monitoring forest health during a simulated disease outbreak. *ISPRS Journal of Photogrammetry and Remote Sensing* **2017**, *131*, 1–14.
138. Dash, J.; Pearse, G.; Watt, M. UAV multispectral imagery can complement satellite data for monitoring forest health. *Remote Sensing* **2018**, *10*, 1216.
139. Dash, J.P.; Watt, M.S.; Paul, T.S.; Morgenroth, J.; Pearse, G.D. Early detection of invasive exotic trees using UAV and manned aircraft multispectral and LiDAR Data. *Remote Sensing* **2019**, *11*, 1812.
140. Zhang, Z.X. Native vegetation classification using remote sensing techniques: A case study of dairy flat regrowth bush by using the AUT Unmanned Aerial Vehicle. Auckland University of Technology, 2014.
141. Scholten, R.C.; Hill, J.; Werner, W.; Buddenbaum, H.; Dash, J.P.; Gallego, M.G.; Rolando, C.A.; Pearse, G.D.; Hartley, R.; Estarija, H.J. Hyperspectral VNIR-spectroscopy and imagery as a tool for monitoring herbicide damage in wilding conifers. *Biol. Invasions* **2019**, *21*, 3395–3413.
142. Yule, I.; Pullanagari, R.; Irwin, M.; McVeagh, P.; White, G.; Keresuturi, M.; Manning, M. Mapping nutrient concentration in pasture using hyperspectral imaging. *Journal of New Zealand Grasslands* **2015**, *77*, 47–50.
143. Cushnahan, T.; Yule, I.; Grafton, M.; Pullanagari, R.; White, M. The classification of hill country vegetation from hyperspectral imagery. In Science and policy: nutrient management challenges for the next generation., Fertilizer and Lime Research Centre, Massey University, Palmerston North, New Zealand., 2017; Vol. 30, p. 9.
144. Pullanagari, R.R.; Kereszturi, G.; Yule, I.J.; Ghamisi, P. Assessing the performance of multiple spectral–spatial features of a hyperspectral image for classification of urban land cover classes using support vector machines and artificial neural network. *Journal of Applied Remote Sensing* **2017**, *11*, 026009.
145. Lambert, S.; Waipara, N.; Black, A.; Mark-Shadbolt, M.; Wood, W. Indigenous biosecurity: Māori responses to kauri dieback and myrtle rust in Aotearoa New Zealand. In *The Human Dimensions of Forest and Tree Health*; Springer, 2018; pp. 109–137.
146. Beck, W.; Müller, J.; Eichhorn, J. Impact of heat and drought on tree and stand vitality—dendroecological methods and first results from Level II-plots in southern Germany. *Schriftenr. Forstl. Fak Univ. Göttingen und Nordwestdtsh. Forstl. Versuchsanst* **2007**, *142*, 120–128.
147. Lindenmayer, D.B.; Likens, G.E. Effective monitoring of agriculture. *J. Environ. Monit.* **2011**, *13*, 1559–1563.
148. Weber, P.; Bugmann, H.; Pluess, A.R.; Walthert, L.; Rigling, A. Drought response and changing mean sensitivity of European beech close to the dry distribution limit. *Trees* **2013**, *27*, 171–181.

149. Singers, N.; Osborne, B.; Lovegrove, T.; Jamieson, A.; Boow, J.; Sawyer, J.; Webb, C. Indigenous terrestrial and wetland ecosystems of Auckland. Auckland Council. Available online: <http://www.knowledgeauckland.org.nz>, (accessed on 20 July 2019).
150. Lee, J.; Cai, X.; Lellmann, J.; Dalponte, M.; Malhi, Y.; Butt, N.; Morecroft, M.; Schönlieb, C.-B.; Coomes, D.A. Individual tree species classification from airborne multisensor imagery using robust PCA. *Ieee Journal of Selected Topics in Applied Earth Observations and Remote Sensing* **2016**, *9*, 2554–2567.
151. Smigaj, M.; Gaulton, R.; Suárez, J.C.; Barr, S.L. Combined use of spectral and structural characteristics for improved red band needle blight detection in pine plantation stands. *For. Ecol. Manage.* **2019**, *434*, 213–223.
152. DOC. The Foliar Browse Index field manual. An update of a method for monitoring possum (*Trichosurus vulpecula*) damage to forest communities; Department of Conservation, Christchurch, New Zealand, 2014; p 56.
153. White, J.C.; Wulder, M.A.; Brooks, D.; Reich, R.; Wheate, R.D.J.R.S.o.E. Detection of red attack stage mountain pine beetle infestation with high spatial resolution satellite imagery. **2005**, *96*, 340–351.
154. Míchez, A.; Piégay, H.; Lisein, J.; Claessens, H.; Lejeune, P.J.E.m.; Classification of riparian forest species and health condition using multi-temporal and hyperspatial imagery from unmanned aerial system. **2016**, *188*, 146.

Chapter II

Detection of New Zealand Kauri Trees with AISA Aerial Hyperspectral Data for Use in Multispectral Monitoring

MDPI Remote Sensing 11 (23), 2865; December 2019

DOI 10.3390/RS11232865

Jane J. Meiforth, Henning Buddenbaum, Joachim Hill, James
Shepherd and David A. Norton

© 2019 by the authors. Submitted for open access publication
under the terms and conditions of the Creative Commons
Attribution (CC BY) license

<http://creativecommons.org/licenses/by/4.0/>.

The paper can be accessed at:

<https://www.mdpi.com/2072-4292/11/23/2865>

Abstract

The endemic New Zealand kauri trees (*Agathis australis*) are of major importance for the forests in the northern part of New Zealand. The mapping of kauri locations is required for the monitoring of the deadly kauri dieback disease (*Phytophthora agathidicida* (PTA)). In this study, we developed a method to identify kauri trees by optical remote sensing that can be applied in an area-wide campaign. Dead and dying trees were separated in one class and the remaining trees with no to medium stress symptoms were defined in the two classes “kauri” and “other”. The reference dataset covers a representative selection of 3165 precisely located crowns of kauri and 21 other canopy species in the Waitakere Ranges west of Auckland. The analysis is based on an airborne hyperspectral AISA Fenix image (437–2337 nm, 1 m² pixel resolution). The kauri spectra show characteristically steep reflectance and absorption features in the near-infrared (NIR) region with a distinct long descent at 1215 nm, which can be parameterised with a modified Normalised Water Index (mNDWI-Hyp). With a Jeffries–Matusita separability over 1.9, the kauri spectra can be well separated from 21 other canopy vegetation spectra. The Random Forest classifier performed slightly better than Support Vector Machine. A combination of the mNDWI-Hyp index with four additional spectral indices with three red to NIR bands resulted in an overall pixel-based accuracy (OA) of 91.7% for crowns larger 3 m diameter. While the user’s and producer’s accuracies for the class “kauri” with 94.6% and 94.8% are suitable for management purposes, the separation of “dead/dying trees” from “other” canopy vegetation poses the main challenge. The OA can be improved to 93.8% by combining “kauri” and “dead/dying” trees in one class, separate classifications for low and high forest stands and a binning to 10 nm bandwidths. Additional wavelengths and their respective indices only improved the OA up to 0.6%. The method developed in this study allows an accurate location of kauri trees for an area-wide mapping with a five-band multispectral sensor in a representative selection of kauri forest ecosystems.

1 Introduction

New Zealand kauri (*Agathis australis* (D.Don) Lindl. ex Loudon) are an important component of New Zealand's northern indigenous forests. The overall distribution of kauri is well known [1,2], but there is an urgent need to locate kauri crowns in more detail for monitoring the deadly kauri dieback disease (*Phytophthora agathidicida* (PTA)). Current methods for mapping of kauri rely on the manual interpretation of nadir and oblique aerial images and photos taken from a helicopter [3,4]. These manual interpretations of aerial images are elaborate and only suitable for smaller areas. Remote sensing enables large-area coverage in a more objective approach [5]. This study analysed the spectral characteristics of kauri crowns and developed a method to identify their exact position in an area-wide pixel-based analysis.

1.1 Research context

Remote sensing technology allows for automatic tree species discrimination based on reflectance signals with passive optical sensors and structural crown characteristics by active LiDAR sensors [6,7]. Multispectral sensors tend to have a limited number of bands, typically up to six, in the visible (VIS) to near-infrared (NIR) spectral range with a bandwidth of at least 10 nm, usually broader. Typically, they use two-dimensional staring arrays that are mounted in the focal plane, such as charge-coupled device elements [8]. Hyperspectral sensors can cover the whole spectral continuum up to the short-wave infrared (SWIR) range with a high number of narrow bands [9]. The bandwidth of hyperspectral sensors for airborne acquisitions is typically around 3 nm in the visible (VIS) to first near-infrared (NIR1) part of the spectrum (Table II-1) and around 10 nm in higher wavelengths. Airborne hyperspectral sensors usually use moving scanner lines in push broom or whiskbroom systems, although first snapshot hyperspectral cameras with staring arrays for airborne use are coming on the market [8–10].

Airborne hyperspectral remote sensing has proven useful in the analysis and identification of individual tree crowns in boreal and temperate [12–15] and subtropical to tropical forests [16–20]. The NIR bands (700 to 1327 nm in this study Table II-1) are important for species classification in tropical forests [16–18], which are perhaps more similar to kauri forests in terms of structural complexity [7]. The reduction of dimensionality and correlation in hyperspectral datasets can significantly improve the accuracy [21–23], as well as the extraction of the sunlit part of the crown [24,25]. An object-based classification can increase the accuracy by balancing the within crown variation, noise and illumination effects, and it allows to integrate additional structural and spatial crown statistics [26–28]. However, the whole processing chain for individual tree crown identification is complex, processing-intensive and error-prone, which can

compromise the advantages of an object-based approach [12,29]. The importance of additional LiDAR data describing height and structural crown characteristics has been confirmed in many studies [13,21,30,31]. However, texture measures can also be integrated based on optical data alone [32].

Table II-1 Spectral ranges with wavelengths used in this study, adapted from Asner [11] to match the used bands of the AISA sensor.

Spectral Range	Electromagnetic Wavelengths
Visible (VIS)	437–700 nm ¹
1st near-infrared (NIR1)	700–970 nm ²
2nd near-infrared (NIR2)	970–1327 nm
1st short-wave infrared (SWIR1)	1467–1771 nm
2nd short-wave infrared (SWIR2)	1994–2337 nm ¹

¹The useable bands of the AISA Fenix sensor cover the range between 437 and 2337 nm. ²The NIR1 range marks the shift between the two sensor parts at 970 nm.

Airborne multispectral sensors are, for the time being, better suited to cover large areas than hyperspectral sensors, with a wider field of view, a larger signal to noise ratio and a more robust technical setup. They are often operated in combination with LiDAR data for tree species classification [33–35]. Fassnacht et al. [34] recommended linking the analytical findings in the hyperspectral space with the operational advantages of multispectral sensors.

Most of the kauri in the study area grow in a more diverse second-growth forest [36]. The young growth form of this evergreen conifer is a conical shape with dense foliage (Figure II-1). They often develop under the protection of angiosperm nurse trees. Kauri leaves are linear, 2–5 cm long, with a smooth leather-like surface. They form a spiky foliage surface with single branches protruding. The leaf colour is less characteristic with variants from yellow- to blue-green [37]. Stressed foliage shows all stages of decline over yellow to brown. The spring aspect features bright green new-growth of kauri leaves [2] and an asynchronous flowering of other canopy species. The spectrally more stable summer aspect can be affected in drought years by early aging and dropping of leaves [38]. Dying stands of infected trees, climbers, vines and epiphytes add to the spectral and spatial complexity of kauri forests, which are, from a remote sensing perspective, more similar to subtropical and tropical forests than to other temperate forests [11,33].

The natural distribution of the endemic New Zealand conifer, kauri, extends over the warm temperate lowland forests of the upper North Island (Figure II-2), although its abundance has been severely impacted by logging associated with European settlement [2]. In the remaining patches of mature kauri forest, the upper canopy is dominated by large dome shape kauri with an open crown structure and scattered foliage (Figure II-1).

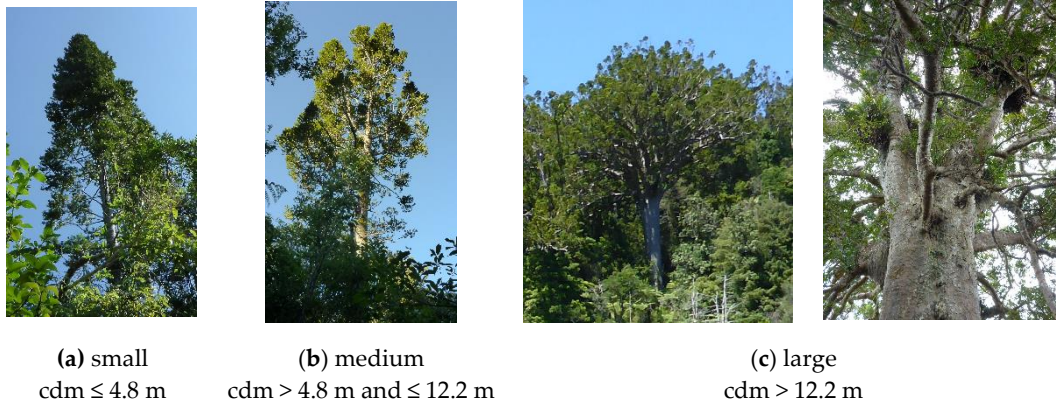


Figure II-1 Kauri growth classes used in this study, according to the mean crown diameter (cdm). (Photos: [39]).

1.2 Objectives and approach

The overall aim of this study was to develop a cost-efficient method to identify the location of kauri trees in New Zealand’s kauri forests based on optical remote sensing. The method should be applicable for wall-to-wall large-area monitoring with multispectral sensors. Dead and dying trees were mapped in a separate class since it was not possible to define spectrally if these are kauri. Moreover, the management needs to document the location of dead trees before they are overgrown or fallen. The resulting “kauri mask” can then be used for further applications such as a detailed analysis of stress symptoms.

The main objectives of this study were:

- Objective 1: Identify and compare the spectra of kauri and associated canopy tree species with no to medium stress symptoms and analyse their spectral characteristics and separability.
- Objective 2: Identify and describe the best spectral indices for the separation of the three target classes “kauri”, “dead/dying trees” and “other” canopy vegetation (see class description in section 3.2).
- Objective 3: Define an efficient classification method to differentiate the three target classes that is applicable for large-area monitoring with multispectral sensors.

We chose a pixel-based approach as it did not require a prior crown-segmentation.

2 Materials and methods

2.1 Study area

Three sites in the Waitakere Ranges Heritage Area, northwest of central Auckland (Figure II-2), cover a representative range of kauri stands in all sizes and stages of stress [36]. The Cascade area (10.3 km²) contains patches of old established kauri stands, the Maungaroa area (5.4 km²) includes mainly second-growth kauri forests, and a diverse selection of mature crowns can be found in the Kauri Grove Valley (1.1 km²). A rough terrain characterises the ranges with elevations from sea level to a maximum of 336 m in the study sites and 474 m at the highest peak [40]. The climate is warm-temperate and influenced by the proximity of the sea [41].

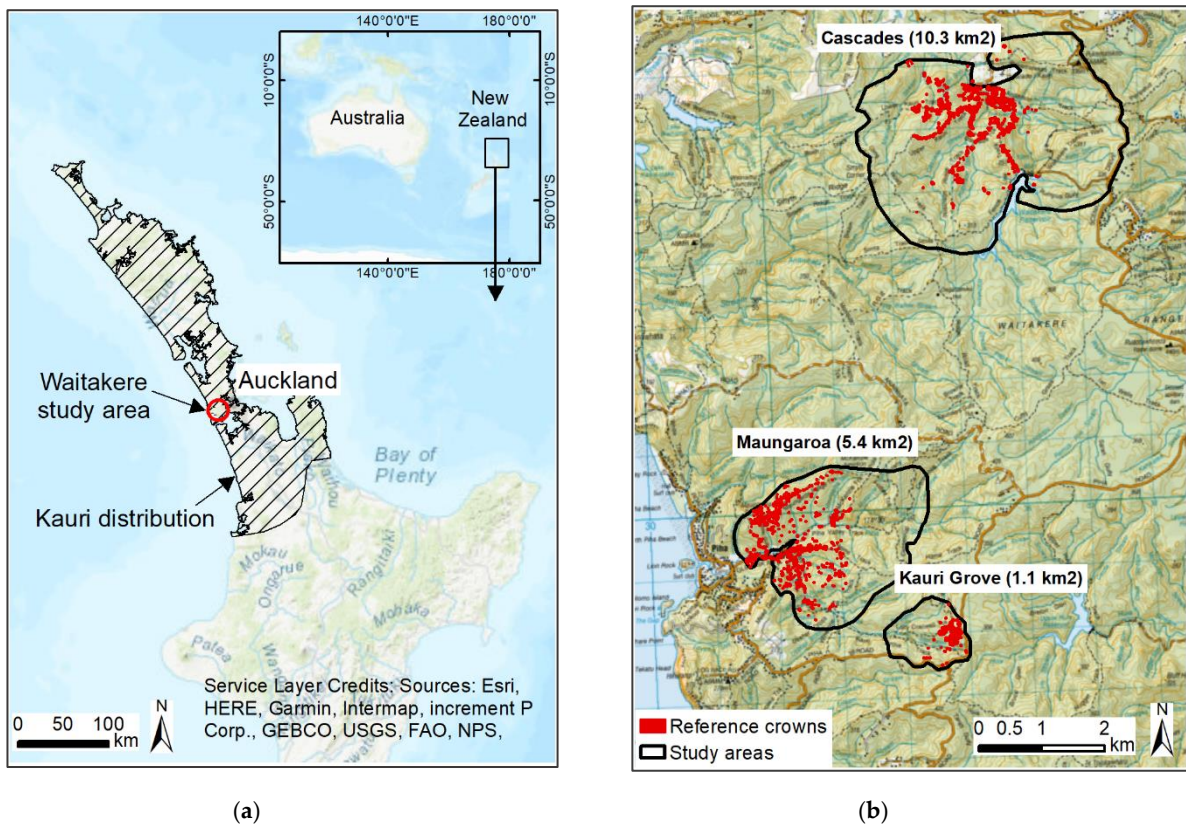


Figure II-2 (a) Location of the Waitakere Ranges on the North Island of New Zealand west of Auckland City. The general area with naturally occurring kauri in New Zealand [2] is marked as hatched. (b) Study sites in the Waitakere Ranges with the reference crowns marked in red (background map: [42]).

2.2 Data and data preparation

LiDAR data (RIEGL LMS-Q1560 sensor, average 35 returns/m² with circa 0.5 ground returns/m²) and RGB aerial images (15 cm) were flown for the three study sites in one acquisition on 30 January 2016. A pit-free terrain model (DTM), surface model (DSM) and crown-height model (CHM) were generated with LAStools [43]. The aerial image was orthorectified in two versions, on the DTM and the DSM. An additional 7.5 cm RGB aerial image was acquired in summer 2017 [44].

The airborne hyperspectral image was acquired on 15 March 2017 with an AISA Fenix hyperspectral sensor at 1 m pixel resolution and was delivered in 23 stripes in radiance units. The sensor features 448 spectral bands with an average bandwidth of 3.6 nm in the VNIR1 region and 10 nm in the NIR2/SWIR-region. The flight conditions were cloud-free but windy, with a high amount of moisture in the forest after recent rain. Reflectance measurements with an ASD field spectrometer were taken as a reference during the flight on homogenous flat areas (grass, gravel, tarmac) and black and white sheets of 5 m × 5 m.

The atmospheric correction was performed using ATCOR 4 [14] with a variable water vapour correction on the 1130 nm spectral region and a “maritime” atmosphere setting for the aerosol parameters. The spectral distortions of the push broom sensor were addressed by developing a sensor model with an adapted shift in the bandwidths. The parameters for the shift were empirically derived for each sensor part (VNIR1 and SWIR) from atmospheric gas absorption features on a statistically homogenous part of the image. The O₂ absorption bands at 760 and 820 nm could be sufficiently corrected by applying the sensor-shift in ATCOR. Remaining spikes and dips in the 940 and 1130 nm regions were removed by applying a non-linear interpolation. The ASD reflectance field measures were used as a reference to evaluate the parameters for the atmospheric correction, not for the analysis itself.

The original image showed some distinct non-periodic, single black and white “bad lines” in the columns of wavelengths at the beginning and end of the spectrum and close to the shift between the VNIR and SWIR sensors. These lines were identified by their mean value compared to the mean values of the direct neighbouring lines according to a local approach described in [45]. For the de-stripping, the pixel values in these lines were replaced with the average of the neighbouring pixels.

The geographic distortions were corrected in a two-step approach: First, the basic corrections for the Global Navigation Satellite System (GNSS) position, altitude, roll, pitch, heading and offset between the inertial measurement unit and lens were applied in PARGE [46]. In a second step, the remaining distortions were corrected with an individual polynomial orthorectification per stripe in ERDAS Imagine based on over 2300 ground control points.

Ninety-six of the 448 bands that were most affected by noise and stripes were removed, leaving 352 useable bands for the analysis. The noisy bands were located in the beginning and end of the spectrum and

in the absorption bands of water. The 23 corrected stripes were stitched together with “mosaic data seamlines” in ArcGIS to three smaller mosaics covering the three study areas before they were combined into one large mosaic covering ca. 9 km² image area.

During fieldwork in the 2015/2016 and 2016/2017 summer months, the reference crowns in denser stands were located with a mapping grade GNSS (Trimble-GeoXH-3.5G) with distance and bearing in circular sampling plots of 20 and 30 m diameter. In open stands, crowns were edited directly on aerial images and a CHM layer on a field tablet. Table II-A1 gives an overview of the reference data with scientific names and the priority of neighbouring canopy species, according to their resemblance to and association with kauri. A threshold of at least 30% dead branches visible in the crown area in the 2017 aerial image was defined to identify the class “dead/dying trees”. The sunlit parts were identified with a threshold on the average of the RGB-NIR bands [47]. The challenge was to define a brightness threshold that removes the core shadow areas without useful spectral information and keep the partly shaded inner-crown pixels that still contribute to the species identification. The threshold on the RGB-NIR average was defined by comparing the resulting areas with manually identified sunlit parts of the crown. A brightness threshold was also calculated on the NIR band only, to match reduced band selections. Edge effects were reduced by removing an internal buffer of 10% crown diameter. The final reference set includes 3165 crowns with a total of 95,194 sunlit pixels in 1 m² resolution (Table II-A1 and Figure II-3).

The crown size classes used in this study refer to the mean crown diameter. It was defined as the average of the maximum and the minimum diameter based on the “minimum bounding geometry – rectangle by width” in ArcGIS. The thresholds for the size classes were empirically defined from the field measurements to mark the transition from small kauri crowns (>3 m to 4.8 m diameter) to the more open medium crown sizes (>4.8 m to <12.2 m diameter) and the large dome shape crowns (>12.2 m diameter) (Figure II-1). In addition, the threshold for the minimum object size for a 1 m pixel resolution was marked in a class of very small crowns of <3 m diameter. The information about the crown size was used to interpret results of the pixel-based classification, not as an attribute in the classification.

As a preparation for a separated analysis for different forest types, two forest stand categories “high” and “low” were segmented on the CHM in eCognition (scale 15 m, shape 0.3 and compactness 0.9 [48]) and defined by a mean height threshold of 21 m.

The crowns and thereby the reference pixels were sorted in three target classes for the analysis:

- “dead/dying trees” with a minimum of 30% visible dead branches in the aerial image;
- “kauri” that were not classified as “dead/dying”; and
- “other” canopy vegetation that was not classified as “dead/dying”.

The crowns in the classes “kauri” and “other” showed no to medium stress symptoms with an intact crown architecture.

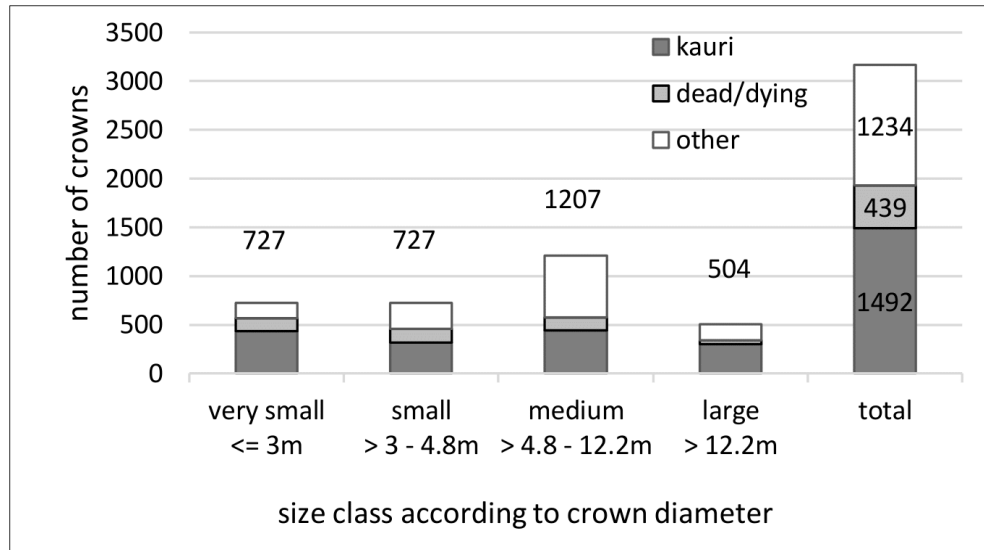


Figure II-3 Reference crowns (total 3165), used in the analysis, per class and diameter.

2.3 Extraction and analysis of spectra and spectral separabilities

Outliers that were caused by mixed pixels, single dead branches or patches of deviant plant material could be visually identified in Envi’s n-D Visualizer with the bands 1, 3 and 5 of a Minimum Noise Transformation (MNF) on all 352 bands [49]. These outlier pixels were removed for each class for test purposes. The mean signatures of kauri and associated tree species, the standard deviation and Jeffries–Matusita separability were calculated both with and without the removal of outlier pixels.

A Random Forest (RF) classification of kauri and 10 neighbouring tree species was calculated with a 10-fold cross-validation in 10 random repetitions. Only crowns larger than 5 m diameter with no or slight stress symptoms were included, to reduce the confusion with mixed pixels and declining foliage. A randomly spread subsample was extracted from the more frequent classes to match the species distribution in the study areas. The results were presented in a confusion matrix.

2.4 Band and indices selection

The aim of the selection process was to identify a set of 4–8 wavelengths and derived indices to distinguish the three target classes. Multispectral sensors usually feature up to six bands, but since an eight-band multispectral sensor was available, a maximum of eight bands for the index combinations was included in the analysis. This objective has two tasks:

1. separate “dead/dying trees” from less symptomatic “kauri” and “other” canopy vegetation; and
2. distinguish “kauri” from “other” canopy vegetation.

Initially, 52 indices were calculated on the 352 selected hyperspectral bands. In noisy areas of the spectrum, the values of three neighbouring bands were averaged. Indices with a high correlation were removed by reducing the number of bands and keeping the best performing indices. For the attribute selection, several ranker methods (Correlation, GainRatio, InfoGain, and Symmetrical Uncertainty) were combined in WEKA [50] by applying a weight according to the ranking results. The final combinations with 4–8 bands were identified with a Wrapper Subset Evaluator and the attribute importance for a RF classification. The same selection process was repeated with indices in only the visible to NIR1 spectral range (VNIR1), up to 970 nm.

2.5 Selection and parametrisation of the classifier

RF and Support Vector Machine (SVM) have been used successfully for tree classification in several studies [51–54]. As non-parametric classifiers, they do not require a normal distribution of the reference data and are well suited to handle a large number of attributes and high variability in the classes [55,56]. The SVM separates the classes by constructing a hyperplane based on support vectors at the outer class edges [57]. The parameters (cost: 1000, gamma: 0.1) were defined in WEKA with the GridSearch package [58]. The Sequential Minimal Optimization function in WEKA for the SVM analysis could handle the three target classes by using pairwise classification.

The RF classifier combines a large number of decision trees based on bootstrap samples with an ensemble learning algorithm [51]. A random selection of a given number of features is used to split each node in the RF implementation in WEKA. The final model is based on the number of similar outcomes (“votes”) from all decision trees [59]. The parameters were systematically tested, and the highest accuracies could be achieved with 500 trees, two attributes per node and a maximum tree depth of 40. The performances of both classifiers with the defined parameters were tested in a five-fold random split of all sunlit pixels with 20 repetitions. As expected, the use of alternative classifiers (Maximum Likelihood, J48 decision tree) yielded inferior results in comparison to RF and SVM.

2.6 Tests to further improve the accuracy

The default classification was calculated on the defined band selections and parameters. Several tests were conducted to improve the accuracies:

- resampling of the original bandwidths to 10 nm, 20 nm and 30 nm;
- addition of three selected texture values on the 800 nm band (data range (7 kernel (k)), variance (7 k) and second moment (3 k)), following the procedure for the indices’ selection;
- addition of a LiDAR CHM as a layer for the classification;

- separate classifications for low and high stands; and
- removal or reclassification of outlier pixels in the training set.

The final accuracies were calculated pixel-based with test pixels in all crowns. Producer's and user's accuracies were determined for the three target classes as the mean values from all repetitions in the RF classifications.

3 Results and interpretations

3.1 Results objective 1: Kauri spectrum

Compared to the mean spectra of other canopy vegetation, the mean spectra of kauri pixels (Figure II-4) show a slightly lower reflectance in the green part of the spectra and lower signals in all spectral regions. The most distinctive features in the kauri spectrum are a steep ascend from 1000 nm to 1070 nm followed by a long descent to the absorption feature at 1215 nm. The bands of the NIR2 range are the most important for kauri identification, followed by the NIR1 and SWIR1 (Figure II-4 and Figure II-5). The spectra of very small kauri crowns (<3 m DM) differ slightly from larger kauri (>4.8 m DM) with a Transformed Divergence value of 1.95 [60].

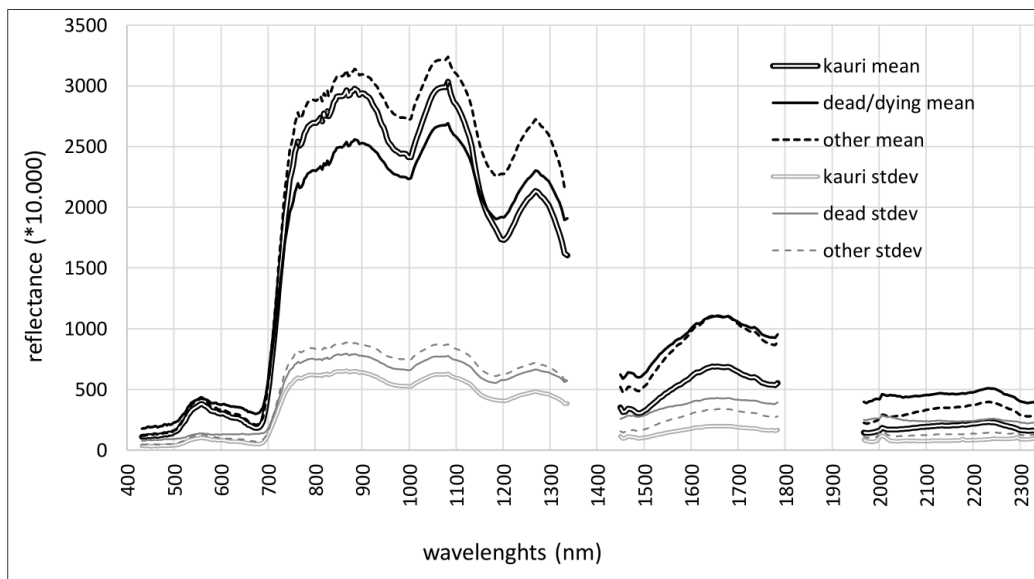


Figure II-4 Mean spectra of the target classes “kauri”, “dead/dying” and “other” with standard deviations (stdev).

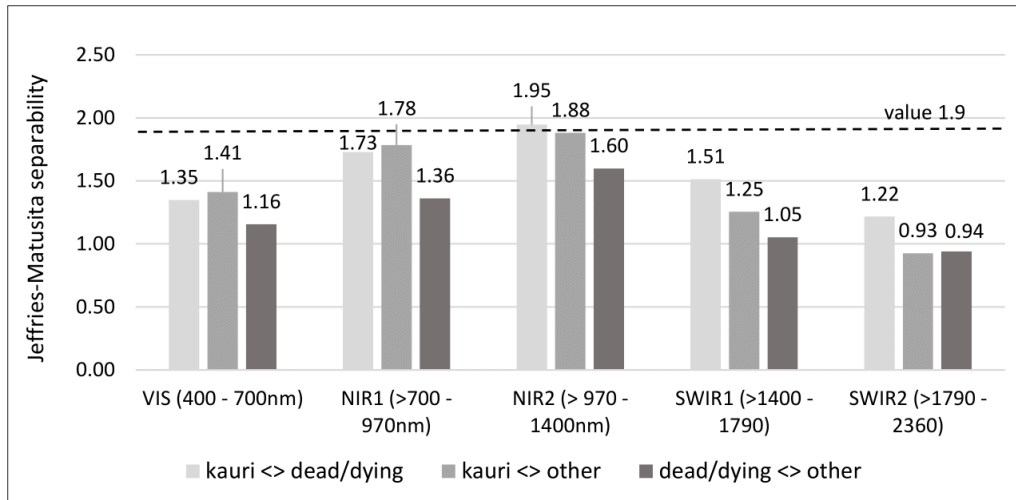


Figure II-5 Jeffries–Matusita separability [61] of the three target classes for different spectral ranges. A value larger than 1.9 indicates a high separability. The analysis was based on MNF transformations for all bands in the different spectral ranges.

With a Jeffries–Matusita value of over 1.9 [61], the pixel-based spectra of 21 other species can all well be separated from the pixel-based kauri spectra (Table II-A2). The separability increases after the removal of outlier pixels. The main species that are incorrectly classified as kauri are rimu, tanekaha, rewarewa, tōtara, miro and kawaka (Table II-A2). These species show similar spectral features to the kauri spectrum with the long descent in the NIR2 range and lower SWIR values (Figure II-6). The spectra of species with a high spectral separability from kauri, such as flax, kānuka, tree fern and pohutukawa have higher reflectance features in the VIS, NIR and SWIR range and a lower descent to the 1215 nm water vapour window (Figure II-7).

The overall high separability of kauri with neighbouring species could also be confirmed in a classification of kauri and 10 other tree species on the full spectral range of the AISA image (Table II-2). Only non-symptomatic crowns larger 5 m diameter were chosen to avoid confusion caused by mixed pixels and declining foliage. The OA of 94.8% and user’s accuracies from 89%¹ for rata to 98.7% for kauri, confirm the high spectral separability of kauri and also between the selected 10 tree species. Most species show high producer’s accuracies of over 93% with 99.1% for kauri. However, tōtara, rewarewa, tanekaha and miro have the lowest producer’s accuracies: from 57% for rewarewa to 76.2% for miro.

¹ Corrected from 98.1% in the published version to 89%

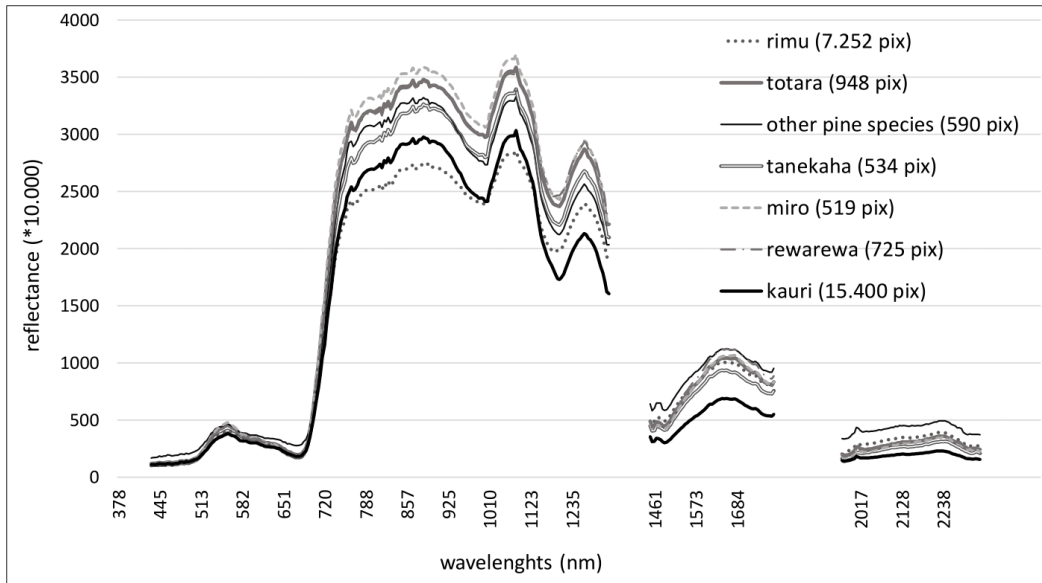


Figure II-6 Mean spectra of kauri (thick black line) and six selected other canopy species (grey) that got most easily confused with kauri. The number of pixels (pix) used to generate the mean spectra is given in parentheses. The spectra of these species show the lowest separability from the kauri spectrum in this study (see Table II-A2).



Figure II-7 Mean spectra of kauri (black) and five other canopy species (grey) that have the highest separabilities from the kauri spectrum in this study (see Table II-A2). The number of pixels (pix) used to generate the mean spectra is given in parentheses.

The category “dead/dying” was difficult to define from the classes “kauri” and “other” with a user’s accuracy of 80.3% and a producer’s accuracy of only 52.1% in the final setup. In a test with aggregated percentages of the classes per reference crown, the producer’s accuracy for the class “dead/dying” could be improved to 75.5% for a minimum threshold of 15% crown area defined as “dead/dying”. The main

characteristic features of the spectra of dead/dying trees are a lower chlorophyll absorption in the red region (around 670 nm), a lower reflectance of green leaf scattering in the NIR1 region (around 800 nm), a blue shift of the red-edge point and overall high values in the SWIR region (Figure II-5). Tests with separate classes for incorrectly classified pixels as well as the inclusion of shadow pixels gave no improvement for the “dead/dying” class.

Table II-2 Confusion matrix and user’s and producer’s accuracies for a RF classification of kauri and ten neighbouring tree species on the full hyperspectral range of the AISA image (first 25 bands of a 35 band MNF transformation) evaluated with a 10-fold cross-validation for the seed value 1. Only sunlit pixels of trees with a minimum diameter of 5 m were chosen to avoid shadows and to reduce the effects of mixed pixels. The selected crowns were either non-symptomatic or showed only mild symptoms of stress.

Classified as ->	Classified											Total	Prod. Acc. ¹
	Kauri	Kahi- katea	Tot ara	Kānuka	Rimu	Rewa -rewa	Tane- kaha	Rata	Miro	Puriri	Pohutu- kawa		
Kauri	7412	1	2	0	50	0	1	13	0	0	0	7479	99.1
Kahikatea	4	2043	1	10	65	3	0	11	4	7	0	2148	95.1
Totara	22	11	903	5	49	2	1	182	6	5	8	1194	75.6
Kānuka	3	6	1	3191	21	0	2	65	0	1	17	3307	96.5
Rimu	25	36	6	14	4446	5	0	97	8	7	0	4644	95.7
Rewarewa	13	38	5	7	18	229	0	81	1	6	4	402	57.0
Tanekaha	6	9	11	3	15	0	204	38	0	0	0	286	71.3
Rata	6	7	4	2	41	1	0	4988	15	24	11	5099	97.8
Miro	9	6	21	1	25	3	0	49	381	1	4	500	76.2
Puriri	0	8	0	5	2	3	0	34	1	1440	22	1515	95.0
Pohutukawa	7	0	0	45	3	0	0	46	0	44	1964	2109	93.1
Total	7507	2165	954	3283	4735	246	208	5604	416	1535	2030	28683	
User’s Accuracy	98.7	94.4	94.7	97.2	93.9	93.1	98.1	89	91.6	93.8	96.7		94.8

¹ Producer’s Accuracy

3.2 Results objective 2: Indices selection

A preselection of 13 best performing indices over the whole spectrum is described in Table II-A3, and their position in relation to the mean spectra of the target classes is illustrated in Figure II-8. Figure II-9 presents the performance of each index to identify the class “dead/dying” and to distinguish “kauri” from “other” canopy vegetation, with the best resulting combinations shown in Figure II-10.

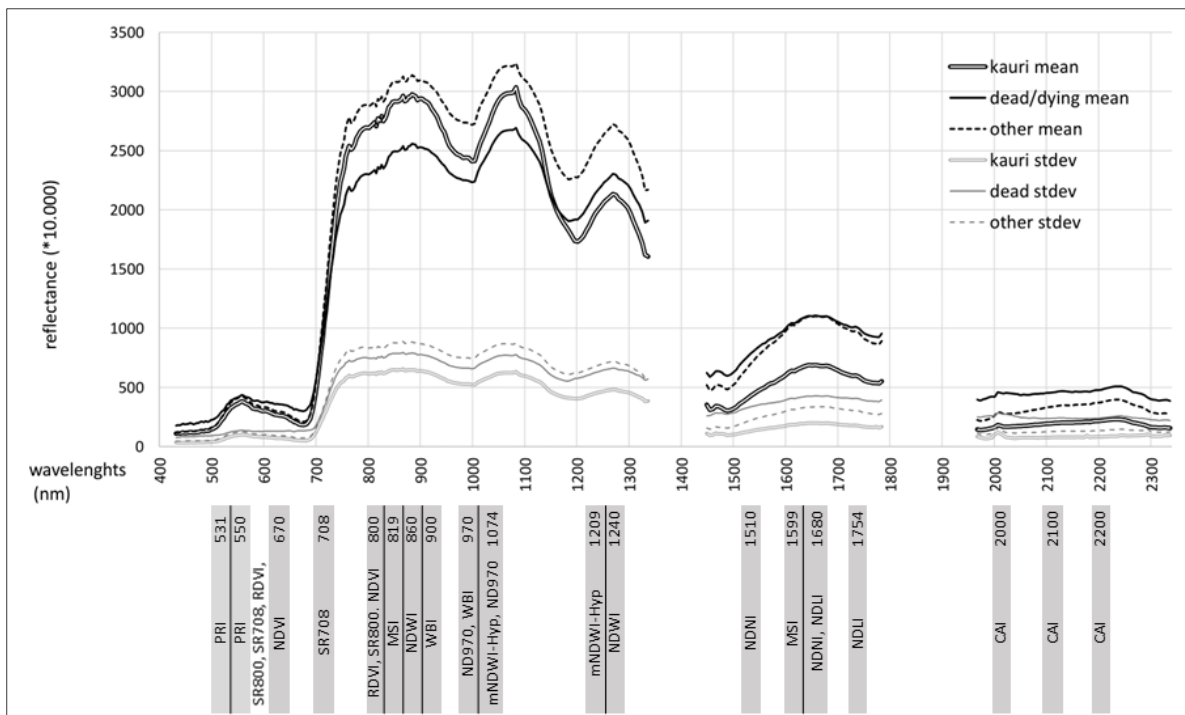


Figure II-8 Mean spectra of the target classes “kauri”, “dead/dying” and “other” with standard deviations (“stdev”). Below: Band positions of 13 selected spectral indices.

For a four-band multispectral sensor, the highest performance of 90.1% OA (Figure II-10) could be achieved with four indices, based on bands in the VIS (670 nm), NIR1 (800 nm) and NIR2 region (1074 and 1209 nm). The combination of three indices on the red and NIR1 bands helped to identify the class “dead/dying” (Figure II-9). The NIR 2 spectral range proved to be the most important for the identification of kauri followed by the NIR1, SWIR1, VIS and SWIR2 spectral ranges (Figure II-4 and Figure II-11).

The best distinction between kauri and other canopy vegetation could be achieved with a normalised index (mNDWI-Hyp, Figure II-12) that captures the distinctive long descent in the NIR2 spectrum. It was first described as an alternative to a Normalised Water Index (NDWI) adapted to Hyperion data [59] and was further modified in this study by using the natural logarithm values to address outliers (after [60]).

Other indices that are useful to identify kauri like the Moisture Stress Index (MSI), NDWI and Water Band Index (WBI) (Figure II-9) also include bands in the NIR1 and NIR2 spectral range. However, in

combination with the best performing mNDWI-Hyp index, they did not increase the OA.

For a five-band sensor, an additional Simple Ratio Index with an extra red-edge band at 708 nm (SR708) increased the OA to 90.8% for all classes on all crown sizes. The combination of the SR708 with the other three indices on four red to NIR1 bands performed best to distinguish the class “dead/dying” Figure II-9. This five-band combination was considered the best trade-off between the number of bands and the resulting accuracy. It was therefore used as the default combination for the development of the finale classification method. The inclusion of further bands and respective indices improved the accuracy only slightly.

An additional band at 970 nm for a six-band sensor allows including a further Normalised Difference Index (ND970) and resulted in an OA of 90.9% (Figure II-10). This index was developed in this study to describe the characteristically steep ascend in the kauri spectra from the first NIR water vapour window at 970 nm to the reflectance feature on 1074 nm (Figure II-5, Table II-A3).

With seven multispectral bands, the best results of 91.3% OA could be achieved by adding the Normalised Difference Nitrogen Index (NDNI) with two bands in the SWIR1 region (Figure II-9, Table C1). It describes the leaf nitrogen concentration in the 1510 nm band in relation to the canopy foliar mass measured at 1680 nm, which again depends on the absorption by leaf and canopy water [62]. The kauri spectrum shows a lower magnitude in the slope between the 1510 nm band versus the reflectance feature at 1680 nm compared to the mean spectrum of the two other target classes (see Figure II-5).

As an alternative for a seven-band sensor, the addition of a Photochemical Reflectance Index (PRI) [63], with two bands in the green region, results in an OA of 91.2% (StD 0.19). This index describes the photosynthetic light use efficiency by carbon dioxide uptake. It captures the slightly lower green reflectance feature in the kauri spectrum. A test confirmed its usability on a resampled 10 nm bandwidth.

With eight spectral bands available, the highest OA of 91.3% (StD 0.2) could be achieved by adding both the 970 nm band for the ND970 index and the two SWIR1 bands for the NDNI index to the five bands of the default setup.

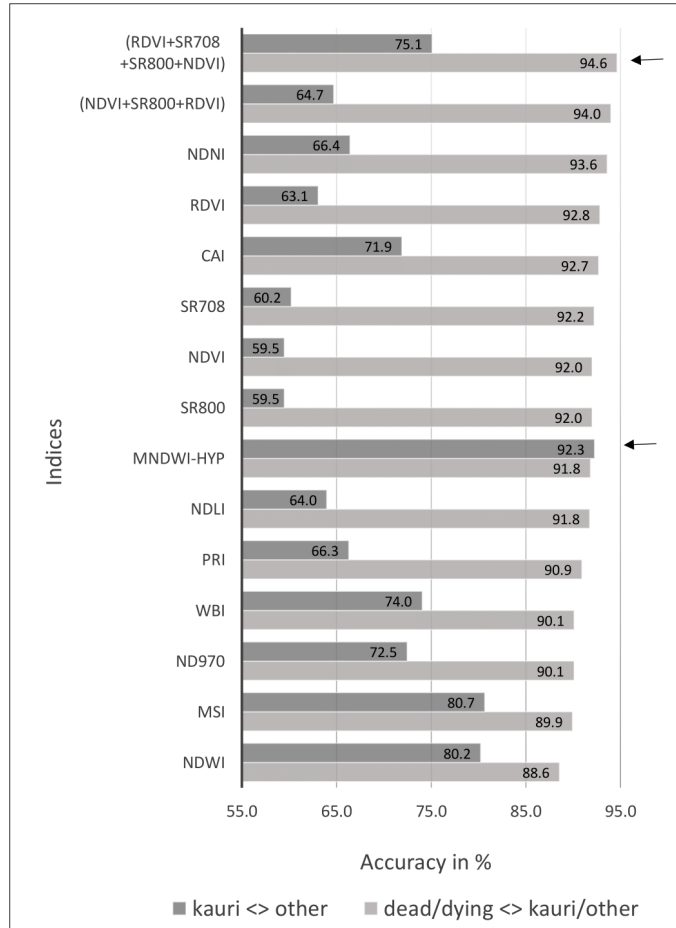


Figure II-9 Performance of selected indices and index combinations to identify the class “dead/dying” (light grey) and to distinguish between “kauri” and “other vegetation” (dark grey) with an RF classification (five-fold random split, 20 repetitions). Please note that the x-axis starts at 55%.

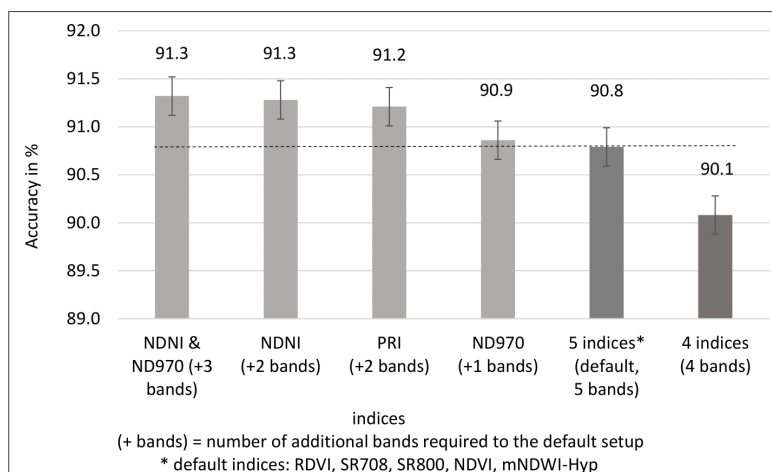


Figure II-10 Performance of the final 4–8-band index combinations to distinguish the three target classes “kauri”, “dead/dying” and “other” canopy vegetation. (RF, five-fold random split, 20 repetitions). Please note that the y-axis starts at 89%.

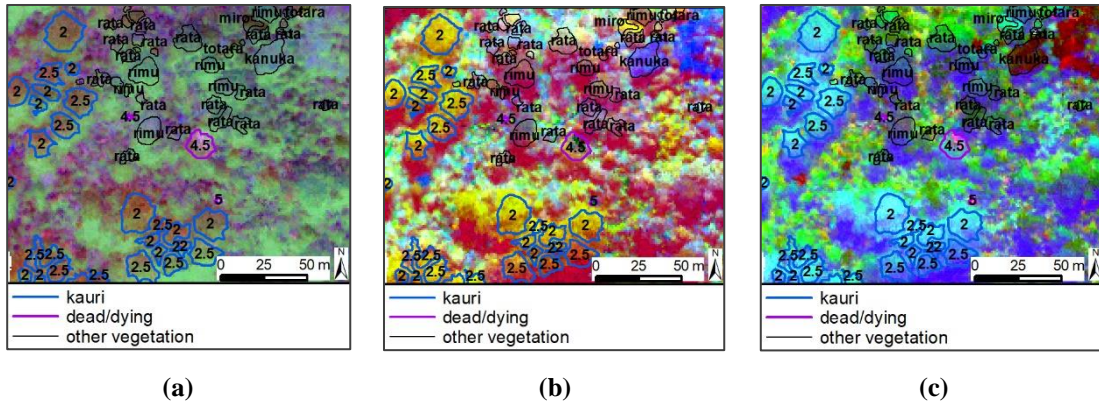


Figure II-11 RGB images of the three first bands of MNF transformations [49] from: **(a)** the VIS to NIR1 spectral range (431–970 nm); **(b)** VIS to NIR2 (431–1327 nm); and **(c)** the full spectral range from VIS to SWIR (431–2337 nm). The importance of the NIR2 and SWIR spectrum is visible in the higher colour contrast of kauri crowns compared to the VNIR image. The numbers in the kauri polygons indicate the stress symptom class for the crown with 1 = non-symptomatic and 5 = dead.

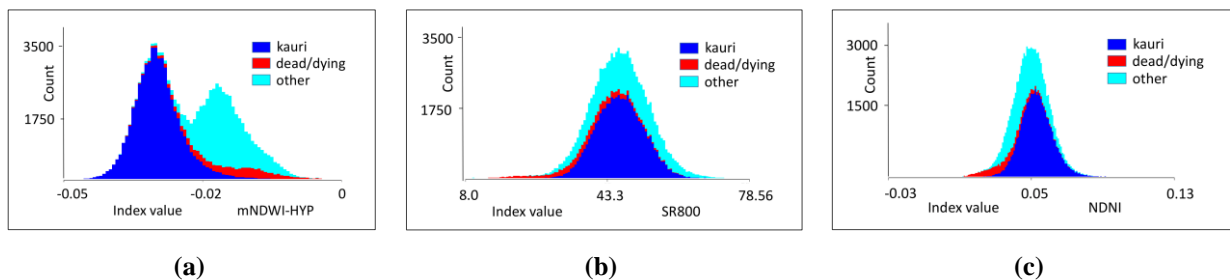


Figure II-12 Histograms for selected indices on sunlit pixels for all crown diameters, with the class “kauri” marked in light blue, the class “dead/dying” in red and the class “other” in dark blue. **(a)** Histogram for the mNDWI-Hyp index, which performed best to separate the class kauri from other vegetation by capturing distinctive features in the NIR2 region. For the separation of the class “dead/dying”, indices in the RED/NIR1 and SWIR region are better suited, such as **(b)** the SR800 and **(c)** the NDNI index (see Table II-A3 for descriptions of these indices).

In general, the NIR2 Indices are more important to distinguish kauri than indices in the visible to NIR1 (VNIR1) range. The best performing VNIR1 index combination for an eight-band sensor includes bands in the 550–970 nm spectral range (Table 3). This combination resulted in 84.6% OA to distinguish the three target classes (Figure II-13). If only six bands are available, three indices on red to NIR1 bands (675–970 nm) classified the three target classes with an OA of 78.4%.

Table II-3 Overview of selected indices for the identification of the three target classes in the visible to NIR1 spectral range (448–970 nm).

Index Abbrev.	Name	Equation	Wavelengths		Source	
RDVI ^{1,2}	Renormalised Difference VI	$RDVI = (R800 - R675) / \sqrt{(R800 + R675)}$	675	800	[64]	
GM1	Gitelson and Merzlyak Index 1	$GM1 = R750 / R550$	550	750	[65]	
SRb2 ²	Simple Ratio Chlorophyll b2	$SRchl b2 = R675 / R710$	675	710	[66]	
LCI ²	Leaf Chlorophyll Index	$LCI = (R850 - R710) / (R850 + R675)$	675	710	850	[65]
WBI ¹	Water Band Index	$WBI = 900 / 970$			900 970	[67]

¹ Indices for a selection with three indices. ² The original wavelengths of the index was slightly modified to reduce the number of bands.

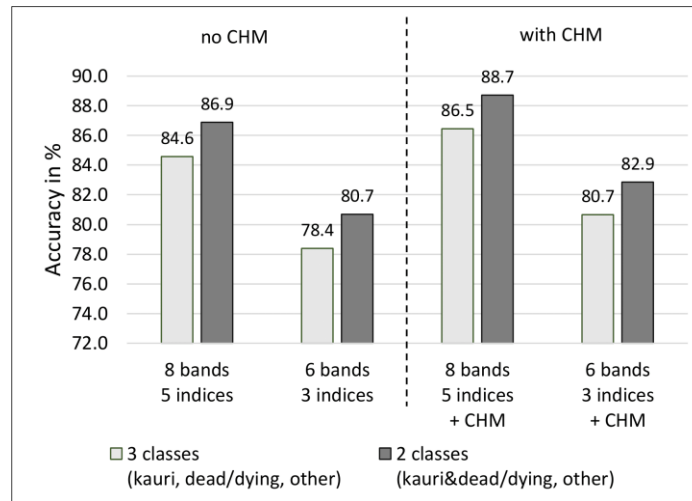


Figure II-13 Overall accuracies for two selected sets of six and eight bands in the visible to NIR1 range. The accuracies are calculated for two and three target classes both with and without an additional CHM layer. The results are based on an RF classification with a three-fold split in 10 repetitions on 94,971 pixel values, including small crowns (<3 m diameter). The standard deviations vary from 0.12 to 0.2.

3.3 Results objective 3: Method Development

The final accuracies are based on an image with five wavelengths (10 nm bandwidth) and five derived indices including the NIR2 bands, according to the recommended index selection for the whole spectrum in the previous sections. It enabled the distinction of “kauri and dead/dying trees” from “other canopy vegetation” (two classes) with a pixel-based overall accuracy (OA) of 93.4%. The three classes with “dead/dying crowns” as a separated category could be identified with 91.3% OA (Table II-4, Test E). The separation of the class “dead/dying” from the class “other” poses the main challenge, while the pixel-based user’s and producer’s accuracies for the class “kauri” are close to 95% (Table II-4). These results are based

on a RF classification. The RF classifier performed with 90.9% OA for the default setup slightly better than the SVM classifier (89.5% OA), at half of the processing time and it was easier to optimise. The resulting maps for the final setup that was applied to independent test crowns in 10 repetitions for the three study areas are shown in Figure II-14.

The accuracies for index combinations that include only bands in the visible to NIR1 range are significantly lower with 84.6% OA for three classes on eight bands and 78% on six bands. Combining the classes “kauri” and “dead/dying” improved the OA to 86.9% for the eight-band selection (see Figure II-13). Further improvements of about 2% could be achieved by adding a CHM layer.

The full spectral range of 25 MNF bands resulted in overall pixel-based accuracy of 93.9% for three classes and 96.2% for two classes. Attempts to remove mixed pixels and noise by excluding noisy bands with an MNF forward and backward transformation did not improve the OA.

A binning to 10 nm helped to remove noise and redundancies (Table II-4, Tests B1 and B2), while 20 and 30 nm resampling proved to be too coarse to capture the small spectral windows of the selected indices.

A separated classification for low and high stands (Table II-4, Test C) improved the accuracy by 1.5%. Adding a CHM layer achieved a similar improvement, but it was not used for the final setups, because the LiDAR data does not match the hyperspectral image sufficiently for a direct pixel-based combination. Additional texture features based on the 800 nm NIR band gave a slight improvement in the classification of small crowns but lowered the overall accuracy in the larger crowns. In addition, the partial removal of outliers in the training set (Table II-4, Test D) resulted in a slightly enhanced OA of 0.7%. This method was not applied for the final accuracies because it is too elaborate for large-area applications.

Post-processing by reclassifying kauri pixels with a height lower than 4 m to the class “other” improved wrongly classified lower shrub areas, but it requires a spatially matching CHM. The merging of singular pixels with a majority kernel according to the stand situation improved the pixel-based accuracy and should be considered for further analysis.

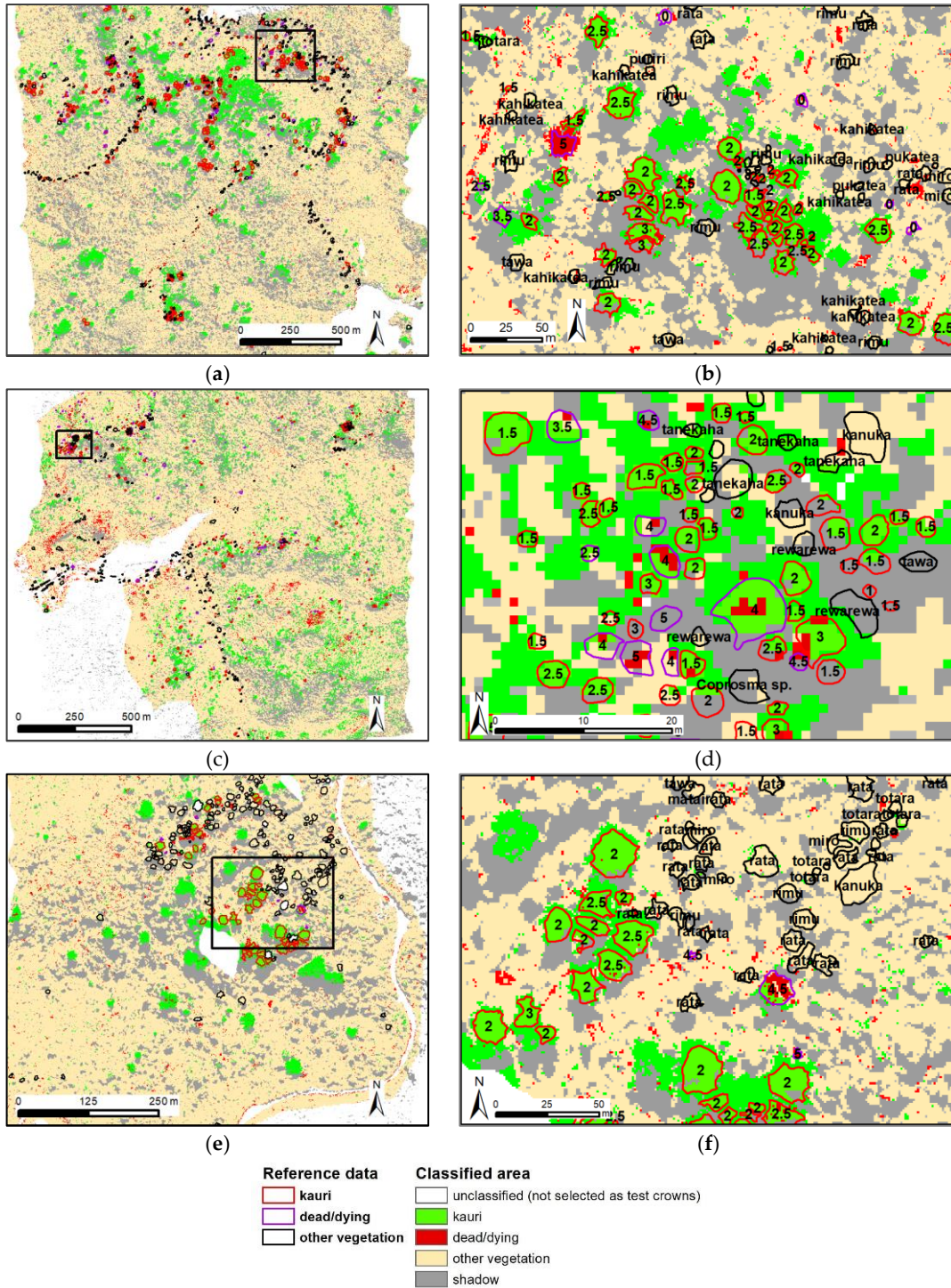


Figure II-14 Combined results of 10 RF classifications with a 5-fold stratified random split with different seed values. Overview (left) and detailed maps (right) for the Cascades (a, b), Maungaroa (c, d) and Kauri Grove area (e, f). The numbers indicate the stress symptom classes in kauri crowns (1 = non-symptomatic, 5 = dead).

Table II-4. Overall accuracies with standard deviations of the default, test and final setups. The classifications are pixel-based with training and test data selected on all crowns (RF, five-fold stratified random split in 10 repetitions).

		2 Classes			3 Classes			User's Accuracy			Producer's Accuracy		
		All DM	≥3 m	< 3 m	All DM	≥3 m	< 3 m	Kauri	Dead/Dying	Other	Kauri	Dead/Dying	Other
Test A (default)	Training and test: all outliers included. Indices on original bandwidths for the default 5 indices on 5 bands	92.1 (0.1)	92.5 (0.1)	66.9 (1.7)	89.9 (0.2)	90.3 (0.2)	64.6 (1.7)	93.1 (0.9)	78.7 (1.6)	86.7 (0.8)	94.3 (0.3)	45.0 (1.3)	93.0 (1.0)
Test B1	Resampling to 10 nm	93.0 (0.1)	93.4 (0.1)	67.2 (1.1)	91.0 (0.1)	91.4 (0.1)	65.0 (1.5)						
Test B2	Resampling to 20 nm ¹⁾	92.8 (0.2)	93.2 (0.2)	67.0 (2.8)	90.7 (0.2)	91.1 (0.2)	64.7 (3.0)						
Test C	Separate classification for low and high stands	93.4 (0.1)	93.7 (0.1)	70.8 (1.9)	91.4 (0.1)	91.7 (0.1)	67.5 (1.8)						
Test D	Outliers removed in the training set that confuse "kauri" with "other" and pixels that cause confusion with "dead/dying" < 3 m diameter	92.6 (0.1)	93.0 (0.1)	68.3 (1.4)	90.6 (0.1)	91.0 (0.1)	65.8 (1.3)						
Test E (final)	Training and test: all outliers included. 5 bands (10 nm), 5 indices; no textures, low and high stands separated. No post-processing	93.4 (0.1)	93.8 (0.1)	69.0 (2.1)	91.3 (0.1)	91.7 (0.1)	66.6 (2.0)	94.6 (0.2)	80.3 (0.7)	88.3 (0.3)	94.8 (0.2)	52.1 (1.4)	94.7 (0.3)

¹⁾ Lower resolutions (30nm, 40nm) were tested and lead to a further decline in the accuracy. (This comment was added afterwards, it is not included in the published version of the paper.)

4 Discussion and recommendations for further analysis

The use of a multispectral sensor with at least five bands in the VIS to NIR2 range is recommended for the detection of kauri and dead/dying trees. This study confirms the findings of Asner [68], Clark et al. [69] and Ferreira et al. [20] about the importance of the NIR spectrum for the identification of tree species in a diverse forest environment.

Index combinations with bands only in the visible to NIR1 range (up to 970 nm) perform significantly lower than index combinations that include NIR2 and SWIR bands. The overall accuracy was only 84.6% for three target classes on all crown sizes in the visible to NIR1 range, compared to 89.9% accuracy for a similar setup that includes bands in the NIR2 spectrum. If only bands in the VNIR1 spectral range are available, a combination with LiDAR attributes should be tested, ideally in an object-based approach [26–28].

The characteristic high reflectance in the kauri spectrum at 1070 nm indicates a particularly high amount of scattering of radiation at air–cell–water edges in the complex structure of the kauri foliage and the thick kauri leaves [11,62,70]. The pronounced water vapour window at 1215 nm is caused by a strong absorption from high leaf, respective crown water content. These results confirm the field observations that kauri crowns are more distinct in structural features than in colour. Since there was a lot of moisture in the forest on the flight day of the AISA sensor, the performance of the selected indices should also be tested under dryer conditions.

Other well-performing indices to identify kauri such as the MSI and NDWI also have bands in the NIR1 and NIR2 range and confirm the importance of structural features and water content for kauri identification. The lower reflectance values of kauri in all spectral regions is most likely caused by the more open crown structure in medium and large kauri compared to neighbouring species.

The main species that are incorrectly classified as kauri tend to have a similar “rough” foliage or needle-like leaves such as rimu, tanekaha, rewarewa, tōtara, miro and kawaka (Table II-4, Test B1). Species with similar conical shapes in smaller growth stages such as tanekaha, rimu, kahikatea and rewarewa are easily confused with small kauri. They show low producer’s accuracies from 57% for rewarewa to 76.2% for miro in the individual species classification (Table II-2). While rata has overall high user’s and producer’s accuracies of 89.0% and 97.8%, it has wrongly classified pixels with all other tree species, including kauri. This confusion is most likely caused by the fact that rata starts its growing cycle as an epiphyte and occurs therefore as part of the foliage on other trees.

The category “dead/dying” is difficult to define because of the graded transition from the two other classes for trees with declining foliage and a higher amount of shadow and mixed reflectance with

understory layers. In addition, canopy vegetation with a high amount of carbon fibre such as flax and cabbage trees, wooden seed capsules on kānuka and older dry foliage on rimu were wrongly classified as “dead/dying”. In addition, specular reflections on the smooth waxy surface of kahikatea trees and the shiny leaves of tree ferns cause confusion with the class “dead/dying”. Higher producer’s accuracy in a test with a crown-aggregated setup revealed that misclassification of the class “dead/dying” is partly caused by single pixels on dead branch material in otherwise less symptomatic crowns. While the classification of these pixels is correct, they appear as wrongly classified in the confusion matrix because the reference is crown based.

A separated classification for low and high stands (Table II-4, Test C) improved the OA about 1.5%. This can be explained by a reduced variability in the dataset after separating young trees with dense foliage and lower shrub layers from the mature trees in the higher stands. An alternative to consider different size classes is the direct inclusion of a CHM as an additional layer. For a pixel-based classification, this requires a sub-pixel matching between the optical data and the CHM, which is difficult to achieve in a varied topography with large trees.

The partial removal of outliers in the training set (Table II-4, Test D) reduced the effect of mixed pixels, especially for small crowns and resulted in a slightly enhanced OA by 0.7%. However, this analysis is elaborate and should only be considered if it is not possible to include LiDAR data or obtain optical data in a higher spatial resolution, which will reduce the number of mixed pixels.

The 1 m pixel size of the AISA Fenix image put some constraints on the analysis of crowns with a diameter smaller than 3 m, with an overall accuracy of 66.6% in the final setup (Table II-4, Test E). The identification of small crowns requires a sub-meter spatial resolution, to avoid the effect of mixed pixels.

While some spaceborne hyperspectral sensors cover the recommended bands in the NIR2, their spatial resolution of, e.g. 30 m for the Prisma [71] and the EnMAP mission [72] is too coarse for individual tree crown identification. For larger pixel sizes, also in Landsat and Sentinel satellite images, the detection of stands with younger kauri trees should be further investigated with a spectral unmixing approach for homogenous stand units in combination with LiDAR attributes. The potential of the bright green spring aspect for kauri identification could be analysed in a time series of high-resolution satellite data.

The RF classifier is very efficient to handle classes with a high spectral variability; however, the resulting model is difficult to understand. The clear separation of the “kauri” class in the histogram of the mNDWI index (Figure II-12) indicates that a manual decision tree can be developed, which would be easier to understand and to implement.

While the large reference dataset of kauri in different growth and symptom stages is representative for the Waitakere Ranges, the indices and model for kauri identification should be tested and if necessary readjusted in other kauri forests with a different amount and composition of neighbouring species.

5 Conclusions

This study is the first to analyse the spectra of kauri and the main neighbouring canopy tree species with an airborne hyperspectral sensor on the full VIS to SWIR spectral range. The main objectives were: (1) to describe the kauri spectra and analyse its separability from other neighbouring tree species; (2) to identify the best spectral indices to separate the class “kauri” from “other” and “dead dying” canopy vegetation; and (3) to define a method for classification of the three target classes that is applicable for large-area monitoring with multispectral sensors.

Kauri crowns have characteristic spectra with a steep reflectance feature in the NIR2 spectral region at 1070 nm, a distinct descent to the water vapour windows at 1215 nm, and lower reflectance features in the green and SWIR spectral region than other canopy vegetation. The spectral characteristics indicate that kauri crowns are more distinct in their structural than biochemical features. The high separabilities of the kauri spectra from 21 other tree species and canopy vegetation with a Jeffries–Matusita separability larger 1.9 could be confirmed with a high OA of 94.8% for the classification of non-symptomatic crowns larger 5 m diameter of kauri and 10 other tree species.

For the use on a five-band multispectral sensor, five indices (Table II-A3) in the VIS to NIR2 range performed best to distinguish the three target classes “kauri”, “dead/dying trees” and “other canopy vegetation”. They are suitable for multispectral area-wide forest mapping.

The RF classifier performed slightly better than Support Vector Machine. The final results with 91.7% OA are based on a separated RF classification of low and high forest stand, a binning to 10 nm bandwidth and the removal of very small crowns (<3 m diameter). The class “kauri” could be discriminated with high user’s and producer’s accuracies of 94.6% and 94.7% from other canopy vegetation by using the selected five bands from the red spectrum at 670 to 209 nm in the NIR2 spectrum. The main challenge was the confusion between the classes “dead/dying” and “other” canopy vegetation. A further improvement to 93.8% OA could be achieved by combining “kauri” and “dead/dying” trees in one class as a “kauri mask” for the further analysis, e.g. of stress symptoms. Additional indices enhance the overall accuracy only slightly, up to 0.6% for an eight-band sensor.

The method for accurate, cost efficient, wall-to-wall mapping of kauri trees presented in this study has important implications for the monitoring of canopy symptoms of kauri dieback disease over the entire distribution of New Zealand’s native kauri forests.

Author Contributions: Conceptualisation, J.M.; methodology, J.M.; software, J.M.; validation, J.M.; formal analysis, J.M.; investigation, J.M.; resources, J.M. and J.S.; data curation, J.M.; writing – original draft preparation, J.M.; writing – review and editing, J.M., H.B., J.H., J.S. and D.N.; visualisation, J.M.; supervision, H.B., J.H., J.S. and D.N.; project administration, J.M. and D.N.; and funding acquisition, J.M., D.N. and J.H.

Funding: The Ministry of Primary Industries funded most of the remote sensing data (agreement No. 17766), while the University of Canterbury, the University of Trier and FrontierSI (former CRC SI) Australia provided scholarships for living costs, fieldwork, equipment and additional LiDAR data. Digital Globe and Blackbridge helped with grants for satellite data. Auckland Council supported the fieldwork and supplied LiDAR data and aerial images and Landcare Research provided field equipment. Rapidlasso and Harris Geospatial helped with grants for software licenses. Henning Buddenbaum was supported within the framework of the EnMAP project (FKZ 50 EE 1530) by the German Aerospace Center (DLR) and the Federal Ministry of Economic Affairs and Energy. The publication was funded by the Open Access Fund of Universität Trier and the German Research Foundation (DFG) within the Open Access Publishing funding programme.

Acknowledgments: Our sincere thanks go to all people and institutions who supported this project. We are especially grateful to Nick Waipara, Lee Hill and Yue Chin Chew from Auckland Council who helped to establish the project and provided data. Justin Morgenroth at the University of Canterbury helped with the initial budget setup. The Kauri Dieback Programme (Planning and Intelligence Team) gave constructive feedback and support during this research. We also like to thank Fredrik Hjelm from the Living Tree Company and Joanne Peace for their excellent support during the fieldwork. Jeanette Allen, Vicki Wilton and Nicole Gellner helped with the University administration.

Conflicts of Interest: The authors declare no conflict of interest.

Appendix II-A

Table II-A1 Number of crowns and sunlit/shadow pixel for all reference data used in the analysis sorted according to the main classes and species resp. vegetation groups.

	Common Name	Scientific Name	Crowns	Pixels ¹	
kauri	kauri	<i>Agathis australis</i> (D.Don) Lindl. ex Loudon	1483	57,700	
	kauri group/stand	<i>Agathis australis</i> (D.Don) Lindl. ex Loudon	9	850	
dead/dying	kauri dead/dying	<i>Agathis australis</i> (D.Don) Lindl. ex Loudon	326	5329	
	unknown dead/dying	NN	91	1937	
	other dead/dying	NN	22	839	
other 1. priority	kahikatea	<i>Dacrycarpus dacrydioides</i> (A.Rich.) de Laub.	87	2932	
	kānuka	<i>Kunzea</i> spp.	218	4224	
	miro	<i>Prumnopitys ferruginea</i> (D.Don) de Laub.	21	780	
	pohutukawa	<i>Metrosideros excelsa</i> Sol. ex Gaertn.	52	2273	
	puriri	<i>Vitex lucens</i> Kirk	40	1741	
	rata	<i>Metrosideros robusta</i> A.Cunn.	102	6504	
	rewarewa	<i>Knightia excelsa</i> R.Br.	93	1082	
	rimu	<i>Dacrydium cupressinum</i> Sol. ex G.Forst	226	10,841	
	tanekaha	<i>Phyllocladus trichomanoides</i> G.Benn ex D.Don	126	964	
	taraire	<i>Beilschmiedia tarairi</i> (A.Cunn.) Benth. & Hook.f. ex Kirk	11	253	
	taraire/puriri	NN	3	79	
	tōtara	<i>Podocarpus totara</i> D.Don	37	1761	
	other 2. priority	broadleaf mix	NN	16	370
		cabbage tree	<i>Cordyline australis</i> (G.Forst.) Endl.	25	302
coprosma sp.		<i>Coprosma</i> spp.	56	790	
flax		<i>Phormium tenax</i> J.R.Forst. & G.Forst.	3	91	
karaka		<i>Corynocarpus laevigatus</i> J.R.Forst. & G.Forst.	4	73	
kowhai		<i>Sophora</i> spp.	5	119	
kawaka		<i>Libocedrus plumosa</i> (D.Don) Sarg.	4	84	
matai		<i>Prumnopitys taxifolia</i> (Sol. ex D.Don) de Laub.	3	103	
nikau		<i>Rhopalostylis sapida</i> H.Wendl. & Drude	27	431	
other pine trees		NN	4	360	
pukatea		<i>Laurelia novae-zelandiae</i> A.Cunn.	8	215	
shrub mix (nikau, tree fern, cabbage...)		NN	13	1346	
tawa		<i>Beilschmiedia tawa</i> (A.Cunn.) Benth. & Hook.f. ex Kirk	23	965	
tree fern		<i>Cyathea</i> spp.	20	294	
other species (not kauri)		NN	7	406	
Total				3165	106,028

¹ In total, 10,834 shadow pixels, 95,194 sunlit pixels

Appendix II-B

Table II-A2 Spectral separability and confusion of the class “kauri” with “other tree species”. The Jeffries–Matusita separability is given both for all sunlit pixels and a pixel set with removed outliers. A value over 1.9 indicates a high spectral separability.

“Other” classified as “kauri”	Jeffries–Matusita Separability to the kauri spectrum		Confusion of kauri with other species ²		
	All sunlit pixels ⁴	Outliers removed ⁴	Mean No. of confused pixels	Mean per cent confused	Mean No. of test pixels
rimu ¹	1.948	1.995	73.3	0.2%	1821.1
totara ¹	1.929	1.979	50.3	1.1%	321.6
other pine species ^{1,3}	1.997	2.000	34.2	4.3%	88.6
tanekaha ¹	1.860	1.992	27.7	2.1%	169.5
rata	1.989	1.998	25.9	0.3%	1189.3
rewarewa ¹	1.968	1.995	8.8	2.1%	175.6
miro	1.960	1.995	8.4	2.6%	139.8
kahikatea	1.983	1.993	6.4	0.7%	530.5
pohutukawa	1.997	1.999	4.6	0.8%	441.8
coprosma sp.	NN	NN	4.3	3.4%	143.3
kawaka	1.999	2.000	3.6	4.1%	709
tawa	1.996	2.000	1	1.6%	114.9
puriri	1.990	1.999	0.9	0.9%	235.7
scrub mix	1.988	1.997	0.9	4.9%	62.6
karaka	2.000	2.000	0.7	15.8%	9
nikau	1.998	2.000	0.6	1.6%	28.1
pukatea	NN	NN	0.6	3.9%	18.4
tree fern	2.000	2.000	0.3	2.1%	8.7
taraire	1.990	1.999	0.2	2.1%	7.7
broadleaf mix	NN	NN	0.1	0.2%	5.8
kānuka	1.996	2.000			
flax	2.000	2.000			
kānuka flowering	2.000	2.000			
kowhai	2.000	2.000			

1 Main species that were confused with kauri.

2 Mean values of a RF classification in a five-fold split in 10 repetitions.

3 Planted pine trees close to the Piha settlement, without species identification.

4 The headers of the columns were switched as a correction to the published version.

Appendix II-C

Table II-A3 Selected indices for the detection of kauri and dead/dying trees.

Name	Equation	Name, description (sensitive to...)	Literature
Selected indices for a 5-band sensor			
SR800 ¹	$= \frac{R800}{R670}$	Simple Ratio 800/670 ...chlorophyll concentration and Leaf Area Index (LAI)	[73]
SR708	$= \frac{R670}{R708}$	Simple Ratio 670/708 ...chlorophyll concentration and LAI	[66] (modified)
RDVI ¹	$= \frac{R800 - R670}{\sqrt{R800 + R670}}$	Renormalised Difference VI ...chlorophyll concentration and LAI	[64]
NDVI ¹	$= \frac{R800 - R670}{R800 + R670}$	Normalised Difference VI ...chlorophyll concentration and LAI	[74]
mNDWI-Hyp	$= \frac{\log(R1074)^{-1} - \log(R1209)^{-1}}{\log(R1074)^{-1} + \log(R1209)^{-1}}$	Modified Normalised Difference Water Index - Hyperion ...vegetation canopy water content and canopy structure	[75] (modified)
Additional indices for a 6–8-band sensor			
ND970	$= \frac{R1074 - R970}{R1074 + R970}$	Normalised Difference 1074/970 ...vegetation canopy water content and canopy structure	This study
PRI	$= \frac{R531 - R570}{R531 + R570}$	Photochemical Reflectance Index ...photosynthetic light use efficiency of carotenoid pigments	[63]
NDNI	$= \frac{\log(R1510)^{-1} - \log(R1680)^{-1}}{\log(R1510)^{-1} + \log(R1680)^{-1}}$	Normalised Nitrogen Index ...canopy nitrogen	[76]
Other selected indices			
WBI	$= \frac{R970}{R900}$	Water Band Index ...relative water content at leaf level	[67]
MSI	$= \frac{R1599}{R819}$	Moisture Stress Index ...moisture stress in vegetation	[77]
NDWI	$= \frac{R860 - R1240}{R860 + R1240}$	Normalised Difference Water Index ...total water content	[78]
NDLI	$= \frac{\log(R1754)^{-1} - \log(R1680)^{-1}}{\log(R1754)^{-1} + \log(R1680)^{-1}}$	Normalised Difference Lignin Index ...leaf and canopy lignin content	[79]
CAI	$= 0.5 * (2000 + 2200) - 2100$	Cellulose Absorption Index ...cellulose, dried plant material	[80]

1) The value for the R800 band was averaged with the values of the two neighbouring bands, to reduce noise.

6 References

1. MPI. *Kauri Dieback Sampling Locations*; Ministry of Primary Industries: Wellington, New Zealand, 2018.
2. Ecroyd, C. Biological flora of New Zealand 8. *Agathis australis* (D. Don) Lindl.(Araucariaceae) Kauri. *N. Z. J. Bot.* **1982**, *20*, 17–36.
3. Waipara, N.W.; Hill, S.; Hill, L.M.W.; Hough, E.G.; Horner, I.J. Surveillance methods to determine tree health, distribution of kauri dieback disease and associated pathogens. *N. Z. Plant Prot.* **2013**, *66*, 235–241.
4. Jamieson, A.; Bassett, I.E.; Hill, L.M.W.; Hill, S.; Davis, A.; Waipara, N.W.; Hough, E.G.; Horner, I.J. Aerial surveillance to detect kauri dieback in New Zealand. *N. Z. Plant Prot.* **2014**, *67*, 60–65.
5. Bock, C.H.; Poole, G.H.; Parker, P.E.; Gottwald, T.R. Plant disease severity estimated visually, by digital photography and image analysis, and by hyperspectral imaging. *Crit. Rev. Plant Sci.* **2010**, *29*, 59–107.
6. Jones, H.G.; Vaughan, R.A. *Remote Sensing of Vegetation: Principles, Techniques, and Applications*; Oxford University Press: New York, NY, USA, 2010.
7. Thenkabail, P.S.; Lyon, J.G.; Huete, A. *Fundamentals, Sensor Systems, Spectral Libraries, and Data Mining for Vegetation*; CRC Press: Boca Raton, FL, USA, 2018
8. Sandau, R. *Digital Airborne Camera: Introduction and Technology*; Springer Science & Business Media: New York, NY, USA, 2009.
9. Petrie, G.; Walker, A.S. Airborne digital imaging technology: A new overview. *Photogramm. Rec.* **2007**, *22*, 203–225.
10. Hagen, N.A.; Gao, L.S.; Tkaczyk, T.S.; Kester, R.T. Snapshot advantage: A review of the light collection improvement for parallel high-dimensional measurement systems. *Opt. Eng.* **2012**, *51*, 111702.
11. Asner, G.P. Hyperspectral remote sensing of canopy chemistry, physiology, and biodiversity in tropical rainforests. In *Hyperspectral Remote Sensing of Tropical and Sub-Tropical Forests*; CRC Press: Boca Raton, FL, USA, 2008; pp. 261–296.
12. Dalponte, M.; Ørka, H.O.; Ene, L.T.; Gobakken, T.; Næsset, E. Tree crown delineation and tree species classification in boreal forests using hyperspectral and ALS data. *Remote Sens. Environ.* **2014**, *140*, 306–317.
13. Jones, T.G.; Coops, N.C.; Sharma, T. Assessing the utility of airborne hyperspectral and LiDAR data for species distribution mapping in the coastal Pacific Northwest, Canada. *Remote Sens. Environ.* **2010**, *114*, 2841–2852.
14. Richter, R.; Schläpfer, D. ATCOR-4 User Guide, Version 7.3.0, April 2019. In *Atmospheric/Topographic Correction for Airborne Imagery*; ReSe Applications LLC: Wil, Switzerland, Version; 2019.
15. Trier, Ø.D.; Salberg, A.-B.; Kermit, M.; Rudjord, Ø.; Gobakken, T.; Næsset, E.; Aarsten, D. Tree species classification in Norway from airborne hyperspectral and airborne laser scanning data. *Eur. J. Remote Sens.* **2018**, *51*, 336–351.
16. Asner, G.P.; Martin, R.E. Airborne spectranomics: Mapping canopy chemical and taxonomic diversity in tropical forests. *Front. Ecol. Environ.* **2009**, *7*, 269–276.
17. Carlson, K.M.; Asner, G.P.; Hughes, R.F.; Ostertag, R.; Martin, R.E. Hyperspectral remote sensing of canopy biodiversity in Hawaiian lowland rainforests. *Ecosystems* **2007**, *10*, 536–549.
18. Clark, M.L., Identification of Canopy Species in Tropical Forests Using Hyperspectral Data. In Thenkabail, P.S.; Lyon, J.G.; Huete, *Hyperspectral Remote Sensing of Vegetation*, 2nd Edition, Volume 3, Biophysical and Biochemical Characterisation and Plant Species Studies, CRC Press: Boca Raton, New York ; 2018 p. 423.
19. Féret, J.-B.; Asner, G.P. Tree species discrimination in tropical forests using airborne imaging spectroscopy. *IEEE Trans. Geosci. Remote Sens.* **2013**, *51*, 73–84.
20. Ferreira, M.P.; Zortea, M.; Zanotta, D.C.; Shimabukuro, Y.E.; de Souza Filho, C.R. Mapping tree species in tropical seasonal semi-deciduous forests with hyperspectral and multispectral data. *Remote Sens. Environ.* **2016**, *179*, 66–78.
21. Dalponte, M.; Bruzzone, L.; Gianelle, D. Fusion of hyperspectral and LIDAR remote sensing data for classification of complex forest areas. *Geoscience and Remote Sensing, IEEE Trans. Geosci. Remote Sens.* **2008**, *46*, 1416–1427.
22. Peerbhay, K.Y.; Mutanga, O.; Ismail, R. Commercial tree species discrimination using airborne AISA Eagle hyperspectral imagery and partial least squares discriminant analysis (PLS-DA) in KwaZulu–Natal, South Africa. *ISPRS J. Photogramm. Remote Sens.* **2013**, *79*, 19–28.
23. Shen, X.; Cao, L. Tree-species classification in subtropical forests using airborne hyperspectral and LiDAR data. *Remote Sens.* **2017**, *9*, 1180.

24. Asner, G.P.; Warner, A.S. Canopy shadow in IKONOS satellite observations of tropical forests and savannas. *Remote Sens. Environ.* **2003**, *87*, 521–533.
25. Kempeneers, P.; Vandekerckhove, K.; Devriendt, F.; van Coillie, F. Propagation of shadow effects on typical remote sensing applications in forestry. In Proceedings of the 2013 5th Workshop on Hyperspectral Image and Signal Processing: Evolution in Remote Sensing (WHISPERS), Gainesville, FL, USA, 26–28 June 2013.
26. Blaschke, T. Object based image analysis for remote sensing. *ISPRS J. Photogramm. Remote Sens.* **2010**, *65*, 2–16.
27. Heumann, B.W. An object-based classification of mangroves using a hybrid decision tree—Support vector machine approach. *Remote Sens.* **2011**, *3*, 2440–2460.
28. Machala, M.; Zejdová, L. Forest mapping through object-based image analysis of multispectral and LiDAR aerial data. *Eur. J. Remote Sens.* **2014**, *47*, 117–131.
29. Leckie, D.; Gougeon, F.; Hill, D.; Quinn, R.; Armstrong, L.; Shreenan, R. Combined high-density lidar and multispectral imagery for individual tree crown analysis. *Can. J. Remote Sens.* **2003**, *29*, 633–649.
30. Ghosh, A.; Ewald Fassnacht, F.; Joshi, P.K.; Koch, B. A framework for mapping tree species combining hyperspectral and LiDAR data: Role of selected classifiers and sensor across three spatial scales. *Int. J. Appl. Earth Obs. Geoinf.* **2014**, *26*, 49–63.
31. Zhang, C.; Qiu, F. Mapping individual tree species in an urban forest using airborne lidar data and hyperspectral imagery. *Photogramm. Eng. Remote Sens.* **2012**, *78*, 1079–1087.
32. Buddenbaum, H.; Schlerf, M.; Hill, J. Classification of coniferous tree species and age classes using hyperspectral data and geostatistical methods. *Int. J. Remote Sens.* **2005**, *26*, 5453–5465.
33. Baldeck, C.A.; Asner, G.P.; Martin, R.E.; Anderson, C.B.; Knapp, D.E.; Kellner, J.R.; Wright, S.J. Operational tree species mapping in a diverse tropical forest with airborne imaging spectroscopy. *PLoS ONE* **2015**, *10*, e0118403.
34. Fassnacht, F.E.; Latifi, H.; Stereńczak, K.; Modzelewska, A.; Lefsky, M.; Waser, L.T.; Straub, C.; Ghosh, A. Review of studies on tree species classification from remotely sensed data. *Remote Sens. Environ.* **2016**, *186*, 64–87.
35. Holmgren, J.; Persson, Å.; Söderman, U. Species identification of individual trees by combining high resolution LiDAR data with multi-spectral images. *Int. J. Remote Sens.* **2008**, *29*, 1537–1552.
36. Singers, N.; Osborne, B.; Lovegrove, T.; Jamieson, A.; Boow, J.; Sawyer, J.; Hill, K.; Andrews, J.; Hill, S.; Webb, C. *Indigenous terrestrial and wetland ecosystems of Auckland*; Auckland Council: Auckland, New Zealand, 2017. Available online: <http://www.knowledgeauckland.org.nz> (accessed on 20/07/2019).
37. Steward, G.A.; Beveridge, A.E. A review of New Zealand kauri (*Agathis australis* (D. Don) Lindl.): Its ecology, history, growth and potential for management for timber. *N. Z. J. For. Sci.* **2010**, *40*, 33–59.
38. Macinnis-Ng, C.; Schwendenmann, L. Litterfall, carbon and nitrogen cycling in a southern hemisphere conifer forest dominated by kauri (*Agathis australis*) during drought. *Plant Ecol.* **2015**, *216*, 247–262.
39. Meiforth, J., Photos, Waitakere Ranges. Photos taken during fieldwork in January to March 2016, 2016
40. Jongkind, A.; Buurman, P. The effect of kauri (*Agathis australis*) on grain size distribution and clay mineralogy of andesitic soils in the Waitakere Ranges, New Zealand. *Geoderma* **2006**, *134*, 171–186.
41. Chappell, P.R. *The Climate and Weather of Auckland*; Niwa Science and Technology Series; NIWA: Auckland, 2012;
42. LINZ, NZ Topo50. Topographical Map for New Zealand. 2019. <https://www.linz.govt.nz/land/maps/topographic-maps/topo50-maps>. Accessed on 20/07/2019)
43. Khosravipour, A.; Skidmore, A.K.; Isenburg, M. Generating spike-free digital surface models using LiDAR raw point clouds: A new approach for forestry applications. *Int. J. Appl. Earth Obs. Geoinf.* **2016**, *52*, 104–114.
44. Auckland Council, A. Auckland 0.075m Urban Aerial Photos (2017), RGB, Waitakere Ranges. 2017. <https://data.linz.govt.nz/layer/95497-auckland-0075m-urban-aerial-photos-2017/> (accessed on 12/04/2019).
45. Datt, B.; McVicar, T.R.; van Niel, T.G.; Jupp, D.L.B.; Pearlman, J.S. Preprocessing EO-1 Hyperion hyperspectral data to support the application of agricultural indexes. *IEEE Trans. Geosci. Remote Sens.* **2003**, *41*, 1246–1259.
46. Schlaepfer, D. PARGE—Parametric Geocoding & Orthorectification for Airborne Optical Scanner Data. Available online: <http://www.rese.ch/products/parge/> (accessed on 21/03/2019).
47. Adeline, K.R.M.; Chen, M.; Briottet, X.; Pang, S.K.; Paparoditis, N. Shadow detection in very high spatial resolution aerial images: A comparative study. *ISPRS J. Photogramm. Remote Sens.* **2013**, *80*, 21–38.
48. Trimble, .eCognition® Developer 9.3. User Guide. Trimble Germany GmbH: Munich, Germany, 2018.

49. Green, A.A.; Berman, M.; Switzer, P.; Craig, M.D. A transformation for ordering multispectral data in terms of image quality with implications for noise removal. *IEEE Trans. Geosci. Remote Sens.* **1988**, *26*, 65–74.
50. Witten, I.H.; Frank, E.; Hall, M.A.; Pal, C.J. *Data Mining: Practical Machine Learning Tools and Techniques*; Morgan Kaufmann: San Francisco, CA, USA, 2016.
51. Belgiu, M.; Drăguț, L. Random forest in remote sensing: A review of applications and future directions. *ISPRS J. Photogramm. Remote Sens.* **2016**, *114*, 24–31.
52. Dalponte, M.; Ørka, H.O.; Gobakken, T.; Gianelle, D.; Næsset, E. Tree species classification in boreal forests with hyperspectral data. *IEEE Trans. Geosci. Remote Sens.* **2013**, *51*, 2632–2645.
53. Fassnacht, F.E.; Neumann, C.; Förster, M.; Buddenbaum, H.; Ghosh, A.; Clasen, A.; Joshi, P.K.; Koch, B. Comparison of feature reduction algorithms for classifying tree species with hyperspectral data on three central European test sites. *IEEE J. Sel. Top. Appl. Earth Obs. Remote Sens.* **2014**, *7*, 2547–2561.
54. Raczko, E.; Zagajewski, B. Comparison of support vector machine, random forest and neural network classifiers for tree species classification on airborne hyperspectral APEX images. *Eur. J. Remote Sens.* **2017**, *50*, 144–154.
55. Bollandsås, O.M.; Maltamo, M.; Gobakken, T.; Næsset, E. Comparing parametric and non-parametric modelling of diameter distributions on independent data using airborne laser scanning in a boreal conifer forest. *Forestry* **2013**, *86*, 493–501.
56. James, G.; Witten, D.; Hastie, T.; Tibshirani, R. *An Introduction to Statistical Learning*; Springer: Springer, New York, NY, 2013; Volume 112.
57. Bruzzone, L.; Chi, M.; Marconcini, M. A novel transductive SVM for semisupervised classification of remote-sensing images. *IEEE Trans. Geosci. Remote Sens.* **2006**, *44*, 3363–3373.
58. Chang, C.-C.; Lin, C.-J. LIBSVM: A Library for Support Vector Machines [EB/OL]. 2001. Available online: <https://www.csie.ntu.edu.tw/~cjlin/libsvm/> (accessed 06/05/2019).
59. Breiman, L. Random forests. *Mach. Learn.* **2001**, *45*, 5–32.
60. Richards, J.A. *Remote Sensing Digital Image Analysis*; Springer: Berlin/Heidelberg, Germany, 1999; Volume 3.
61. Jeffreys, H. An invariant form for the prior probability in estimation problems. *Proc. R. Soc. Lond. Ser. A. Math. Phys. Sci.* **1946**, *186*, 453–461.
62. Serrano, L.; Penuelas, J.; Ustin, S.L. Remote sensing of nitrogen and lignin in Mediterranean vegetation from AVIRIS data: Decomposing biochemical from structural signals. *Remote Sens. Environ.* **2002**, *81*, 355–364.
63. Gamon, J.; Penuelas, J.; Field, C. A narrow-waveband spectral index that tracks diurnal changes in photosynthetic efficiency. *Remote Sens. Environ.* **1992**, *41*, 35–44.
64. Roujean, J.-L.; Breon, F.-M. Estimating PAR absorbed by vegetation from bidirectional reflectance measurements. *Remote Sens. Environ.* **1995**, *51*, 375–384.
65. Datt, B. A new reflectance index for remote sensing of chlorophyll content in higher plants: Tests using Eucalyptus leaves. *J. Plant Physiol.* **1999**, *154*, 30–36.
66. Datt, B. Remote sensing of chlorophyll a, chlorophyll b, chlorophyll a + b, and total carotenoid content in eucalyptus leaves. *Remote Sens. Environ.* **1998**, *66*, 111–121.
67. Peñuelas, J.; Filella, I.; Biel, C.; Serrano, L.; Savé, R. The reflectance at the 950–970 nm region as an indicator of plant water status. *Int. J. Remote Sens.* **1993**, *14*, 1887–1905.
68. Asner, G.P. Biophysical and biochemical sources of variability in canopy reflectance. *Remote Sens. Environ.* **1998**, *64*, 234–253.
69. Clark, M.L.; Roberts, D.; Clark, D. Hyperspectral discrimination of tropical rain forest tree species at leaf to crown scales. *Remote Sens. Environ.* **2005**, *96*, 375–398.
70. Hill, J. State-of-the-Art and Review of Algorithms with Relevance for Retrieving Biophysical and Structural Information on Forests and Natural Vegetation with Hyper-Spectral Remote Sensing Systems. In: Kaufmann, H., et al (2010): Hyperspectral algorithms: report in the frame of EnMAP preparation activities, Potsdam: Deutsches GeoForschungsZentrum GFZ, *Scientific Technical Report (STR)*; 10/08, **2010**.
71. Loizzo, R.; Guarini, R.; Longo, F.; Scopa, T.; Formaro, R.; Facchinetti, C.; Varacalli, G. PRISMA: The Italian hyperspectral mission. In Proceedings of the IGARSS 2018 - 2018 IEEE International Geoscience and Remote Sensing Symposium, Valencia, Spain, 22–27 July 2018.

72. Guanter, L.; Kaufmann, H.; Segl, K.; Foerster, S.; Rogass, C.; Chabrillat, S.; Kuester, T.; Hollstein, A.; Rossner, G.; Chlebek, C.; Straif, C.; et al. The EnMAP spaceborne imaging spectroscopy mission for earth observation. *Remote Sens.* **2015**, *7*, 8830–8857.
73. Birth, G.S.; McVey, G.R. Measuring the Color of Growing Turf with a Reflectance Spectrophotometer 1. *Agron. J.* **1968**, *60*, 640–643.
74. Rouse, J.W., Jr.; Haas, R.H.; Schell, J.A.; Deering, D.W. Monitoring the Vernal Advancement and Retrogradation (Green Wave Effect) of Natural Vegetation. NASA Technical Report; Texas A&M University: College Station, TX, USA, 1973.
75. Ustin, S.L.; Roberts, D.A.; Gardner, M.; Dennison, P. Evaluation of the potential of Hyperion data to estimate wildfire hazard in the Santa Ynez Front Range, Santa Barbara, California. In Proceedings of the IEEE International Geoscience and Remote Sensing Symposium, Toronto, ON, Canada, 24–28 June 2002.
76. Fourty, T.; Baret, F.; Jacquemoud, S.; Schmuck, G.; Verdebout, J. Leaf optical properties with explicit description of its biochemical composition: Direct and inverse problems. *Remote Sens. Environ.* **1996**, *56*, 104–117.
77. Hunt, E.R., Jr.; Rock, B.N. Detection of changes in leaf water content using near-and middle-infrared reflectances. *Remote Sens. Environ.* **1989**, *30*, 43–54.
78. Gao, B.-C. NDWI—A normalized difference water index for remote sensing of vegetation liquid water from space. *Remote Sens. Environ.* **1996**, *58*, 257–266.
79. Melillo, J.M.; Aber, J.D.; Muratore, J.F. Nitrogen and lignin control of hardwood leaf litter decomposition dynamics. *Ecology* **1982**, *63*, 621–626.
80. Nagler, P.L.; Inoue, Y.; Glenn, E.P.; Russ, A.L.; Daughtry, C.S.T. Cellulose absorption index (CAI) to quantify mixed soil–plant litter scenes. *Remote Sens. Environ.* **2003**, *87*, 310–325.



© 2019 by the authors. Submitted for possible open access publication under the terms and conditions of the Creative Commons Attribution (CC BY) license (<http://creativecommons.org/licenses/by/4.0/>).

Chapter III

Monitoring of Canopy Stress Symptoms in New Zealand Kauri Trees - analysed with AISA Hyperspectral Data

MDPI Remote Sensing 12(6), 926; March 2020

DOI 10.3390/rs12060926

Jane J. Meiforth, Henning Buddenbaum, Joachim Hill and

James Shepherd

© 2020 by the authors. Submitted for open access publication
under the terms and conditions of the Creative Commons
Attribution (CC BY) license

<http://creativecommons.org/licenses/by/4.0/>.

The paper can be accessed at:

<https://doi.org/10.3390/rs12060926>

Abstract

The endemic New Zealand kauri trees (*Agathis australis*) are under threat by the deadly kauri dieback disease (*Phytophthora agathidicida* (PA)). This study aimed to identify spectral index combinations for characterising visible stress symptoms in the kauri canopy. The analysis is based on an aerial AISA hyperspectral image mosaic and 1258 manually edited reference crowns in three study sites in the Waitakere Ranges west of Auckland. A field-based assessment scheme for canopy stress symptoms (levels 1–5) was further developed for use with RGB aerial images. A combination of four indices with six bands in the spectral range 450–1205 nm resulted in a correlation of 0.93 (mean absolute error 0.27, root mean squared error 0.42) for all crown sizes. Comparable results were achieved with five indices in the 450–970 nm region. A Random Forest (RF) regression gave the most accurate predictions while an M5P regression tree performed nearly as well, and a linear regression resulted in slightly lower correlations. Normalised Difference Vegetation Indices (NDVI) in the near-infrared / red spectral range were the most important index combinations, followed by indices with bands in the near-infrared and a ratio on the red-edge and red bands. A test on different crown sizes revealed that stress symptoms in smaller crowns with denser foliage are best described in combination with pigment-sensitive indices with additional bands in the green and red spectral range. A stratified approach with individual models for pre-segmented low and high forest stands improved the overall performance. The selected indices were also tested in a pixel-based analysis. A manual interpretation of the resulting raster map with stress symptom patterns observed in aerial imagery indicated a good match. With bandwidths of 10 nm and a maximum number of six bands, the selected index combinations can be used for large-area monitoring on an airborne multispectral sensor. This study establishes the base for a cost-efficient, objective monitoring method for stress symptoms in kauri canopies, suitable to cover large forest areas with an airborne multispectral sensor.

1 Introduction

The New Zealand kauri trees (*Agathis australis* (D. Don) Lindl.) are a key species of New Zealand's northern indigenous forests [1] and are of high cultural [2] and ecological significance. The conifers are threatened by the deadly kauri dieback disease (*Phytophthora agathidicida* (PA)). The soil-borne disease was first officially confirmed by Beever [3] in the Waitakere Ranges, although it might have been in New Zealand for decades already [3,4]. Meanwhile, it has been verified over major parts of the kauri distribution area [5]. To date, the monitoring of kauri dieback symptoms has relied on fieldwork and the manual interpretation of aerial images and photos taken from aircraft and helicopters [6,7]. There is a need for a cost-efficient, objective approach for the monitoring of stress symptoms, which allows for the coverage of large areas [8].

1.1 Kauri and kauri dieback disease

The New Zealand kauri is an endemic conifer with a natural distribution in the upper North Island. The existing stands of mature kauri are what remained from extensive logging by European settlers in the 19th and early 20th centuries [9]. Young kauri have a small conical shape with dense foliage. Older kauri emerge over the surrounding vegetation and develop a massive trunk and a large dome-shaped crown [10] with measured diameters of over 30 m and heights of up to 40 m in the study areas. The lanceolate leaves of kauri are broad needle-shaped, ca. 2 to 5 cm long, with a smooth leather-like surface [10] and form a spiky foliage surface. While the foliage of small kauri is dense and evenly spread over the crown, the leaves of medium and large size kauri are arranged in clusters (Figure III-1) which expose gaps, shadows and visible branch material, even in the non-symptomatic stages. The kauri foliage occurs in colour variations from darker yellow-green to lighter blue-green (Figure III-2) [10].

Infection with PA causes lesions in the trunk and roots, which block the transport of water and nutrients [1,3]. The first visible signs of stress in the canopy are yellowing of the leaves and leaf loss in the top of the crowns, which exposes bare branches. In some crowns, the symptoms impair only parts of the upper crown if the transport system is only partially blocked. With progressing decline, the foliage becomes sparse, bare branches become exposed, and the influence of woody material, internal shadows, visible undergrowth and ground litter in the canopy reflectance increases.

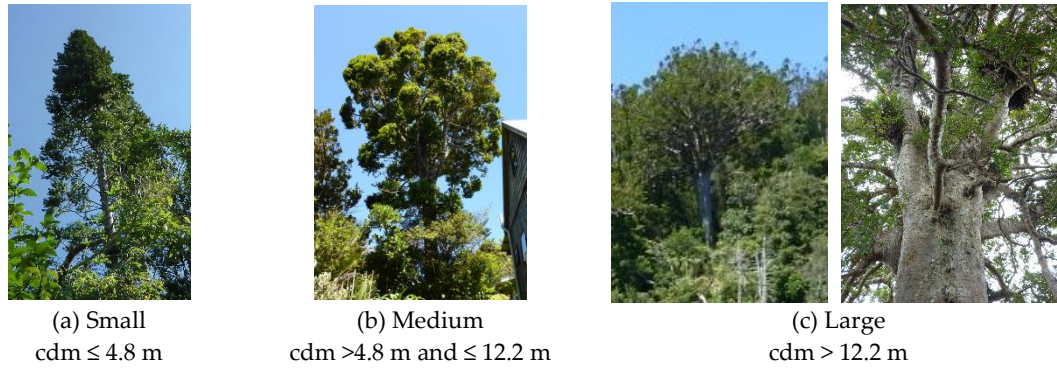


Figure III-1 Kauri growth classes used in this study, according to the mean crown diameter (cdm) [11]. (Photos [12]).



Figure III-2 Mature kauri stand in different foliage colour variations in the Waitakere Ranges shown in (a) oblique view and (b) nadir view [13].

Weakened kauri are less effective in shedding off climbers and epiphytes, which, again, add green plant material in the canopy. In the final stage, the remaining foliage turns brown before it falls off and small branches drop until only a bare skeleton remains. Dead and dying kauri trees are quickly overgrown by undergrowth, neighbouring trees, epiphytes and climbers.

A variety of factors can accelerate the progress and intensify the symptoms of an existing PA infection, including drought conditions, difficult growing conditions on shallow soil and the exposition to strong and salty winds from the sea. These factors alone and also infections with other pathogens, e.g., *Phytophthora cinnamomi* [4,14], can cause similar canopy stress symptoms.

1.2 Remote sensing for stress monitoring

Various authors have found that there is a good relationship between spectrally derived indicators extracted from remotely acquired optical imagery and stress symptoms in tree canopies caused by forest

diseases [15–21].

Airborne hyperspectral images have been used successfully in many studies to analyse tree canopy health in conifers [22–27] and broad-leaved species [28–30]. The full spectral range allows for the processing of a spectral continuum and the identification of important bands from a large range of narrow bands [31] that are sensitive to subtle reflectance changes for early stress detection [32–34]. However, high costs for the data acquisition and maintenance of the sensors, elaborate calibration and processing, and small swath widths qualify airborne hyperspectral sensors for the time being more for analytical research tasks than regular large-area forest monitoring.

Spaceborne imagery is the most cost-efficient option to cover larger areas, as it is comparably easy to process and has been widely used to monitor stress responses in tree canopies [35–42]. However, satellite images often lack the spatial and spectral resolution for an assessment on the individual tree crown level and are bound to certain over-flight times [19,39]. Acquisitions with crewed aircraft are a more expensive option than satellite imagery but provide more flexible timing and higher spatial and spectral resolutions. Unlike unmanned aerial vehicle (UAV) sensors [43], multispectral sensors for crewed aircraft are well suited to large-area coverage with a large swath width, a low noise-to-signal ratio and a robust sensor setup [44–47]. However, the spectral limitation of multispectral sensors to usually four to six bands requires previous knowledge about the best band combinations to detect the target features. The approach in this study combines the strengths of both the hyperspectral and multispectral platforms. We utilized the high spectral resolution imagery from a hyperspectral sensor to define band and index combinations that are suitable to be mounted on a multispectral sensor on a crewed aircraft for large-area stress monitoring in kauri canopies. The spectral ranges used in this study are defined in Table III-1.

Table III-1 Spectral ranges with wavelengths used in this study (adapted from [48]).

Spectral Range	Electromagnetic Wavelengths
Visible (VIS)	437–700 nm ¹
1st near-infrared (NIR1)	> 700–970 nm ²
2nd near-infrared (NIR2)	> 970–1327 nm
1st short-wave infrared (SWIR1)	1467–1771 nm ³
2nd short-wave infrared (SWIR2)	1994–2435 nm ^{1,3}

1 The useable bands of the AISA Fenix image used in this study with low noise levels covered the range between 437 and 2435 nm.

2 The upper band of NIR1 range marks the shift between the two sensor parts at 970 nm.

3 The transition from the NIR to SWIR1 and from SWIR1 to SWIR2 regions is marked by atmospheric water absorption regions.

Vegetation indices (VI) for stress monitoring usually combine bands that are sensitive to the stress parameter(s) with insensitive bands [49]. An ideal VI for stress analysis shows a linear relationship with the targeted symptoms, is equally sensitive for all levels of stress, independent of the scale, and shows minimal

saturation effects [19,50]. VIs were developed for all levels of stress from the first, even pre-visible, reactions on leaf level to obscured canopies of dead crowns.

Pre-visible stress reactions in tree foliage due to reduced transpiration and reduced photosynthetic activity¹⁾ have been successfully detected with thermal sensors [51,52] and narrow optical bands in the visible (VIS) part of the spectrum [53–56]. The first visible¹⁾ stress symptoms are often a reaction to leaf pigment alteration and reduced canopy water content. VIs that provide a direct measure for canopy water content, like the Moisture Stress Index (MSI) [57], the Normalized Difference Water Index (NDWI) [58] and the Water Band Index (WBI) [59], are based on water absorption bands in the near-infrared (NIR) and short-wave infrared (SWIR) regions. The yellowing of leaves as an early stress symptom is related to biochemical changes in the pigment concentrations, especially leaf chlorophyll [60]. Absorption coefficients of chlorophyll are strongest in the blue and red region, around 450 and 680 nm, respectively, where green leaves absorb more than 80% of incident light [61]. While indices in these bands "saturate" rapidly, Gitelson (2003) [61] found that ratios with narrow bands in the green and early red-edge regions are more sensitive to changes in chlorophyll, also at higher chlorophyll concentrations.

So-called "greenness" indices describe the reduction in chlorophyll based on its absorption in the red spectrum in combination with bands in the NIR region around 850 nm that are influenced by strong photon scattering in leaf air–cell–wall interfaces [62,63]. Since these indices are correlated to the amount of photosynthetic active material, they also capture a reduction in leaf area and changes in leaf angle and thereby, structural changes in the canopy [50,61,63,64]. Increased stress leads to a decline in red absorption and a narrowing of the red absorption region, which again causes a blue shift of the red-edge point. The red-edge region is very responsive to changes in chlorophyll content [61,65,66]. Narrowband index combinations with red-edge bands have been successfully used to detect early signs of water stress [67], dying material in *Pinus radiata* [44] and early stress symptoms in conifer woodland [66]. Further indicators of plant stress include a relative increase in carotenoid pigments and a reduction in leaf nitrogen content, which can be detected with indices that contain absorption bands in the blue region (445 nm) for carotenoids [68] and 1510 nm for protein-bound nitrogen [69].

Higher amounts of visible dry litter and dead branches are expressed by subtle reflectance characteristics of cellulose and lignin in the SWIR regions [70]. However, these characteristics are easily obscured by water absorption features and require dry conditions for the most accurate results [62,69,71]. Several studies found a close relationship between bands in the NIR and SWIR region and structural changes in the canopy due to foliage loss [72,73]. Although these relationships are non-linear and therefore difficult to interpret [64], indices in the NIR and SWIR regions were successfully used by Schlerf et al. [74] to estimate the Leaf Area Index (LAI) in Norway spruce forests.

1) This aspect was added afterwards and is not included in the published version of the paper.

The reflectance characteristics of conifers—like a higher absorption, lower transmittance and higher backscattering—are most distinct in the NIR bands [70]. A high optical depth in the NIR spectral region allows a maximum interaction of photons with crown elements in the lower canopy. It thereby enhances the influence of woody material and understory vegetation [57,75].

When upscaling from leaf-scale responses to crown-scale, a range of crown characteristics need to be taken into account, such as foliage condition, canopy structure, the influence of non-photosynthetic branch and stem material, epiphytes and climbers and, depending on the gap fraction, understory vegetation, soils and ground litter as well as illumination conditions, viewing geometry and reflectance from neighbouring trees [48,75,76]. These attributes have different cumulative effects depending on the spatial scale, such that successful indices at leaf-level often show lower performance at crown level [77,78]. Several studies proved that leaf optical properties play only an inferior role in reflectance on canopy scales unless the foliage is dense with a more horizontal orientation and a high LAI [75,79,80].

1.3 Approach and objectives

A method for the detection of kauri trees with indices in the VIS to NIR2 range has already been presented in Meiforth et al. [11]. This study focuses on the spectral analysis of stress responses in kauri crowns over the full hyperspectral range (437–2435 nm) and a reduced range in the visible to NIR1 range (437 – 970 nm). The aim was to identify the best index combinations that are suitable for large-area stress monitoring with a multispectral sensor.

To account for the spectral characteristics on crown level and the assessment scale of whole crowns in the reference data, we use a crown-based scale for the analysis of canopy stress symptoms over the full spectral range from visible to short-wave infrared. We chose to use a combination of indices rather than one single index to account for the wide spectral range of stress symptoms and phenological characteristics of kauri in different growth and stand situations. With regards to the practical implementation, we pay special attention to the performance of the recommended multispectral setup for kauri detection in the context of stress detection. And we also explore index combinations in the VIS to NIR range up to 970 nm (VNIR1), which are easier to realize on a multispectral sensor. A pixel-based application of the developed crown-based model was also tested for a more fine-scale prediction of stress responses, especially in larger crowns.

The objectives of this study are to:

- 1) Identify the best band and index combinations to detect stress symptoms in kauri crowns for both the full spectral range (VIS–SWIR) and the VNIR1 spectral range. The selected band-combinations should not exceed six wavelengths, to be suitable for a multispectral platform.
- 2) Test the performance of a pre-defined band combination for stress detection, which was defined

in Meiforth et al. [11] to locate kauri trees.

- 3) Test the performance of the indices-selection that was developed on mean crown values in a pixel-based approach.

To support objective 1, we analysed the inner- and intra-crown spectral variability and described the spectral characteristics of kauri crowns for different crown size classes and stress symptom stages from non-symptomatic to dead. This study addresses symptoms of stress in the canopy that can be caused by PA, but they can also have a range of other causes, such as drought, insect damage or other diseases. Proof of a PA infection still requires, for the time being, systematic soil sampling and analysis in the laboratory [81].

2 Materials and Methods

2.1 Study area

The study area is located in the Waitakere Ranges, northwest of central Auckland, close to the West Coast. The area has a warm-temperate climate that is influenced by the adjacent sea [82], and rough terrain. The three study sites cover a total area of 1680 ha with 1258 sampled reference crowns (Figure III-3). The sites contain a representative range of kauri stands in all stages of stress, from younger second-growth forests in the Maungaroa area to the remains of mature kauri stands with associated tree species in the Cascade area and Kauri Grove Valley (Figure III-3).

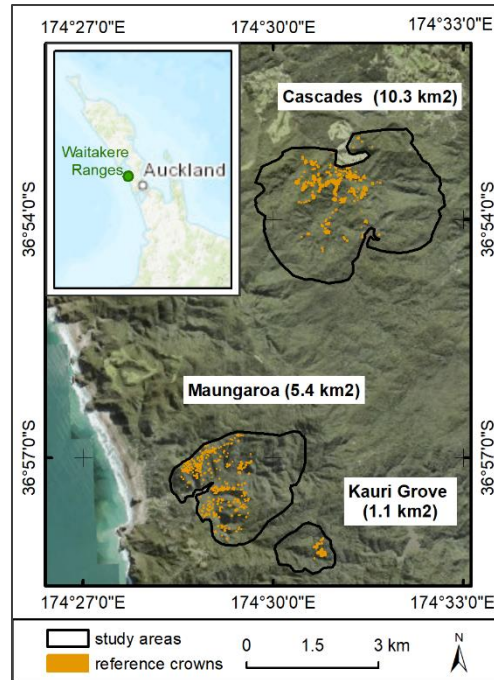


Figure III-3 Study sites in the Waitakere Ranges with the reference crowns marked in orange. The labels give the name of the area and the size in square kilometres. Small map: Location of the Waitakere Ranges on the North Island of New Zealand, west of Auckland City (background maps: [83,84]).

2.2 Remote sensing data and preparation

Figure III-4 provides an overview of the workflow for the data preparation. We used a crown height model (CHM) generated from LiDAR data to locate and edit the crown polygons for the reference crowns that were sampled during the fieldwork. Crown based attributes were calculated as zonal statistics either directly on the hyperspectral image or on (indices) raster that were derived from the hyperspectral image. The attributes were stratified according to the crown size and forest stand situation.

The analysis of kauri stress detection is based on an airborne hyperspectral image flown with an AISA Fenix hyperspectral sensor by Massey University on 15 March 2017. The original image was delivered in 23 strips in radiance values with 448 bands from the visible to SWIR range at 1 m pixel resolution. The sensor features narrow bandwidths of 3.4 nm, on average, in the VNIR1, and 10 nm in the NIR2 to SWIR2 part of the spectrum (Table III-1). The image processing included a geographic correction in PARGE [85], a de-stripping, an atmospheric correction in ATCOR 4 [86], an orthorectification with over 2300 ground control points in ERDAS IMAGINE, the removal of noisy bands and the creation of a seamless mosaic in ArcGIS and ENVI. The processing steps are described in more detail in Meiforth et al. [11]. The final mosaic has a selection of 352 bands and covers a total area of 9 km² over the three study sites.

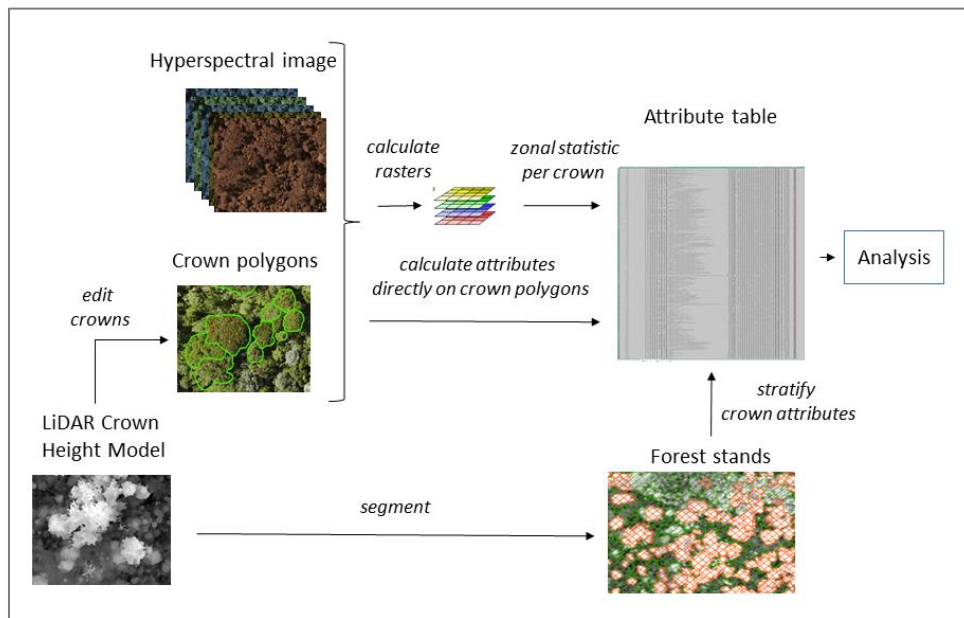


Figure III-4 Workflow for the preparation of crown-based attributes that were used in the analysis.

Spike-free terrain, surface and crown-height models (DTM, DSM and CHM) [87] were created according to a method described in Khosravipour et al. ([87]) with LAStools ([88]). The creation of height models is based on a set of LiDAR data flown with a RIEGL LMS-Q1560 sensor on 30 January 2016 by

AAM NZ Ltd., with 35 returns/m² on average (0.5 ground returns/m²) [87]. The LiDAR point cloud was delivered with the ground points already classified. For the generation of the height models, we filtered out the class 7 “noise”, but kept all other points.

Two sets of Red-Green-Blue (RGB) aerial images served as a reference to assess the canopy stress symptoms in combination with field observations. One set of RGB image was acquired with a 15 cm pixel size on the same flight as the LiDAR data on 30 January 2016 [89]. It was delivered in two versions—orthorectified on the DTM and on the DSM. The second set of RGB aerial images with a higher spatial resolution of 7.5 cm was flown on the 2nd and 3rd of May 2017 [90]. It was delivered in an orthorectified version on the DTM so that high crowns and crowns on steep slopes were partly displaced compared to the correct position on the LiDAR CHM.

2.3 Reference crowns

The locations of the plot areas were pre-selected based on an existing vegetation map [91], aerial images and a LiDAR CHM to provide representative coverage of terrain and growth conditions, tree sizes and symptom stages. The recorded numbers and attributes of kauri crowns were evaluated regularly during the fieldwork to ensure a balanced distribution of growth and symptom classes in the reference data set.

Two methods for locating reference crowns in the field were used, depending on the stand situation. In closed, dense stands, the crowns were located in circular sampling plots of 20 and 30 m diameter with distance and bearing to a centre point, which was positioned with a mapping grade GNSS (Trimble-GeoXH-3.5G, Trimble Geospatial NZ). In combination with the recorded cardinal crown spread in the field, it was possible to accurately position the resulting crown pattern on the LiDAR CHM, which served as the main spatial reference. In more open stands, where it was possible to identify single crowns on aerial images, the crown locations were directly edited in the field as point locations on a field tablet, so that the crown polygon could be delineated afterwards on the LiDAR CHM. Some dead trees were directly identified on the aerial images. While all reference crowns with foliage were identified as kauri, in the category of dead trees, especially in the smaller sizes, it was not always possible to distinguish the species.

The polygons for each reference crown were edited on the LiDAR CHM. A buffer of 10% of the crown diameter was removed from the outer edge to avoid edge effects. The core shadow areas were removed based on a brightness threshold on the average of the RGB-NIR bands. To avoid the effects of mixed pixels, with the 1 m pixel size, only crowns with a mean diameter larger than 3 m were used for this analysis. The final reference set includes 1258 crowns with a total sunlit area of 56,629 m². The crowns were sorted into three size classes according to their growth forms and average crown diameter (Figure III-1). Table III-2 shows the distribution of crown size classes per symptom class, which reflects the crown situation in the

study areas, with most of the crowns classified as symptom class 2 and more medium crown sizes (549) than smaller (378) and larger crown sizes (331).

Table III-2 Overview of stress symptom classes in the reference crowns per size class according to the mean diameter.

		Stress symptom class ³					Total
		1	2	3	4	5	
Crown size class ¹	large	34 ²	249	17	19	12	331
	medium	23 ²	374	44	42	66	549
	small	61	176	35	48	58	378
total		84	833	96	109	136	1258

¹ Crown size classes according to mean crown diameter (small = 3 to ≤ 4.8 m, medium= 4.8 to ≤ 12.2 m and large >12.2 m diameter). ² Large and medium crowns that were non-symptomatic with dense foliage, but a more open canopy than smaller crowns, were noted with the value 1.5 in the analysis. ³ Stress symptom classes were defined from 1 = non-symptomatic to 5 = dead (see assessment scheme in Appendix III-B).

2.4 Field attributes and stress assessment

The recorded attributes in the field included the stem position, the cardinal crown spread, the stem diameter at breast height [92], the canopy base height, an estimated crown density and a foliage coverage according to the “Foliage Cover Scale” in Department of Conservation (DOC) [93]. Optical characteristics like the yellowing of leaves and anomalies like epiphytes or double stems were noted, and each recorded kauri was documented with a canopy photo. Dead branches were documented in six percentage classes according to an index developed by the Department of Conversion [93]. The field staff assessed an overall classification of stress symptoms in the canopy from 1 = “non-symptomatic” to 5 = “dead”, corresponding to the classification scheme of Auckland Council (Figure III-A1 in Appendix A). The experienced staff ensured that the field reference data were comparable to the surveys of the previous years.

The final assessment of stress symptoms was based on an evaluation of the fieldwork and visible stress symptoms on RGB aerial images from 2016 and 2017. Deviations from the overall field score were reviewed in more detail by assessing the particular field attributes and canopy photos. To secure an objective and coherent assessment, we developed an assessment scheme for the interpretation of visible stress symptoms on RGB aerial images in 5 symptom levels (Table III-A1 in Appendix III-B). It takes into account the leaf colour from green, through yellowing, to browning, visible foliage gaps and bare branches. Level 1 describes closed green foliage without visible gaps or branch material and only applies to smaller and some medium kauri sizes. For large and medium kauri crowns that do not show any signs of stress, but still feature a higher number of gaps and visible branch material, we applied the value 1.5.

2.5 Calculation and selection of crown based attributes

The mean spectra of kauri crowns in different size and symptom classes, and their standard deviations, were calculated in ENVI from the selected sunlit parts of the crowns.

A height threshold of 21 m was defined to distinguish “high” and “low” forest stands, which were automatically segmented on the LiDAR CHM in eCognition (scale 15 m, shape 0.3 and compactness 0.9 [94]). Figure 5 illustrates that high forest stands contain a greater number of large (52%) and medium (37%) kauri crown sizes, while low forest stands feature mainly medium-sized (50%) and small-sized (48%) kauri crowns, with the occasional single large crown (3%).

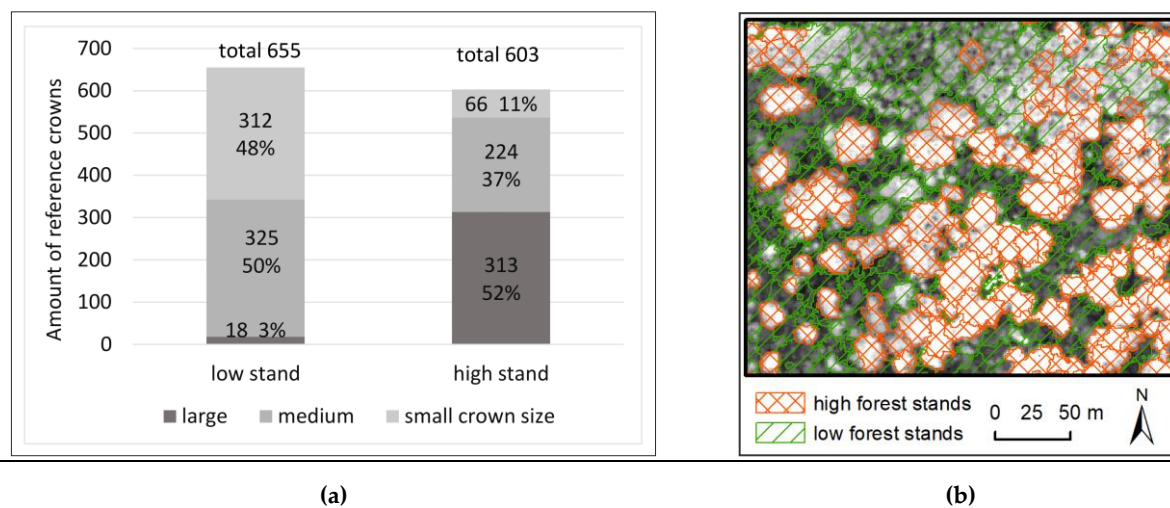


Figure III-5 (a) Crown size classes of the reference crowns (total 1258), used in the analysis per low and high forest stand situation. The crown size classes correspond to the classes used in Table III-2. (b) Low and high forest stands were distinguished with an average height of 21 m on pre-segmented stand polygons based on a LiDAR CHM [89].

The aim of the attribute selection was to identify a set of wavelengths and derived indices with a high correlation to the stress symptom levels. The indices should be based on no more than six bands in total and be efficient in bandwidths of at least 10 nm, to match the requirements for multispectral airborne acquisitions.

The initial selection of 95 indices for the whole spectral range was based on the selection of indices for forest health evaluation in ENVI [95] and the EnMAP toolbox [96] and supplemented with indices from the literature review on VIs summarised previously. The indices were calculated as raster images on the 352 selected hyperspectral bands that were resampled to 10 nm bandwidths with the “Spectral resampling tool” in ENVI. The wavelengths of some indices were slightly modified to reduce the number of required bands for the final index selection. These indices are marked with a prefix “m” in Table III-A2 in Appendix C.

The resulting index rasters were normalised from 0 to 1 with a linear transformation. The mean index

values of the sunlit crown parts were calculated with a zonal statistic tool in QGIS. The analysis was performed on the aggregated mean crown values, to match the crown-based reference data. Highly correlated indices were removed by keeping indices with fewer bands. A first subset was defined by combining the results of a wrapper-, a classifier- and a correlation-based feature subset selection in WEKA [97]. The further selection process was based on a take-one-out method with a Random Forest regression in 10-fold cross-validation under consideration of the best correlation and attribute importance for a maximum of six bands. The selection process was repeated with indices only in the visible to NIR1 spectral range (437 to 970 nm) and for individual crown size classes.

2.6 Selection and parameterisation of the algorithms

Following other studies on tree health assessment [28,98], we applied a regression approach to analyse the continuous stress symptom responses in kauri crowns. The predicted range of values from a regression analysis is better suited to match the gradually declining symptoms in the forest crowns than nominal categories. There is a lot more information in the spectral indices than a 5-step reference scheme can capture, and the regression approach enables to better utilize this information. The continuous range of output values in a regression helps to improve the distinction of first stages of decline, which are of special interest for the management and to account for the spectral differences in the different growth stages.

We compared the performance of six regression models in WEKA (Random Forest, Reduced-Error Pruning Tree, Random Tree, Decision Stump, k Nearest Neighbour and Elastic Net) in a 3-fold random split of all reference crowns in 1000 repetitions, by calculating the correlation coefficient with standard deviations. The Random Forest (RF) regression performed best.

The RF algorithm creates a large number of decision trees from bootstrap samples and predicts the mean value of the individual trees [99]. RF models are robust against outliers in training data, can handle a wide variety in the reference data and produce high correlations between the predicting variables [100]. They do not have requirements for the data distribution and do not tend to overfit [101,102]. We parameterised the model to a depth of 8 and set the number of iterations to 300 according to the learning curve for an out-of-bag accuracy. However, the resulting algorithm was still relatively complicated—a maximum tree depth of 8 resulted in a regression tree with 199 nodes.

For an easier application, we also calculated a linear regression (LR) and M5P regression in WEKA. While the RF model requires a file to be transferred to other datasets, the resulting models of the M5P and LR can be plotted as an equation, which can be directly applied to new data. The LR is a simple parametric statistical model that is fast to train. The WEKA implementation estimates coefficients for a line or hyperplane to fit the training data by reducing the complexity of the learned model with a ridge

regularisation technique [103]. However, the LR works best with a linear relationship between the criterion and predictor variable. The M5P regression in WEKA combines several linear regression models in a tree-based structure, a method that is better adapted to non-linear relationships and can handle tasks with a high dimensionality [104]. Based on a systematic test, we pruned the M5P decision tree to a minimum number of 50 instances allowed at each node.

To account for the different assumptions of the RF, M5P and LR models and deviations in the reference scheme from an ideal linear relationship with equal variances, we only used the correlation value to train and compare the models. The mean absolute error (MAE) and the root-mean-square error (RMSE) were used to compare different test setups within one model, not between the different models. We also tested a rescaling of the reference values, to establish a more linear relationship between the results and reference values for an easier interpretation of the predictions.

2.7 Test of Pixel-Based Application

According to the scale of the crown reference data, the development of the model to predict canopy stress symptoms was based on mean crown values. However, a crown-segmentation is elaborate and introduces additional mistakes [105–107]. An area-based method would be easier to apply and enable the direct use of predefined kauri locations from Meiforth et al. [11] as a mask for further stress analysis. Moreover, the resulting pixel-based map gives a more representative description of partly declining crowns. The results can still be aggregated in a crown- or stand-based manner afterwards if needed. To test the pixel-based application, we applied an RF regression on the raster images of the chosen index combination for the full spectral range. We then compared the resulting stress index values visually with the values of the reference crowns and the RGB aerial images.

3 Results

3.1 Inter- versus within crown-variability

The spectra of non-symptomatic kauri crowns are described in detail in Meiforth et al. [11]. Figure III-6 shows that the variability of the reflectance values between different kauri crowns (a, b) exceeds the maximum variability of reflectance within single kauri crowns (c, d), expressed by the standard deviation per crown. The reflectance values were multiplied by 10000. Large and small crowns show overall the same reflectance patterns, with low separabilities in all spectral regions (Table III-A3 in Appendix D). Large crowns show a higher within-crown variability, while the inter-crown variability is higher in small crowns. The spectral regions with the highest variability are the NIR1 and NIR2 range from 750 to 1400 nm both

between and within kauri crowns. The difference in reflectance values between crowns at the NIR plateau at 870 nm reaches 3230 in small crowns and 2770 in large crowns, while the standard deviation of the reflectance at 870 nm of small crowns goes up to 1250 in small crowns and 1500 in large crowns.

This is also confirmed by the higher separability values and the higher differences in the shape values in the NIR1 and NIR2 spectral ranges, while the differences in the amplitude of the mean crown spectra are most distinct in the visible and SWIR spectral ranges (Table III-A3 in Appendix D).

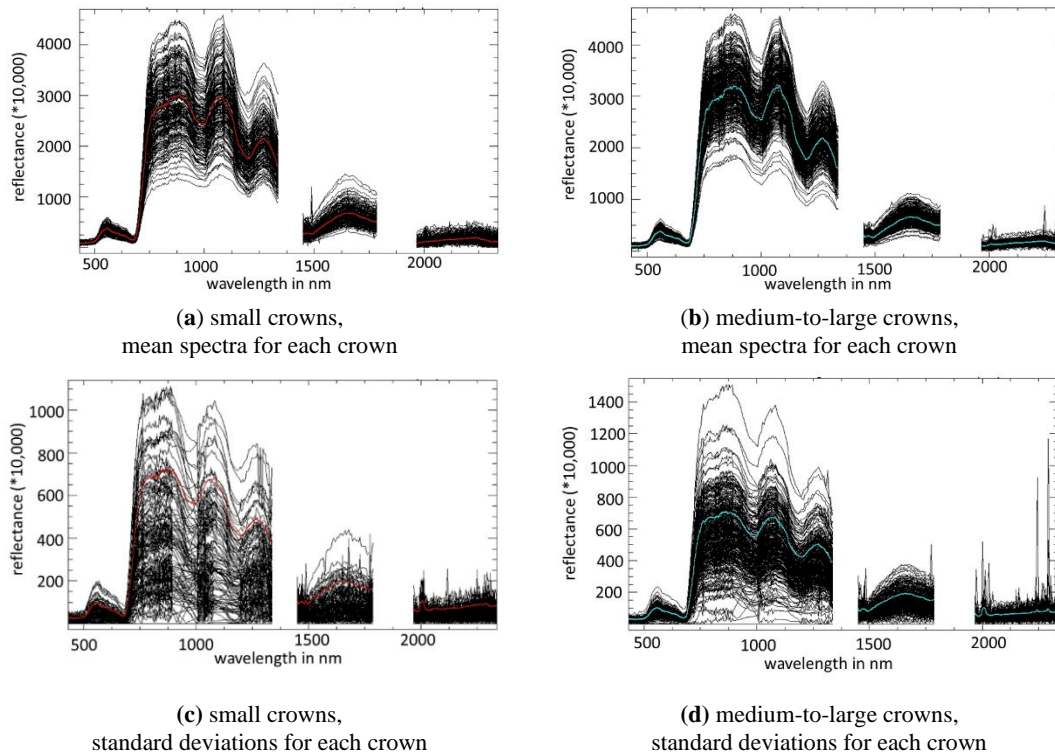


Figure III-6 Inter-crown (a, b) and within-crown (c, d) spectral variability for the sunlit part of 189 non-symptomatic small kauri crowns (crown diameter > 3–4.8 m) (a, c) and 337 large kauri crowns with no visible stress symptoms (crown diameter >12.8 m) (b, d). The mean spectra are marked in colour.

3.2 Spectral characteristics of kauri for different stress symptom and size classes

The mean spectra and standard deviations of all reference crowns for three stress levels are illustrated in Figure III-7. The spectra of non-symptomatic crowns show the characteristic spectral features for kauri with two even peaks in the NIR2, a steep ascent to the 1074 nm peak and a long steep descent to the pronounced absorption feature at 1215 nm [11]. With increasing stress levels, the chlorophyll absorption in the visible spectral range decreases, especially in the blue and red regions, which leads to a decline in the “green peak” from 409 to 360 reflectance between the non-symptomatic and medium-stress stages. Lower overall reflectance in the NIR1 and a reduced absorption in the red lead to a blue shift in the red-edge

spectral region at around 750 nm. The NIR plateau at 880 nm, the reflectance “peak” at 1070 nm and the following water absorption feature decline significantly, which leads to a flattening of the adjacent slopes, so that the spectra lose characteristic kauri features. The mean reflectance at the NIR1 plateau around 880 nm drops between the non-symptomatic and medium stress levels from 3470 to 2695. However, the decline in the reflectance feature at 1280 nm is less distinct with a drop of reflectance values from 2323 to 2067. Also noticeable is a blue shift in the water vapour valley between 1150 and 1190 nm. Stress responses in the SWIR region include a rise in overall reflectance values, a steeper slope in the SWIR1 region and more distinct absorption features. The difference in SWIR1 values is most distinct between the mean spectra of medium stress levels and dead crowns with a raise at 1650 nm from 760 to 1360 reflectance. In addition, the standard deviation increases with increasing stress levels and is particularly high for the mean spectra of dead trees in the SWIR region.

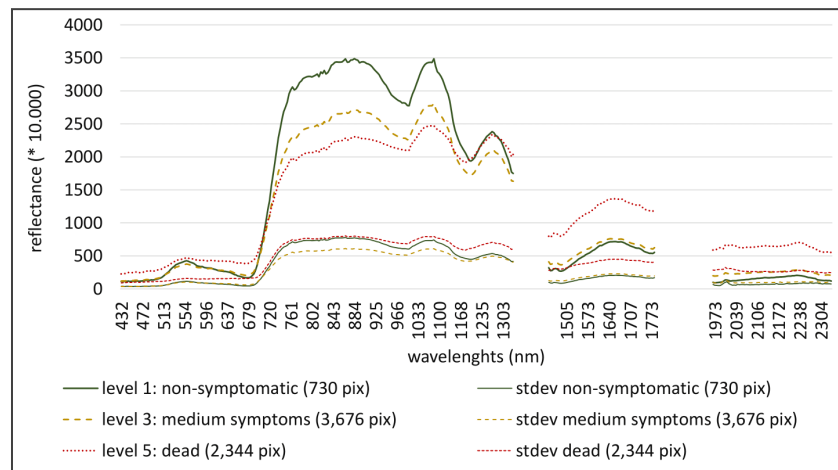


Figure III-7 Mean spectra (bold signatures) and standard deviation (stdev, thin signatures) of kauri in three symptom levels: Non-symptomatic (level 1, green), medium symptoms (level 3, orange) and dead trees (level 5, red). The number of pixels (pix) for the different levels is given in parentheses.

While the overall spectral patterns of the different crown sizes (Figure III-8) are similar to the mean spectra of all size classes combined (Figure III-7), there are some distinct differences between the size classes. In the non-symptomatic condition, the smaller crown sizes show higher reflectance values, with more pronounced reflectance “peaks”, especially in the green and SWIR1 spectral region, than the medium and large crown sizes. With increasing stress symptoms, the reflectance values of smaller crowns decline at a higher rate than the reflectance values of larger crowns. The spectra of non-symptomatic large crowns show a slightly lower absorption in the blue and red bands and overall lower reflectance in the green and NIR spectral range.

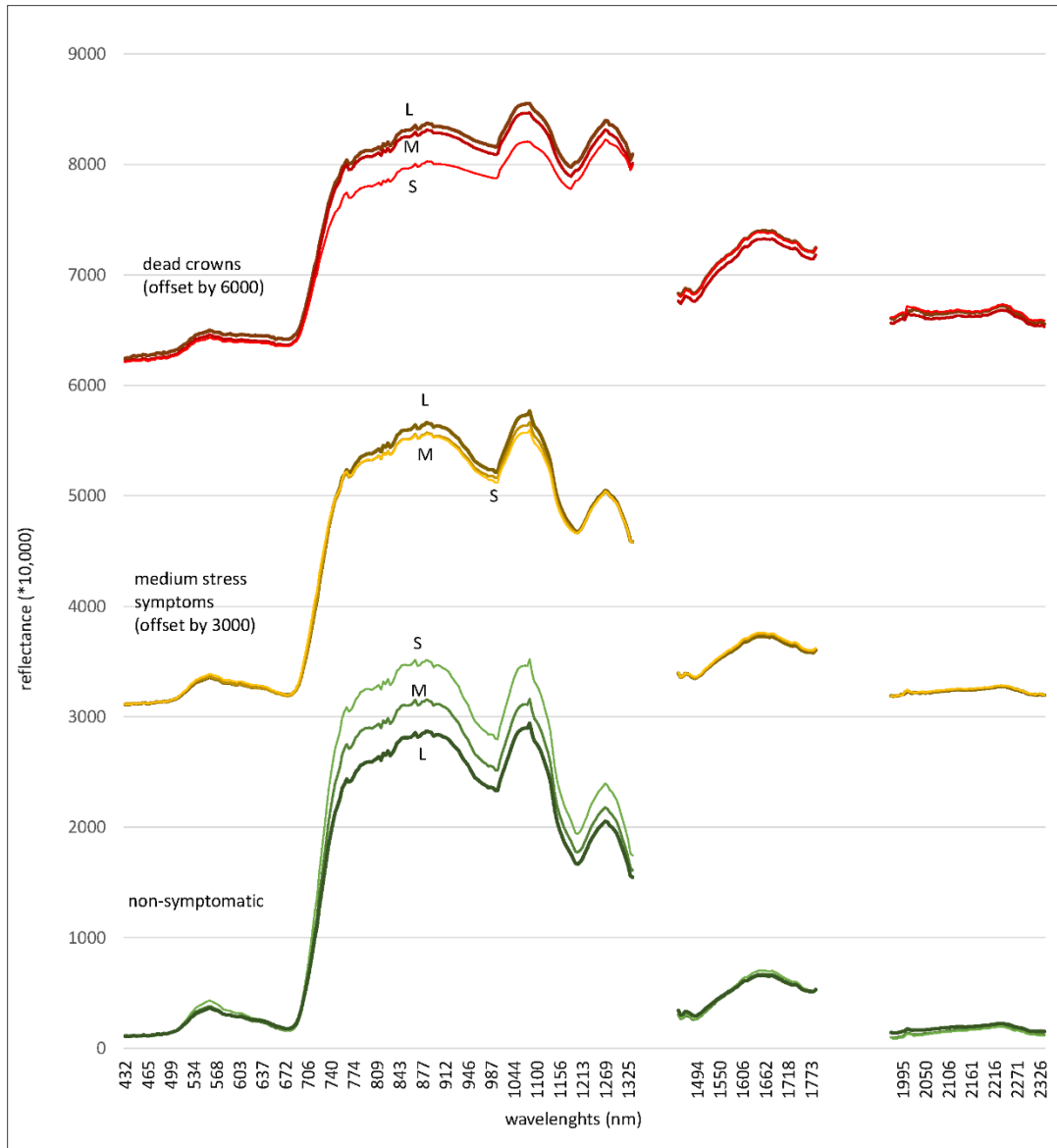


Figure III-8 Spectra of kauri in three different size classes according to their mean crown diameter (cdm) (S = small 3–4.8 m cdm, M = medium >4.8–12.2 m cdm, L = large >12.2 m cdm) sorted in three symptom levels: “Non-symptomatic” (green), “medium stress symptoms” (orange) and “dead crowns” (red), which include visible undergrowth and epiphytes. For better readability, the spectra of crowns with medium symptoms and dead trees were offset by 3000 and 6000 units, respectively.

3.3 Objective 1: Best correlating band and index combinations with canopy stress symptoms

Table III-3 and Table III-4 give an overview of the regression results for the selected index combinations in the full spectral range and the VNIR1 spectral range. A detailed description of the indices is provided in Table III-A2 in Appendix C. Overall, the Random Forest (RF) regression performed best, while the results of the M5P regression were usually better than the linear regression (LR) and equal or slightly lower than the RF regression. In the following sections, we use the correlations to the stress symptom levels of the RF regression to compare the performance of different indices combinations.

3.3.1 Indices for stress detection in the full spectral range (VIS–SWIR2)

The best band combination (“baseline combination”) for a six-band sensor on the full spectral range achieved a correlation of 0.932 in an RF regression (Table III-3). It includes four indices with a Normalized Vegetation Index from Haboudane (NDVI-H) on NIR1/red bands as the most important index, followed by a simple ratio (SR670, 800) on the same bands, a Leaf Water Vegetation Index 2 (LWVI2) in the NIR2 range and a Blue-Green Pigment Index (BGI). A four-band combination without the blue and green bands was slightly less accurate, with a correlation of 0.926. Additional two indices on four bands in the SWIR1 and SWIR2 regions allow adding the Normalized Difference Nitrogen Index (NDNI) and a modified Short-wave Infrared Green Vegetation Index (mSWIRVI), which enhanced the correlation to 0.938.

An individual RF regression of the six-band combination for the different crown sizes resulted in a lower performance of only the small (0.92) and large (0.89) crowns than the results for all crown sizes (0.93). In contrast, the correlation for the medium crowns was higher with 0.945 (Table III-3). A similar test with the four-band combination without the blue and green bands performed slightly worse than the “baseline” six-band combination. An application of the baseline combination for crowns in different forest stands reached a correlation of 0.933 in low stands and 0.905 for high stands.

With individually selected six-band index combinations for each crown size class, the overall performance could only be slightly enhanced for the small and large crown sizes (about 0.01 correlation). The best performing indices for the small crown sizes include the LWVI2 and a modified Red-Green pigment index (mRGI) in combination with an NDNI. The NDVI-H and mSWIRVI indices were most important for the medium crown sizes, followed by the NDNI. The index combination for large crowns contains the Moisture Stress Index (MSI) with bands in the NIR1 and SWIR1, followed by a simple ratio on red and early red-edge (mSRa) bands and the mSWIRVI with bands in the SWIR2 region.

The median values in Figure III-9a illustrate a reasonable fit of the baseline model for stress symptoms in all crown sizes. However, the diagram reveals a higher overlap in the first stress categories (1 and 2). The later stages of stress and the dead crowns also show a higher range of outliers. A rescaling of the reference values for dead crowns from 5 to 8 (Figure III-9b) establishes a more linear relationship between the

predicted and actual values. A test of the correlation coefficients after the rescaling revealed that they were mainly unchanged or even partly improved compared to the results of the original scale from 1 to 5.

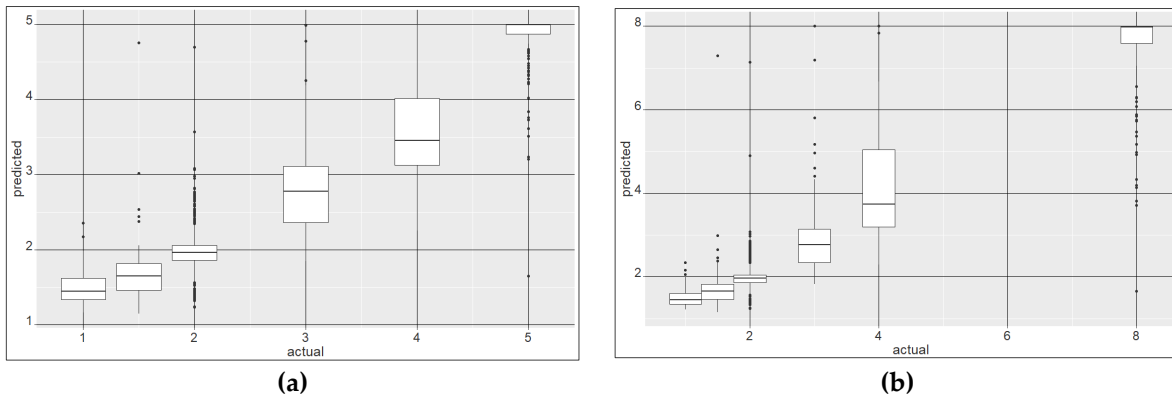


Figure III-9 Box-plot diagrams of the predicted values versus the actual reference crown values for crowns in all sizes classes. Figure (a) shows the results of the original scale from 1 = “non-symptomatic” to 5 = “dead”. Figure (b) shows the results for a rescaled range, with the former value 5 for dead trees changed to value 8. The analysis is based on an RF regression with 1000 iterations in 10-fold cross-validation on the baseline 6-band index combination for the full spectral range.

3.3.2. Indices for stress detection in the VIS-NIR1 spectral range

Table III-4 gives an overview of the performance of selected index combinations in the visible to NIR1 spectral range. A combination of three indices on five wavelengths in the VNIR1 range (437–970 nm) achieved a correlation of 0.92 to the numeric stress symptom classes on all crown sizes. An NDVI on a NIR1 and red band (mNDVI-A 900 and 685 nm) had the highest attribute importance in this combination. Other selected indices include the mRGI, the Gitelson and Merzlyak index-2 (GM2 750 and 700 nm) and a modified Ratio Vegetation Index (mRVI 750 and 685 nm) [108]. The correlation could be increased to 0.93 with an additional band at 970 nm and the Water Band Index (WBI), a ratio on the 900 and 970 nm bands. This index combination is further referred to as the “VNIR1-baseline” index combination. The application of the six-band VNIR1-baseline index combination for crowns in different forest stands results in a correlation of 0.93 for low stands and 0.90 for high stands.

With individual RF models developed for each of the three crown sizes on the VNIR1 baseline combination, the model for medium crown sizes achieved the highest correlation of 0.94, followed by small crowns with 0.90 and large crowns with 0.88 correlation.

Individual attribute selection for the three crown sizes slightly enhances the performance. The small crowns achieve a correlation of 0.92 with three indices on bands in the visible (Photochemical Reflectance Index, PRI), red and NIR spectral range (mNDVI-A, WBI). For the medium crowns, three indices with bands in the blue, red and NIR region resulted in a correlation of 0.94. The selection includes the Lichtenthaler Index (LIC2, [109]), which was developed on narrow bands to document a functional decline

in chlorophyll fluorescence. Although the 10 nm bandwidths in this setup are probably too coarse for this purpose, the LIC2 band combination performed better than a modified Blue-Red Pigment Index (BRI) [110] on the 450 to 685 nm bands.

The index selection for the large crown sizes has the lowest correlation, with 0.89, and includes an NDVI on a red and NIR1 band, the WBI on the 900 and 970 nm bands and a green-red ratio (M. Locherer Chlorophyll Index (MLO 531/645) [111]).

Table III-3 Indices and regression results for the full spectral range (VIS to SWIR2). Resulting correlations (Corr), mean absolute errors (MAE) and root mean squared errors (RMSE) are given for a Random Forest (RF), M5P and Linear Regression (LR) on selected index combinations in the VIS-SWIR2 spectral range. The analysis was carried out in WEKA on 1258 reference crowns on symptom classes in the range from 1 to 5 with a random 3-fold split in 1000 repetitions. Bold text marks the four most important wavelengths in the respective index combination.

Crown/ stand sizes	# of bands	Centre wavelengths of selected bands in nm ²					Indices	RF Regression			M5P Regression			Linear Regression		
		VIS	NIR1	NIR2	SWIR1	SWIR2		Corr ⁴ (stdev)	MAE ³	RMSE	Corr ⁴ (stdev)	MAE ³	RMSE	Corr ⁴ (stdev)	MAE ³	RMSE
Best index combinations for all crown sizes																
All Crown Sizes	10	450, 550, 670	800	1094, 1205	1510, 1680	2090, 2210	NDVI-H, LWVI2, mSWIRVI, NDNI, BGI, SR(670,800)	0.938 (0.01)	0.25	0.4	0.93 (0.01)	0.28	0.43	0.91 (0.01)	0.36	0.49
	6 ¹	450, 550, 670	800	1094, 1205			NDVI-H, LWVI2, BGI, SR(670,800)	0.932 (0.01)	0.27	0.42	0.93 (0.01)	0.28	0.43	0.90 (0.01)	0.37	0.5
	4	670	800	1094, 1205			NDVI-H, LWVI2, SR(670,800)	0.926 (0.01)	0.28	0.44	0.93 (0.01)	0.28	0.44	0.90 (0.01)	0.38	0.51
Baseline index combination (6 bands, 4 indices) applied to different crown sizes in individual models																
Small	6	450, 550, 670	800	1094, 1205			NDVI-H, LWVI2, BGI, SR(670,800)	0.919 (0.02)	0.39	0.55	0.91 (0.02)	0.43	0.58	0.90 (0.01)	0.47	0.6
Medium	6	450, 550, 670	800	1094, 1205			NDVI-H, LWVI2, BGI, SR(670,800)	0.945 (0.01)	0.25	0.38	0.93 (0.01)	0.3	0.42	0.91 (0.01)	0.36	0.48
Large	6	450, 550, 670	800	1094, 1205			NDVI-H, LWVI2, BGI, SR(670,800)	0.887 (0.05)	0.18	0.34	0.86 (0.05)	0.26	0.39	0.86 (0.05)	0.26	0.39
4-Band index combination applied to different crown sizes in individual models																
Small	6	670	800	1094, 1205			NDVI-H, LWVI2, SR(670,800)	0.915 (0.02)	0.39	0.56	0.91 (0.02)	0.43	0.58	0.90 (0.01)	0.47	0.6
Medium	6	670	800	1094, 1205			NDVI-H, LWVI2, SR(670,800)	0.936 (0.01)	0.26	0.41	0.93 (0.01)	0.3	0.43	0.91 (0.01)	0.36	0.49
Large	6	670	800	1094, 1205			NDVI-H, LWVI2, SR(670,800)	0.878 (0.05)	0.18	0.35	0.86 (0.05)	0.26	0.39	0.86 (0.05)	0.26	0.39

1 baseline model with four indices on six wavelengths developed on the mean crown spectra for all crown size classes. 2 the bands were resampled to 10 nm bandwidths before calculating the indices. 3 Mean absolute error. 4 Correlation with standard deviation in parenthesis.

Table III-3 (continued)

Crown/ stand sizes	# of bands	Centre wavelengths of selected bands in nm ²					Indices	RF Regression			M5P Regression			Linear Regression		
		VIS	NIR1	NIR2	SWIR1	SWIR2		Corr ⁴ (stdev)	MAE ³	RMSE	Corr ⁴ (stdev)	MAE ³	RMSE	Corr ⁴ (stdev)	MAE ³	RMSE
Baseline index combination (6 bands, 4 indices) applied for crowns in low and high forest stands with individual models																
Low	6	450, 550, 670	800	1094, 1205			NDVI-H, LWVI2, BGI, SR(670,800)	0.933 (0.01)	0.32	0.49	0.93 (0.01)	0.36	0.51	0.90 (0.01)	0.45	0.58
High	6	450, 550, 670	800	1094, 1205			NDVI-H, LWVI2, BGI, SR(670,800)	0.905 (0.03)	0.2	0.36	0.91 (0.03)	0.23	0.36	0.88 (0.03)	0.29	0.4
Best index combinations for individual crown sizes																
Small	6	550, 685		1094, 1205	1510, 1680		LWVI2, mRGI, NDNI	0.930 (0.01)	0.36	0.51	0.92 (0.02)	0.4	0.55	0.90 (0.01)	0.46	0.6
Medium	6	670	800		1510, 1680	2090, 2210	NDVI-H, mSWIRVI, NDNI	0.947 (0.01)	0.24	0.37	0.93 (0.01)	0.29	0.42	0.90 (0.01)	0.35	0.5
Large	6	675, 700	819		1600	2090, 2210	MSI, mSRa, mSWIRVI	0.897 (0.05)	0.17	0.32	0.87 (0.04)	0.24	0.37	0.87 (0.04)	0.24	0.37

1 baseline model with four indices on six wavelengths developed on the mean crown spectra for all crown size classes. 2 the bands were resampled to 10 nm bandwidths before calculating the indices. 3 Mean absolute error. 4 Correlation with standard deviation in parenthesis.

Table III-4 Indices and regression results for the VIS-NIR1 spectral range. Resulting correlations, mean errors and root mean squared errors (RMSE) are given for a Random Forest (RF), M5P and Linear Regression (LR) on selected index combinations in the VIS-NIR1 spectral range. The analysis was carried out in WEKA on 1258 reference crowns on symptom classes in the range from 1 to 5 with a random 3-fold split in 1000 repetitions. Bold text marks the four most important wavelengths according to the attribute importance for the index selection.

Crown size	# of bands	Centre Wavelengths in nm (10nm bandwidths)		Indices ¹	RF Regression			M5P Regression			Linear Regression		
		VIS	NIR1		Corr ⁵ (Stdev)	MAE ⁴	RM SE	Corr ⁵ (Stdev)	MAE ⁴	RM SE	Corr ⁵ (Stdev)	MAE ⁴	RM SE
VNIR index combinations on all crown sizes													
All	6 ²	550, 685 ³ , 700, 750	900 , 970	mNDVI-A, mRVI, mRGI, GM2, WBI	0.93 (0.01)	0.28	0.43	0.925 (0.01)	0.29	0.44	0.89 (0.01)	0.4	0.53
	5	550, 685 ³ , 700, 750	900	mNDVI-A, mRGI, mRVI, GM2	0.92 (0.01)	0.29	0.46	0.92 (0.01)	0.31	0.45	0.88 (0.01)	0.4	0.56
VNIR baseline index combination applied on individual crown sizes with individual models													
Small	6 ²	550, 685 ³ , 700, 750	900 , 970	mNDVI-A, mRVI, mRGI, GM2, WBI	0.90 (0.02)	0.42	0.58	0.90 (0.02)	0.44	0.6	0.89 (0.02)	0.47	0.62
Medium	6 ²	550, 685 ³ , 700, 750	900 , 970	mNDVI-A, mRVI, mRGI, GM2, WBI	0.94 (0.01)	0.27	0.38	0.94 (0.01)	0.29	0.4	0.92 (0.01)	0.35	0.45
Large	6 ²	550, 685 ³ , 700, 750	900 , 970	mNDVI-A, mRVI, mRGI, GM2, WBI	0.88 (0.04)	0.24	0.34	0.86 (0.04)	0.27	0.38	0.87 (0.04)	0.27	0.37
VNIR index combinations in an RF Regression selected for different crown sizes separately													
Small	5	531 , 570 , 685	900 , 970	mNDVI-A, PRI, WBI	0.90 (0.02)	0.43	0.61	0.89 (0.02)	0.45	0.63	0.84 (0.02)	0.59	0.77
Medium	6	440, 670 , 690	800 , 900 , 970	NDVI-H, WBI, LIC2	0.94 (0.01)	0.26	0.39	0.93 (0.01)	0.43	0.45	0.89 (0.01)	0.38	0.54
Large	5	531, 645 , 685	860 , 900 , 970	mNDVI-A, WBI, MLO	0.89 (0.05)	0.18	0.34	0.86 (0.05)	0.39	0.39	0.85 (0.05)	0.26	0.39
VNIR baseline index combination applied in individual models for different stand situations													
Low	6 ²	550, 685 ³ , 700, 750	900 , 970	mNDVI-A, mRVI, mRGI, GM2, WBI	0.93 (0.01)	0.34	0.51	0.92 (0.01)	0.37	0.53	0.89 (0.01)	0.47	0.61
High	6 ²	550, 685 ³ , 700, 750	900 , 970	mNDVI-A, mRVI, mRGI, GM2, WBI	0.90 (0.03)	0.21	0.37	0.89 (0.03)	0.24	0.38	0.87 (0.02)	0.29	0.42

¹ The order of the indices indicates their importance in the RF regression. ² Baseline model for the VNIR1 spectral range with 5 bands on 6 indices. ³ The original wavelengths values for bands on 680 and 690 nm, were replaced with 685 nm, to reduce the number of required bands. ⁴ Mean absolute error. ⁵ Correlation with standard deviation in parenthesis.

3.4 Objective 2: Test performance of pre-selected index combination

The selected band combination for the identification of kauri includes five indices on three wavelengths in the red to NIR1 region (670, 700 and 800 nm) and two wavelengths in the NIR2 region (1074 and 1209 nm) [11] (Table III-5). With an overall correlation of 0.93 in an RF regression for all crown sizes, this index combination performed well in the canopy stress analysis (Table III-6). Further bands in the SWIR that were selected for kauri identification did not improve the accuracy. A test of the five indices for the different crown sizes resulted in the lowest correlation for large crowns (0.89), followed by 0.92 for small crowns and the highest correlation for medium crowns (0.94). The performance for crowns in low stands, with a 0.93 correlation, is higher than for crowns in high forest stands, with 0.90.

Table III-5 Index selection for the identification of kauri defined by Meiforth et al. [11].

Abbrev.	Equation	Name, Description	Literature
SR800	$= \frac{R800}{R670}$	Simple Ratio 800/670 chlorophyll concentration and LAI	[108]
SR708	$= \frac{R670}{R708}$	Simple Ratio 670/708 chlorophyll concentration and LAI	[112]
RDVI	$= \frac{R800 - R670}{\sqrt{R800 + R670}}$	Renormalized Difference VI chlorophyll concentration and LAI	[113]
NDVI	$= \frac{R800 - R670}{R800 + R670}$	Normalized Difference VI chlorophyll concentration and LAI	[114]
mNDWI-Hyp	$= \frac{\log(R1074)^{-1} - \log(R1209)^{-1}}{\log(R1074)^{-1} + \log(R1209)^{-1}}$	Modified Normalized Difference Water Index-Hyperion; vegetation canopy water content and canopy structure	[115]

Table III-6 Resulting correlations, mean absolute errors (MAE) and root mean squared errors (RMSE) for a Random Forest (RF), M5P and Linear Regression (LR) on a 5-band index combination in the VIS-NIR2 range, that was selected for the identification of kauri in Meiforth et al. [12] (Table III-5). The analysis was carried out in WEKA on the mean indices values of 1258 reference crowns with reference symptom classes in the range from 1 to 5 and a random 3-fold split in 1000 repetitions.

Crown/ stand situation	RF Regression			M5P Regression			Linear Regression		
	Corr. ¹	MAE	RMSE	Corr. ¹	MAE	RMSE	Corr. ¹	MAE	RMSE
All crowns	0.93 (0.01)	0.27	0.43	0.93 (0.01)	0.29	0.44	0.91 (0.01)	0.36	0.49
Small crowns	0.92 (0.02)	0.39	0.56	0.91 (0.02)	0.42	0.58	0.91 (0.02)	0.46	0.59
Medium crowns	0.94 (0.01)	0.25	0.39	0.94 (0.01)	0.29	0.42	0.92 (0.01)	0.35	0.46
Large crowns	0.89 (0.05)	0.19	0.34	0.84 (0.05)	0.27	0.41	0.87 (0.05)	0.25	0.37
Low stands	0.93 (0.01)	0.33	0.49	0.93 (0.01)	0.35	0.5	0.91 (0.01)	0.43	0.57
High stands	0.90 (0.03)	0.21	0.36	0.92 (0.01)	0.23	0.36	0.89 (0.01)	0.28	0.38

¹ Correlation with standard deviations in parentheses.

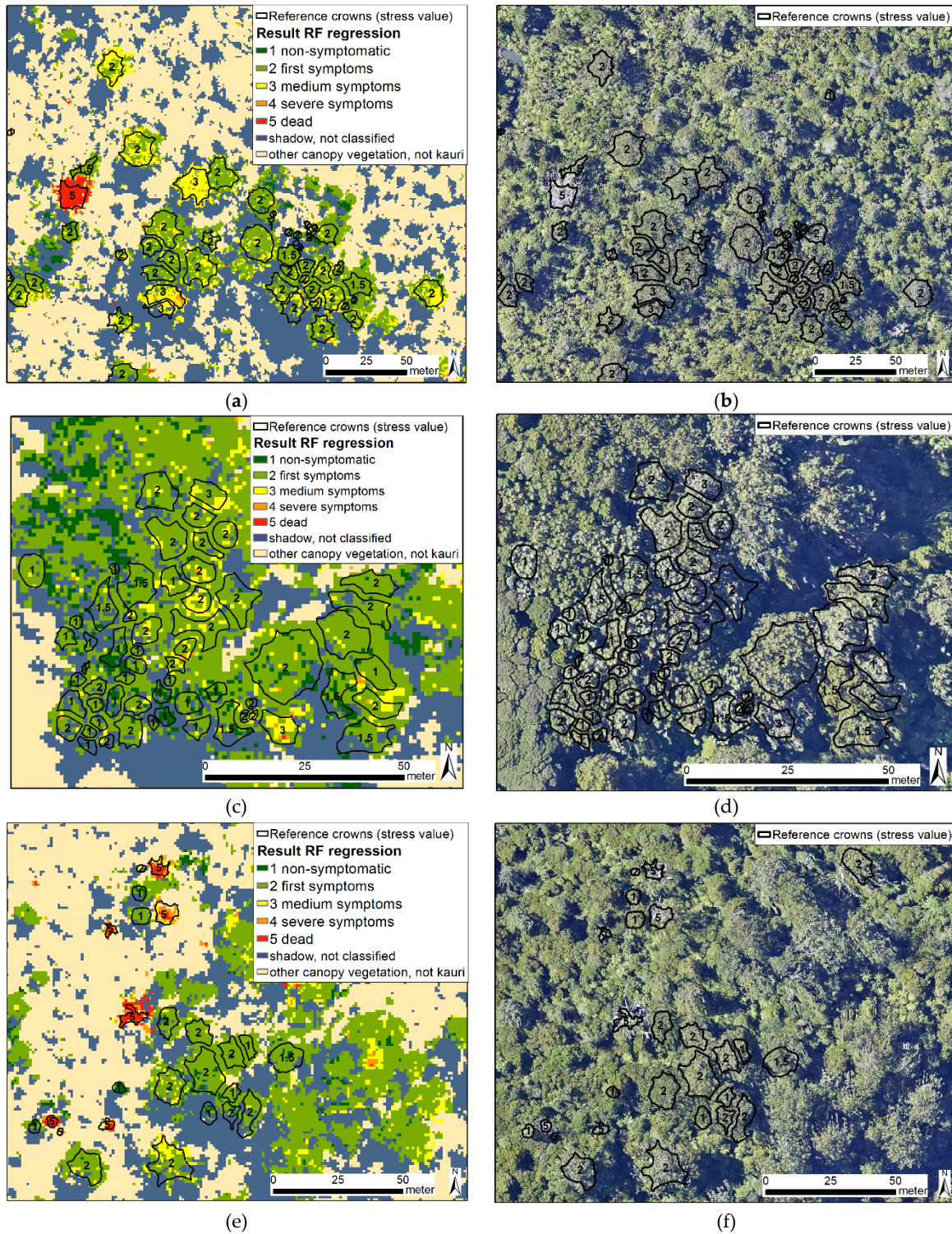


Figure III-10 Resulting maps (a, c, e) and corresponding RGB aerial images (b, d, f) (2016) [89] of a pixel-based application of the baseline index combination for three forest stands with marked reference crowns and their reference symptom class values. The analysis was carried out as a Random Forest regression in the EnMAP toolbox [96] on selected indices raster for the full spectral range.

3.5 Objective 3: Test pixel-based application

A visual comparison of the pixel-based values in the resulting RF regression map with the crown-based reference values and the aerial images from 2016 and 2017 over the whole area showed an overall good match. Figure III-10 shows the resulting map and the aerial image from 2016 in three scenes, which cover both open and closed stands with larger and smaller tree sizes in all symptom stages. The manual comparison showed that dead and dying trees are classified well, and the heterogeneous stress patterns in larger and partly dying crowns were also described correctly.

4 Discussion

4.1 Discussion: Crown variability and crown spectra in different stress levels

The higher variability of reflectance values between different kauri crowns compared to the within-crown variability (Figure III-6) indicates that environmental factors account for the spectral response of the trees at the crown level. The higher spectral variability between the different crowns in the small size group is most likely caused by mixed pixels with neighbouring areas. In a non-symptomatic stage, the overall high spectral variability in the NIR region reflects the importance and range of structural characteristics for the spectra of kauri crowns like the crown architecture, canopy thickness, leaf area and leaf angle. The variability in the visible and short-wave infrared bands, in contrast, is comparatively low, which indicates a high absorption by leaf pigments and canopy water (Figure III-6 and Figure III-7).

In declining kauri canopies, the loss of photosynthetic foliage causes reduced chlorophyll and water absorption, which leads to a characteristic increase in reflectance values in the VIS and SWIR spectral regions (Figure III-7). The overall lower reflectance and less pronounced water absorption features in the NIR range in declining crowns can be explained by reduced scattering processes and water concentration due to foliage loss. Strong water absorption features from green leaf material dominate the spectral response in the SWIR region at high LAI [69], the loss of leaf material and canopy water and a relative increase in woody stem material and litter allow the spectral absorption features of cellulose and lignin in the SWIR regions to emerge at around 1754, 2100 and 2262 nm [116,117]. The higher percentage of stem material in declining canopies contributes to a higher reflectance in the red spectral region, a decreased magnitude of the NIR plateau, an increase in SWIR reflectance and an equalization of the local maxima in the NIR and SWIR regions [118].

The increasing spectral variability with rising stress levels, especially in dead crowns, can be explained by the spectral influence of understorey vegetation, ground material and a variable number of epiphytes, climbers and dry litter in the crowns. The remaining vegetation and water absorption features in the mean

spectra of dead crowns are caused by photosynthetic active sub-canopy vegetation and epiphytes. These effects correspond to the observations of Baret et al. [119] and Asner [118] that the crown reflectance is mainly influenced by the gap fraction when the vegetation cover is less than 70%–80%.

The phenological differences between the dense homogenous foliage in smaller kauri compared to the open, heterogeneous crown structure of large kauri is also reflected in their spectral response. Already in the non-symptomatic stage, large kauri crowns show a higher within-crown spectral variability, which is caused by the stronger influence of internal shadows, woody material and understory reflectance in the open dome shape crown structure. The higher reflectance of small non-symptomatic kauri crowns compared to larger crown sizes corresponds to the findings of Rautiainen et al. [70]. She observed a higher reflectance for an immature Norway spruce stand compared to a mature stand at all spatial scales, which she attributed to different leaf biochemical properties, denser foliage and a higher tree density in smaller stands, with less shadowing between the crowns. With increasing stress levels, the NIR reflectance values of the smaller crown sizes decline disproportionately faster than the NIR response of larger crown sizes (Figure III-8). This effect can be explained by the stronger influence of photosynthetic active green undergrowth and epiphytes in the more open larger crown sizes.

4.2 Discussion objective 1: Index combinations for stress detection

A description of the observed spectral responses in kauri crowns in different stress and growth stages requires the combination of indices in different spectral ranges. With overall high correlations of 0.93 in an RF regression for five canopy stress symptom classes, the six-band baseline combinations in both the full spectral range and the VNIR1 range (Table III-4) are well suited to describe stress symptoms in kauri canopies of all sizes. The continuous output range of the chosen regression approach allows a detailed assessment of the severity of stress symptoms, especially in the early symptom stages. Structural indices like NDVIs and simple ratios with bands in the NIR1 and red spectrum have the highest attribute importance in the RF regression for an overall stress detection for all crown and stand situations¹. The 900 nm NIR band of the mNDVI-A [120] that was selected in the VNIR1 range is also sensitive to the amount of dry matter, which might compensate for the missing SWIR bands in the VNIR1 selection. In the more advanced stages, the loss of foliage and branch material causes structural changes and a further loss of canopy water, which are captured in the selected Leaf Water Vegetation Index (LWVI), with bands in the NIR2 spectral region (1094, 1205 nm) [121] and the WBI and MSI for the VNIR1 spectral range.

¹ Sentence changed from the published version: The most important VIs for stress detection for all crown and stand situations are NDVIs and simple ratios with bands in the NIR1 and red spectrum, which describe the efficiency drop of photosynthetic absorption in the red band and the decrease of reflectance in the NIR1 region.

To account for the spectral properties in different size classes, we tested two stratified approaches: A distinction between small, medium and large crown sizes according to their mean diameter and separation of crowns in low and high forest stands. In small kauri crown sizes with denser foliage, indices in the red and green part of the visible spectrum like the mRGI and PRI were selected. These are more sensitive to pigment changes, and they perform better than NIR1/red band combinations in dense foliage with high LAI and high concentrations of chlorophyll when NIR1/red indices easily saturate [122]. Furthermore, the NDNI (1510 and 1680 nm) that was selected for small crown sizes in the full spectral range is sensitive to changes in foliar nitrogen content [69,123]. The mRGI is also included in the VNIR1 baseline combination together with the GM2 index that captures a blue shift of the red-edge region [124]. For the more open medium and large crown sizes, the selected mSWIRVI with bands in the SWIR2 region (2090 and 2210 nm) on the full spectral range is sensitive to the influence of dry matter with cellulose reflectance features [117,125].

While these individual band and index selections for different crown sizes showed the highest performances for both the full spectral range and the VNIR range, individual models for the different crown sizes on the same 6-band baseline combination performed nearly as well. The slightly lower correlations on the baseline combination for large crowns (0.89 and 0.88) compared to medium (0.94 and 0.94), and small crown sizes (0.92 and 0.90) can most likely be explained by the higher spectral variability in the larger crowns already in the non-symptomatic stages. Moreover, some large crowns show heterogeneous stress patterns with different symptom stages in different parts of the crown. Medium crown sizes are less influenced by mixed pixels than small crowns and more homogenous than larger crowns. The larger number of medium crowns in the reference crown set, according to the crown size distribution in the study areas, might contribute to the better fit of the model for medium crown sizes.

Compared to the application of the baseline indices to small and large crowns, the correlations of different RF models for crowns in low and high forest stands on the same index combination are slightly higher, with 0.94 (VNIR1: 0.93) for low stands and 0.90 (VNIR1 0.90) for high forest stands. These higher correlations can presumably be attributed to the influence of the easier to describe medium crown sizes in both stand situations (Figure III-5).

4.3 Discussion objective 2: Performance of band selection for kauri detection

The five-band index combination that was selected to identify kauri trees in Meiforth et al. [12] with bands in the red, red-edge, NIR1 and NIR2, is similar to the baseline combination for stress detection on the full spectral range. It showed a comparably high correlation of 0.93 with the stress symptom classes on all crown sizes. The lower performance of this index combination for small crowns with denser foliage can be explained by the lack of bands in the green spectrum, which are sensitive to pigment-related reflectance

features. The index combination also contains the mNDWI-H, which describes the characteristic spectral reflectance and absorption features of kauri in the NIR2 (1074, 1209). These spectral features are most likely caused by photon scattering in the thick kauri leaves at the mesophyll and the air–cell–wall interfaces, the characteristic spiky foliage surface and the open crown structure in larger kauri that allow the woody material from the massive stem and branches to influence the crown reflectance. The more a kauri crown declines and loses its foliage, the more it also loses these characteristic structural features. In conclusion, this five-band index combination can be used for stress detection in kauri crowns. However, it should be improved for smaller crowns by adding a green band. And it would need to be tested for the use in other species.

4.4 Discussion objective 3: Pixel-based application

The observed high correlation of the pixel-based implementation with the visible stress symptoms in a visual comparison with the aerial images (Figure III-10) indicates that this is a practical approach. However, the results should be tested more thoroughly, ideally with sub-canopy reference data, that need to be accurately aligned with the remote sensing image used in the analysis. The aerial image from 2017 that matches the same season as the hyperspectral data was unfortunately not sufficiently aligned for such an analysis. A pixel-based approach allows for an easy application since this method does not require a prior crown-segmentation. It enables a more detailed assessment of larger crowns, which often show heterogenic symptom patterns. It also gives more flexibility to define the aggregated reporting units from single crowns to homogenous forest stands. Furthermore, it allows the direct usage of the pixel-based kauri mask, described in Meiforth et al. [12]. The crown-based results indicate that further improvements of the pixel-based regression map can be achieved in separate analyses for low and high forest stands. For the large-area monitoring of forest situations like the Waitakere Ranges with a multispectral sensor, we recommend a pixel size at around 0.5 m, which is large enough to level out extremes but small enough to capture small crown sizes.

4.5 Discussion: Application and further analysis

While the RF regression results in high correlations between the predicted and actual values, a slightly non-linear relationship, especially towards the dead and dying crowns, results in a shift between the predicted and actual value range. A rescaling of the value for the dead trees from value 5 to value 8, improves the match between the predicted and actual values (Figure III-9). The resulting levels “5 to 8” describe different portions of dead branch material and shadows, which cause extreme values. The correlation coefficients for the rescaled value range remained mainly unchanged compared to the original range from

1 to 5. The rescaling simplifies the interpretation of the predicted values, while the new resulting values from 6 to 8 have no influence on the practical implementation since all crowns with values equal or higher 5 can be treated as “dead”.

Another possibility to address the non-linearity in the higher levels of stress symptoms is to first distinguish the dead and dying trees in a binary classification and then apply the regression to the remaining first to medium symptom stages, which feature a more linear relationship. A test with a binary RF classification showed that the aggregated class “dead/dying” can be distinguished with user’s and producer’s accuracies of 87.6% respective 93.32% (Table III-A4 in Appendix E). This approach should be tested in further studies.

The use of the resulting maps for management purposes requires an interpretation to translate the detected stress symptoms into a health assessment. Canopy stress symptoms in kauri can have a range of causes besides a PA infection, such as water shortage and unfavourable growing conditions [4,126]. The application of time series allows detecting characteristic temporal trends and spatial patterns of infection symptoms and can help to distinguish between different causes of stress [15,127–130].

High spectral resolution satellite data like Sentinel-2 and WorldView02 should be tested for cost-efficient large-area stress detection in time series. The combination with LiDAR attributes can also improve the detection of canopy stress symptoms, especially for more advanced stress levels with textural and structural changes in the canopy caused by defoliation [131–134]. The challenging sub-pixel co-location between optical and LiDAR datasets might be overcome with new multispectral waveform LiDAR sensors that allow the direct combination of LiDAR data with multispectral wavelengths in one dataset [135].

5 Conclusions

The analysis of an airborne AISA hyperspectral image proved that a combination of six spectral bands in the VNIR1 range (550–970 nm) is sufficient to capture the full range of canopy stress symptoms in kauri trees on a numeric scale from 1 to 5 with a high correlation of 0.93 (mean absolute error of 0.28, RMSE 0.43) in a Random Forest (RF) regression. A more linear relationship between predicted and actual values can be achieved by rescaling the value for dead trees from 5 to 8. The easier to implement MSP algorithm performed nearly as well as a more complicated RF regression model. The most important indices are sensitive to structural changes and canopy water, while stress symptoms in smaller kauri crowns with denser foliage are best described with additional bands in the green and red spectrum, which are sensitive to pigment changes.

The study was designed to be applicable to large-area monitoring with a large representative reference set of 1258 crowns, and selected bandwidths of 10 nm that can be used on multispectral sensors. Based on

the reference crowns and field assessment data, we developed a numeric assessment scheme for canopy stress symptoms in kauri trees on RGB aerial images, which are better suited for an assessment of the upper crown canopy than a limited view through the undergrowth and canopy from the ground.

Comparable correlations to the VNIR1 selection were achieved with six bands in the VNIR2 spectrum (450–1205 nm), while additional bands in the SWIR enhanced the correlation slightly. However, we recommend the use of the six-band combination in the VNIR1 range instead of the full spectral range since it is easier to implement, the VNIR bands have a higher signal to noise ratio and are less influenced by species-specific structural crown attributes.

The spectral differences of kauri crowns in different size classes respective stand situations advise a stratified approach. We recommend the application of the six-band baseline combination with individual models for pre-selected crown sizes, respective crowns in low and high forest stands.

While the analysis is based on mean crown spectra to match the scale of the reference data, an easier to apply pixel-based application seem to match well with the observed stress symptoms in the field and aerial images. However, this approach needs to be tested more thoroughly in other areas with matching reference data.

The results of this study have important implications for the monitoring of canopy stress symptoms in kauri trees in New Zealand. The objective, cost-efficient method for large-area monitoring of canopy stress symptoms with a multispectral sensor can help to target the required fieldwork and support management decisions to prevent the further spread of the kauri dieback disease.

Supplementary Materials: The following are available online at <http://www.mdpi.com/2072-4292/12/6/926/s1>, Table III-S1: Algorithms for the Linear and M5P regression for the selected baseline models in WEKA on the full spectral range (VIS to SWIR2). Baseline models on the visible to SWIR2 (full) spectral range for all crown sizes., Table III-S2: Algorithms for the Linear and M5P regression for the selected baseline models in WEKA on the visible (VIS) to near-infrared1 (NIR1) spectral range. Baseline models on the visible to NIR1 spectral range for all crown sizes.

Author Contributions: Conceptualization, J.M.; methodology, J.M.; software, J.M.; validation, J.M.; formal analysis, J.M.; investigation, J.M.; resources, J.M., J.S.; data curation, J.M.; writing—original draft preparation, J.M.; writing—review and editing, J.M., H.B., J.H., J.S.; visualisation, J.M.; supervision, H.B., J.H., J.S.; project administration, J.M., J.H.; funding acquisition, J.M., J.H., J.S.

Funding: The Kauri Dieback Programme (NZ) funded most of the remote sensing data (Ministry for Primary Industries agreement nr 17766), while the University of Canterbury (NZ), Landcare Research (NZ), the University of Trier (Germany), and FrontierSI (former CRCSI) Australia supported living costs, fieldwork, equipment and additional LiDAR data. Auckland Council supported the fieldwork and supplied LiDAR data and aerial images. Rapidlasso and Harris Geospatial supplied grants for software licenses. Henning Buddenbaum was supported within the framework of the EnMAP project (FKZ 50 EE 1530) by the German Aerospace Center (DLR) and the Federal Ministry of Economic Affairs and Energy. Landcare Research funded the open-access fee for the publication.

Acknowledgments: Our sincere thanks go to all people and institutions who supported this project. We are especially grateful to David Norton, who helped with the administration and gave inputs for the fieldwork and ecological aspects of the analysis. Nick Waipara, Lee Hill and Yue Chin Chew from Auckland Council helped to establish the project and provided data. The Kauri Dieback Programme (Planning and Intelligence Team) gave constructive feedback and support during this research. We also like to thank the staff of the Arataki visitor centre, Fredrik Hjelm from the Living Tree Company and Joanne Peace for their excellent support and guidance during the fieldwork. Our thanks go to Massey University for the provision of the hyperspectral data acquisition as well as AAM NZ Ltd. for the acquisition and processing of airborne LiDAR data for Waitakere. Jeanette Allen, Vicki Wilton and Nicole Gellner helped with the University administration.

Conflicts of Interest: The authors declare no conflict of interest.


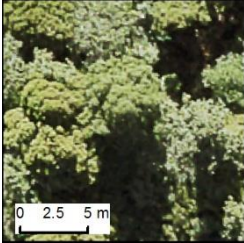

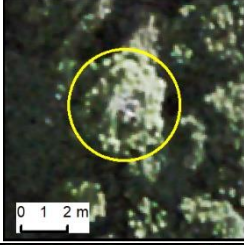

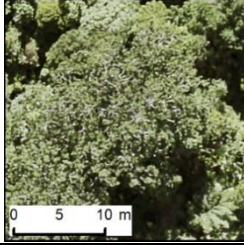
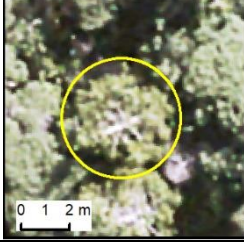
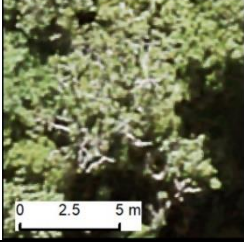
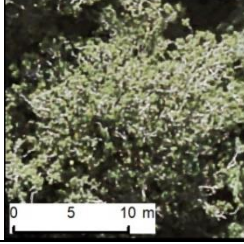
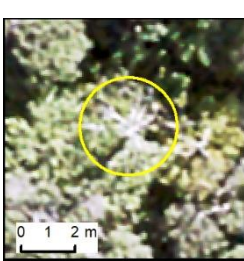
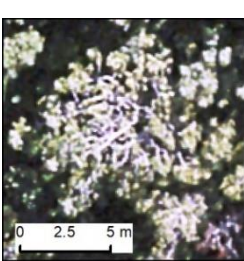
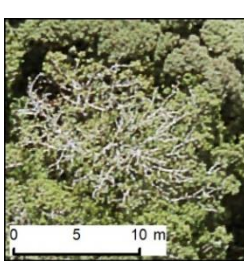
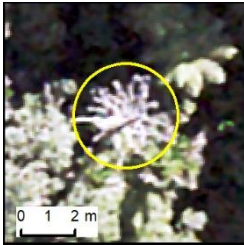
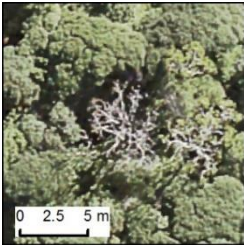
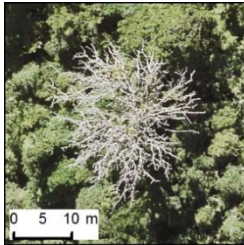
Appendix III-A



Figure III-A1 Photo illustration of the canopy score scheme for kauri used by Auckland Council in 2015 with five classes [136]: 1 = Healthy crown—no visible signs of dieback, 2 = Foliage/canopy thinning, 3 = Some branch dieback, 4 = Severe dieback, 5 = Dead.

Appendix III-B

Table III-A1 Assessment scheme for stress symptoms in kauri crowns based on RGB aerial images [89,90] for five canopy stress symptom classes and three crown sizes.

Symptom class	Description	Size small ¹	Size medium ¹	Size large ¹
Value 1— No Symptoms	Leaves: green, green/blue; Canopy density: dense, no to small gaps; Bare branches: <1%			
Value 2— First Symptoms/ Open Crowns	Leaf colour: green to yellowish; Canopy density: small gaps; Bare branches: 1 to 5% (small branches)			
Value 3— Medium Symptoms	Leaves: green with yellow or brown; Canopy density: small to medium gaps visible; Bare branches: 5%–30%			
Value 4— Severe Symptoms	Leaves: yellow-green to brown; Canopy density: sparse, many gaps, understory partly visible; Bare branches: >=30% visible as linear structures Epiphytes and climbers possible			
Value 5— Dead Trees	Leaves: dead, brown leaves possible Epiphytes and climbers possible; Canopy density: Gaps and understory visible, Bare branches: 100% dead branches, visible as linear structures			

¹ The crown size classes are defined according to their mean crown diameter, see 1. Non-symptomatic large and medium crowns with open canopies were given the value 1.5 in the analysis.

Appendix III-D

Table III-A3 Comparison of the spectra for small (3–4.8m diameter) versus medium and large crowns (>4.8m diameter) for each spectral region. The values for the Jeffries Matusita [140] and Transformed Divergence [141] separabilities were calculated on the pixel spectra and range from 0 to 2, a value lower 1.9 indicates a low separability. The values for the amplitude D and shape θ were calculated on the mean crown spectra, according to Price 1994 [142].

	Wavelengths	Jeffries Matusita Separability	Transformed Divergence	Amplitude D	Shape θ
VIS	437–700 nm	1.401	1.460	1.54	0.002
NIR1	700–970 nm	1.475	1.529	1.28	0.013
NIR2	970–1327 nm	1.419	1.524	1.13	0.013
SWIR1	1467–1771 nm	1.369	1.456	1.51	0.006
SWIR2	1994–2435 nm	1.373	1.461	1.55	0.003

Appendix III-E

Table III-A4 RF classification (1000 repetitions, 10-fold cross-validation) for the baseline VNIR index combination (6 bands, 5 indices) on 2 aggregated classes, to distinguish dead and dying trees (“level 45”) from the other symptom stages (“level 123”).

	Level 123	Level 45	Total	Producer’s Accuracy
Level 123	1043	13	1056	98.8
Level 45	25	177	202	87.6
Total	1068	190	1258	
User’s Accuracy	97.7	93.2		97.0

6 References

1. Wyse, S.V.; Burns, B.R.; Wright, S.D. Distinctive vegetation communities are associated with the long-lived conifer *Agathis australis* (New Zealand kauri, Araucariaceae) in New Zealand rainforests. *Austral Ecol.* **2014**, *39*, 388–400.
2. Shortland, T.; Wood, W. *Kia Toitu He Kauri, Kauri Dieback Tangata Whenua Roopu Cultural Impact Assessment*; Repo Consultancy Limited: Whangarei, New Zealand, 2011.
3. Beever, R.E.; Waipara, N.W.; Ramsfield, T.D.; Dick, M.A.; Horner, I.J. Kauri (*Agathis australis*) under threat from *Phytophthora*. *Phytophthoras For. Nat. Ecosyst.* **2009**, *74*.
4. Sanson, J. *Independent Review of the State of Kauri Dieback Knowledge*; Lincoln University: Lincoln, New Zealand, 2016.
5. MPI. *kauri Dieback Distribution. A Map Published on the Kauri Dieback Website*. Ministry for Primary Industries, Biosecurity New Zealand, Wellington. 2020 Available online: https://www.kauridieback.co.nz/media/2037/kauri-dieback-distribution_20190930_350dpi.jpg (accessed on 1 February 2020).
6. Alastair Jamieson, L.H.; Nick, W.; Jack, C. *Survey of Kauri Dieback in the Hunua Ranges; Pseudomonas & Phytophthora*; New Zealand Plant Protection Society: Auckland, New Zealand, 2011; pp. 60–65.
7. Waipara, N.; Hill, S.; Hill, L.; Hough, E.; Horner, I. Surveillance methods to determine tree health, distribution of kauri dieback disease and associated pathogens. *N. Z. Plant Prot.* **2013**, *66*, 235–241.
8. MPI. *Kia toitu he kauri—Keep kauri standing. New Zealand's strategy for managing kauri dieback disease*. *Minist. Prim. Ind.* **2014**, *2014*, 24.
9. Ecroyd, C. Biological flora of New Zealand 8. *Agathis australis* (D. Don) Lindl. (Araucariaceae) Kauri. *N. Z. J. Bot.* **1982**, *20*, 17–36.
10. Steward, G.A.; Beveridge, A.E. A review of New Zealand kauri (*Agathis australis* (D. Don) Lindl.): Its ecology, history, growth and potential for management for timber. *N. Z. J. For. Sci.* **2010**, *40*, 33–59.
11. Meiforth, J.J.; Buddenbaum, H.; Hill, J.; Shepherd, J.; Norton, D.A. Detection of New Zealand Kauri Trees with AISA Aerial Hyperspectral Data for Use in Multispectral Monitoring. *Remote Sens.* **2019**, *11*, 2865.
12. Meiforth, J.J. *Photos, Waitakere ranges photo staken during fieldwork in January to March 2016; Waitakere Ranges*. New Zealand. 2016.
13. Auckland Council. *Helicopter Survey for Kauri Dieback in the Waitakere Ranges*; Unpublished aerial photos; Auckland Council: Auckland, New Zealand, 2016.
14. Scott, P.; Williams, N. *Phytophthora diseases in New Zealand forests*. *N.Z. J. For.* **2014**, *59*, 14–21.
15. Hall, R.; Castilla, G.; White, J.; Cooke, B.; Skakun, R.J. Remote sensing of forest pest damage: A review and lessons learned from a Canadian perspective. *Can. Entomol.* **2016**, *148*, S296–S356.
16. Senf, C.; Seidl, R.; Hostert, P. Remote sensing of forest insect disturbances: Current state and future directions. *Int. J. Appl. Earth Obs. Geoinf.* **2017**, *60*, 49–60.
17. Stone, C.; Mohammed, C. Application of remote sensing technologies for assessing planted forests damaged by insect pests and fungal pathogens: A review. *Curr. For. Rep.* **2017**, *3*, 75–92.
18. Wulder, M.A.; Dymond, C.C.; White, J.C.; Leckie, D.G.; Carroll, A.L. Surveying mountain pine beetle damage of forests: A review of remote sensing opportunities. *For. Ecol. Manag.* **2006**, *221*, 27–41.
19. Silva, C.R.; Olthoff, A.; de la Mata, J.A.D.; Alonso, A.P. Remote monitoring of forest insect defoliation. A review. *For. Syst.* **2013**, *22*, 377–391.
20. Lausch, A.; Erasmi, S.; King, D.; Magdon, P.; Heurich, M. Understanding forest health with remote sensing—part I—A review of spectral traits, processes and remote-sensing characteristics. *Remote Sens.* **2016**, *8*, 1029.
21. Lausch, A.; Erasmi, S.; King, D.; Magdon, P.; Heurich, M. Understanding forest health with remote sensing—part II—A review of approaches and data models. *Remote Sens.* **2017**, *9*, 129.
22. Coops, N.; Stanford, M.; Old, K.; Dudzinski, M.; Culvenor, D.; Stone, C. Assessment of *Dothistroma* needle blight of *Pinus radiata* using airborne hyperspectral imagery. *Phytopathology* **2003**, *93*, 1524–1532.
23. Misurec, J.; Kopacková, V.; Lhotakova, Z.; Albrechtova, J.; Hanus, J.; Weyermann, J.; Entcheva-Campbell, P. Utilization of hyperspectral image optical indices to assess the Norway spruce forest health status. *J. Appl. Remote Sens.* **2012**, *6*, 063545.

24. Abdel-Rahman, E.M.; Mutanga, O.; Adam, E.; Ismail, R. Detecting *Sirex noctilio* grey-attacked and lightning-struck pine trees using airborne hyperspectral data, random forest and support vector machines classifiers. *ISPRS J. Photogramm. Remote Sens.* **2014**, *88*, 48–59.
25. Fassnacht, F.E.; Latifi, H.; Ghosh, A.; Joshi, P.K.; Koch, B. Assessing the potential of hyperspectral imagery to map bark beetle-induced tree mortality. *Remote Sens. Environ.* **2014**, *140*, 533–548.
26. Näsi, R.; Honkavaara, E.; Blomqvist, M.; Lyytikäinen-Saarenmaa, P.; Hakala, T.; Viljanen, N.; Kantola, T.; Holopainen, M. Remote sensing of bark beetle damage in urban forests at individual tree level using a novel hyperspectral camera from UAV and aircraft. *Urban For. Urban Green.* **2018**, *30*, 72–83.
27. Sandino, J.; Pegg, G.; Gonzalez, F.; Smith, G. Aerial mapping of forests affected by pathogens using UAVs, hyperspectral sensors, and artificial intelligence. *Sensors* **2018**, *18*, 944.
28. Pontius, J.; Martin, M.; Plourde, L.; Hallett, R. Ash decline assessment in emerald ash borer-infested regions: A test of tree-level, hyperspectral technologies. *Remote Sens. Environ.* **2008**, *112*, 2665–2676.
29. Pu, R.; Kelly, M.; Anderson, G.L.; Gong, P.J.P.E.; Sensing, R. Using CASI hyperspectral imagery to detect mortality and vegetation stress associated with a new hardwood forest disease. *Photogramm. Eng. Remote Sens.* **2008**, *74*, 65–75.
30. Michez, A.; Piégay, H.; Lisein, J.; Claessens, H.; Lejeune, P. Classification of riparian forest species and health condition using multi-temporal and hyperspatial imagery from unmanned aerial system. *Environ. Monit. Assess.* **2016**, *188*, 146.
31. Thenkabail, P.S.; Lyon, J.G.; Huete, A. *Hyperspectral Remote Sensing of Vegetation*; CRC Press: Boca Raton, FL, USA, 2011.
32. Lawrence, R.; Labus, M. Early detection of Douglas-fir beetle infestation with subcanopy resolution hyperspectral imagery. *West. J. Appl. For.* **2003**, *18*, 202–206.
33. López-López, M.; Calderón, R.; González-Dugo, V.; Zarco-Tejada, P.; Fereres, E. Early detection and quantification of almond red leaf blotch using high-resolution hyperspectral and thermal imagery. *Remote Sens.* **2016**, *8*, 276.
34. Lowe, A.; Harrison, N.; French, A.P. Hyperspectral image analysis techniques for the detection and classification of the early onset of plant disease and stress. *Plant Methods* **2017**, *13*, 80.
35. Dotzler, S.; Hill, J.; Buddenbaum, H.; Stoffels, J. The Potential of EnMAP and Sentinel-2 Data for Detecting Drought Stress Phenomena in Deciduous Forest Communities. *Remote Sens.* **2015**, *7*, 14227–14258.
36. Garrity, S.R.; Allen, C.D.; Brumby, S.P.; Gangogadagamage, C.; McDowell, N.G.; Cai, D.M. Quantifying tree mortality in a mixed species woodland using multitemporal high spatial resolution satellite imagery. *Remote Sens. Environ.* **2013**, *129*, 54–65.
37. Meng, J.; Li, S.; Wang, W.; Liu, Q.; Xie, S.; Ma, W. Mapping forest health using spectral and textural information extracted from spot-5 satellite images. *Remote Sens.* **2016**, *8*, 719.
38. Townsend, P.A.; Singh, A.; Foster, J.R.; Rehberg, N.J.; Kingdon, C.C.; Eshleman, K.N.; Seagle, S.W. A general Landsat model to predict canopy defoliation in broadleaf deciduous forests. *Remote Sens. Environ.* **2012**, *119*, 255–265.
39. Wang, J.; Sammis, T.W.; Gutschick, V.P.; Gebremichael, M.; Dennis, S.O.; Harrison, R.E. Review of satellite remote sensing use in forest health studies. *Open Geogr. J.* **2010**, *3*, 28–42.
40. Wang, H.; Pu, R.; Zhang, Z. Mapping Robinia Pseudoacacia Forest Health Conditions by Using Combined Spectral, Spatial and Textural Information Extracted from Ikonos Imagery. *Int. Arch. Photogramm. Remote Sens. Spatial Inf. Sci.* **2016**, *XLI-B8*, 1425–1429.
41. Waser, L.T.; Küchler, M.; Jütte, K.; Stampfer, T. Evaluating the potential of WorldView-2 data to classify tree species and different levels of ash mortality. *Remote Sens.* **2014**, *6*, 4515–4545.
42. White, J.C.; Wulder, M.A.; Brooks, D.; Reich, R.; Wheate, R.D. Detection of red attack stage mountain pine beetle infestation with high spatial resolution satellite imagery. *Remote Sens. Environ.* **2005**, *96*, 340–351.
43. Aasen, H.; Honkavaara, E.; Lucieer, A.; Zarco-Tejada, P.J. Quantitative remote sensing at ultra-high resolution with UAV spectroscopy: A review of sensor technology, measurement procedures, and data correction workflows. *Remote Sens.* **2018**, *10*, 1091.

44. Coops, N.C.; Goodwin, N.; Stone, C.; Sims, N. Application of narrow-band digital camera imagery to plantation canopy condition assessment. *Can. J. Remote Sens.* **2006**, *32*, 19–32.
45. Pietrzykowski, E.; Sims, N.; Stone, C.; Pinkard, L.; Mohammed, C. Predicting *Mycosphaerella* leaf disease severity in a *Eucalyptus globulus* plantation using digital multi-spectral imagery. *South. Hemisph. For. J.* **2007**, *69*, 175–182.
46. Zarco-Tejada, P.J.; Berni, J.A.; Suárez, L.; Sepulcre-Cantó, G.; Morales, F.; Miller, J.R. Imaging chlorophyll fluorescence with an airborne narrow-band multispectral camera for vegetation stress detection. *Remote Sens. Environ.* **2009**, *113*, 1262–1275.
47. Meddens, A.J.; Hicke, J.A.; Vierling, L.A. Evaluating the potential of multispectral imagery to map multiple stages of tree mortality. *Remote Sens. Environ.* **2011**, *115*, 1632–1642.
48. Asner, G.P. Hyperspectral remote sensing of canopy chemistry, physiology, and biodiversity in tropical rainforests. In *Hyperspectral Remote Sensing of Tropical and Sub-Tropical Forests*; Kalacska, M., Sances, G.A., Eds.; Azofeita CRC Press: Boca Raton, FL, USA, 2008; pp. 261–296.
49. Jensen, J.R. *Introductory Digital Image Processing: A Remote Sensing Perspective*, 4th ed.; Pearson Education, Inc.: Glenview, IL, USA, 2016.
50. Kaufmann, H.E.A. *Hyperspectral Algorithms: Report in the Frame of EnMAP Preparation Activities*; Deutsches GeoForschungsZentrum GFZ: Potsdam, Germany, 2010.
51. Berni, J.; Zarco-Tejada, P.; Sepulcre-Cantó, G.; Fereres, E.; Villalobos, F. Mapping canopy conductance and CWSI in olive orchards using high resolution thermal remote sensing imagery. *Remote Sens. Environ.* **2009**, *113*, 2380–2388.
52. Calderón, R.; Navas-Cortés, J.; Zarco-Tejada, P. Early detection and quantification of *Verticillium* wilt in olive using hyperspectral and thermal imagery over large areas. *Remote Sensing.* **2015**, *7*, 5584–5610.
53. Strasser, R.J.; Srivastava, A. Polyphasic chlorophyll a fluorescence transient in plants and cyanobacteria. *Photochem. Photobiol.* **1995**, *61*, 32–42.
54. Zarco-Tejada, P.J.; Miller, J.R.; Mohammed, G.; Noland, T.L.; Sampson, P. Vegetation stress detection through chlorophyll a+ b estimation and fluorescence effects on hyperspectral imagery. *J. Environ. Qual.* **2002**, *31*, 1433–1441.
55. Blackburn, G.A. Hyperspectral remote sensing of plant pigments. *J. Exp. Bot.* **2006**, *58*, 855–867.
56. Suárez, L.; Zarco-Tejada, P.J.; Sepulcre-Cantó, G.; Pérez-Priego, O.; Miller, J.; Jiménez-Muñoz, J.; Sobrino, J. Assessing canopy PRI for water stress detection with diurnal airborne imagery. *Remote Sens. Environ.* **2008**, *112*, 560–575.
57. Hunt Jr, E.R.; Rock, B.N. Detection of changes in leaf water content using near-and middle-infrared reflectances. *Remote Sens. Environ.* **1989**, *30*, 43–54.
58. Gao, B.-C. NDWI—A normalized difference water index for remote sensing of vegetation liquid water from space. *Remote Sens. Environ.* **1996**, *58*, 257–266.
59. Peñuelas, J.; Filella, I.; Biel, C.; Serrano, L.; Save, R. The reflectance at the 950–970 nm region as an indicator of plant water status. *Int. J. Remote Sens.* **1993**, *14*, 1887–1905.
60. Hendry, G.A.; Houghton, J.D.; Brown, S.B. The degradation of chlorophyll-a biological enigma. *New Phytol.* **1987**, *1987*, 255–302.
61. Gitelson, A.A.; Gritz, Y.; Merzlyak, M.N. Relationships between leaf chlorophyll content and spectral reflectance and algorithms for non-destructive chlorophyll assessment in higher plant leaves. *J. Plant Physiol.* **2003**, *160*, 271–282.
62. Woolley, J.T. Reflectance and transmittance of light by leaves. *Plant Physiol.* **1971**, *47*, 656–662.
63. Tucker, C.J. Red and photographic infrared linear combinations for monitoring vegetation. *Remote Sens. Environ.* **1979**, *8*, 127–150.
64. Glenn, E.; Huete, A.; Nagler, P.; Nelson, S. Relationship between remotely-sensed vegetation indices, canopy attributes and plant physiological processes: What vegetation indices can and cannot tell us about the landscape. *Sensors* **2008**, *8*, 2136–2160.
65. Jago, R.A.; Cutler, M.E.; Curran, P.J. Estimating canopy chlorophyll concentration from field and airborne spectra. *Remote Sens. Environ.* **1999**, *68*, 217–224.

66. Eitel, J.U.; Vierling, L.A.; Litvak, M.E.; Long, D.S.; Schulthess, U.; Ager, A.A.; Krofcheck, D.J.; Stoscheck, L. Broadband, red-edge information from satellites improves early stress detection in a New Mexico conifer woodland. *Remote Sens. Environ.* **2011**, *115*, 3640–3646.
67. Kim, Y.; Glenn, D.M.; Park, J.; Ngugi, H.K.; Lehman, B.L. Hyperspectral image analysis for water stress detection of apple trees. *Comput. Electron. Agric.* **2011**, *77*, 155–160.
68. Penuelas, J.; Baret, F.; Filella, I. Semi-empirical indices to assess carotenoids/chlorophyll a ratio from leaf spectral reflectance. *Photosynthetica* **1995**, *31*, 221–230.
69. Serrano, L.; Penuelas, J.; Ustin, S.L. Remote sensing of nitrogen and lignin in Mediterranean vegetation from AVIRIS data: Decomposing biochemical from structural signals. *Remote Sens. Environ.* **2002**, *81*, 355–364.
70. Rautiainen, M.; Lukeš, P.; Homolova, L.; Hovi, A.; Pisek, J.; Mottus, M. Spectral properties of coniferous forests: A review of in situ and laboratory measurements. *Remote Sensing* **2018**, *10*, 207.
71. Zagolski, F.; Pinel, V.; Romier, J.; Alcaide, D.; Fontanari, J.; Gastellu-Etchegorry, J.; Giordano, G.; Marty, G.; Mougin, E.; Joffre, R. Forest canopy chemistry with high spectral resolution remote sensing. *Int. J. Remote Sens.* **1996**, *17*, 1107–1128.
72. Gong, P.; Pu, R.; Biging, G.S.; Larrieu, M.R. Estimation of forest leaf area index using vegetation indices derived from Hyperion hyperspectral data. *IEEE Trans. Geosci. Remote Sens.* **2003**, *41*, 1355–1362.
73. Barry, K.M.; Stone, C.; Mohammed, C. Crown-scale evaluation of spectral indices for defoliated and discoloured eucalypts. *Int. J. Remote Sens.* **2008**, *29*, 47–69.
74. Schlerf, M.; Atzberger, C.; Hill, J. Remote sensing of forest biophysical variables using HyMap imaging spectrometer data. *Remote Sens. Environ.* **2005**, *95*, 177–194.
75. Asner, G.P. Biophysical and biochemical sources of variability in canopy reflectance. *Remote Sens. Environ.* **1998**, *64*, 234–253.
76. Ollinger, S.V. Sources of variability in canopy reflectance and the convergent properties of plants. *New Phytol.* **2011**, *189*, 375–394.
77. Zarco-Tejada, P.J.; Miller, J.R.; Morales, A.; Berjón, A.; Agüera, J. Hyperspectral indices and model simulation for chlorophyll estimation in open-canopy tree crops. *Remote Sens. Environ.* **2004**, *90*, 463–476.
78. Hernández-Clemente, R.; Navarro-Cerrillo, R.M.; Suárez, L.; Morales, F.; Zarco-Tejada, P.J. Assessing structural effects on PRI for stress detection in conifer forests. *Remote Sens. Environ.* **2011**, *115*, 2360–2375.
79. Baret, F.; Vanderbilt, V.C.; Steven, M.D.; Jacquemoud, S. Use of spectral analogy to evaluate canopy reflectance sensitivity to leaf optical properties. *Remote Sens. Environ.* **1994**, *48*, 253–260.
80. Kupiec, J.; Curran, P. Decoupling effects of the canopy and foliar biochemicals in AVIRIS spectra. *Int. J. Remote Sens.* **1995**, *16*, 1731–1739.
81. Bellgard, S.E.; Weir, B.S.; Pennycook, S.R.; Paderes, E.P.; Winks, C.; Beever, R.E. Specialist Phytophthora Research: Biology, Pathology Ecology and Detection of PTA. *Mpi Contract* **2013**, *2013*, 11927.
82. Chappell, P.R. The climate and weather of Auckland. *Niwa Sci. Technol. Ser. Auckl.* **2012**, *2013*, 60.
83. ESRI. World Topographic Map-WMTS service. Sources: Esri, HERE, Garmin, Intermap, INCREMENT P, GEBCO, USGS, FAO, NPS, NRCAN, GeoBase, IGN, Kadaster NL, Ordnance Survey, Esri Japan, METI, Esri China (Hong Kong), © OpenStreetMap contributors, GIS User Community; ESRI: Redlands, CA, USA, 2020.
84. LINZ. Auckland 0.5m Rural Aerial Photos (2010–2012). National Imagery. WMS Service. Available online: <https://data.linz.govt.nz/layer/51769-auckland-05m-rural-aerial-photos-2010-2012/> (accessed on 15 October 2019).
85. Schlaepfer, D. PARGE-Parametric Geocoding & Orthorectification for Airborne Optical Scanner Data. Available online: <http://www.rese.ch/products/parge/> (accessed on 11 June 2019).
86. Richter, R.; Schläpfer, D. ATCOR-4 User Guide, Version 7.3.0, April 2019. *Atmospheric/Topographic Correction for Airborne Imagery*; ReSe Applications LLC: Wil, Switzerland, 2019.
87. Khosravipour, A.; Skidmore, A.K.; Isenburg, M. Generating spike-free digital surface models using LiDAR raw point clouds: A new approach for forestry applications. *Int. J. Appl. Earth Obs. Geoinf.* **2016**, *52*, 104–114.
88. rapidlasso-GmbH. LASTools. Software Suite for LiDAR Processing. Developed by Martin Isenburg. Available online: <https://rapidlasso.com/lastools/> (accessed on 1 October 2019).

89. MPI. Airbone LiDAR and RGB aerial images in the Waitakere Ranges. In Flown by AAM-New Zealand for the Ministry for Primary Industries on the 30 January 2016; MPI: Wellington, New Zealand, 2016.
90. Auckland Council, A. Auckland 0.075m Urban Aerial Photos (2017), RGB, Waitakere Ranges. Available online: <https://data.linz.govt.nz/layer/95497-auckland-0075m-urban-aerial-photos-2017/> (accessed on 12 April 2019).
91. Singers, N.; Osborne, B.; Lovegrove, T.; Jamieson, A.; Boow, J.; Sawyer, J.; Webb, C. *Indigenous Terrestrial and Wetland Ecosystems of Auckland*; Auckland Council: Auckland, New Zealand, 2017. Available online: <http://www.knowledgeauckland.org.nz> (accessed on 20 July 2019).
92. Hurst, J.; Allen, R. *A Permanent Plot Method for Monitoring Indigenous Forests-Expanded Manual, Version 4*; Landcare Research Contract report LC0708/028; Landcare Research New Zealand Limited: Lincoln, New Zealand, 2007.
93. DOC. The Foliar Browse Index field manual. In An Update of a Method for Monitoring Possum (*Trichosurus Vulpecula*) Damage to Forest Communities; Department of Conservation: Christchurch, New Zealand, 2014.
94. Trimble. *eCognition® Developer 9.3 User Guide*; Trimble Germany GmbH: Munich, Germany, 2018; p. 274.
95. Harris-Geospatial. Vegetation Indices in Envi. Available online: <http://www.harrisgeospatial.com/docs/VegetationIndices.html> (accessed on 10 October 2018).
96. van der Linden, S.; Rabe, A.; Held, M.; Jakimow, B.; Leitão, P.; Okujeni, A.; Schwieder, M.; Suess, S.; Hostert, P. The EnMAP-Box—A toolbox and application programming interface for EnMAP data processing. *Remote Sens.* **2015**, *7*, 11249–11266.
97. Witten, I.H.; Frank, E.; Hall, M.A.; Pal, C.J. *Data Mining: Practical Machine Learning Tools and Techniques*; Morgan Kaufmann: San Francisco, CA, USA, 2016.
98. Lazaridis, D.C.; Verbesselt, J.; Robinson, A.P. Penalized regression techniques for prediction: A case study for predicting tree mortality using remotely sensed vegetation indices. *Can. J. For. Res.* **2010**, *41*, 24–34.
99. Belgiu, M.; Drăguț, L. Random forest in remote sensing: A review of applications and future directions. *ISPRS J. Photogramm. Remote Sens.* **2016**, *114*, 24–31.
100. Pal, M. Random forest classifier for remote sensing classification. *Int. J. Remote Sens.* **2005**, *26*, 217–222.
101. Breiman, L. Random forests. *Mach. Learn.* **2001**, *45*, 5–32.
102. Gislason, P.O.; Benediktsson, J.A.; Sveinsson, J.R. Random forests for land cover classification. *Pattern Recog. Lett.* **2006**, *27*, 294–300.
103. Breiman, L. Statistical modeling: The two cultures. *Qual. Control Appl. Stat.* **2003**, *48*, 81–82.
104. Quinlan, J.R. Learning with continuous classes. In Proceedings of the 5th Australian Joint Conference on Artificial Intelligence; Hobart, Tasmania, 16–18 November 1992; pp. 343–348.
105. Dalponte, M.; Ørka, H.O.; Ene, L.T.; Gobakken, T.; Næsset, E. Tree crown delineation and tree species classification in boreal forests using hyperspectral and ALS data. *Remote Sens. Environ.* **2014**, *140*, 306–317.
106. Kaartinen, H.; Hyypä, J.; Yu, X.; Vastaranta, M.; Hyypä, H.; Kukko, A.; Holopainen, M.; Heipke, C.; Hirschmugl, M.; Morsdorf, F. An international comparison of individual tree detection and extraction using airborne laser scanning. *Remote Sens.* **2012**, *4*, 950–974.
107. Zhen, Z.; Quackenbush, L.J.; Zhang, L. Trends in automatic individual tree crown detection and delineation—Evolution of LiDAR data. *Remote Sens.* **2016**, *8*, 333.
108. Birth, G.S.; McVey, G.R. Measuring the Color of Growing Turf with a Reflectance Spectrophotometer 1. *Agron. J.* **1968**, *60*, 640–643.
109. Lichtenthaler, H.K. Vegetation stress: An introduction to the stress concept in plants. *J. Plant Physiol.* **1996**, *148*, 4–14.
110. Zarco-Tejada, P.J.; Berjón, A.; López-Lozano, R.; Miller, J.R.; Martín, P.; Cachorro, V.; González, M.; De Frutos, A. Assessing vineyard condition with hyperspectral indices: Leaf and canopy reflectance simulation in a row-structured discontinuous canopy. *Remote Sens. Environ.* **2005**, *99*, 271–287.
111. Locherer, M. Capacity of the Hyperspectral Satellite Mission EnMAP for the Multiseasonal Monitoring of Biophysical and Biochemical Land Surface Parameters in Agriculture by Transferring an Analysis Method for Airborne Image Spectroscopy to the Spaceborne Scale; Imu: Munic, Germany, 2014.
112. Datt, B. Remote sensing of chlorophyll a, chlorophyll b, chlorophyll a+ b, and total carotenoid content in eucalyptus leaves. *Remote Sens. Environ.* **1998**, *66*, 111–121.

113. Roujean, J.-L.; Breon, F.-M. Estimating PAR absorbed by vegetation from bidirectional reflectance measurements. *Remote Sens. Environ.* **1995**, *51*, 375–384.
114. Rouse Jr, J.W.; Haas, R.H.; Schell, J.; Deering, D. Monitoring the vernal advancement and retrogradation (green wave effect) of natural vegetation. In *NASA Gsfc Type Report*; Texas A&M University: College Station, TX, USA, 1973.
115. Ustin, S.L.; Roberts, D.A.; Gardner, M.; Dennison, P. Evaluation of the potential of Hyperion data to estimate wildfire hazard in the Santa Ynez Front Range, Santa Barbara, California. In *Proceedings of IEEE International Geoscience and Remote Sensing Symposium*, Toronto, ON, Canada, 24–28 June 2002; pp. 796–798.
116. Curran, P.J.; Dungan, J.L.; Macler, B.A.; Plummer, S.E.; Peterson, D.L. Reflectance spectroscopy of fresh whole leaves for the estimation of chemical concentration. *Remote Sens. Environ.* **1992**, *39*, 153–166.
117. Nagler, P.L.; Inoue, Y.; Glenn, E.; Russ, A.; Daughtry, C. Cellulose absorption index (CAI) to quantify mixed soil-plant litter scenes. *Remote Sens. Environ.* **2003**, *87*, 310–325.
118. Asner, G.P.; Knapp, D.E.; Cooper, A.N.; Bustamante, M.M.; Olander, L.P. Ecosystem structure throughout the Brazilian Amazon from Landsat observations and automated spectral unmixing. *Earth Interact.* **2005**, *9*, 1–31.
119. Baret, F.; Clevers, J.; Steven, M. The robustness of canopy gap fraction estimates from red and near-infrared reflectances: A comparison of approaches. *Remote Sens. Environ.* **1995**, *54*, 141–151.
120. Aparicio, N.; Villegas, D.; Araus, J.; Casadesus, J.; Royo, C. Relationship between growth traits and spectral vegetation indices in durum wheat. *Crop Sci.* **2002**, *42*, 1547–1555.
121. Galvao, L.S.; Formaggio, A.R.; Tisot, D.A. Discrimination of sugarcane varieties in Southeastern Brazil with EO-1 Hyperion data. *Remote Sens. Environ.* **2005**, *94*, 523–534.
122. Gitelson, A.A.; Merzlyak, M.N. Remote estimation of chlorophyll content in higher plant leaves. *Int. J. Remote Sens.* **1997**, *18*, 2691–2697.
123. Fourty, T.; Baret, F.; Jacquemoud, S.; Schmuck, G.; Verdebout, J. Leaf optical properties with explicit description of its biochemical composition: Direct and inverse problems. *Remote Sens. Environ.* **1996**, *56*, 104–117.
124. Clark, R.N.; King, T.V.; Ager, C.; Swayze, G.A. Initial Vegetation Species and Senescence/Stress Indicator Mapping in the San Luis Valley, Colorado Using Imaging Spectrometer Data; NASA: Washington, DC, USA, 1995.
125. Lobell, D.B.; Asner, G.P.; Law, B.E.; Treuhaft, R.N. Subpixel canopy cover estimation of coniferous forests in Oregon using SWIR imaging spectrometry. *J. Geophys. Res. Atmos.* **2001**, *106*, 5151–5160.
126. Beauchamp, A.J. The Detection of Phytophthora Taxon “Agathis” in the Second Round of Surveillance Sampling- With Discussion of the Implications for Kauri Dieback Management of All Surveillance Activity; Department of Conservation: Auckland, New Zealand, 2013.
127. Wulder, M.A.; White, J.C.; Coops, N.C.; Butson, C.R. Multi-temporal analysis of high spatial resolution imagery for disturbance monitoring. *Remote Sens. Environ.* **2008**, *112*, 2729–2740.
128. Verbesselt, J.; Robinson, A.; Stone, C.; Culvenor, D. Forecasting tree mortality using change metrics derived from MODIS satellite data. *For. Ecol. Manage.* **2009**, *258*, 1166–1173.
129. Verbesselt, J.; Hyndman, R.; Newnham, G.; Culvenor, D. Detecting trend and seasonal changes in satellite image time series. *Remote Sens. Environ.* **2010**, *114*, 106–115.
130. Meigs, G.W.; Kennedy, R.E.; Gray, A.N.; Gregory, M.J. Spatiotemporal dynamics of recent mountain pine beetle and western spruce budworm outbreaks across the Pacific Northwest Region, USA. *For. Ecol. Manage.* **2015**, *339*, 71–86.
131. Solberg, S.; Næsset, E.; Hanssen, K.H.; Christiansen, E. Mapping defoliation during a severe insect attack on Scots pine using airborne laser scanning. *Remote Sens. Environ.* **2006**, *102*, 364–376.
132. Kantola, T.; Vastaranta, M.; Yu, X.; Lyytikäinen-Saarenmaa, P.; Holopainen, M.; Talvitie, M.; Kaasalainen, S.; Solberg, S.; Hyyppä, J. Classification of defoliated trees using tree-level airborne laser scanning data combined with aerial images. *Remote Sens.* **2010**, *2*, 2665–2679.
133. Vastaranta, M.; Kantola, T.; Lyytikäinen-Saarenmaa, P.; Holopainen, M.; Kankare, V.; Wulder, M.; Hyyppä, J.; Hyyppä, H. Area-based mapping of defoliation of Scots pine stands using airborne scanning LiDAR. *Remote Sens.* **2013**, *5*, 1220–1234.

134. Shendryk, I.; Broich, M.; Tulpure, M.G.; McGrath, A.; Keith, D.; Alexandrov, S.V. Mapping individual tree health using full-waveform airborne laser scans and imaging spectroscopy: A case study for a floodplain eucalypt forest. *Remote Sens. Environ.* **2016**, *187*, 202–217.
135. Hakala, T.; Nevalainen, O.; Kaasalainen, S.; Mäkipää, R. Multispectral Lidar Time Series of Pine Canopy Chlorophyll Content. *Biogeosciences* **2015**, *12*, 1629–1634.
136. Hill, L. and Waipara N. Canopy Score Illustration for Kauri Dieback Field Survey conducted for Auckland Council, Biosecurity Department. Auckland, New Zealand, 2010.
137. Gamon, J.; Penuelas, J.; Field, C. A narrow-waveband spectral index that tracks diurnal changes in photosynthetic efficiency. *Remote Sens. Environ.* **1992**, *41*, 35–44.
138. Haboudane, D.; Miller, J.R.; Pattey, E.; Zarco-Tejada, P.J.; Strachan, I.B. Hyperspectral vegetation indices and novel algorithms for predicting green LAI of crop canopies: Modeling and validation in the context of precision agriculture. *Remote Sens. Environ.* **2004**, *90*, 337–352.
139. Pearson, R.L.; Miller, L.D. Remote mapping of standing crop biomass for estimation of the productivity of the shortgrass prairie. In Proceedings of the Eighth International Symposium on Remote Sensing of Environment, Ann Arbor, MI, USA, 2–6 October 1972; Volume VIII, p. 1355.
140. Jeffreys, H. An invariant form for the prior probability in estimation problems. *Proc. R. Soc. London. Ser. A Math. Phys. Sci.* **1946**, *186*, 453–461.
141. Richards, J.A. *Remote Sensing Digital Image Analysis*; Springer: Berlin, Germany, 1999; Volume 3.
142. Price, J.C. How unique are spectral signatures? *Remote Sens. Environ.* **1994**, *49*, 181–186.



© 2020 by the authors. Submitted for possible open access publication under the terms and conditions of the Creative Commons Attribution (CC BY) license (<http://creativecommons.org/licenses/by/4.0/>).

Chapter IV

Stress Detection in New Zealand Kauri Canopies with WorldView- 2 Satellite and LiDAR Data

Jane J. Meiforth, Henning Buddenbaum, Joachim Hill, James
Shepherd and John Dymond

This paper was submitted on the 01st of May 2020 to the MDPI journal "Remote Sensing". It was still under review at the time this thesis was submitted for examination.

Abstract

New Zealand kauri trees are threatened by the kauri dieback disease (*Phytophthora agathidicida* (PA)). In this study, we investigate the use of WorldView-2 (WV2) satellite and Light Detection and Ranging (LiDAR) data for detecting stress symptoms in the canopy of kauri trees. A total of 1089 reference crowns were located in the Waitakere Ranges west of Auckland and assessed by fieldwork and the interpretation of aerial images. Canopy stress symptoms were graded based on five basic stress levels and further refined for the first symptom stages. The crown polygons were manually edited on a LiDAR crown height model. Crowns with a mean diameter smaller than 4 m caused most outliers with the 1.8 m pixel size of WV2 multispectral bands, especially at the more advanced stress levels of dying and dead trees. The exclusion of crowns with a diameter smaller than 4 m increased the correlation in an object-based Random Forest regression from 0.85 to 0.89 with only WV2 attributes (Root Mean Squared Error (RMSE) of 0.48, Mean Absolute Error (MAE) of 0.34). Additional LIDAR attributes increased the correlation to 0.92 (RMSE of 0.43, MAE of 0.31). A red/near-infrared (NIR) Normalized Difference Vegetation Index and a ratio of the red and green bands are the most important indices for an assessment of the full range of stress symptoms. For the detection of first stress symptoms, an NDVI on the red-edge and green bands increased the performance. The method presented in this study shows promising results for a cost-efficient stress monitoring of kauri crowns over large areas. It should be tested in a full processing chain with automatic kauri identification and crown-segmentation.

Keywords: WorldView-2; kauri; *Agathis australis*; stress detection; forest health; PA; *Phytophthora agathidicida*

1 Introduction

The deadly kauri dieback disease (*Phytophthora agathidicida* (PA)) was first officially confirmed as a new pathogen by Beever in 2008 [1] in the Waitakere Ranges west of Auckland and later taxonomically described by Weir et al. [2]. Meanwhile, it was detected over most of the natural distribution range of New Zealand kauri [3]. The endemic kauri trees (*Agathis australis*) are a key species for the forest ecosystems on the North Island [4], a famous tourist attraction, and of high cultural significance for the Māori [5,6]. Regular monitoring of stress symptoms in tree canopies requires a cost-efficient, objective method that is suitable for covering large areas and able to detect first signs of stress. Multispectral band and index combinations for the detection of kauri and canopy stress symptoms have been identified by Meiforth et al. [7,8]. Airborne Light Detection and Ranging (LiDAR) data recently became available for the northern kauri forests, so that the main part of the distribution range of kauri trees in New Zealand is now covered. In this study, we analyse the use of WorldView-2 (WV2) satellite data in combination with LiDAR data to detect stress symptoms in kauri trees in an object-based approach on manually segmented kauri crowns.

1.1 Kauri trees and kauri dieback symptoms

Kauri trees show a large phenological variety, from young conical trees with dense foliage to large open dome-shaped crowns (Figure IV-1). The mature trees develop a massive trunk and large side branches, and reach heights of up to 40 m in the study areas. The color of the foliage in non-symptomatic kauri varies, depending on the exposition to light and thickness of the wax coating, from light green to a darker blue-green. The flat lanceolate needle-like leaves create a spiky foliage surface. The foliage forms clusters in the medium growth stages and mature crowns show a more open canopy [5], with visible branch material and gaps from an aerial viewpoint. Stress symptoms of PA first become visible as a yellowing and thinning of foliage, which exposes small top branches. Later stages of stress lead to structural changes caused by an ongoing loss of foliage, with an increase of visible bare branch material and gaps, until the tree dies [1,9]. The higher gap fraction increases the influence of undergrowth on the canopy reflectance. Small trees with a conical shape develop first a bare top of the main stem, while the foliage in the lower part of the canopy is affected in later stages. However, these types of symptoms can also have other causes, such as continuing drought periods [10], storm damage, or other diseases [1].

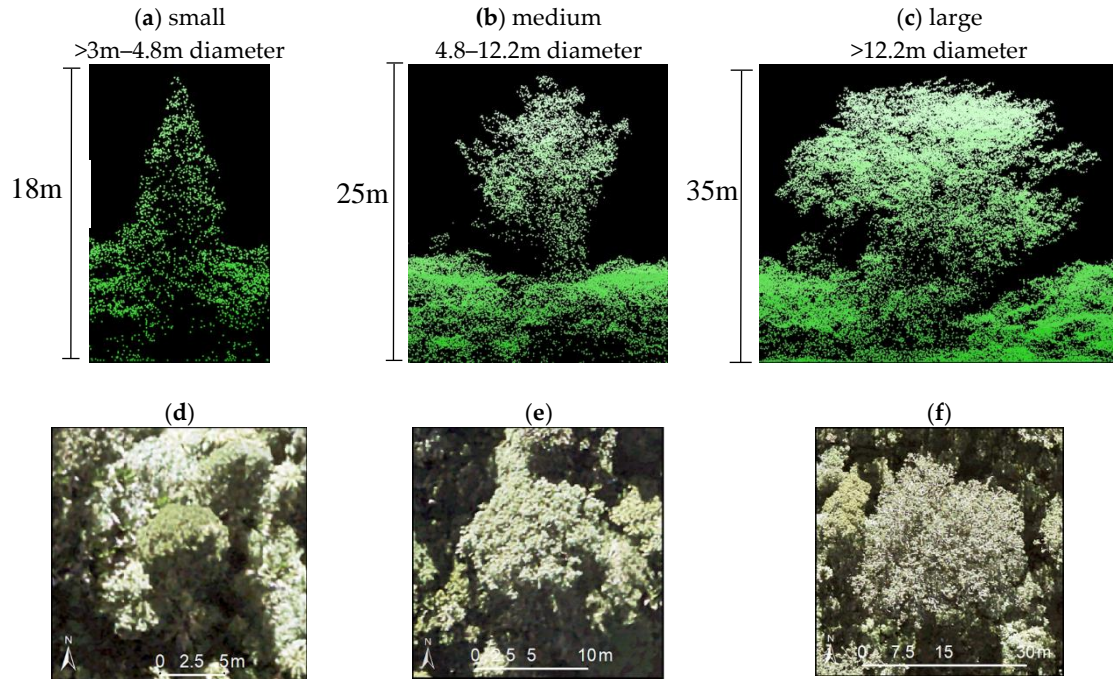


Figure IV-1 Kauri crown size classes: Non-symptomatic small, medium, and large kauri crowns, as a profile on a Light Detection and Ranging (LiDAR) point cloud (a, b, c) [11] and on 7.5 cm RGB aerial images below (d, e, f) [12].

1.2 Study area

The Waitakere Ranges on the West coast of Auckland are amongst the highest PA-affected forest areas, and the first officially confirmed site in New Zealand with a verified PA infection (Figure IV-2a, [1]). The ranges are characterized by a warm temperate climate and a rough terrain, with steep slopes and elevations from sea level to 474 m [13]. The three selected study sites (Figure IV-2b) cover trees with the full range of symptom stages in both homogenous and mixed stands, with mainly second-growth kauri forests in the Maungaroa area, larger trees in the Kauri Grove area and all growth stages of kauri in the Cascades.

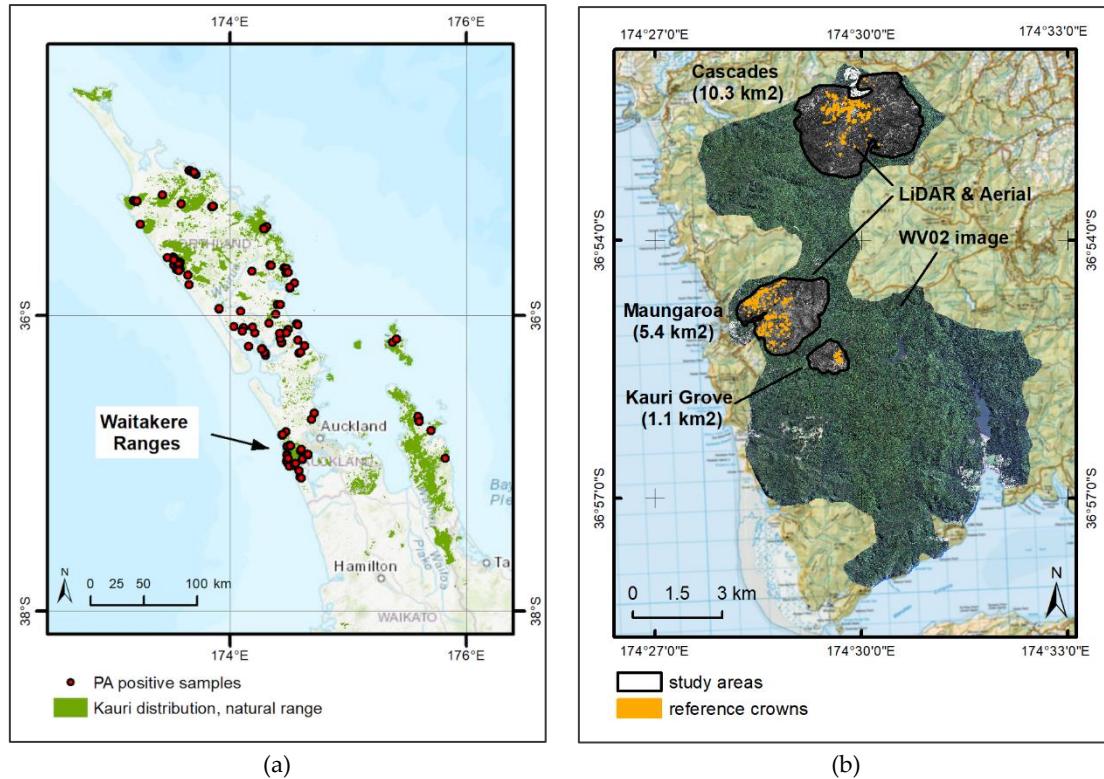


Figure IV-2 (a) Location of the Waitakere Ranges on the North Island of New Zealand west of Auckland City, with the natural range of kauri distribution and *Phytophthora agathidicida* (PA)-positive samples [14,15]. (b) Study sites and extent of the remote sensing datasets in the Waitakere Ranges, with the reference crowns marked in orange (background map: LINZ 2019 [16]).

1.3 Research background

High-resolution satellites have been successfully used to monitor forest health [17,18], both at a stand level [19-23] and individual tree crown level [24-27].

Amongst the most widely used vegetation indices for canopy stress detection with broader bandwidths of satellite images are combinations of near-infrared (NIR) and red bands, which provide a measure for chlorophyll reflectance in green vegetation. Other widely used indices are based on red and green bands sensitive to stress-related changes in leaf pigment compositions and bands in the NIR spectrum, which are influenced by the amount of leaf and canopy water and thus also structural changes due to foliage loss [17,28-31].

A new generation of commercial high-resolution satellites, such as WorldView (WV) and RapidEye (RE), launched in 2009 and 2008, respectively, have provided additional red-edge bands (WV, 705–745 nm; RE, 690-730 nm). In green vegetation, the red-edge region covers a steep increase in reflectance values between the red and NIR1 spectra and shows a high sensitivity to changes in chlorophyll, which causes a blue shift of the central red-edge region. Several studies have successfully applied spectral indices with red-

edge bands from satellite data for stress detection in tree canopies. Oumar and Mutanga [32] utilized indices on the NIR and red-edge bands from WV2 data to detect a decline in Eucalypt plantations in South Africa. Ortiz et al. [21] detected early stages of bark beetle attack by combining TerraSAR-X and RapidEye data. Eitel et al. [33] proved that a Normalized Difference Vegetation Index (NDVI) with a red-edge band is suitable for detecting early stress symptoms in conifer woodland trees in New Mexico.

Textural information derived from satellite imagery has successfully been used to assess structural features in tree canopies [34-36]. It also improved the analysis of stress symptoms in tree canopies, especially in later stages of decline with structural changes in the canopy [23,27].

Stress symptoms in kauri trees were analysed with airborne hyperspectral data in Meiforth et al. [8]. According to this study, a NIR/red NDVI, followed by indices with bands in the NIR and red-edge range are the most important for describing the full range of stress symptoms. However, pigment-sensitive indices with green and red bands had a higher importance for the detection of stress symptoms in smaller crowns with denser foliage. Indices with NIR bands, such as the Water Band Index (WBI) at 900 and 970 nm, were more relevant to describe stress symptoms in larger crown sizes with an open crown structure. The NIR bands are sensitive to structural changes and changes in the leaf water content. The paper recommends a stratified approach according to different growth stages of kauri.

An appropriate spatial resolution for the target objects is important for the successful use of satellite imagery, in order to avoid mixed pixels with shadow, neighboring vegetation, and soil [37]. In Meiforth et al. [8], a minimum crown diameter of 3 m was defined for stress detection in kauri trees for the 1 m resolution of a hyperspectral image. Fassnacht et al. [38] found that the 5 m pixel resolution of their HyMAP data was too coarse to evaluate bark beetle infections at crown level. However, dead trees could still be mapped with a high overall accuracy (84%–96%). Immitzer et al. [39] and Pu and Shawn [40] only used tree crowns that could be manually identified on WV2 respective Ikonos images. Immitzer et al. defined at least two pixels (=4 m) per object as the minimum target size for an analysis of tree canopies with a WV2 image. Other studies have analysed larger forest stands. Meddens et al. [41] discovered that a spatial resolution of 2.4 m performed best when mapping the infestation of forest stands with mountain pine beetle infection in Colorado. They demonstrated that a higher spatial resolution also increases the variability within the same level of crown damage and can cause a problematic “salt and pepper” effect in a pixel-based analysis. Lottering [42] and Ismail et al. [43] showed that higher-resolution data (1.25 and <1.75 m) is better suited to detecting early stages of stress in eucalyptus stands and a pine plantation, while later stages of stress are best described with lower spatial resolutions of 2.5 and 2.3 m.

An object-based approach is well-suited to handling a high variance in target objects [44-47]. Several studies have found that object-based methods are superior to pixel-based methods for single tree crown analysis [39,48-50]. They have also been successfully applied for stress analysis and change detections in

tree canopies [51-53]. For use in forest areas, an object-based approach requires a prior segmentation of crowns with respect to homogenous forest stands. An object-based analysis simplifies the combination of different data sources under the requirement that these are accurately aligned [54-56]. However, an essential condition for utilizing the advantages of an object-based approach is, that the pixel size is significantly smaller than the average size of the objects of interest [46].

The fusion of multispectral bands with a higher-resolution panchromatic channel, so-called PAN sharpening, allows the creation of a higher-spatial-resolution multispectral image. It can improve the use of textural attributes in an object-based analysis [57]. While some pan-sharpening methods can alter the spectral information, certain techniques, such as the Gram-Schmidt and Ehlers pan-sharpening methods, have been tested and shown to be superior for preserving the spectral values [58,59].

Stress symptoms in tree canopies caused by soil pathogens are expressed as a multifactor gradient with different states of chlorosis and defoliation, until only bare branches are left [30]. While classification algorithms only distinguish between discrete classes, regression algorithms give a more detailed description of symptom stages with a continuous output. A regression approach also facilitates a more differentiated evaluation of changes in a time series. Training based on the correlation coefficient allows regression models to handle a high variance in the data. Several studies have successfully used regression approaches to analyse stress symptoms in tree canopies [23,60], predict tree mortality [61], and evaluate foliar moisture [62]. However, a non-linear relationship in the numeric range of reference values causes a shift between the scales of the reference and predicted values. Meiforth et al. [8] enhanced the linearity by rescaling the value range and also suggested testing a two-step approach, in which the dead and dying trees are first identified in a binary classification. The remaining stress levels can then be analysed in a regression approach.

Light Detection and Ranging (LiDAR) systems generate an accurate, high-resolution, three-dimensional point cloud, which enable to segment single tree crowns and homogenous units of forest stands [63-68]. LiDAR data allows estimating crown parameters, such as the tree height, crown shape, canopy density, foliage texture, and structural crown characteristics [69,70]. The LiDAR intensity values add a spectral component as the amount of reflected energy at the peak amplitude of the returned LiDAR signal in the near-infrared region, usually at 1064 or 1550 nm. Intensity data has been successfully used to describe tree canopies and detect tree species [64,71-73]. The suitability of LiDAR attributes for assessing structural crown characteristics as a measure of defoliation has been proven in Scots pine forests at both stand level [74-76] and single tree level [75]. In combination with biochemical and biophysical information from passive optical sensors, LiDAR data can demonstrably enhance individual tree analysis [39,55,64,77,78].

1.4 Objectives

Spectral indicators with a sensitivity to stress symptoms in kauri trees have already been defined in Meiforth et al. [8] for use with an airborne multispectral system. This study analyses whether these findings can be implemented in an operational detection strategy based on WV2 satellite data. With LiDAR data available for most of the distribution range of New Zealand kauri, LiDAR-based crown attributes were integrated for crown stratification and to test their use for stress detection. The study pays special attention to differentiating early signs of stress. It has the following objectives:

1. Test the performance of WV2 attributes for crown-based stress detection in kauri trees and define the recommended minimum crown size.
2. Test a two-step method on WV2 attributes by first identifying dead and dying trees in a classification and then applying a regression for the remaining stress symptom levels.
3. Test the performance of LiDAR attributes in combination with WV2 data for canopy stress detection.

A minimum requirement for the performance of the developed method for a value range of symptom levels from 1 to 5 is a root mean square error (RMSE) smaller than 0.5, so that the predicted symptom values stay mainly within one reference symptom level. While the analysis in this study is based on manually edited crowns, the application for monitoring does require additional steps to automatically pre-segment crowns with respect to homogenous stand units for the existing LiDAR data and to define kauri trees.

2 Materials and methods

2.1 LiDAR data and aerial images

Airborne LiDAR data was obtained for the study areas on the 30 January 2016 by AAM New Zealand, with a Q1560 LiDAR sensor (400 kHz, 58° field of view) [11]. The sensor achieved five pulses/m² on average, which resulted in 35 average returns/m² and 0.17 m average point spacing. The ground return, however, was significantly less, with 0.8–1.5 ground returns per m² in the dense forest stands. The sensor utilises the 1064 nm wavelength to record intensity.

A Digital Terrain Model (DTM), Digital Surface Model (DSM), and ground normalized Crown Height Model (CHM) were generated in LAStools [79] with the “spike-free” method, according to Khosravipoura et al. [80]. Outliers that were classified as “noise” were removed. The method uses all returns to create a triangular irregular network (TIN) from the highest returns downwards. The user defines a “freeze distance” for the maximum length of the triangle sides, and an “insertion buffer” in a vertical downward direction, which defines the points that are included in the TIN creation, before the freezing process starts. All triangles

which sides are shorter than the freeze distance are preserved and underlying points are ignored in the further steps of the TIN creation for the remaining LiDAR points. This method prevents the creation of downward spikes. In the final step, the surface model is created through a linear interpolation of the spike-free TIN. As a rule of thumb, the lengths of the triangle sides should be around three times the average pulse spacing. We calculated two versions of height models with freeze distances of 0.6 m and 1 m and a pixel size of 0.25 m, which is larger than the average pulse spacing of the last returns of 0.23 m for this dataset.

A three-band RGB aerial image was acquired during the same flight as the LiDAR data collection, with a 15 cm pixel resolution. It was delivered in two versions, orthorectified on the surface model and the terrain model [11]. Another aerial image was obtained by order of Auckland Council in May 2017, with three RGB bands at a 7.5 cm resolution and orthorectified on a DTM [12].

2.2 WorldView-2 image

The WV2 image was captured on 15 March 2017 at 11:33 a.m. (local time) during cloud-free conditions. It covers 100 km² of the Waitakere Ranges (Figure IV-2b) and was delivered as standard imagery with nearest neighbour resampling in an “ortho ready” format. The eight multispectral bands have a resolution of 1.8 m, and the PAN channel features a 0.45 m resolution (Table IV-1, Figure IV-3). They reach up to 1043 nm wavelength but they do not cover the characteristic spectral pattern of kauri trees in the NIR2 range (Figure IV-3).

Table IV-1 WorldView-2 image: Wavelengths, bandwidths, and spatial resolution [87]

Nr.	Band name	Center wavelength (nm)	Lower band edge (nm)	Upper band edge (nm)	Spatial resolution in m
	Panchromatic	627	447	808	0.45
1	Coastal Blue	427	396	458	1.8
2	Blue	478	442	515	1.8
3	Green	546	506	586	1.8
4	Yellow	608	584	632	1.8
5	Red	659	624	694	1.8
6	Red-Edge	724	699	749	1.8
7	NIR1	833	765	901	1.8
8	NIR2	949	856	1043	1.8

Atmospheric correction of the multispectral bands was carried out with the Fast Line-of-sight Atmospheric Analysis of Hypercubes (FLAASH) module in ENVI, which incorporates the MODTRAN radiation transfer model [81]. The eight multispectral bands were pan-sharpened to a 0.5 m resolution with the Gram-Schmidt method [82] using ENVI’s SPEAR tools. The Gram-Schmidt method performs well in retaining spectral information [58,83] and has been used in several studies with satellite images for the

analysis of tree canopies [84,85]. The pan-sharpened image was georeferenced with a second-order polynomial transformation based on 1102 ground control points. The LiDAR CHM and the aerial image were used as a reference. Shadow areas were defined with a threshold value of 300 on a brightness layer, to match manually identified outer crown shadows while keeping internal crown shadows. The brightness layer was calculated as the average of the blue, green, red, and NIR1 bands [86].

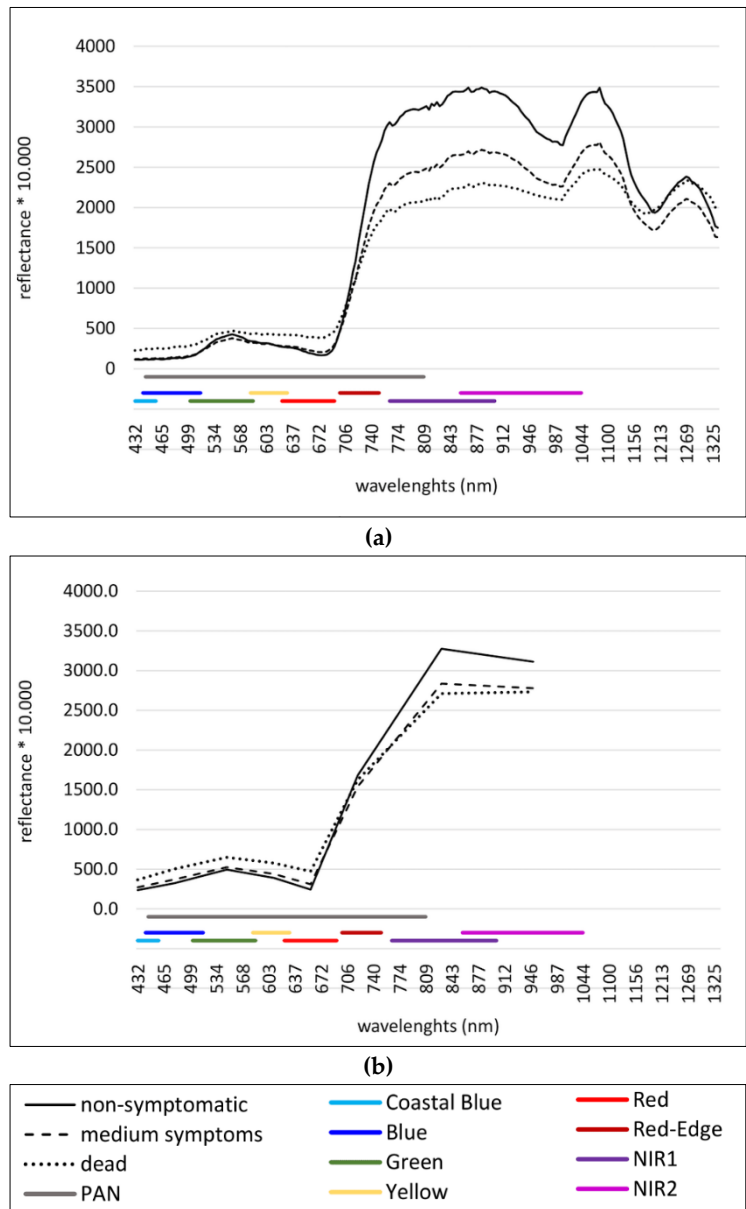


Figure IV-3 Position of WV2 bands and kauri spectra for non-symptomatic, medium and dead crowns based on (a) an AISA hyperspectral image (448 spectral bands) and (b) the pan-sharpened WV2 multispectral bands [7,87].

2.3 Reference crown set

The reference crown set with 1089 crowns of kauri and dead/dying trees is based on the crown locations and attributes acquired during fieldwork in the summer of 2015/16 and complemented and updated during the summer season of 2016/17 [7,8] (Table IV-2). The recorded crown attributes in the field include basic metrics, such as the stem diameter at breast height, the cardinal crown spread, and the canopy base height, as well as a detailed description of canopy characteristics, such as an estimated crown density, coverage in percentage classes [88], and the amount of dead branches [88]. In addition, other signs of stress were recorded such as decoloration of the foliage and the amount of epiphytes. The crowns used in this analysis have a mean diameter of at least 3 m and were stratified into three growth stages using the mean crown diameter (Figure IV-1). An outer buffer of 10% of the mean diameter was removed before the analysis to reduce edge effects. After removing the shadow areas, only crowns with sunlit areas larger than 50% compared to the full crown size were considered for the analysis.

2.4 Reference values for stress assessment

An overall canopy score for stress symptoms was assessed for each crown at five levels, from 1 for non-symptomatic dense foliage, to 5 for “dead tree”. This score was based on the fieldwork and the assessment of aerial images, according to a method described by Meiforth et al. [8]. For a more detailed evaluation of the first stress symptoms, the stress levels 1 to 3 were refined in half-steps (Figure IV-4) for this study. Level 1 describes crowns with non-symptomatic dense green foliage, which is mainly found in small and some medium crowns. Level 1.5 applies to crowns with still green, but more open foliage, with exposed gaps and single patches of visible branch material from an aerial viewpoint. This level is typically found in non-symptomatic medium and larger crowns. The stress level 2 features visible smaller branches over the full crown extent and the partial yellowing of foliage. Further increasing gaps and visible small to medium bare branches are the main visible characteristics of level 2.5 in the aerial images, as well as a more intense yellowing in some trees. Level 3 features large branches that become visible as linear structures. Level 4 marks a degree of foliage loss that deteriorates the overall crown architecture and shows a decoloration from yellow-green to brown in the remaining foliage. Level 5 describes dead crowns, and also includes different amounts of photosynthetic active undergrowth and epiphytes. Figure IV-5 gives an impression of the crown polygons for different forest stands on the WV2 image with an indication of the crown stress symptom values. To account for the fact that the LiDAR data was acquired in 2016, one season before the WV2 image, the aerial images from both years were compared, and crowns that showed visible changes or where the status of the crown could not be identified on both aerial images were removed. Since

both summers were relatively moist, the stress symptoms had not changed as rapidly as in a drought situation.

Table IV-2 Distribution of crown size classes according to their mean diameter per stress symptom level for the refined 7 step reference system with symptom levels from 1 = non-symptomatic to 5 = dead.

Size class	Crown diameter	Stress level							Total
		level 1	level 1.5	level 2	level 2.5	level 3	level 4	level 5	
Very small	3 - 4m	35	39	29	24	25	12	30	194
Small	4 - 4.8m	15	21	18	14	18	7	24	117
Medium	4.8 - 12.2m	20	117	126	87	61	10	63	484
Large	>12.2 m		29	144	78	26	3	14	294
Total		70	206	317	203	130	32	131	1089

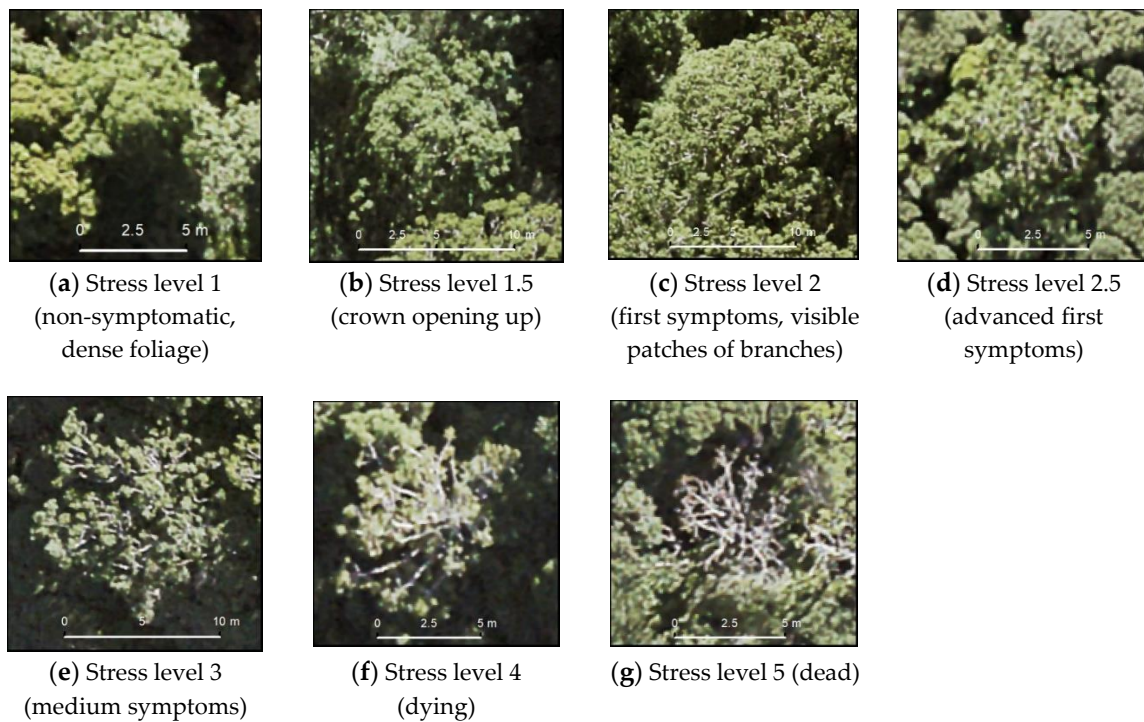


Figure IV-4 Aerial images from (a) non-symptomatic kauri, several states of decline in kauri crowns (b-f), to (g) dead trees. All crowns have a medium-size (mean diameter 4 to 12.2 m) [12].

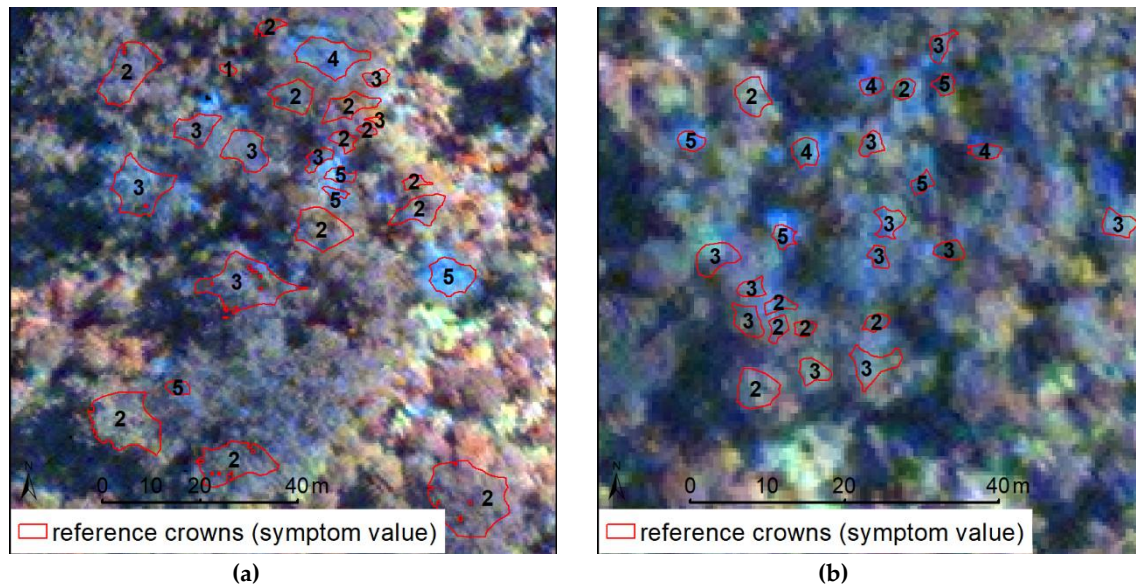


Figure IV-5 Reference crowns in a high kauri stand (a) and a low stand (b), with symptom values from 1 = non-symptomatic to 5 = dead, on a NIR1-Green-Blue composite of the WorldView-2 (WV2) image.

2.5 Attribute calculation

A total of 203 LiDAR attributes were calculated for crown stratification and stress detection. For the stratification of crown sizes, basic crown metrics were derived from the coarser CHM with the 1 m spike-free threshold, such as the maximum crown height and mean diameter. Figure IV-6 gives an overview of the workflow for the attribute calculation.

For stress detection, LiDAR attributes were calculated on both versions of the DSM and CHM (0.6 m and 1 m spike-free threshold). They describe the shape, the crown structure and texture. The range of attributes covers height ratios, percentiles and bincentiles, point density and coverage, shape roundness, slope, and curvatures, as well as first- and second-order texture measures, such as the variance, range, kurtosis, homogeneity, and skewness (see Table IV-A1, Appendix A). These measures were either calculated directly on the LiDAR point cloud for the crown polygons or first calculated as rasters with different kernel sizes. If possible, statistics were calculated on the DSM to avoid distortions caused by a ground normalization of the CHM on steep terrain. We also calculated statistics from the intensity values of the first returns. Height cutoffs of six and eight meters for calculation of the density and coverage on the LiDAR point cloud for low and high stands, were derived from the field measurements of the canopy base height. Table IV-A1 in Appendix A gives an overview of the attributes and tools.

Spectral (43) and textural (111) attributes were calculated on the eight pan-sharpened multispectral WV2 bands with the band math tool in ENVI. The original set of 31 calculated vegetation indices is based on literature research. They also include the best performing indices from the hyperspectral analysis

presented in Meiforth et al. [8], as far as the wavelengths and bandwidths of the WV2 image allowed a calculation. In addition to the indices, bands from a Minimum Noise Fracture (MNF) transformation, a three-band Munsell Hue-, Saturation-, and Value-Transformation (HSVM) and a brightness layer [86] were calculated. 110 texture rasters were based on the PAN channel and band 7 with occurrence and co-occurrence matrices on different kernel sizes. For more details, see Table IV-A2 in Appendix A.

The rasters were scaled to the 1-99 or 2-98 percentiles, according to the histogram distribution, to remove outliers. The resulting attribute rasters were aggregated on the crown polygons with the zonal statistic tool in QGIS by the mean crown value and the standard deviation for the spatial attributes.

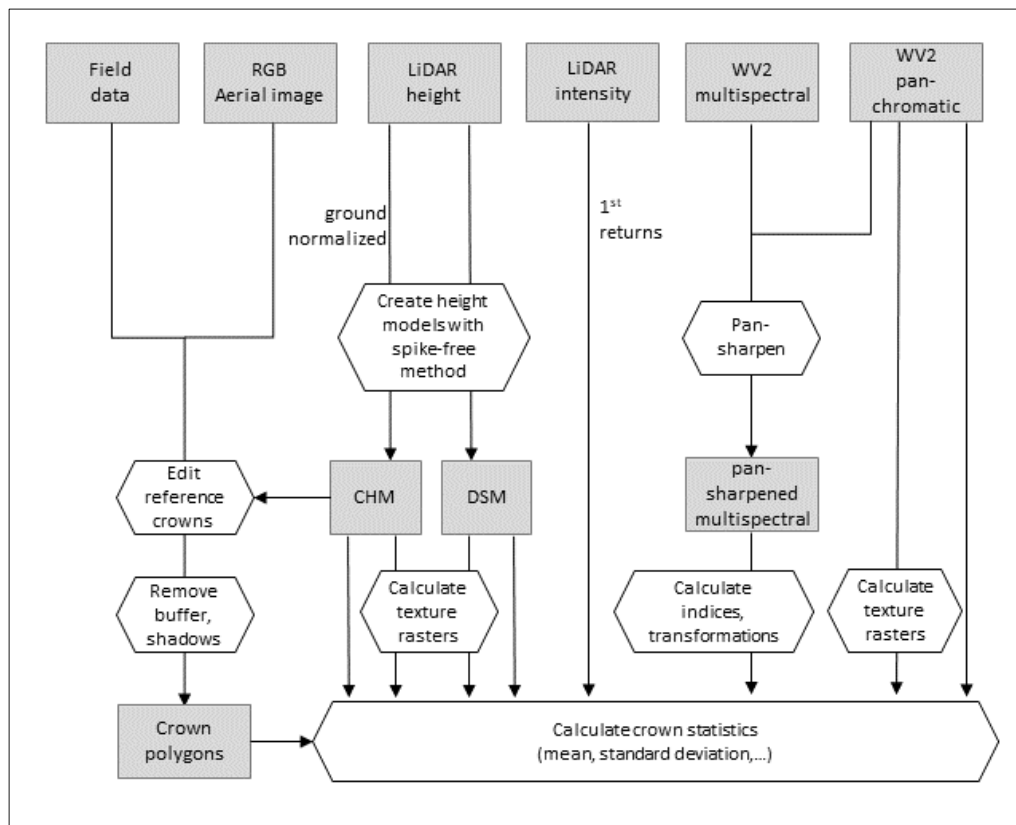


Figure IV-6 Workflow diagram for the attribute calculation.

2.6 Attribute selection and regression approach

The aim of the attribute selection was to identify the subset of attributes with the highest correlation to the stress symptom levels. First, highly correlated and redundant attributes were removed. The attributes were clustered according to their origin (WV2, LiDAR height and LiDAR intensity) and function as spectral or structural. In each of the clusters, pre-selection was performed with a Wrapper Subset Evaluator [89,90],

which outperformed other subset selection methods, such as the Correlation-based Feature Selection (Cfs) and Classifier Subset Evaluator. We used the open source data mining software WEKA, which was developed by the Waikato University in New Zealand [91].

The wrapper method evaluates attribute combinations with a specified machine learning algorithm based on a defined evaluation criterion. We used a Random Forest (RF) regression in 200 iterations, with the Pearson correlation coefficient (correlation) as the evaluation measure. The RF regression also corresponds to the algorithm used for the analysis in this paper and a former analysis of kauri stress symptoms [8]. RF is a non-parametric algorithm that does not require a certain distribution of data [92]. It can handle a large number of input variables with a high variance and is less sensitive to overfitting, unless the data is noisy [93]. To avoid overfitting, we tested and pruned the RF tree to a maximal depth of eight. We tested several search methods and “best first” with bidirectional selection, and a search termination of eight consecutive non-improving nodes gave the best results. The “best first” method combines a backward elimination with a forward selection by finding the best attribute subset from the Wrapper Subset Evaluator. The pre-selected subsets were complemented with other attributes highly correlated to the stress levels, which were identified with the Correlation Attribute Evaluator in WEKA. The subset selection of all attributes was repeated, with different seed values. Depending on the number of attributes selected, the resulting attributes from all subsets were again combined, and the subset selection was repeated with a different range of seed values, in order to reduce the selection to the most relevant attributes. Figure IV-7 shows four raster images of the selected attributes.

The performance of each subset from the final selection round was then tested in an RF regression with a three-fold split and 1000 repetitions, to define the best performing subset. The correlation, the root mean squared error (RMSE), and the mean absolute error (MAE) were calculated as evaluation metrics. When two subsets performed equally well, the one with fewer attributes was chosen. The importance of each attribute in the final selection was calculated as the average impurity decrease for the RF regression.

We also tested an approach that was discussed in Meiforth et al. [8], by first identifying the dead and dying trees in a binary RF classification, before applying a regression for the lower symptom levels.

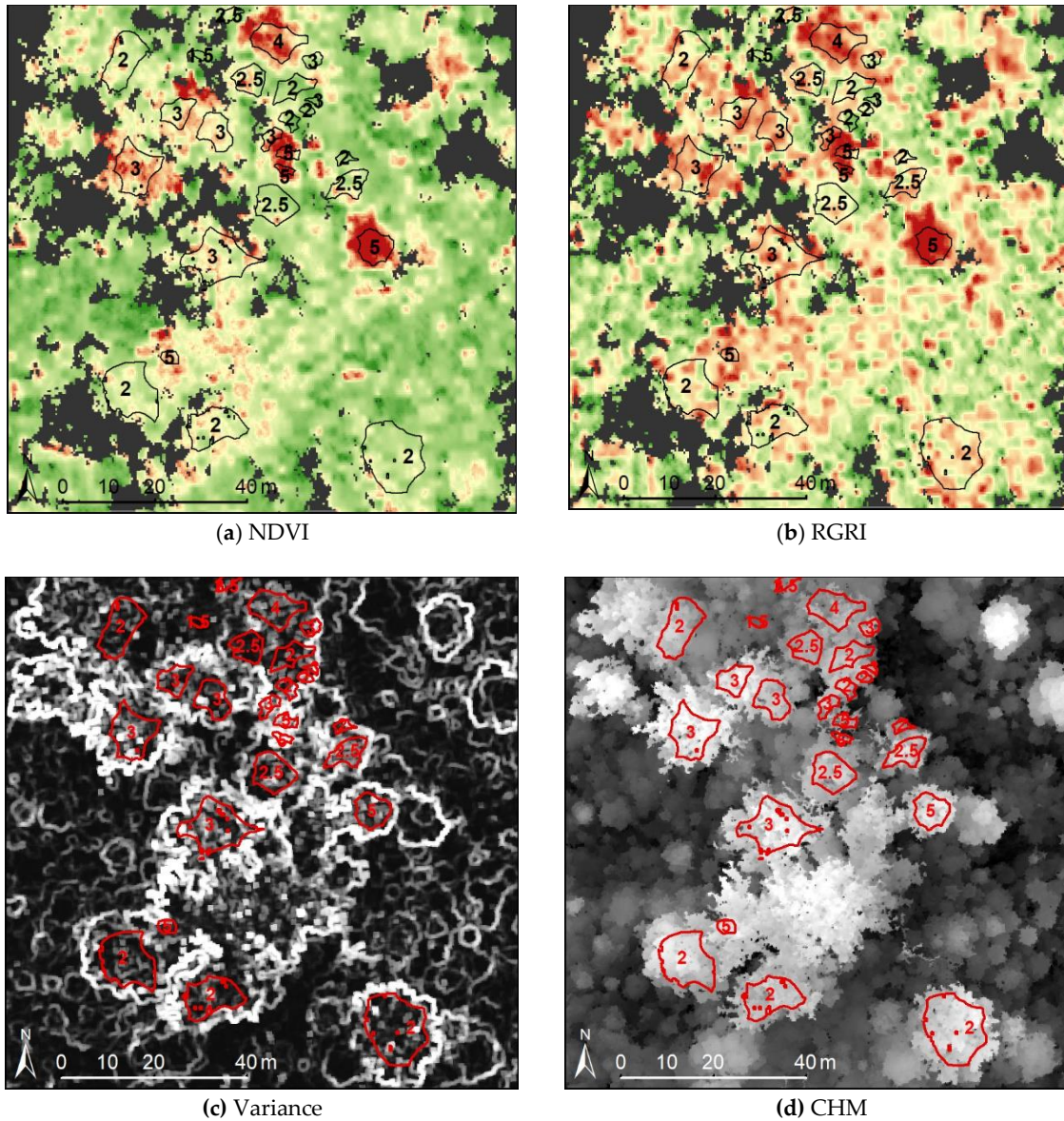


Figure IV-7 Raster datasets of selected attributes with reference crowns marked as red polygons and labelled stress symptom values. The images show (a) a Normalized Difference Vegetation Index (NDVI) on red and NIR1 bands (NDVI_75), (b) the Red-Green Ratio Index (RGRI) on the red and green bands, (c) a variance raster for a 5x5 kernel on a Crown Height Model (CHM), and (d) a CHM with a freeze distance of 0.60 m. The grey areas on the spectral rasters (a and b) mark shadows and no-data pixels that were masked out for the analysis.

3 Results

3.1 Results objective 1: Performance of WV2 attributes and minimum crown size

A selection of eight WV2 attributes and the maximum crown height resulted in a correlation of 0.85 and an RMSE of 0.59 for all 1089 crowns with a minimum diameter of 3 m (Table IV-3, Table IV-A3 in Appendix B). For a minimum crown diameter of 4 m, the correlation increased to 0.89, while the RMSE decreased to 0.48 (Table IV-3). Figure IV-8 and Figure IV-9 show that mainly the small crown sizes and higher stress levels caused outliers (error > 1). The boxplot diagram in Figure IV-10a confirms the overall good match of the model, with a correlation of 0.89 for all crowns with a diameter larger than 4 m. However, the first quartiles of the half-step levels (1 to 1.5 and 2 to 2.5) and the levels 3 and 4 overlap, while the first quartiles of the other levels are more separated. The diagram also shows a slightly non-linear relationship between the actual and predicted values, especially towards the dead and dying trees. After a rescaling of the value for dead trees from 5 to 7, a more linear relationship could be established, facilitating the interpretation of the results (Figure IV-10b). The correlation for the rescaled value range remained unchanged, while the RMSE and MAE values increased with the higher value range.

The most important attributes are a combination of red/NIR1 bands in a Normalized Vegetation Index (NDVI₇₅), followed by a ratio of the red and green bands (Red-Green Ratio Index (RGRI)) and the standard deviation of the first band of an MNF transformation (Table IV-4). Mean crown values of a Green NDVI (gNDVI) with red-edge and green bands, the red-edge band, and a brightness layer were also selected. Further attributes include the mean value of a seven-pixel kernel of the PAN band and the range of a three-pixel kernel on the NIR1 band.

An MSP and linear regression resulted in slightly lower correlations (0.87 and 0.86, respectively) and higher RMSE values (0.52 and 0.55, respectively) compared to the RF regression (correlation of 0.89, RMSE of 0.48) for the seven stress levels and crowns with a diameter larger than 4 m.

A comparison with a reference scheme on the basic five stress levels showed a lower performance (correlation of 0.88, RMSE of 0.55) than the seven-level reference scheme with a more detailed assessment of the first symptoms (Table IV-A3 in Appendix B). While the gNDVI and red-edge band were not selected for the five stress levels, a ratio of the two NIR bands (modified Normalized Difference Water Index (mNDWI)) improved the performance.

Table IV-3 Test of different minimum crown diameters for WV2 attributes for all crowns for seven stress levels. In addition to eight WV2 attributes, the maximum crown height value was included for crown stratification. The performance was tested with an RF regression with three random folds in 1000 repetitions and a depth of 8.

Crown diameter	No of crowns	Corr. ¹	RMSE	MAE
>3.0 m	1089	0.85	0.59	0.4
>3.5 m	1000	0.86	0.56	0.38
>4.0 m	895	0.89	0.48	0.34
>4.5 m	825	0.9	0.45	0.32
>5.0 m	753	0.9	0.44	0.31

1) Correlation

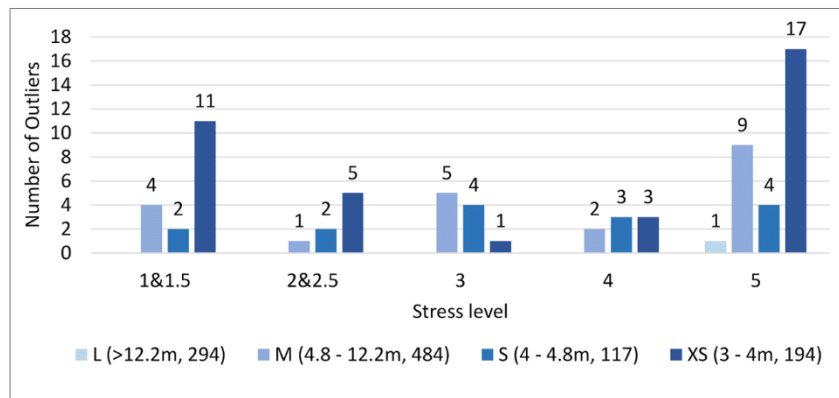


Figure IV-8 Bar chart showing the absolute numbers of outliers (error > 1) in four crown diameter classes (total 1089) and five aggregated stress levels for a Random Forest (RF) regression with nine attributes in a 10-fold cross validation.

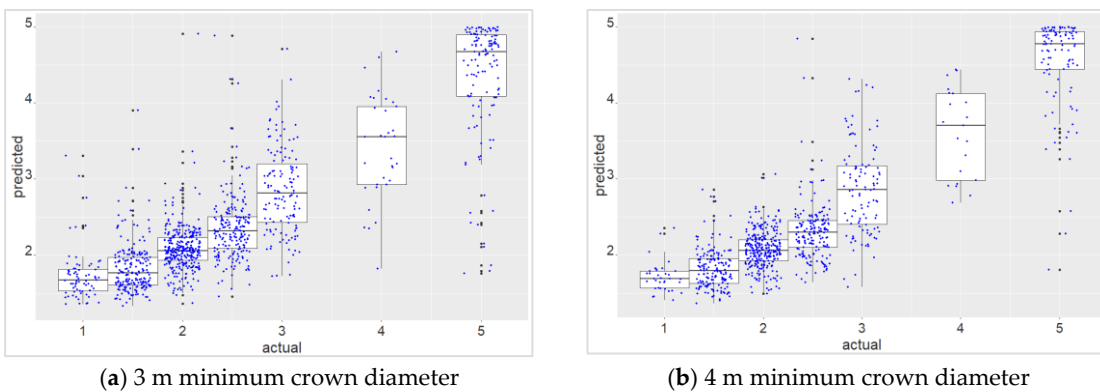


Figure IV-9 A combination of jitter- and boxplot diagrams for an RF regression on WV2 attributes for the seven stress levels, based on (a) crowns with a diameter larger than 3 m (1089) and (b) crowns with a diameter larger than 4 m (895).

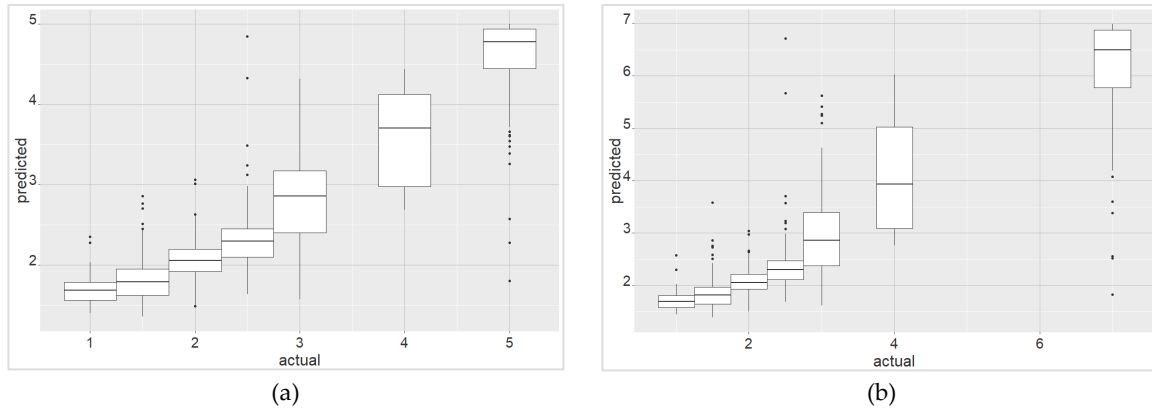


Figure IV-10 Boxplot for the predicted and actual values from an RF regression on the seven-level reference scheme for crowns with a diameter larger than 4 m (total 895). Figure (a) shows the basic scale from 1 to 5 and figure (b) presents the results after rescaling the value 5 for “dead” tree crowns to 7.

Table IV-4 Selection of WV2 attributes and their importance for a description of the seven-level reference scheme for canopy stress symptoms. The maximum crown height value was added for crown stratification. The attribute importance (imp.) for the RF regression was calculated as the average impurity decrease and converted to percentage values.

Abbr.	Att. Imp. %	Correlation	Crown Statistic	Description	Algorithm	Reference
NDVI	32.5	-0.83	mean	Normalized Difference VI	$(b7 - b5)/(b7 + b5)$	[94,95]
RGRI	25.0	0.79	mean	Red-Green Ratio Index	$b5/b3$	[96]
MNF1	12.6	0.68	stdev	1st band of an MNF transformation		[97]
gNDVI	9.2	0.70	mean	Green Normalized Difference VI	$(b6 - b3)/(b6 + b3)$	[98]
b7O3rg	4.3	-0.05	mean	Range of a 3x3 kernel of band 7		[99]
Bright	3.9	-0.14	mean	Brightness band	$(b2 + b3 + b5 + b7)/4$	[86]
b06	3.7	-0.15	mean	Mean of band 6 (red-edge)		
PO7mn	2.8	-0.21	stdev	Mean of a 7x7 kernel of the PAN band		[99]
CHM	5.8	-0.18	max	Maximum height on a CHM raster (1 m freeze distance)		[80]

Table IV-5 Performance of an RF regression for the basic five-level reference scheme and the refined reference scheme with seven stress levels based on WV2 attributes for crowns with a diameter larger than 4 m. The correlation (corr.), root mean squared error (RMSE) and mean absolute error (MAE) were calculated for an RF regression (depth 8, 200 iterations) in a three-fold random split with 1000 repetitions.

	Nr Att.	Corr.	RMSE	MAE
5 level, basic reference scheme (1 - 2 - 3 - 4 - 5)	8	0.88	0.55	0.38
7 level, refined reference scheme (1 - 1.5 - 2 - 2.5 - 3 - 4 - 5)	9	0.89	0.48	0.34

3.2 Results objective 2: Classification to identify dead and dying trees

Dying and dead trees (level 4 and 5) with a diameter larger than 4 m could be identified in an RF classification based on WV2 attributes, with a user's accuracy of 84.3% and a producer's accuracy of 88.7% (Table IV-6). The remaining stress levels from 1 (non-symptomatic) to 3 (medium symptoms) could be described for crowns larger than 4 m, with an RMSE value of 0.37 (MAE of 0.28, correlation of 0.72). The main differences in the attribute selection to the full symptom range are the higher importance of the gNDVI with red-edge and green bands and the selection of the mNDWI on the NIR bands for the first stress levels from 1 to 3 (Table IV-A3 in Appendix B).

Table IV-6 Confusion matrix for an RF classification to identify dead and dying trees (level 4 and 5) with WV2 and LiDAR attributes for crowns with a diameter larger than 4 m (895 total).

Classified as -->	Level 1-3	Level 4, 5	Total	User's Acc.
Level 1-3	761	13	774	98.3
Level 4, 5	19	102	121	84.3
Total	780	115	895	
Producer's Acc.	97.6	88.7		96.4

3.3 Results Objective 3: Test the performance of LiDAR attributes for stress detection

The combination with LiDAR attributes improved the stress detection compared to only WV2 attributes for all tested reference schemes (Table IV-7). For crowns larger than 4 m and seven stress levels, the correlation increased from 0.89 to 0.92 and the RMSE was lowered from 0.49 to 0.43. While the removal of very small crowns under 4 m diameter notably improved the correlation and RMSE for WV2 attributes, the correlation for only LiDAR attributes did not change and the RMSE only improved slightly (Figure IV-11).

The most important attributes for a combination of LiDAR and WV2 data (Table IV-8) are the NDVI on the red/NIR1 bands, followed by the ratio between the maximum height and the 50 percentile crown height (R_max_P50) and the average intensity values. The standard deviation of the first MNF band was also selected with a high importance amongst other spatial attributes for crowns with a diameter larger than 4 m.

Both the identification of dead and dying trees (Table IV-9, Table IV-A4) as well as the detection of first stress symptoms (level 1 to 3), improved with additional LiDAR attributes. In the attribute selection for the first stress symptom, the intensity values had a higher importance, while the R_max_P50 and Brightness attributes were not selected (Table IV-8).

Table IV-7 Performance of an RF regression for the first stress symptoms and seven stress levels with and without LiDAR attributes. The resulting values are based on individual attribute selections for each setup and crowns with a diameter larger than 4 m (total 895 crowns).

	No crowns	WV2 ¹				WV2 & LiDAR			
		No Att.	Corr. ²	RMSE	MAE	No Att.	Corr. ²	RMSE	MAE
7 level reference scheme (1 – 1.5 – 2 – 2.5 – 3 – 4 – 5)	895	9	0.89	0.48	0.34	11	0.92	0.43	0.31
First symptoms (1 – 1.5 – 2 – 2.5 – 3)	774	9	0.72	0.37	0.28	6	0.76	0.34	0.26

¹ The attributes include the maximum crown height value based on the LiDAR CHM for stratification. ² Correlation

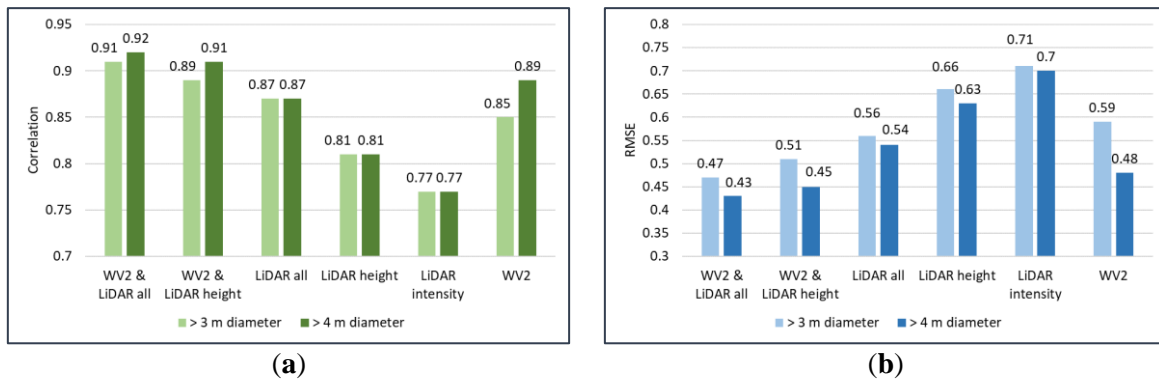


Figure IV-11 Correlations (a) and RMSE (b) of WV2 and LiDAR attributes for an RF regression on seven stress symptom levels. The performance was tested for crowns with a mean diameter larger than 3 m (light color, total 1089) and larger than 4 m (dark color, total 895). The RF regression was carried out in 1000 repetitions for a random three-fold split with a tree depth of eight.

Table IV-8 Selected attributes for a stress analysis with WV2 and LiDAR attributes for seven stress levels and the first symptoms of stress (level 1 to 3) for crowns with a diameter larger than 4 m. The attribute importance in % is based on an RF regression in a 10-fold cross validation.

	Crown statistics	First symptoms		7-Level symptoms		Description	Source
		Imp. %	Corr.	Imp. %	Corr.		
NDVI75	mean	31.8	-0.67	33.3	-0.83	Normalized Difference Vegetation Index (b7 – b5)/(b7 + b5)	[94,95]
R_max_P50				21.5	0.61	Ratio max. height and 50 percentile	[79]
intensity	mean	26.9	-0.60	16.8	-0.71	Intensity values	[79]
MNF_b1	st. dev.	10.1	0.38	14.1	0.68	1st band of a MNF transformation	[97,100]
Pan_k7m	st. dev.	7.8	-0.22			Mean of a 7x7 kernel on the PAN band	[99]
Cg1Cor7	mean	13.3	-0.35	4.5	-0.43	Correlation on a 7x7 kernel CHM ¹	[99]
CHM ¹	max.	10.0	0.14	3.8	-0.18	Maximum crown height from a CHM	[79]
b7_k3Rg	mean			3.5	-0.05	Range of a 3x3 kernel on band 7	[99]
Bright	mean			2.4	-0.14	Brightness layer (b2 + b3 + b5 + b7)/4	[86]

¹ The CHM was calculated with a 1 m spike-free threshold according to the method of Khosravipoura [80].

Table IV-9 Accuracies (Acc.) for an RF classification to identify dead and dying trees (level 4 and 5) with WV2 and LiDAR attributes for crowns with a diameter larger than 3 m (1089 total) and larger than 4 m (895 total). The RF classifier was set up with 1000 iterations in a 10-fold cross-validation.

Attribute Type	Min. Crown Diameter	No Attributes	Overall Accuracy	Level 4 and 5 (Dying and Dead Trees)	
				User's Acc.	Prod. Acc.
WV2	3 m	5	94.9	73.6	90.2
WV2 & LIDAR	3 m	7	96.7	87.1	90.4
WV2	4 m	5	96.4	84.3	88.7
WV2 & LiDAR	4 m	6	97.2	86.0	92.9

4 Discussion

The high overall performance of WV2 attributes with a correlation of 0.89 (RMSE of 0.48, MAE of 0.34) for the seven stress symptom levels and crowns with a diameter larger than 4 m diameter showed that WV2 data is well-suited to describing stress symptoms in kauri canopies. The seven-level reference scheme includes a refined description of the first stress symptoms, which is important for an early identification of potentially infected stands.

4.1 Discussion: Minimum crown size and stratified approach

The high number of outliers in crowns with a diameter smaller than 4 m, especially for dead and dying trees, is an indicator that the multispectral resolution of 1.8 m in the WV2 image causes mixed pixels in small crowns and is too coarse to detect the small bare top branch of severely affected small crowns. Misalignment between the WV2 image and the CHM can also cause errors; however, this cannot be completely avoided, especially in steep terrain with high crown heights [101].

For the use of only WV2 attributes on the full range of stress symptoms, a minimum crown size of at least 4 m is recommended, which improves the correlation from 0.85 to 0.89 and the RMSE from 0.59 to 0.48. Stands with kauri of smaller crown sizes should be pre-segmented and analysed in homogenous stand units.

The different appearance of kauri growth stages requires a stratified approach [8]. If only WV2 data is available for regular monitoring, the inclusion of the maximum crown height derived from LiDAR data of former years allows such a stratification.

4.2 Discussion: Attribute performance

According to the findings presented in Meiforth et al. [8], an NDVI with a red and NIR1 band combination (NDVI_75) and a red-green ratio (RGRI) are the most important attributes for stress detection in the full seven-level symptom range (32.5% and 25% importance, respectively), including dead and dying trees. While the NDVI_75 saturates for high chlorophyll concentrations, it is able to capture the loss of photosynthetic activity and structural changes caused by foliage loss [94,95]. The also selected RGRI combination, the green NDVI (9.2% importance), and the mean of the red-edge band (3.7%) are more sensitive to pigment changes [98,102]. The standard deviation of the first band of an MNF transformation (12.6% importance) and the range of the NIR1 band (4.3%) provide information on structural and textural crown characteristics, which are influenced by a higher number of large bare branches and internal shadows. The same features are also captured by a selected brightness layer (3.9%). These attributes have a higher importance in a five-level reference scheme with a greater emphasis on advanced stress levels (Table IV-A3, Appendix B).

For the detection of first stress symptoms in trees with still an intact crown architecture (level 1 to 3), the green NDVI has a higher importance. It detects the blue shift of the red-edge point caused by a decline in photosynthetic activity and changes in the foliage pigment concentrations [102]. A modified Normalized Difference Water Index (mNDWI) for the NIR1 and NIR2 bands was also selected for the first stress levels, and is sensitive to a reduction of leaf-cell wall scattering and reduced canopy water caused by foliage loss [103].

4.3 Discussion: Dealing with non-linearity: Rescaling and a two-step approach

While the RF regression is well suited to handle non-linear relationships, the boxplot in Figure IV-10a shows that the medians of the resulting values for dead and dying crowns are slightly lower than the actual values. This effect of non-linearity is mainly caused by the more extreme reflectance values of dead branches and shadows in the later stages of decline.

A rescaling of the reference values for the dead crowns (i.e. subdividing the range for this crown state in several levels of severity) suggested in Meiforth et al. [8] leads to a better match between the medians of the results compared to the actual values (Figure IV-10b), while the overall correlation coefficients remain unchanged. Merging the mapped severity classes again after the prediction process allows to maintain the original value range from 1 (non-symptomatic) to 5 (dead), which also corresponds to the field reference scheme used by Auckland Council. A change detection however should be based on the original resulting values to utilize the detailed information in the continuous output range of the regression analysis.

The test of a two-step approach showed that the identification of dead and dying crowns in a binary RF classification requires additional LiDAR data for a stress description of crown sizes smaller than 4 m (Table IV-9). If only WV2 attributes are available, the minimum crown size should be 4 m mean diameter. Although, even for crowns larger than 4 m, ca. 15% of the dead and dying crowns were still misclassified as less symptomatic. The remaining lower stress levels from 1 to 3 can be described in a regression with the pre-selected attribute sets with an RMSE of 0.37. However, the mistakes from prior classification need to be added to these results, which makes the interpretation more complicated, especially when this method is used in a change detection. For an easier interpretation, we recommend using only a regression approach.

4.4 Discussion: Performance of additional LiDAR attributes for stress detection

The increasing performance with additional LiDAR attributes for stress detection can be explained by the additional 3D information in a higher spatial resolution, a high spatial accuracy and the spectral information in the intensity values. The ratio between the maximum crown height and 50-percentile height has a high importance for reference schemes that include dead and dying crowns, but it was not selected to assess the first stress symptoms. The advanced loss of foliage is characterized by a lower 50-percentile height of the LiDAR returns, while the maximum height in the form of branches still remains high, even in the later stress stages, caused by the remaining (dead) branches. Further selected LiDAR height attributes describe textural characteristics, as an indicator of foliage loss that exposes gaps and bare branches, such as the variance, standard deviation, and cross-curvature in CHM and DSM models. However, the performance of these attributes depends on an accurate spatial alignment, since their values increase on the edge of the crowns (Figure IV-7c). For the time being, the acquisition of airborne LiDAR data is still too expensive for regularly monitoring stress symptoms.

4.5 Discussion: Recommendations for further studies

The resulting stress symptom values of the remote sensing analysis need to be interpreted to translate them into health categories by local experts considering the growth stage, the stand situation, the environmental conditions, and other possible causes of stress. Spatiotemporal dynamics of stress symptoms over several years analysed in change detections might also help to distinguish between PA infection and other causes of stress [20,104,105]. We also recommend testing the use of the original, not pan-sharpened multispectral bands, especially for the stress detection in medium and larger crown sizes.

Further studies should investigate crown- and stand-segmentation in kauri forests based on LiDAR data. Zörner et al. [106] developed a method for large tree detection in native New Zealand forest in the Wellington region. Another promising method for canopy segmentation was developed by Wagner et al.

[68] in an Atlantic rainforest based on a U-net convolutional network.

A stand-based analysis of stress symptoms with satellite data requires a better understanding of spectral stress responses in associated tree species. Meiforth et al. [7] showed that the effect of waxy, shiny foliage surface in kahikatea, wooden seed capsules in kānuka, and the influence of older needle cohorts in perennial conifers like rimu can lead to confusion with dead and dying crowns [7]. A spectral unmixing of forest stands with known spectra of kauri and other tree species might also help with the interpretation of stress assessment in mixed forest stands [37,107,108].

We also recommend testing the use of other datasets, which offer more cost-efficient options, such as optical height models derived from stereo-images, instead of LiDAR [109]. Additionally, the newly launched constellations of micro-satellites could be tested, which offer opportunities for producing very-high-spatial-resolution data at a relatively low cost [110].

5 Conclusions

This study presents a method for detecting stress symptoms in the canopies of New Zealand kauri trees with LiDAR and WV2 data based on 1089 manually segmented crowns. A reference scheme for stress symptoms in five levels was refined to seven levels with a higher differentiation of the first stages of stress. A crown diameter of 4 m was determined as the recommended minimum object size for stress detection, to avoid higher numbers of outliers and mixed pixels for smaller crown sizes. A selection of eight WV2 attributes in combination with the maximum crown height resulted in a correlation of 0.89 (RMSE of 0.48, MAE of 0.34) in an RF regression for crown sizes larger than 4 m. The performance was further improved by adding LiDAR attributes (correlation of 0.92, RMSE of 0.43). For a cost efficient regular monitoring of stress symptoms, we recommend the use of WV2 satellite data on pre-segmented crowns with a diameter larger than 4 m and homogenous stand units for smaller crown sizes. The maximum crown height should be included in the analysis to allow for a stratification. With the newly available LiDAR data for crown-segmentation over the main distribution area of natural kauri forests, the results of this study have important implications for cost-efficient large-area monitoring of stress symptoms in New Zealand's kauri forests.

Author Contributions: Conceptualization, J.M., J.H., J.S., and J.D.; methodology, J.M., J.H., H.B.; software, J.M.; validation, J.M.; formal analysis, J.M.; investigation, J.M.; resources, J.M. and J.S.; data curation, J.M.; writing—original draft preparation, J.M.; writing—review and editing, J.M., H.B., J.H., J.S., and J.D.; visualization, J.M.; supervision, H.B., J.H., and J.S.; project administration, J.M. and J.H.; funding acquisition, J.M., J.H., J.S., and J.D.

Funding: The Kauri Dieback Programme (NZ) funded most of the remote sensing data (Ministry for Primary Industries agreement nr 17766), while the University of Canterbury (NZ), Landcare Research (NZ), the University of Trier (Germany), and FrontierSI (former CRCIS) Australia supported living costs, fieldwork, equipment, and additional LiDAR data. Auckland Council supported the fieldwork and supplied LiDAR data and aerial images. The DigitalGlobe Foundation granted satellite images. Rapidlasso and Harris Geospatial supplied grants for software licenses. Henning Buddenbaum was supported within the framework of the EnMAP project (FKZ 50 EE 1530) by the German Aerospace Center (DLR) and the Federal Ministry of Economic Affairs and Energy. Landcare Research funded the publication costs.

Acknowledgments: Our sincere thanks go to all people and institutions who supported this project. We are especially grateful to David Norton, who helped with the administration and provided input for the fieldwork and ecological aspects of the analysis. Nick Waipara, Lee Hill, and Yue Chin Chew from Auckland Council helped to establish the project and provided data. The Kauri Dieback Programme (Planning and Intelligence Team) gave constructive feedback and support during this research. We would also like to thank the staff of the Arataki visitor centre, Fredrik Hjelm from the Living Tree Company, and Joanne Peace for their excellent support and guidance during the fieldwork. Our thanks go to Massey University for the provision of the hyperspectral data acquisition, as well as AAM NZ Ltd. for the acquisition and processing of airborne LiDAR data. Jeanette Allen, Vicki Wilton, and Nicole Gellner helped with the university administration.

Conflicts of Interest: The authors declare no conflicts of interest.

Appendix IV-A

Table IV-A1 LiDAR attributes (203 total).

Total	Based on	Attributes ²	Software/tools
14	Intensity values	Avg, qav, std, ske, kur Percentiles (01, 05, 10, 25, 50, 75, 90, 95, 99)	LAStools, LAScanopy
88	DSM ¹	Stdev, var, rang, crosc, longc, mnc, mxc, slp, avgdev, kur, skw, on 3x3, 5x5, 7x7 kernel size	QGIS zonal statistic, GRASS: r.param.scale
55	CHM ¹	Mean, max, stdev, rang, med, maj, var, vart, prc conv,sa, var, ent, asm, con, cor, idm, con, cor > all attributes were calculated on 3, 5, 7 kernel sizes	QGIS zonal statistic GRASS: r.statistics, r.texture, r.slope.aspect
13	Crown polygon	Ratio mdm/height; Ratio of max height with/95, 75 and 50 percentile and avg height of outer crown edge; Difference of max height with 75 and 50 percentile, peak density, height, mdm, shp area and roundness (shp area/lengths), average height of outer crown edge	ArcGIS tools
33	LiDAR point cloud	Std, ske, kur, cov, dns (cut value 6 m and 8 m), min, max, avg, avg 1st return, percentiles (01, 05, 10, 25, 50, 75, 90, 95, 99), bincentiles (10, 20, 30, 40, 50, 60, 70, 80, 90)	LAStools LAScanopy

¹ The Digital Surface Model (DSM) and the Crown Height Model (CHM) were calculated with LAStools as spike-free rasters, according to Khosravipoura et al. [80], in two versions with a “freeze distance” of 60 and 100 cm. ² Abbreviations, see below

Table IV-A2 Attributes calculated on the WorldView-2 image (154 total).

Total	Attributes ²	Crown statistic	Software
8	Multispectral bands 1–8	mean	ENVI
1	MNF transformation (1st band)	stdev	ENVI
4	HSVM transformation (3 bands), Brightness layer (1 band)	mean	ENVI
31	31 Vegetation Indices	mean	ENVI
110	Textures on PAN channel and band 7 (NIR1) with 3x3, 5x5, and 7x7 kernels: Rang, mean, var, ent, skw, hom, con, cor, sm, dis	mean stdev	ENVI

² Abbreviations for table A1 and A2

asm	angular second moment	mdm	mean diameter
avg	average	mnc	mean curvature
avgdev	average deviation	mxo	max curvature
con	contrast	planc	plan curvature
cor	correlation	prc conv	percent convex
cov	coverage	prof c	profile curvature
crosc	cross-sectional curvature	qav	quadratic average
dis	dissimilarity	rang	range
dns	density	skw	skewness
ent	entropy	slp	slope
hom	homogeneity	sm	second moment
idm	inverse difference	stedv	standard deviation
kur	kurtosis	var	variance
longc	longitudinal curvature	vart	variety
maj	majority		

Appendix IV-B

Table IV-A3 Selected attributes and attribute importance in percent for different stress symptom references (basic 5 levels¹, first symptoms², refined 7 levels³) based on crowns with a diameter larger than 4 m for WV2 attributes. The attribute importance for an RF regression was calculated as the average impurity decrease and converted to percentages.

Abbrev.	Band	5 level ¹ Imp. %	First ² Imp. %	7 Level ³ Imp. %	Crown Statistic	Description	Algorithm	Ref.
NDVI	5, 7	32.2	26.7	31.5	mean	Normalized Difference VI	$(b7 - b5)/(b7 + b5)$	[94,95]
RGRI	3, 5	29.5	20.3	24.2	mean	Red Green Ratio Index	$b5/b3$	[96]
MNF1	all	15.2	9.9	12.3	st. dev	1st band of an MNF transformation		[97]
gNDVI	3, 6		13.1	9	mean	Green Normalized Difference VI	$(b6 - b3)/(b6 + b3)$	[98]
mNDWI	7, 8	5.0	5.7		mean	Modified Normalized Difference Water Index	$(b7 - b8)/(b7 + b8)$	[103]
Bright	2, 3, 5, 7	4.7		3.8	mean	Brightness band	$(b2 + b3 + b5 + b7)/4$	[86]
b6	6			3.6	mean	Mean of band 6		
b7_3kr	7		7.4	4.2	mean	Range of a 3x3 kernel on band 7		[99]
b7_5kr	7		8.8		st. dev	Range of a 5x5- kernel on band 7		[99]
Pn_k7sm	PAN	3.7			mean	Second moment of a 3x3 kernel on the PAN band		[99]
Pn_k7mn	PAN	3.6	8.0	2.7	st. dev	Mean of a 7x7 kernel on the PAN band		[99]
CHM		6.2		5.7	max	Maximum height on CHM raster (spike-free thresh. 1m)		[80]

¹ 5-level value range (1 – 2 – 3 – 4 – 5);

² First Symptoms value range (1 – 1.5 – 2 – 2.5 – 3);

³ 7-level value range (1 – 1.5 – 2 – 2.5 – 3 – 4 – 5).

Appendix IV-C

Table IV-A4 Selected attributes to identify dead and dying trees for all crown sizes (total 1089) with a Random Forest classifier based on WV2 attributes only (WV2) and in combination with LiDAR attributes (WV2 & LiDAR). The attribute importance was calculated as the average impurity decrease.

Abbrev.	Crown statistic	Description	WV2				WV2 & LiDAR				Ref.
			1089 Cr. > 3 m		895 Cr. > 4 m		1089 Cr. > 3 m		895 Cr. > 4 m		
			imp. %	corr.	imp. %	corr.	imp. %	corr.	imp. %	corr.	
NDVI_75	mean	Normalized Difference VI $(b7 - b5)/(b7 + b5)$			25.8	0.75			15.7	0.75	[94,95]
MCARI	mean	Modified chlorophyll absorption in reflectance index $1.2*(2.5*(b7-b5)-1.3*(b7-b3))$							16.2	0.39	[111]
gNDVI	mean	Green Normalized Difference VI $(b6 - b3)/(b6 + b3)$	26.7	0.55							[98]
RDVI	mean	Renormalized Difference VI $(b7-b5)/\sqrt{b7+b5}$	22.2	0.51							[111]
ARVI	mean	Atmospherically Resistant Vegetation Index $(b7) - (2*b5-b2)/(b7) + (2*b5-b2)$	18.5	0.70			16.5	0.70			[112]
MNF_1st	st. dev.	1st band of an MNF transformation							15.5	0.65	[97]
Pan_k3sk	mean	Skewness of a 3x3 kernel on the PAN band	17.2	0.01							[99]
Bright	mean	Brightness band $(b2 + b3 + b5 + b7)/4$			20.2	0.06					[86]
Pan_k3hm	mean	Homogeneity of a 3x3 kernel on the PAN band			21.4	0.10					[99]
Pan_k5Cr	mean	Correlation of a 5x5 kernel on the PAN band			15.7	0.03					[99]
b7_k3rg	mean	Range of a 3x3 kernel on the band 7	15.5	0.02	16.9	0.07	18.2	0.02	16.4	0.07	[99]
intensity	skewness	LiDAR intensity value					14.7	0.55	12.1	0.52	[79]
D6_k5var	variance	Variance of a 5x5 kernel on the DSM (spike-free thresh. 0.6m)					13.8	0.17			[99]
Cg6_k5var	median	Variance of a 5x5 kernel on the CHM (spike-free thresh. 0.6m)							12.3	0.51	[99]
RatDMHght		Ratio between the mean diameter and maximum height					13.6	0.00			
R_max_P50		Ratio between the maximum height and the 50 percentile					11.4	0.58			
CHM	maximum	Maximum height on CHM raster (spike-free thresh. 1m)					11.8	0.28	11.8	0.27	[80]

6 References

1. Beever, R.E.; Waipara, N.W.; Ramsfield, T.D.; Dick, M.A.; Horner, I.J. Kauri (*Agathis australis*) under threat from *Phytophthora*. *Phytophthora For. Nat. Ecosyst.* **2009**, *74*, 74–85.
2. Weir, B.S.; Paderes, E.P.; Anand, N.; Uchida, J.Y.; Pennycook, S.R.; Bellgard, S.E.; Beever, R.E. A taxonomic revision of *Phytophthora* Clade 5 including two new species, *Phytophthora agathidicida* and *P. cocois*. *Phytotaxa* **2015**, *205*, 21–38.
3. MPI. Map “Kauri Dieback Distribution” Available online: https://www.kauridieback.co.nz/media/2037/kauridieback-distribution_20190930_350dpi.jpg (accessed on 20 February 2020).
4. Ecroyd, C. Biological flora of New Zealand 8. *Agathis australis* (D. Don) Lindl. (Araucariaceae) Kauri. *N. Z. J. Bot.* **1982**, *20*, 17–36.
5. Steward, G.A.; Beveridge, A.E. A review of New Zealand kauri (*Agathis australis* (D. Don) Lindl.): Its ecology, history, growth and potential for management for timber. *N. Z. J. For. Sci.* **2010**, *40*, 33–59.
6. Shortland, T.; Wood, W. Kia Toitu He Kauri, Kauri Dieback Tangata Whenua Roopu Cultural Impact Assessment. Report by Repo Consultancy Ltd., Commissioned by the Ministry of Primary Industries NZ/the Kauri Dieback Programme. Available online: <https://www.kauridieback.co.nz/media/1813/shortland-wood-2011.pdf> (accessed on the 5 March 2020).
7. Meiforth, J.J.; Buddenbaum, H.; Hill, J.; Shepherd, J.; Norton, D.A. Detection of New Zealand Kauri Trees with AISA Aerial Hyperspectral Data for Use in Multispectral Monitoring. *Remote Sens.* **2019**, *11*, 2865.
8. Meiforth, J.J.; Buddenbaum, H.; Hill, J.; Shepherd, J. Monitoring of Canopy Stress Symptoms in New Zealand Kauri Trees Analysed with AISA Hyperspectral Data. *Remote Sens.* **2020**, *12*, 926.
9. Bellgard, S.; Weir, B.; Pennycook, S.R.; Paderes, E.P.; Winks, C.; Beever, R.E.; Williams, S. *Specialist Phytophthora Research: Biology, Pathology, Ecology and Detection of PTA.*; Final Report for the New Zealand Ministry for Primary Industries: Wellington, New Zealand, 2013.
10. Macinnis-Ng, C.; Schwendenmann, L. Litterfall, carbon and nitrogen cycling in a southern hemisphere conifer forest dominated by kauri (*Agathis australis*) during drought. *Plant Ecol.* **2015**, *216*, 247–262.
11. Ministry of Primary Industries. *Airbone LiDAR and RGB Aerial Images in the Waitakere Ranges*; Ministry of Primary Industries: Wellington, New Zealand, 2016.
12. Auckland Council 0.075m Urban Aerial Photos RGB, Waitakere Ranges. Available online: <https://data.linz.govt.nz/layer/95497-auckland-0075m-urban-aerial-photos-2017/> (accessed on 12 April 2019).
13. Jongkind, A.; Buurman, P. The effect of kauri (*Agathis australis*) on grain size distribution and clay mineralogy of andesitic soils in the Waitakere Ranges, New Zealand. *Geoderma* **2006**, *134*, 171–186.
14. MPI. Map Data (Shp Files) for PTA Positive Sampling Sites (updated 23 January 2019) and the Natural Range of Kauri Distribution. Regulations for Use and Liability are Stated on the Map. Available online: https://www.kauridieback.co.nz/media/2037/kauri-dieback-distribution_20190930_350dpi.jpg (accessed on 13 February 2020).
15. ESRI. World Topographic Map-WMTS service. Map data. Sources: Esri, HERE, Garmin, Intermap, INCREMENT P, GEBCO, USGS, FAO, NPS, NRCAN, GeoBase, IGN, Kadaster NL, Ordnance Survey, Esri Japan, METI, Esri China (Hong Kong), © OpenStreetMap contributors, GIS User Community. 2020.
16. LINZ. NZ Topo50. Topographical Map for New Zealand. Imported on April 14, 2019 from 445 GeoTIFF Sources in NZGD2000/New Zealand Transverse Mercator 2000. Available online: <https://www.linz.govt.nz/land/maps/topographic-maps/topo50-maps>. (accessed on 20 July 2019).
17. Wang, J.; Sammis, T.; Gutschick, V.P.; Gebremichael, M.; Dennis, S.O.; Harrison, R.E. Review of Satellite Remote Sensing Use in Forest Health Studies. *Open Geogr. J.* **2010**, *3*, 28–42.
18. Pause, M.; Schweitzer, C.; Rosenthal, M.; Keuck, V.; Bumberger, J.; Dietrich, P.; Heurich, M.; Jung, A.; Lausch, A. In Situ/Remote Sensing Integration to Assess Forest Health—A Review. *Remote Sens.* **2016**, *8*, 471.
19. Townsend, P.A.; Singh, A.; Foster, J.; Rehberg, N.J.; Kingdon, C.C.; Eshleman, K.; Seagle, S.W. A general Landsat

- model to predict canopy defoliation in broadleaf deciduous forests. *Remote Sens. Environ.* **2012**, *119*, 255–265, doi:10.1016/j.rse.2011.12.023.
20. Garrity, S.R.; Allen, C.D.; Brumby, S.P.; Gangodagamage, C.; McDowell, N.G.; Cai, D.M. Quantifying tree mortality in a mixed species woodland using multitemporal high spatial resolution satellite imagery. *Remote Sens. Environ.* **2013**, *129*, 54–65, doi:10.1016/j.rse.2012.10.029.
 21. Ortiz, S.M.; Breidenbach, J.; Kändler, G. Early Detection of Bark Beetle Green Attack Using TerraSAR-X and RapidEye Data. *Remote Sens.* **2013**, *5*, 1912–1931.
 22. Dotzler, S.; Hill, J.; Buddenbaum, H.; Stoffels, J. The Potential of EnMAP and Sentinel-2 Data for Detecting Drought Stress Phenomena in Deciduous Forest Communities. *Remote Sens.* **2015**, *7*, 14227–14258.
 23. Meng, J.; Li, S.; Wang, W.; Liu, Q.; Xie, S.; Ma, W. Mapping Forest Health Using Spectral and Textural Information Extracted from SPOT-5 Satellite Images. *Remote Sens.* **2016**, *8*, 719, doi:10.3390/rs8090719.
 24. White, J.C.; Wulder, M.A.; Brooks, D.; Reich, R.; Wheate, R.D. Detection of red attack stage mountain pine beetle infestation with high spatial resolution satellite imagery. *Remote Sens. Environ.* **2005**, *96*, 340–351, doi:10.1016/j.rse.2005.03.007.
 25. Nitesh, P.; Ismail, R. Discriminating the occurrence of pitch canker fungus in Pinus radiata trees using QuickBird imagery and artificial neural networks. *South. For. J. For. Sci.* **2013**, *75*, 29–40.
 26. Waser, L.T.; Küchler, M.; Jütte, K.; Stampfer, T. Evaluating the Potential of WorldView-2 Data to Classify Tree Species and Different Levels of Ash Mortality. *Remote Sens.* **2014**, *6*, 4515–4545.
 27. Wang, H.; Pu, R.; Zhang, Z. Mapping Robinia Pseudoacacia Forest Health Conditions by Using Combined Spectral, Spatial and Textural Information Extracted from Ikonos Imagery. *ISPRS Int. Arch. Photogramm. Remote Sens. Spat. Inf. Sci.* **2016**, 1425–1429, doi:10.5194/isprs-archives-XLI-B8-1425-2016.
 28. Tuominen, J.; Lipping, T.; Kuosmanen, V.; Haapanen, R. Remote sensing of forest health. In *Geoscience and Remote Sensing*; IntechOpen: London, UK, 2009.
 29. Jones, H.G.; Vaughan, R.A. *Remote Sensing of Vegetation: Principles, Techniques, and Applications*; Oxford University Press: Oxford, UK, 2010.
 30. Lausch, A.; Erasmi, S.; King, D.; Magdon, P.; Heurich, M. Understanding Forest Health with Remote Sensing – Part I – A Review of Spectral Traits, Processes and Remote-Sensing Characteristics. *Remote Sens.* **2016**, *8*, 1029.
 31. Thenkabail, P.S.; Lyon, J.G.; Huete, A. *Fundamentals, Sensor Systems, Spectral Libraries, and Data Mining for Vegetation*; CRC Press: Boca Raton, FL, USA, 2018.
 32. Oumar, Z.; Mutanga, O. Integrating environmental variables and WorldView-2 image data to improve the prediction and mapping of Thaumastocoris peregrinus (bronze bug) damage in plantation forests. *ISPRS J. Photogramm. Remote Sens.* **2014**, *87*, 39–46.
 33. Eitel, J.U.; Vierling, L.A.; Litvak, M.E.; Long, D.S.; Schulthess, U.; Ager, A.A.; Krofcheck, D.J.; Stoscheck, L. Broadband, red-edge information from satellites improves early stress detection in a New Mexico conifer woodland. *Remote Sens. Environ.* **2011**, *115*, 3640–3646.
 34. Kayitakire, F.; Hamel, C.; Defourny, P. Retrieving forest structure variables based on image texture analysis and IKONOS-2 imagery. *Remote Sens. Environ.* **2006**, *102*, 390–401.
 35. Ozdemir, I.; Karnieli, A. Predicting forest structural parameters using the image texture derived from WorldView-2 multispectral imagery in a dryland forest, Israel. *Int. J. Appl. Earth Obs. Geoinf.* **2011**, *13*, 701–710.
 36. Eckert, S. Improved forest biomass and carbon estimations using texture measures from WorldView-2 satellite data. *Remote Sens.* **2012**, *4*, 810–829.
 37. Somers, B.; Verbesselt, J.; Ampe, E.M.; Sims, N.; Verstraeten, W.W.; Coppin, P. Spectral mixture analysis to monitor defoliation in mixed-aged Eucalyptus globulus Labill plantations in southern Australia using Landsat5-TM and EO-1Hyperion data. *Int. J. Appl. Earth Obs. Geoinf.* **2010**, *12*, 270–277.
 38. Fassnacht, F.E.; Latifi, H.; Ghosh, A.; Joshi, P.K.; Koch, B.J.R.S.o.E. Assessing the potential of hyperspectral imagery to map bark beetle-induced tree mortality. *Remote Sens. Environ.* **2014**, *140*, 533–548.
 39. Immitzer, M.; Atzberger, C.; Koukal, T. Tree species classification with random forest using very high spatial resolution 8-band WorldView-2 satellite data. *Remote Sens.* **2012**, *4*, 2661–2693.
 40. Pu, R.; Landry, S. A comparative analysis of high spatial resolution IKONOS and WorldView-2 imagery for

- mapping urban tree species. *Remote Sens. Environ.* **2012**, *124*, 516–533.
41. Meddens, A.J.; Hicke, J.A.; Vierling, L.A.J.R.S.o.E. Evaluating the potential of multispectral imagery to map multiple stages of tree mortality. *Remote Sens. Environ.* **2011**, *115*, 1632–1642.
 42. Lottering, R.; Mutanga, O. Optimising the spatial resolution of WorldView-2 pan-sharpened imagery for predicting levels of *Gonipterus scutellatus* defoliation in KwaZulu-Natal, South Africa. *ISPRS J. Photogramm. Remote Sens.* **2016**, *112*, 13–22.
 43. Ismail, R.; Mutanga, O.; Kumar, L.; Bob, U. Determining the optimal spatial resolution of remotely sensed data for the detection of sirenix noctilio infestations in pine plantations in kwazulu-natal, south africa. *South Afr. Geogr. J.* **2008**, *90*, 22–31.
 44. Van de Voorde, T.; De Genst, W.; Canters, F.; Stephenne, N.; Wolff, E.; Binard, M. Extraction of land use/land cover related information from very high resolution data in urban and suburban areas. Remote Sensing in Transition. In Proceedings of the 23rd Symposium of the European Association of Remote Sensing Laboratories, Ghent, Belgium, 2–5 June 2003; pp. 237–244.
 45. Gao, Y.; Mas, J.F. A comparison of the performance of pixel-based and object-based classifications over images with various spatial resolutions. *Online J. Earth Sci.* **2008**, *2*, 27–35.
 46. Blaschke, T. Object based image analysis for remote sensing. *ISPRS J. Photogramm. Remote Sens.* **2010**, *65*, 2–16, doi:10.1016/j.isprsjprs.2009.06.004.
 47. Boggs, G.S. Assessment of SPOT 5 and QuickBird remotely sensed imagery for mapping tree cover in savannas. *Int. J. Appl. Earth Obs. Geoinf.* **2010**, *12*, 217–224.
 48. Yan, G.; Mas, J.F.; Maathuis, B.; Xiangmin, Z.; Van Dijk, P. Comparison of pixel-based and object-oriented image classification approaches—A case study in a coal fire area, Wuda, Inner Mongolia, China. *Int. J. Remote Sens.* **2006**, *27*, 4039–4055.
 49. Weih, R.C.; Riggan, N.D. Object-based classification vs. pixel-based classification: Comparative importance of multi-resolution imagery. *Int. Arch. Photogramm. Remote Sens. Spat. Inf. Sci.* **2010**, *38*, C7.
 50. Whiteside, T.G.; Boggs, G.S.; Maier, S.W. Comparing object-based and pixel-based classifications for mapping savannas. *Int. J. Appl. Earth Obs. Geoinf.* **2011**, *13*, 884–893.
 51. Desclée, B.; Bogaert, P.; Defourny, P. Forest change detection by statistical object-based method. *Remote Sens. Environ.* **2006**, *102*, 1–11.
 52. Stagakis, S.; González-Dugo, V.; Cid, P.; Guillén-Climent, M.L.; Zarco-Tejada, P.J. Monitoring water stress and fruit quality in an orange orchard under regulated deficit irrigation using narrow-band structural and physiological remote sensing indices. *ISPRS J. Photogramm. Remote Sens.* **2012**, *71*, 47–61.
 53. Gärtner, P.; Förster, M.; Kurban, A.; Kleinschmit, B. Object based change detection of Central Asian Tugai vegetation with very high spatial resolution satellite imagery. *Int. J. Appl. Earth Obs. Geoinf.* **2014**, *31*, 110–121, doi:10.1016/j.jag.2014.03.004.
 54. Sasaki, T.; Imanishi, J.; Ioki, K.; Morimoto, Y.; Kitada, K. Object-based classification of land cover and tree species by integrating airborne LiDAR and high spatial resolution imagery data. *Landsc. Ecol. Eng.* **2012**, *8*, 157–171.
 55. Zhang, Z.; Liu, X. WorldView-2 satellite imagery and airborne LiDAR data for object-based forest species classification in a cool temperate rainforest environment. In *Developments in Multidimensional Spatial Data Models*; Springer: Berlin/Heidelberg, Germany, 2013; pp. 103–122.
 56. Machala, M.; Zejdová, L. Forest mapping through object-based image analysis of multispectral and LiDAR aerial data. *Eur. J. Remote Sens.* **2014**, *47*, 117–131.
 57. Wang, H.; Pu, R.; Zhu, Q.; Ren, L.; Zhang, Z. Mapping health levels of *Robinia pseudoacacia* forests in the Yellow River delta, China, using IKONOS and Landsat 8 OLI imagery. *Int. J. Remote Sens.* **2015**, *36*, 1114–1135.
 58. Nikolakopoulos, K.; Oikonomidis, D. Quality assessment of ten fusion techniques applied on Worldview-2. *Eur. J. Remote Sens.* **2015**, *48*, 141–167.
 59. Jovanović, D.; Govedarica, M.; Sabo, F.; Važić, R.; Popović, D. Impact analysis of pansharpening Landsat ETM+, Landsat OLI, WorldView-2, and Ikonos images on vegetation indices. In Proceedings of the Fourth International Conference on Remote Sensing and Geoinformation of the Environment (RSCy2016), Paphos, Cyprus, 4–8 April 2016; p. 968814.

60. Pontius, J.; Martin, M.; Plourde, L.; Hallett, R. Ash decline assessment in emerald ash borer-infested regions: A test of tree-level, hyperspectral technologies. *Remote Sens. Environ.* **2008**, *112*, 2665–2676.
61. Lazaridis, D.C.; Verbesselt, J.; Robinson, A.P. Penalized regression techniques for prediction: A case study for predicting tree mortality using remotely sensed vegetation indices. *Can. J. For. Res.* **2010**, *41*, 24–34.
62. Toomey, M.; Vierling, L.A. Multispectral remote sensing of landscape level foliar moisture: Techniques and applications for forest ecosystem monitoring. *Can. J. For. Res.* **2005**, *35*, 1087–1097.
63. Dalponte, M.; Ørka, H.O.; Ene, L.T.; Gobakken, T.; Næsset, E. Tree crown delineation and tree species classification in boreal forests using hyperspectral and ALS data. *Remote Sens. Environ.* **2014**, *140*, 306–317.
64. Fassnacht, F.E.; Latifi, H.; Stereńczak, K.; Modzelewska, A.; Lefsky, M.; Waser, L.T.; Straub, C.; Ghosh, A. Review of studies on tree species classification from remotely sensed data. *Remote Sens. Environ.* **2016**, *186*, 64–87.
65. Zhen, Z.; Quackenbush, L.J.; Zhang, L. Trends in automatic individual tree crown detection and delineation – Evolution of LiDAR data. *Remote Sens.* **2016**, *8*, 333.
66. Barnes, C.; Balzter, H.; Barrett, K.; Eddy, J.; Milner, S.; Suárez, J.C. Individual Tree Crown Delineation from Airborne Laser Scanning for Diseased Larch Forest Stands. *Remote Sens.* **2017**, *9*, 231.
67. McMahon, C.A. Remote sensing pipeline for tree segmentation and classification in a mixed softwood and hardwood system. *PeerJ* **2019**, *6*, e5837.
68. Wagner, F.H.; Sanchez, A.; Tarabalka, Y.; Lotte, R.G.; Ferreira, M.P.; Aidar, M.P.; Gloor, E.; Phillips, O.L.; Aragão, L.E. Using the U-net convolutional network to map forest types and disturbance in the Atlantic rainforest with very high resolution images. *Remote Sens. Ecol. Conserv.* **2019**, *5*, 360–375, doi:10.1002/rse2.111.
69. Li, J.; Hu, B.; Noland, T.L. Classification of tree species based on structural features derived from high density LiDAR data. *Agric. For. Meteorol.* **2013**, *171*, 104–114, doi:10.1016/j.agrformet.2012.11.012.
70. Wilkes, P.; Jones, S.D.; Suarez, L.; Haywood, A.; Mellor, A.; Woodgate, W.; Soto-Berelev, M.; Skidmore, A.K. Using discrete-return airborne laser scanning to quantify number of canopy strata across diverse forest types. *Methods Ecol. Evol.* **2015**, *7*, 700–712, doi:10.1111/2041-210x.12510.
71. Kim, S.; McGaughey, R.J.; Andersen, H.-E.; Schreuder, G. Tree species differentiation using intensity data derived from leaf-on and leaf-off airborne laser scanner data. *Remote Sens. Environ.* **2009**, *113*, 1575–1586.
72. Korpela, I.; Ørka, H.O.; Maltamo, M.; Tokola, T.; Hyypä, J. Tree species classification using airborne LiDAR—effects of stand and tree parameters, downsizing of training set, intensity normalization, and sensor type. *Silva Fenn.* **2010**, *44*, 319–339.
73. Hovi, A.; Korhonen, L.; Vauhkonen, J.; Korpela, I. LiDAR waveform features for tree species classification and their sensitivity to tree-and acquisition related parameters. *Remote Sens. Environ.* **2016**, *173*, 224–237.
74. Solberg, S.; Næsset, E.; Hanssen, K.H.; Christiansen, E. Mapping defoliation during a severe insect attack on Scots pine using airborne laser scanning. *Remote Sens. Environ.* **2006**, *102*, 364–376.
75. Kantola, T.; Vastaranta, M.; Yu, X.; Lyytikäinen-Saarenmaa, P.; Holopainen, M.; Talvitie, M.; Kaasalainen, S.; Solberg, S.; Hyypä, J. Classification of defoliated trees using tree-level airborne laser scanning data combined with aerial images. *Remote Sens.* **2010**, *2*, 2665–2679.
76. Vastaranta, M.; Kantola, T.; Lyytikäinen-Saarenmaa, P.; Holopainen, M.; Kankare, V.; Wulder, M.; Hyypä, J.; Hyypä, H. Area-based mapping of defoliation of Scots pine stands using airborne scanning LiDAR. *Remote Sens.* **2013**, *5*, 1220–1234.
77. Dalponte, M.; Bruzzone, L.; Gianelle, D. Tree species classification in the Southern Alps based on the fusion of very high geometrical resolution multispectral/hyperspectral images and LiDAR data. *Remote Sens. Environ.* **2012**, *123*, 258–270, doi:10.1016/j.rse.2012.03.013.
78. Alonzo, M.; Bookhagen, B.; Roberts, D.A. Urban tree species mapping using hyperspectral and lidar data fusion. *Remote Sens. Environ.* **2014**, *148*, 70–83.
79. rapidlasso-GmbH. LAStools. Software Suite for LiDAR processing. Developed by Martin Insenburg. Available online: <https://rapidlasso.com/lastools/> (accessed on 05. Mai 2019).
80. Khosravipoura, A.; Skidmore, A.K.; Insenburg, M. Generating spike-free digital surface models using LiDAR raw point clouds: A new approach for forestry applications. *Int. J. Appl. Earth Obs. Geoinf.* **2016**, *52*, 104–114.
81. Matthew, M.W.; Adler-Golden, S.M.; Berk, A.; Richtsmeier, S.C.; Levine, R.Y.; Bernstein, L.S.; Acharya, P.K.;

- Anderson, G.P.; Felde, G.W.; Hoke, M.L. Status of atmospheric correction using a MODTRAN4-based algorithm. In Proceedings of the Algorithms for multispectral, hyperspectral, and ultraspectral imagery VI, Baltimore, MA, USA, 29 April–2 May 2013; pp. 199–207.
82. Laben, C.A.; Brower, B.V. Process for Enhancing the Spatial Resolution of Multispectral Imagery Using Pan-Sharpener. U.S. Patent 6,011,875, 4 January 2000.
83. Padwick, C.; Deskevich, M.; Pacifici, F.; Smallwood, S. WorldView-2 pan-sharpening. In Proceedings of the ASPRS 2010 Annual Conference, San Diego, CA, USA, 26–30 April 2010.
84. Li, D.; Ke, Y.; Gong, H.; Li, X. Object-based urban tree species classification using bi-temporal WorldView-2 and WorldView-3 images. *Remote Sens.* **2015**, *7*, 16917–16937.
85. Hartling, S.; Sagan, V.; Sidike, P.; Maimaitijiang, M.; Carron, J. Urban Tree Species Classification Using a WorldView-2/3 and LiDAR Data Fusion Approach and Deep Learning. *Sensors* **2019**, *19*, 1284.
86. Adeline, K.; Chen, M.; Briottet, X.; Pang, S.; Paparoditis, N. Shadow detection in very high spatial resolution aerial images: A comparative study. *ISPRS J. Photogramm. Remote Sens.* **2013**, *80*, 21–38.
87. Globe, D. WorldView-2 Data Sheet. Available online: <https://gbdxdocs.digitalglobe.com/docs/worldview-2> (accessed on 1 February 2020).
88. DOC. The Foliar Browse Index field manual. In *An Update of a Method for Monitoring Possum (Trichosurus vulpecula) Damage to Forest Communities*; Department of Conservation, Wellington, NZ, 2014.
89. Kohavi, R.; John, G.H. Wrappers for feature subset selection. *Artif. Intell.* **1997**, *97*, 273–324.
90. Gutlein, M.; Frank, E.; Hall, M.; Karwath, A. Large-scale attribute selection using wrappers. In Proceedings of the 2009 IEEE Symposium on Computational Intelligence and Data Mining, Nashville, TN, USA, 30 March–2 April 2009; pp. 332–339.
91. Witten, I.H.; Frank, E.; Hall, M.A.; Pal, C.J. *Data Mining: Practical machine learning tools and techniques*; Morgan Kaufmann: **2016**.
92. Breiman, L. Random forests. *Mach. Learn.* **2001**, *45*, 5–32.
93. Belgiu, M.; Drăguț, L. Random forest in remote sensing: A review of applications and future directions. *ISPRS J. Photogramm. Remote Sens.* **2016**, *114*, 24–31.
94. Datt, B. Remote sensing of chlorophyll a, chlorophyll b, chlorophyll a+ b, and total carotenoid content in eucalyptus leaves. *Remote Sens. Environ.* **1998**, *66*, 111–121.
95. Rouse, J.W., Jr.; Haas, R.H.; Schell, J.; Deering, D. Monitoring the Vernal Advancement and Retrogradation (Green Wave Effect) of Natural Vegetation, NASA Gsfct Type Report; Texas A&M University: College Station, TX, USA, 1973.
96. Gamon, J.; Surfus, J. Assessing leaf pigment content and activity with a reflectometer. *New Phytol.* **1999**, *143*, 105–117.
97. Green, A.A.; Berman, M.; Switzer, P.; Craig, M.D. A transformation for ordering multispectral data in terms of image quality with implications for noise removal. *IEEE Trans. Geosci. Remote Sens.* **1988**, *26*, 65–74.
98. Metternicht, G. Vegetation indices derived from high-resolution airborne videography for precision crop management. *Int. J. Remote Sens.* **2003**, *24*, 2855–2877.
99. Haralick, R.M.; Shanmugam, K.; Dinstein, I.H. Textural Features for Image Classification. *IEEE Trans. Syst. Man Cybern.* **1973**, *SMC-3*, 610–621, doi:10.1109/TSMC.1973.4309314.
100. Kruse, F.; Lefkoff, A.; Boardman, J.; Heidebrecht, K.; Shapiro, A.; Barloon, P.; Goetz, A. *The Spectral Image Processing System (SIPS): Software for Integrated Analysis of AVIRIS Data*; NASA: Washington, DC, USA, 1992.
101. Khosravipour, A.; Skidmore, A.K.; Wang, T.; Isenburg, M.; Khoshelham, K. Effect of slope on treetop detection using a LiDAR Canopy Height Model. *ISPRS J. Photogramm. Remote Sens.* **2015**, *104*, 44–52, doi:10.1016/j.isprsjprs.2015.02.013.
102. Gitelson, A.A.; Merzlyak, M.N. Remote estimation of chlorophyll content in higher plant leaves. *Int. J. Remote Sens.* **1997**, *18*, 2691–2697.
103. Gao, B.-C. NDWI—A normalized difference water index for remote sensing of vegetation liquid water from space. *Remote Sens. Environ.* **1996**, *58*, 257–266.
104. Meigs, G.W.; Kennedy, R.E.; Gray, A.N.; Gregory, M.J. Spatiotemporal dynamics of recent mountain pine beetle

- and western spruce budworm outbreaks across the Pacific Northwest Region, USA. *For. Ecol. Manag.* **2015**, *339*, 71–86.
105. Verbesselt, J.; Hyndman, R.; Newnham, G.; Culvenor, D. Detecting trend and seasonal changes in satellite image time series. *Remote Sens. Environ.* **2010**, *114*, 106–115.
 106. Zörner, J.; Dymond, J.R.; Shepherd, J.D.; Wisser, S.K.; Jolly, B. LiDAR-based regional inventory of tall trees—Wellington, New Zealand. *Forests* **2018**, *9*, 702.
 107. Goodwin, N.; Coops, N.C.; Stone, C. Assessing plantation canopy condition from airborne imagery using spectral mixture analysis and fractional abundances. *Int. J. Appl. Earth Obs. Geoinf.* **2005**, *7*, 11–28.
 108. Delalieux, S.; Zarco-Tejada, P.J.; Tits, L.; Bello, M.Á.J.; Intrigliolo, D.S.; Somers, B. Unmixing-based fusion of hyperspatial and hyperspectral airborne imagery for early detection of vegetation stress. *IEEE J. Sel. Top. Appl. Earth Obs. Remote Sens.* **2014**, *7*, 2571–2582.
 109. Maack, J.; Kattenborn, T.; Fassnacht, F.E.; Enßle, F.; Hernández, J.; Corvalán, P.; Koch, B. Modeling forest biomass using Very-High-Resolution data—Combining textural, spectral and photogrammetric predictors derived from spaceborne stereo images. *Eur. J. Remote Sens.* **2015**, *48*, 245–261.
 110. Chen, X.; Zhao, Y.; Zhu, X.; Bai, Y.; Zhang, Y. Micro/Nano-Satellites: Opportunities and Challenges. *Aerospace China*. **2016**, *6*.
 111. Haboudane, D.; Miller, J.R.; Pattey, E.; Zarco-Tejada, P.J.; Strachan, I.B. Hyperspectral vegetation indices and novel algorithms for predicting green LAI of crop canopies: Modeling and validation in the context of precision agriculture. *Remote Sens. Environ.* **2004**, *90*, 337–352.
 112. Kaufman, Y.J.; Tanre, D. Atmospherically resistant vegetation index (ARVI) for EOS-MODIS. *IEEE Trans. Geosci. Remote Sens.* **1992**, *30*, 261–270.



© 2020 by the authors. Submitted for possible open access publication under the terms and conditions of the Creative Commons Attribution (CC BY) license (<http://creativecommons.org/licenses/by/4.0/>).

Chapter V

Synthesis

1 Main findings

This chapter summarizes the main findings of the three papers as well as general “lessons learned” that can be helpful for future remote sensing projects in New Zealand’s native forests.

1.1 Main findings paper I: Kauri identification

The aim of this study was to develop a method to identify kauri trees by optical RS, which can be applied in area-wide monitoring. The analysis was based on an airborne hyperspectral AISA Fenix image (437–2337 nm, 1 m² pixel resolution). The reference dataset covered a representative selection of 3165 precisely located crowns of kauri and 21 other canopy species in three study sites in the Waitakere Ranges west of Auckland. The method for kauri identification distinguishes three classes: “kauri with no to medium stress symptoms”, “other canopy vegetation with no to medium stress symptoms” and “dead and dying trees”.

The hyperspectral analysis revealed a characteristic reflectance pattern of kauri trees with a distinct long descent in the far near-infrared (NIR2) region caused by structural crown characteristics. This spectral feature can be described with a modified Normalised Water Index (mNDWI-Hyp). This index allows identifying kauri trees with high user’s and producer’s accuracies of 94.6% and 94.8% in a Random Forest (RF) classification from 21 other canopy vegetation spectra and dead and dying trees. A minimum crown diameter of 3 m was defined for the use of the AISA image with a 1m pixel size. The RF classifier performed slightly better than Support Vector Machine.

The main species that were confused with kauri in the classification show similar spectral features in the far NIR region and tend to have a similar “rough” foliage or needle-like leaves, such as rimu, tanekaha, rewarewa, tōtara, miro and kawaka. In addition, species with similar conical shapes in smaller growth stages, such as tanekaha, rimu, kahikatea and rewarewa, are easily confused with small kauri.

However, the separation of “dead/dying trees” from “other” canopy vegetation presented the main challenge. The overall accuracy (OA) of 91.7% in distinguishing the three classes was achieved with a combination of five indices on five bands in the red to NIR2 spectrum (670–1209 nm) and a bandwidth of 10 nm. This band combination can be utilised on an airborne multispectral sensor for cost-efficient large-area monitoring. The OA can be improved to 93.8% by combining “kauri” and “dead/dying” trees into one class, separately classifying low and high forest stands and a binning to 10 nm bandwidths. Additional indices with further wavelengths only improved the OA up to 0.6%.

1.2 Main findings paper II: Analysis of kauri stress symptoms with hyperspectral data

This part of the study analysed the spectral reflectance characteristics of kauri in different growth stages and stress levels. These findings informed the selection of spectral indices and the method for identifying visible stress symptoms in the kauri canopy. The canopy stress symptoms of 1258 manually edited reference crowns larger than 3 m in diameter were assessed in a field-based stress evaluation scheme with five stress levels. This assessment scheme was further developed for use with RGB aerial images. An object-based crown-level approach was used to match the crown based reference data and allowed separate analyses of different growth stages.

The analysis of non-symptomatic crowns with an aerial AISA hyperspectral image showed a high spectral variability between small kauri crowns and high inner-crown variability for large crowns. It also revealed different stress responses between different crown sizes, with more pigment-sensitive features in the dense foliage of small crowns and a stronger influence of understory vegetation in the more open canopy of larger crowns.

A combination of five indices on six bands in the VNIR1 region (450–970 nm) achieved a correlation of 0.93 (MAE 0.28, RMSE 0.43) in an RF regression for all crown sizes for five stress levels from non-symptomatic to dead. The addition of bands in the far NIR2 region with four indices on six bands from 450 to 1205 nm improved the results only slightly, with a correlation of 0.93 (MAE 0.27, RMSE 0.42). An RF regression gave the most accurate predictions, while a M5P regression tree performed nearly as well, and a linear regression resulted in slightly lower performance.

The most important index combination for the full symptom range was an NDVI in the near-infrared/red spectral range, followed by indices with red-edge and NIR bands. However, stress symptoms in smaller crowns with denser foliage are best described in combination with indices in the visible spectral range from green to red, which are sensitive to changes in the pigment composition.

A stratified approach with individual models for pre-segmented low and high forest stands improved the overall performance. The chosen bandwidth of 10 nm and a maximum number of six bands for the selected index combinations are suitable for large-area monitoring on an airborne multispectral sensor.

The recommended index selection for kauri identification with five spectral bands also performed well for stress detection, with an overall correlation of 0.93 for five stress levels. The combination can be further improved for small crowns by adding a band in the green spectral range. However, this band and index combination is adapted to the characteristic spectral features of kauri in the far near-infrared and should be tested before using it for stress analysis in other tree species. The use of the selected indices in a pixel-based analysis showed a good match compared to stress symptom patterns on aerial imagery. However, the pixel-based approach should be tested more thoroughly with matching reference data on a pixel scale.

1.3 Main findings paper III: Use of WV2 satellite data and LiDAR for kauri stress detection

The aim of this study was to test the use of a pan-sharpened WorldView-2 (WV2) satellite image and LiDAR data to detect stress symptoms in the canopy of kauri trees. The canopy conditions of 1089 manually edited reference crowns were assessed in the field and with RGB aerial images for five basic levels of canopy stress symptoms (1 – 2 – 3 – 4 – 5), with a refinement for the first symptom stages in half-level steps (1 – 1.5 – 2 – 2.5 – 3 – 4 – 5). Crowns with a mean diameter smaller than 4 m caused most of the outliers, especially in the more advanced stress levels of dying and dead trees. A correlation of 0.89 with only WV2 attributes (RMSE 0.48 and MAE of 0.34) could be achieved with an RF regression for crowns with a mean diameter larger than 4 m. A combination with LiDAR attributes enhanced the correlation to 0.92 (RMSE 0.43, MAE 0.31). The attribute selection confirmed the findings of the second study, with a red/near-infrared NDVI as the most important index for stress assessment over the full symptom range, followed by a ratio on red and green bands. It also confirmed the importance of pigment-sensitive indices with green, red and red-edge bands to improve the detection of first stress symptoms.

1.4 General lessons learned for further remote sensing work in New Zealand's native forests

The identification of a characteristic spectral feature for kauri crowns in the far NIR2 spectral region confirmed the value of hyperspectral data for identifying spectral characteristics of tree species as well as the importance of bands in the far near-infrared for species identification. Standard airborne multispectral sensors and satellite images usually do not capture these bands in the required bandwidth and spatial resolution.

A further finding relevant for future studies is the need for a high amount of reference crowns to capture the range of canopy species and their varieties, such as growth stages, stress levels and the influence of epiphytes and climbers.

The study highlights the need to address the occurrence of dead and dying crowns already for the species identification, especially in declining forests, such as PA-infected kauri forests. They are quickly overgrown in this dynamic forest environment, and their location needs to be documented.

High-resolution aerial images ($\leq 15\text{cm}$) were found to be well suited for representative and cost-efficient assessment of crown conditions in the upper canopy. The field assessment from the ground, however, proved to be challenging, especially in high and dense forest stands.

A challenge for both species identification and stress detection were mixed pixels in small crowns with conical shapes. To avoid these mixed pixels, an appropriate minimum crown size was defined according to the spatial resolution of the spectral images. The 1 m pixel size of the hyperspectral image required a

minimum crown size of 3 m, while a 4 m minimum crown size significantly improved the performance of the WV2 analysis. The WV2 image has an original pixel size of 1.8 m in the multispectral bands.

The RF algorithm proved to be superior to other algorithms, both for kauri classification and in a regression analysis for stress detection. RF algorithms can handle large variability within the reference classes and symptom values without an assumption of their distribution.

A further general finding is the recommendation to stratify the analysis according to the different growth stages of kauri. Individual index combinations for three different growth stages or two stand situations improved the performance, and also the inclusion of a LIDAR crown height attribute was an effective alternative approach.

2 Conclusions and outlook

This section highlights the main conclusions and focuses on the implications of the results for a kauri monitoring strategy. It also addresses suggestions for further research and opportunities with new sensor systems.

2.1 Main conclusions

The airborne hyperspectral analysis in this study was the first in New Zealand on native tree species in a natural forest situation. The overall objectives of this study to automatically identify kauri trees and describe canopy stress symptoms with RS data was achieved. The resulting methods enable the identification of kauri trees with high user's and producer's accuracies (>94 %) for selected bands with an airborne multispectral sensor. While the best bands for kauri identification are located in the NIR2 spectral region, stress detection only requires standard bands in the visible to NIR1 spectral range up to 970 nm. Stress monitoring can be based on satellite data, such as the tested WV2 image, as long as small crowns, here < 4 m diameter, are analysed in homogenous segments. The higher spatial resolution and smaller bandwidth of more expensive airborne multispectral data improve stress detection. Canopy stress symptoms in kauri trees could be described by a value range of symptom levels from 1 to 5, with high correlations (0.93 for airborne multispectral data and 0.89 for WV2 data) and RMSE values under 0.5 (0.42 for airborne multispectral and 0.48 for WV2 data).

2.2 Integration of the results in a kauri monitoring strategy

The results of this study present important findings on the use of RS as part of a comprehensive monitoring strategy. The identification of kauri trees or stands can be based on the methods developed in the first paper with an airborne multispectral sensor. The results complement existing knowledge about kauri locations from fieldwork and airborne surveys. For an object-based analysis, LiDAR data can be used for the segmentation of crowns. The minimum crown diameter for segmentation should be chosen according to the spatial resolution of the sensor used for the stress detection. Stands with smaller crowns should be segmented in homogenous units. A cost-efficient method for repeated monitoring of stress symptoms could be based on WV2 data for crown and canopy segments larger than 4 m in diameter. If possible, the attributes should include the maximum crown height based on LiDAR data for a stratification in growth stages. Higher accuracies and smaller object sizes can be realised with an airborne multispectral sensor with bands in the green to NIR1 spectral range.

The acquisition planning should allow for regular monitoring as well as the flexibility to capture special events, such as the effects of storms or droughts. Matching high-resolution aerial images (< 15 cm) from the same season for representative stands can serve as a reference. After significant structural changes in the forest (e.g. caused by severe dieback or a storm), the LiDAR acquisition and segmentation of crowns and stands should be repeated. Dead and dying trees should be documented since they are soon overgrown.

Further details regarding the monitoring method and the presentation of the final maps should be developed in cooperation with the users and management. This includes the choice of the multispectral sensor, which depends on the required spatial resolution, size of the area, terrain situation and available funding

2.3 Suggestions for further research

Further research should prioritise the use of LiDAR data for automatic crown- and stand-segmentation and for its contribution to identifying kauri crowns in combination with multispectral data. As part of this study, automatic crown-segmentation based on LiDAR height models was developed, and the identification of kauri with LiDAR and WV2 data was tested. These analyses showed promising results and are in preparation for publishing.

The use of time series over different seasons for kauri identification, especially the bright green spring aspect of kauri, should be analysed. Change detection in time series for the same season can help to distinguish the progress of infection from other stress factors like drought and to identify possible transmission pathways. Higher spatial resolution data (e.g. from UAV), quantitative measurements of stress

reactions in crowns and controlled experiments in pot trials could help to obtain a better understanding of canopy stress responses and serve as a reference for satellite analysis [1].

A better understanding of the spectral characteristics and stress responses in other species is necessary for the analysis of mixed stands and wall-to-wall forest health monitoring. Crown spectra from an airborne hyperspectral image can be used for spectral unmixing to analyse the species composition in heterogeneous stands. This approach can also improve the use of optical RS data with a lower spatial resolution, such as the freely available Sentinel-2 and Landsat-8 sensor systems.

In combination with the higher frequency and longer duration of drought periods caused by climate change [2], kauri dieback disease could contribute to a shift in species composition in New Zealand kauri forests. Thus, long-term monitoring should include all the main canopy species and focus on the composition and functions of the forest ecosystem [3]. Recent studies have also investigated approaches to integrate traditional Māori knowledge for a holistic approach to forest health management, which also includes social and cultural components [4-6].

Recent technical developments, such as big-data processing on online platforms, offer cost-efficient solutions for hosting and analysing large RS datasets [7]. New sensor systems, including small, cost-efficient satellite constellations [8,9], and multispectral LiDAR, should be tested. Multispectral LiDAR resolves the issue of spatial alignment between optical and LiDAR datasets and has shown promising results for tree species identification [10-11]. In areas where LiDAR data are not available or are too outdated, optical-derived height models from stereo imagery can serve as a cost-efficient alternative [12,13].

3 References

1. Dash, J.; Pearse, G.; Watt, M. UAV multispectral imagery can complement satellite data for monitoring forest health. *Remote Sensing* **2018**, *10*, 1216.
2. IPCC. Climate Change 2013: The Physical Science Basis: Working Group I Contribution to the Fifth Assessment Report of the Intergovernmental Panel on Climate Change; Cambridge University Press, 2014.
3. Lausch, A.; Borg, E.; Bumberger, J.; Dietrich, P.; Heurich, M.; Huth, A.; Jung, A.; Klenke, R.; Knapp, S.; Mollenhauer, H. Understanding forest health with remote sensing, part iii: requirements for a scalable multi-source forest health monitoring network based on data science approaches. *Remote sensing* **2018**, *10*, 1120.
4. Nuttall, P.; Ngakuru, W.; Marsden, M. Te Roroa effects assessment for Kauri Dieback disease—(Phytophthora taxon Agathis—PTA). Report prepared for Te Roroa and the Kauri Dieback Joint Agency Response by Wakawhenua, 2010.
5. Shortland, T.; Wood, W. Kia Toitu He Kauri, Kauri Dieback Tangata Whenua Roopu Cultural Impact Assessment. Report by Repo Consultancy Ltd, commissioned by the Ministry of Primary Industries NZ / the Kauri Dieback Programme. Available online: <https://www.kauridieback.co.nz/media/1813/shortland-wood-2011.pdf> (accessed on 5 March 2020).
6. Lambert, S.; Waipara, N.; Black, A.; Mark-Shadbolt, M.; Wood, W. Indigenous biosecurity: Māori responses to kauri dieback and myrtle rust in Aotearoa New Zealand. In *The Human Dimensions of Forest and Tree Health*, Springer, 2018; pp. 109–137.
7. Gorelick, N.; Hancher, M.; Dixon, M.; Ilyushchenko, S.; Thau, D.; Moore, R. Google Earth Engine: Planetary-scale geospatial analysis for everyone. *Remote Sensing of Environment* **2017**, *202*, 18–27.
8. Chen, X.; Zhao, Y.; Zhu, X.; Bai, Y.; Zhang, Y. Micro/nano-satellites: opportunities and challenges. *Aerospace China* **2016**, *6*.
9. Planet-Labs-Inc. Planet imagery product specifications. Available online: https://assets.planet.com/docs/Planet_Combined_Imagery_Product_Specs_letter_screen.pdf (accessed on 10 April 2020).
10. Budei, B.C.; St-Onge, B. Variability of multispectral lidar 3D and intensity features with individual tree height and its influence on needleleaf tree species identification. *Canadian Journal of Remote Sensing* **2018**, *44*, 263–286.
11. Kukkonen, M.; Maltamo, M.; Korhonen, L.; Packalen, P. Multispectral airborne LiDAR data in the prediction of boreal tree species composition. *IEEE Transactions on Geoscience and Remote Sensing* **2019**.
12. Maack, J.; Kattenborn, T.; Fassnacht, F.E.; Enßle, F.; Hernández, J.; Corvalán, P.; Koch, B. Modeling forest biomass using very-high-resolution data—combining textural, spectral and photogrammetric predictors derived from spaceborne stereo images. *European Journal of Remote Sensing* **2015**, *48*, 245–261.
13. Meng, S.; Pang, Y.; Zhang, Z.; Jia, W.; Li, Z. Mapping aboveground biomass using texture indices from aerial photos in a temperate forest of Northeastern China. *Remote Sensing* **2016**, *8*, 230.

Appendix - Curriculum Vitae

Name Meiforth, Jane Jutta
 Nationality German
 Birth 20.10.1971 Husum, Germany
 Contact 126A Waimairi Road, 8041 Christchurch, New Zealand
 jane.meiforth@pg.canterbury.ac.nz

School

1978 - 1982	Primary School	Grundschule Harkesheide, Norderstedt, Germany
1982 - 1991	Secondary School	Lessing Gymnasium, Norderstedt, Germany

Academic Studies

1991 - 1992	Biology	University of Würzburg, Germany
1992 - 2001	Landscape and Open Space Planning	Leibniz University of Hanover, Germany
2009 - 2010	Nature and Monument Preservation	Technical College Nord Trøndelag, Norway
2012 - 2013	UniGIS Professional (distance study)	University of Salzburg, Austria
since 2015	Doctoral Studies in Remote Sensing and Forestry	University of Trier, Germany and University of Canterbury, New Zealand

Professional work

10 / 2001 – 11 / 2002	Scientific Assistant	Leibniz University of Hanover, Germany
11 / 2001 – 04 / 2002	Freelancer for Geo Information System (GIS) Analysis	Hanover municipality, Germany
04 / 2002 – 02 / 2005	Graduate Engineer for Landscape Planning and GIS	Königslutter municipality, Germany
05 / 2005 – 07 / 2014	Graduate Engineer for Nature Management and GIS analysis	Trondheim municipality, Norway
Since 10 / 2019	Researcher Forest Remote Sensing	Manaaki Whenua Landcare Research, New Zealand